UNIVERSITY OF LEEDS

Dielectrics for High Temperature Capacitors Applications

by

Saeed Ullah Jan

Submitted in accordance with requirements for the degree of Doctor of Philosophy.

The University of Leeds

Institute for Materials Research

School of Chemical and Process Engineering

September, 2015

The candidate confirms that the work submitted is his own, except where work which has formed part of jointly authored publications has been included. The contribution of the candidate and the other authors to this work has been explicitly indicated below. The candidate confirms that appropriate credit has been given within the thesis where references has been made to the work of others.

List of publications:

1. Electrical properties of Ca-modified $N_{0.5}Bi_{0.5}TiO_3$ – $BaTiO_3$ ceramics. Saeed Ullah Jan, Aurang Zeb, Steven J. Milne, (2014). Ceramics International, volume 40 (15439 – 15445).

The majority of the work included within the publication is directly attributable to Mr Saeed Ullah Jan, except for some piezoelectric and ferroelectric measurements, for example polarization electric field (P-E) hysteresis loops and bipolar strain electric field (S-E) loops measurements, which was conducted by Aurang Zeb from the same research group under the guidance of academic Supervisor Steven J. Milne. Results of the publication is discussed in chapter 4.

Acknowledgements

I would like to thank my supervisor Dr Steven J. Milne for their guidance and support for the last 4 years. I am extremely grateful for his motivation and constructive comments I have received during my research. I would like to thank all the IMR staff who were very helpful, in particular the entire LEMAS team, Dr John, Dr Mike and Stuart for every possible help and advice all the times.

I would like to thank the Govt. of Pakistan (HEC) and Islamia College Peshawar (KPK) for sponsoring and also the worthy Vice Chancellor Ajmal Khan for his every possible help during my research.

I would like to thank all other PhD students whom I worked with during my research at Leeds, for their friendship and their possible help in difficult times, especially, Faith Bramdo, Antonio, Taurn Kakkar, Jayakrishnan Chandrappan and A-Zeb and their many years of friendship.

Finally I would like to thank my family and friends for their continuous support, particularly my ever sweet life partner Shahida Saeed who was always there to keep me going in hard times. I would not like to forget enjoying with my sweet Laiba Saeed and Safwan Saeed during my stressed times at Leeds. I also express my sincere gratitude towards my brother in law Rafiq Aslam and sister in law Asia Rafeeq for taking care and provision of all possible facilities to my sweetest and beautiful, Jalwa Saeed, Salwa Saeed and Affan Saeed in Pakistan in my absence. I dedicate this thesis to my father (late) and mother. This task was possible because of the prayers of my mother and relatives.

Abstract

Most of the dielectric materials developed in this thesis were relaxor dielectrics with very broad, frequency dependent peaks in relative permittivity-temperature, ε_r – T, plots. In some cases, plateau-like permittivity plots with very wide temperature ranges of stable permittivity varying by no more than ±15 % were obtained through compositional engineering of the relaxor base material using high levels of lattice substitution of cations of different charge and size to the host lattice.

The solid solution series $(1–x)Na_{0.5}Bi_{0.5}TiO_3 – xBa_{0.8}Ca_{0.2}TiO_3$ [(1–x)NBT–xBCT] was studied initially: it showed little evidence of temperature-stable relative permittivity. However, 0.85NBT – 0.15BCT ceramics modified by $BiMg_{0.5}Ti_{0.5}O_3$, [BMT], were more promising. The series, $(1–x)[0.85Na_{0.5}Bi_{0.5}TiO_3 – 0.15Ba_{0.8}Ca_{0.2}TiO_3] – xBiMg_{0.5}Ti_{0.5}O_3$, x = 0.3, gave ε_r ~ 1720 ± 15 %, in the temperature range 120 to 450 ºC, and low dielectric loss tangent, $\tan\delta \leq 0.02$, over the slightly narrower temperature range, 150 to 360 ºC. Thus an upper operating temperature > 300°C was demonstrated but without also achieving sub-zero temperature capability.

Similarly, the system $(1–x)[0.85Na_{0.5}Bi_{0.5}TiO_3 – 0.15Ba_{0.8}Ca_{0.2}TiO_3] – xLiNbO_3$ abbreviated *[(1–x)[NBT – BCT] – xLN]* gave ε_r ~ 2630 ± 15 % from 50 ºC to 410 ºC, and $\tan\delta \leq 0.02$ from 120 ºC to 400 ºC, at composition x = 0.06. The incorporation of $NaNbO_3$ [NN] in place of $LiNbO_3$ achieved the desired sub-zero temperature capability in relative permittivity, and with an upper temperature limit slightly above 200 ºC. Examples include *(1–x)[NBT – BCT] – xNN* composition x = 0.3 with ε_r = 1400 ± 15 % from -50 to 240 °C and $\tan\delta \leq 0.02$ from 20 ºC to 240

ºC; for x = 0.4, ε_r = 1300 ± 15 % from -70 to 210 °C and tanδ ≤ 0.02 from -10 ºC to 210 ºC.

In terms of the project goal of achieving a temperature range of stable permittivity combined with a low loss extending from temperatures of -55 °C (to meet the Electronic Industry Alliance military specification) up to 300 °C, the binary solid solution system (1–x)$Ba_{0.6}Sr_{0.4}Zr_{0.2}Ti_{0.8}O_3$ – x$BiMg_{0.5}Ti_{0.5}O_3$ *[(1–x)BSZT – xBMT]* was most promising. However there was a trade-off in that permittivity values were lower than the foregoing systems. The (1–x)BSZT – xBMT sample composition x = 0.2 gave ε_r ~ 500 ± 15%, in the temperature range -70 to 300 ºC and tanδ ≤ 0.02, in the range -60 to 300 ºC. This system closely matches the target temperature-range of the project, but the volumetric efficiency of a capacitor made from this dielectric would be compromised due its moderate relative permittivity values. Slightly higher values of relative permittivity were obtained for x = 0.3 in the (1–x)BSZT – xBMT series, with ε_r ~ 590 ± 15%, across the temperature range -60 to 340 ºC, but in this case the temperature range of low dielectric losses tanδ ≤ 0.02 was restricted to -10 to 280 ºC. Piezoelectric properties of selected samples have also been investigated in the thesis.

Table of Contents

Acknowledgements ..... **iii**

Abstract ..... **iv**

Table of Contents ..... **vi**

List of Tables ..... **xiii**

List of Figures ..... **xv**

Abbreviations and Symbols ..... **xxviii**

Chapter 1 ..... **1**

1.1 Introduction 1

1.2 Aims and Objectives 3

Chapter 2 Background science and literature review……4

2.1 Dielectrics 4

2.1.1 Dielectric loss or tanδ 5

2.1.2 Dipole moment μ 6

2.1.3 Capacitors 7

2.2 Electric Polarization 8

2.2.1 Space charge polarization 9

2.2.2 Dipolar or orientational polarization 10

2.2.3 Ionic polarization 10

2.2.4 Electronic polarization or atomic polarization 11

2.3 Ferroelectricity 12

2.4 Perovskites ABO_3 14

2.5 Ferroelectric domains and polarisation-electric field response (P-E) 18

2.6 Curie Weiss law 21

2.7 Relaxor ferroelectrics 22

2.8 Piezoelectricity 24

2.9 Electrostriction 27

2.10 Lead zirconate titanate, PZT 28

2.11 Poling 29

2.12 Lead zirconate titanate based piezoelectrics 30

2.13 Barium titanate - based compositions 31

2.14 Sodium bismuth titanate based solid solutions 36

2.15 Summary 42

2.16 Background science to processing and characterization techniques 44

2.16.1 Calcination 44

2.16.2 Sintering 44

2.16.3 X-ray diffraction 46

2.16.4 Scanning electron microscopy 50

2.16.4.1 Principle of SEM 51

Chapter 3 Experimental methods 54

3.1 Powder fabrication methods 54

3.1.1 Powders preparation 54

3.1.2 Sample preparation methods 55

3.1.2.1 Conventional ball milling 56

3.1.2.2 Drying of Milled powder 57

3.1.3 Calcination 58

3.1.4 Shaping of powder into ceramics 58

3.1.5 Sintering 59

3.1.6 Finishing and grinding of ceramics 62

3.2 Characterization techniques 64

3.2.1 X-ray powder diffraction examinations 64

3.2.2 Scanning electron microscopy (SEM) 64

3.2.3 Transmission electron microscopy (TEM) 64

3.2.4 Electrical measurements 65

3.2.4.1 Dielectric analysis 65

3.2.4.2 Resistivity measurements 66

3.2.5 Piezoelectric measurements 67

3.2.5.1 Poling 67

Chapter 4 Examination of $(1–x)Na_{0.5}Bi_{0.5}TiO_3 – xBa_{0.8}Ca_{0.2}TiO_3$ ceramics **68**

4.1 Introduction 68

4.1.1 Results 70

4.1.2 XRD analysis of $(1–x)Na_{0.5}Bi_{0.5}TiO_3 – xBa_{0.8}Ca_{0.2}TiO_3$ 71

4.1.3 Dielectric Measurements..... 73

4.1.3.1 Modified Curie Weiss law 78

4.1.4 Ferroelectric and piezoelectric properties 79

4.1.5 Microscopic analysis of ceramics 82

4.1.6 Transmission electron microscopy..... 85

4.1.7 Resistivity study 88

4.1.8 Conclusions 89

4.2 Effects of bismuth oxide excess on properties of $(1–x)Na_{0.5}Bi_{0.5}TiO_3 – xBa_{0.8}Ca_{0.2}TiO_3$ ceramics 90

4.2.1 Summary 90

4.2.2 Compositional analysis 91

4.2.3 Examination of powders of crushed ceramics using XRD 92

4.2.4 Dielectric characterization 94

4.2.4.1 Modified Curie Weiss law 99

4.2.5 Ferroelectric and piezoelectric properties 101

4.2.6 Microstructural analysis 105

4.2.7 Resistivity study 107

4.2.8 Overall Conclusions 109

Chapter 5 Study of the properties of $(1–x)[(Na_{0.5}Bi_{0.5}TiO_3)_{1-y} – (Ba_{0.8}Ca_{0.2}TiO_3)_y] – xBiMg_{0.5}Ti_{0.5}O_3$ ternary system……...111

5.1 Introduction 111

5.1.1 X-ray examination 113

5.1.2 Dielectric analysis 115

5.1.3 Ferroelectric and piezoelectric measurements 121

5.1.4 Microstructural study 123

5.1.5 Conclusions: 125

5.2 Examination of the effects of 3wt.% Bi_2O_3 on (1–x)[$0.85Na_{0.5}Bi_{0.5}TiO_3 – 0.15Ba_{0.8}Ca_{0.2}TiO_3$] – $xBiMg_{0.5}Ti_{0.5}O_3$ 126

5.2.1 Relative permittivity 127

5.2.2 Conclusions from 3wt.% Bi_2O_3 modified ceramics 130

5.3 Examination of (1–x)[$(Na_{0.5}Bi_{0.5}TiO_3)_{1-y} – (Ba_{0.8}Ca_{0.2}TiO_3)_y$] – $xBiMg_{0.5}Ti_{0.5}O_3$ 131

5.3.1 X-ray powder diffraction examination 131

5.3.2 Relative permittivity analysis 132

5.3.3 Conclusions from effects of ceramics with different x, y concentrations 136

Chapter 6 Dielectric properties of ternary system (1–x)[$0.85Na_{0.5}Bi_{0.5}TiO_3 – 0.15Ba_{0.8}Ca_{0.2}TiO_3$] – $xLiNbO_3$ …… 137

6.1 Introduction 137

6.2 Batch calculations 138

6.3 X-ray diffraction study 139

6.4 Dielectric analysis 142

6.4.1 Modified Curie Weiss law 147

6.5 Microstructural analysis 148

6.6 Piezoelectric measurements 148

6.7 dc resistivity measurements 149

6.8 Conclusions 151

Chapter 7 Dielectric properties of ternary system, (1–x)[0.85$Na_{0.5}Bi_{0.5}TiO_3$ – 0.15$Ba_{0.8}Ca_{0.2}TiO_3$] – x$NaNbO_3$ ……...152

7.1 Introduction 152

7.2 Results and discussion 153

7.2.1 X- ray analysis 153

7.3 Dielectric properties 155

7.3.1 Modified Curie Weiss law 159

7.4 Density and microstructural analysis 160

7.5 Resistivity analysis 162

7.6 Conclusions 163

Chapter 8 Dielectric properties of (1–x)$Ba_{0.6}Sr_{0.4}Zr_{0.2}Ti_{0.8}O_3$ – x$BiMg_{0.5}Ti_{0.5}O_3$ solid solutions ……164

8.1 Introduction 164

8.2 Results 165

8.2.1 X-ray diffraction analysis of (1–x)$Ba_{0.6}Sr_{0.4}Zr_{0.2}Ti_{0.8}O_3$ – x$BiMg_{0.5}Ti_{0.5}O_3$ 165

8.2.2 Relative permittivity of solid solutions (1-x)$Ba_{0.6}Sr_{0.4}Zr_{0.2}Ti_{0.8}O_3$ – x$BiMg_{0.5}Ti_{0.5}O_3$ ($0 \leq x \leq 0.8$). 166

8.2.2.1 Modified Curie Weiss law 170

8.2.3 Resistivity analysis 171

8.2.4 Polarization-electric field hysteresis loop 172

8.2.5 Microstructural examination 174

8.3 Conclusions 175

Chapter 9 Overall discussions and conclusions 176

Future work 183

Appendix 1 184

Table A1.1 List of ionic radii of selected elements discussed in the solid solutions in this study. 184

References 185

List of Tables

Table 3.1 Chemical purity and supplier of raw powders. 55

Table 3. 2 Sintering temperature and dwell times for ceramics discussed in chapter 4, 5, 6, 7, and 8. 61

Table 4. 1 The calculated wt.% contribution of precursors in ceramic system $(1–x)Na_{0.5}Bi_{0.5}TiO_3 – xBa_{0.8}Ca_{0.2}TiO_3$, $(0 \leq x \leq 1)$. 70

Table 4.2 Summary of dielectric properties of $(1–x)Na_{0.5}Bi_{0.5}TiO_3 – xBa_{0.8}Ca_{0.2}TiO_3$. 78

Table 4.3 Piezoelectric and ferroelectric properties of $(1–x)Na_{0.5}Bi_{0.5}TiO_3 – xBa_{0.8}Ca_{0.2}TiO_3$ ceramics 82

Table 4.4 Dielectric properties of $(1–x)Na_{0.5}Bi_{0.5}TiO_3 – xBa_{0.8}Ca_{0.2}TiO_3$ + 3wt.% Bi_2O_3 ceramics. 99

Table 4.5 Summary of the comparison of standard and 3wt.% Bi_2O_3 -modified $(1–x)Na_{0.5}Bi_{0.5}TiO_3 – xBa_{0.8}Ca_{0.2}TiO_3$.ceramics. 101

Table 4.6 Ferroelectric and Piezoelectric properties of ceramics system, $(1–x)Na_{0.5}Bi_{0.5}TiO_3 – xBa_{0.8}Ca_{0.2}TiO_3$ + 3wt.% Bi_2O_3. 104

Table 4.7 A comparison of ferroelectric and piezoelectric properties of bismuth oxide excess and standard $(1–x)Na_{0.5}Bi_{0.5}TiO_3 – xBa_{0.8}Ca_{0.2}TiO_3$ ceramics. 105

Table 5.1 Calculated wt.% of each precursor in $(1–x)[0.85\ Na_{0.5}Bi_{0.5}TiO_3 – 0.15Ba_{0.8}Ca_{0.2}TiO_3] – xBiMg_{0.5}Ti_{0.5}O_3$ ceramics system. 113

Table 5.2 Dielectric properties of (1–x)[0.85$Na_{0.5}Bi_{0.5}TiO_3$ – 0.15$Ba_{0.8}Ca_{0.2}TiO_3$] – x$BiMg_{0.5}Ti_{0.5}O_3$, ($0 \leq x \leq 0.7$) system. 120

Table 5.3 Comparison of dielectric properties of unmodified and 3wt.% Bi_2O_3-modified (1–x)[0.85$Na_{0.5}Bi_{0.5}TiO_3$ – 0.15$Ba_{0.8}Ca_{0.2}TiO_3$] – x$BiMg_{0.5}Ti_{0.5}O_3$ ceramics. 129

Table 5.4 A summary of dielectric properties of (1–x)[$(Na_{0.5}Bi_{0.5}TiO_3)_{1-y}$ – $(Ba_{0.8}Ca_{0.2}TiO_3)_y$] – x$BMg_{0.5}Ti_{0.5}O_3$ [(x,y) = (0.4, 0.05), (0.3, 0.3), (0.4, 0.3), (0.4, 0.4)] ceramics. 135

Table 6.1 Calculations of wt.% of raw powders of ceramics series (1–x)[0.85 $Na_{0.5}Bi_{0.5}TiO_3$ – 0.15$Ba_{0.8}Ca_{0.2}TiO_3$] – x$LiNbO_3$, ($0 \leq x \leq 0.1$). 138

Table 6.2 Summary of dielectric properties of ceramics series (1–x)[0.85 $Na_{0.5}Bi_{0.5}TiO_3$ – 0.15$Ba_{0.8}Ca_{0.2}TiO_3$] – x$LiNbO_3$, ($0 \leq x \leq 0.15$) at 1 kHz. ... 146

Table 7.1 The weight percent contribution of each precursor in ceramics series (1–x)[0.85$Na_{0.5}Bi_{0.5}TiO_3$ – 0.15$Ba_{0.8}Ca_{0.2}TiO_3$] – x$NaNbO_3$, ($0 \leq x \leq 0.5$). 153

Table 7.2 Summary of the dielectric properties of ceramics system (1–x) [0.85$Na_{0.5}Bi_{0.5}TiO_3$ – 0.15$Ba_{0.8}Ca_{0.2}TiO_3$] – x$NaNbO_3$, ($0 \leq x \leq 0.5$). 159

Table 8.1 Summary of dielectric properties of (1–x)$Ba_{0.6}Sr_{0.4}Zr_{0.2}Ti_{0.8}O_3$ – x$BiMg_{0.5}Ti_{0.5}O_3$ ceramics 170

List of Figures

Figure 2.1 Phasor diagram of (a) ideal and (b) real capacitor. Modified as (Moulson, 2003 Wolfe, 2015) 6

Figure 2.2 Schematic representation of dipole moment. 6

Figure 2.3 Schematic diagram of air filled and dielectric filled capacitor.(Levi, 2009) 8

Figure 2.4 Space charge polarization. Modified after (Moulson and Herbert, 2003) 9

Figure 2.5 Dipolar polarization mechanism. Modified as (DoITPoMS, Access date 19th Sep 2015) 10

Figure 2.6 Ionic polarization mechanism. Modified as (DoITPoMS, Access date 19th Sep 2015) 11

Figure 2.7 Electronic polarization in the unstressed and stressed conditions. Modified as (DoITPoMS, Access date 19th Sep 2015) 12

Figure 2.8 Variation in relative permittivity with a.c frequency. Modified as (Moulson and Herbert, 2003) 12

Figure 2.9 Polarization mechanism in ABO_3 Perovskite unit cell. 13

Figure 2.10 Cubic perovskite ABO_3 structure unit cell. Modified as (Rödel et al., 2009). The shaded volume represents oxygen octahedra. 14

Figure 2.11 Unit cells of Cubic and Tetragonal $BaTiO_3$ showing the corner sharing TiO_6 octahedra and off centred Ti ion. (Taken from Steven J. Milne Lecture PEME1730) 16

Figure 2.12 Unit cell phase transformations in barium titanate. Modified as (Jaffe, 1971) 17

Figure 2.13 The seven crystal systems and fourteen Bravias lattices. (Pietrovito . A, 2015) 17

Figure 2.14 A schematic representations of 90º and 180º domains. (Moulson and Herbert, 2003) 18

Figure 2.15 A typical ferroelectric polarization-electric field hysteresis loop. (Taken from Steven J. Milne lecture PEME 1710)..... 20

Figure 2.16 Temperature-dependent relative permittivity plot of single crystal $BaTiO_3$. (Jaffe, 1971, Moulson and Herbert, 2003)..... 21

Figure 2.17 The temperature dependence of the real part of the dielectric permittivity measured at different frequencies for single crystal of relaxor compound $Pb(Mg_{1/3}Nb_{2/3}O_3)$. (Shvartsman, 2012)..... 22

Figure 2.18 (a) Direct piezoelectric effect and (b) converse piezoelectric effect. Modified as (Moulson and Herbert, 2003)..... 26

Figure 2.19 Phase Diagram of the PZT system. (Shrout and Zhang, 2007) 29

Figure 2.20 Representation of (a) unpoled and (b) poled ceramics. 29

Figure 2.21 Temperature-dependent relative permittivity at frequencies 1 kHz – 1 MHz for $(1–x)Ba_{0.8}Ca_{0.2}TiO_3 – xBi(Mg_{0.5}Ti_{0.5})O_3$, (x = 0.5). (Zeb, 2011) 33

Figure 2.22 Temperature-dependent relative permittivity and tanδ at frequencies 1 kHz – 1 MHz for for $0.45Ba_{0.8}Ca_{0.2}TiO_3 – (0.55 – x) Bi(Mg_{0.5}Ti_{0.5})O_3 – xNaNbO_3$, (x = 0).(Zeb, 2013)..... 33

Figure 2.23 Temperature-dependent relative permittivity and tanδ at frequencies 1 kHz – 1 MHz for $Ba_{0.8}Ca_{0.2}TiO_3 – xBiZn_{0.5}Ti_{0.5}O_3$, (x = 0.3). 34

Figure 2.24 Temperature-dependent relative permittivity and tanδ at 1 kHz and 10 kHz, for $BaTiO_3 – BiZn_{0.5}Ti_{0.5}O_3 – NaNbO_3$. (Raengthon, 2013)..... 35

Figure 2.25 Temperature-dependent relative permittivity and tanδ at 1 kHz – 1 MHz for $0.7BaTiO_3 – 0.3BiScO_3$. (Ogihara, 2009) 35

Figure 2.26 Temperature-dependent relative permittivity and tanδ of stoichiometric (S) and 2 mol% Ba deficient (-2Ba) (a and b) $50BaTiO_3 – 25BiZn_{0.5}Ti_{0.5}O_3 – 25BiScO_3$ (c and d) $55BaTiO_3 – 22.5BiZn_{0.5}Ti_{0.5}O_3 – 22.5BiScO_3$ and (e and f) $60BaTiO_3 – 20BiZn_{0.5}Ti_{0.5}O_3 – 20BiScO_3$ ceramics. (Raengthon et al. 2012)..... 36

Figure 2.27 NBT Pervoskite pseudo-cubic structure, Oxygen (O) at each six edges of octahedra, not shown for clear view of B-cation). (Aksel., 2010)..... 38

Figure 2.28 Temperature-dependent relative permittivity and tanδ of $(1–x)[0.94\ Na_{0.5}Bi_{0.5}TiO_3 – 0.06BaTiO_3] – xK_{0.5}Na_{0.5}NbO_3$ (a) x = 0.09 (b) x = 0.12, (c) x = 0.15, and (d) x = 0.18 (Dittmer 2011) 40

Figure 2.29 Temperature-dependent relative permittivity and loss factor for $(1 – x)\ [0.6Na_{0.5}Bi_{0.5}TiO_3 – 0.4Bi_{0.5}K_{0.5}TiO_3] – xK_{0.5}Na_{0.5}NbO_3$ of x = 0.08, 0.10, 0.12, 0.15) up to 400 ºC. (Dittmer, 2012) 41

Figure 2.30 (a) A schematic diagram showing three spherical particles and the various mass transport paths that provide neck growth and in some cases pore shrinkage (b) neck formation in spherical particles. (German, 2010) 45

Figure 2.31 (a) Generation of X-rays (Poppe et al., 2001), (b) Characteristic X-rays generation (Seibert, 2004) and (c) Intensity V.s wavelength of X-rays (Moulson and Herbert, 2003) 47

Figure 2.32 Interference of electromagnetic waves. (Horton, 2008) 48

Figure 2.33 X-Ray diffraction and Bragg's law. (Callister, 2000) 49

Figure 2.34 (a) A schematic diagram of electron microscope (Atteberry, 2014) and (b) Interaction of electrons with specimen. (Reimer, 1998)..... 52

Figure 3.1 A photograph of ball milling machine and the grinding media. 57

Figure 3.2 A photograph of solvent distillation reflux kit. 57

Figure 3.3 Photographs of (a) Uniaxial press and electronic balance and (b) Cold isostatic press, Vacuum pump and ceramics in evacuated white gloves. 59

Figure 3.4 Heating profile for sintering ceramics reported in Chapters, 4 - 8. 60

Figure 3.5 A photograph of grinding/polishing machine Motopal 2000. 62

Figure 3.6 Flow chart of ceramic processing steps leading to characterizations. 63

Figure 3.7 A photograph of the equipment used for dielectric measurements. 66

Figure 4.1 (a) XRD patterns of the ceramic system $(1–x)Na_{0.5}Bi_{0.5}TiO_3 – xBa_{0.8}Ca_{0.2}TiO_3$, $(0 \leq x \leq 1)$.and (b) A broad view of 111, 002/200 peaks, the shaded region shows a mixed phase region (T = Tetragonal and C = Cubic). 71

Figure 4.2 Variation in lattice parameters of ceramic system $(1–x)Na_{0.5}Bi_{0.5}TiO_3 – xBa_{0.8}Ca_{0.2}TiO_3$, $(0 \leq x \leq 1)$, the shaded region shows a mixed phase region. 73

Figure 4.3 Temperature-dependent relative permittivity (ε_r) and loss tangent (tanδ) of $(1–x)Na_{0.5}Bi_{0.5}TiO_3 – xBa_{0.8}Ca_{0.2}TiO_3$, (a) x = 0, (b) x = 0.05, (c) x = 0.08, (d) x = 0.1, (e) x = 0.12 and (f) x = 0.15. (data set continued in Figure 4.4) 74

Figure 4.4 Temperature-dependent relative permittivity (ε_r) and loss tangent (tanδ) of $(1–x)Na_{0.5}Bi_{0.5}TiO_3 – xBa_{0.8}Ca_{0.2}TiO_3$, (a) x = 0.2, (b) x = 0.3, (c) x = 0.4, (d) x = 0.5, (e) x = 0.6 and (f) x = 0.7. (data set continued in Figure 4.5) 75

Figure 4.5 Temperature-dependent relative permittivity (ε_r) and loss tangent (tanδ) of $(1–x)Na_{0.5}Bi_{0.5}TiO_3 – xBa_{0.8}Ca_{0.2}TiO_3$, (a) x = 0.8, (b) x = 0.9 and (c) x = 1 76

Figure 4.6 $\ln(1/\varepsilon – 1/\varepsilon_m)$ as a function of $\ln(T – T_m)$ of ceramic series $(1–x)Na_{0.5}Bi_{0.5}TiO_3 – xBa_{0.8}Ca_{0.2}TiO_3$, x = 0 – 1.0. 79

Figure 4.7 P-E hysteresis loops of $(1–x)Na_{0.5}Bi_{0.5}TiO_3 – xBa_{0.8}Ca_{0.2}TiO_3$, (a) x = 0 – 0.1(b) x = 0.12 – 0.3 and (c) x = 0.4 – 1.0. 81

Figure 4.8 Bipolar strain S versus electric field of $(1–x)Na_{0.5}Bi_{0.5}TiO_3 – xBa_{0.8}Ca_{0.2}TiO_3$, (a) x = 0 – 0.15 and (b) x = 0.3 – 1. 81

Figure 4.9 Geometrical densities of $(1–x)Na_{0.5}Bi_{0.5}TiO_3 – xBa_{0.8}Ca_{0.2}TiO_3$. 83

Figure 4.10 SEM micrographs of standard $(1–x)Na_{0.5}Bi_{0.5}TiO_3 – xBa_{0.8}Ca_{0.2}TiO_3$ system (a) x = 0, (b) x = 0.2, (c) x = 0.4, d) x = 0.7, (e) x = 0.8 and (f) x = 1.0. 84

Figure 4.11 TEM images of $(1–x)Na_{0.5}Bi_{0.5}TiO_3 – xBa_{0.8}Ca_{0.2}TiO_3$.system, (a–b) x = 0.1 and (c) x = 0.2..... 85

Figure 4.12 TEM elemental maps of (1–x)$Na_{0.5}Bi_{0.5}TiO_3$ – x$Ba_{0.8}Ca_{0.2}TiO_3$, x = 0.1 with dark field Ba, Bi, Ca, Na, Ti, and O EDX maps. 86

Figure 4.13 TEM elemental maps of (1–x)$Na_{0.5}Bi_{0.5}TiO_3$ – x$Ba_{0.8}Ca_{0.2}TiO_3$, x = 0.2 with dark field Ba, Bi, Ca, Na, Ti, and O EDX maps. 87

Figure 4.14 Resistivity as a function of inverse absolute temperature for (1–x)$Na_{0.5}Bi_{0.5}TiO_3$ – x$Ba_{0.8}Ca_{0.2}TiO_3$, x = 0 - 0.1. 88

Figure 4.15 (a) XRD patterns of (1–x)$Na_{0.5}Bi_{0.5}TiO_3$ – x$Ba_{0.8}Ca_{0.2}TiO_3$ + 3wt.% Bi_2O_3 ceramic system and (b) A broad view of 111, 002/200 XRD peaks, the shaded region shows a mixed phase region (T = Tetragonal and C = Cubic) (See Figure 4.1a-b for standard samples). 93

Figure 4.16 Variation of lattice parameters of ceramic series (1–x)$Na_{0.5}Bi_{0.5}TiO_3$ – x$Ba_{0.8}Ca_{0.2}TiO_3$ + 3wt.% Bi_2O_3 , the shaded region show a mixed phase region. 94

Figure 4.17 Temperature-dependent relative permittivity (ε_r) and loss tangent (tanδ) of ceramics, (1–x)$Na_{0.5}Bi_{0.5}0TiO_3$ – x$Ba_{0.8}Ca_{0.2}TiO_3$ + 3wt.% Bi_2O_3, for (a) x = 0, (b) x = 0.05, (c) x = 0.08, (d) x = 0.1, (e) x = 0.12 and (f) x = 0.15. (data set continued in Figure 4.17) 96

Figure 4.18 Temperature-dependent relative permittivity (ε_r) and loss tangent (tanδ) of ceramics, (1–x)$Na_{0.5}Bi_{0.5}TiO_3$ – x$Ba_{0.8}Ca_{0.2}TiO_3$ + 3wt.% Bi_2O_3, for (a) x = 0.2, (b) x = 0.3, (c) x = 0.4, (d) x = 0.5, (e) x = 0.6 and (f) x = 0.7. (data set continued in Figure 4.18) 97

Figure 4.19 Temperature-dependent relative permittivity (ε_r) and loss tangent (tanδ) of ceramics, (1–x)$Na_{0.5}Bi_{0.5}TiO_3$ – x$Ba_{0.8}Ca_{0.2}TiO_3$ + 3wt.% Bi_2O_3, for (a) x = 0.8 and (b) x = 0.9. 98

Figure 4.20 Temperature difference between lower temperature anomaly at T_1 and high temperature anomaly at T_2/T_m for both standard and 3wt.% Bi_2O_3 excess $(1–x)Na_{0.5}Bi_{0.5}TiO_3 – xBa_{0.8}Ca_{0.2}TiO_3$ ceramics, (x = 0 – 0.4). 98

Figure 4.21 $\ln(1/\varepsilon – 1/\varepsilon_m)$ as a function of $\ln(T – T_m)$ for $(1–x)Na_{0.5}Bi_{0.5}TiO_3 – xBa_{0.8}Ca_{0.2}TiO_3$ + 3wt.% Bi_2O_3 ceramics, x = 0 – 0.9. 100

Figure 4.22 P-E hysteresis loop for compositions $(1–x)Na_{0.5}Bi_{0.5}TiO_3 – xBa_{0.8}Ca_{0.2}TiO_3$ + 3wt.% Bi_2O_3, $0 \leq x \leq 0.15$. 103

Figure 4.23 Bipolar strain S versus electric field for compositions $(1–x)Na_{0.5}Bi_{0.5}TiO_3 – xBa_{0.8}Ca_{0.2}TiO_3$ + 3wt.% Bi_2O_3, $0 \leq x \leq 0.15$. 103

Figure 4.24 Plots showing comparison of values of effective piezoelectric constant d_{33}^* and coercive field E_C for unmodified (black and semi black spheres) and 3wt.% Bi_2O_3 modified (pink and semi pink spheres) $(1–x)Na_{0.5}Bi_{0.5}TiO_3 – xBa_{0.8}Ca_{0.2}TiO_3$ system. 104

Figure 4.25 SEM micrographs of $(1–x)Na_{0.5}Bi_{0.5}TiO_3 – xBa_{0.8}Ca_{0.2}TiO_3$ + 3wt.% Bi_2O_3, for (a) x = 0.05 (b) x = 0.2 (c), x = 0.3 (d), x = 0.5 (e), x = 0.7 and (f) x = 0.9. 106

Figure 4.26 Geometrical densities of ceramics system, $(1–x)Na_{0.5}Bi_{0.5}TiO_3 – xBa_{0.8}Ca_{0.2}TiO_3$ + 3wt% Bi_2O_3. 107

Figure 4.27 Resistivity as a function of inverse absolute temperature for $(1–x)Na_{0.5}Bi_{0.5}TiO_3 – xBa_{0.8}Ca_{0.2}TiO_3$ + 3wt.% Bi_2O_3, x = 0 – 0.1. 108

Figure 5.1(a) XRD patterns of (1–x)[0.85 $Na_{0.5}Bi_{0.5}TiO_3$ – 0.15$Ba_{0.8}Ca_{0.2}TiO_3$] – x$BiMg_{0.5}Ti_{0.5}O_3$, ($0 \leq x \leq 0.7$) and (b) a zoomed view of 111, 002/200 peaks (T = tetragonal, C = cubic) (c) A magnified XRD pattern of x = 0.7, showing secondary phases. 114

Figure 5.2 Illustration of the location of compositions (1–x)[0.85$Na_{0.5}Bi_{0.5}TiO_3$ – 0.15$Ba_{0.8}Ca_{0.2}TiO_3$] – x$BiMg_{0.5}Ti_{0.5}O_3$, ($0 \leq x \leq 0.7$) in the ternary system. 115

Figure 5.3 Temperature-dependant relative permittivity (ε_r) and loss tangent (tanδ) of ceramics (1–x)[0.85$Na_{0.5}Bi_{0.5}TiO_3$ – 0.15$Ba_{0.8}Ca_{0.2}TiO_3$] – x$BiMg_{0.5}Ti_{0.5}O_3$, (a) x = 0 (b) x = 0.05 (c) x = 0.1(d) x = 0.2 (e) x = 0.3 (f) x = 0.4 (data set continued in Figure 5.4) 118

Figure 5.4 Temperature-dependant relative permittivity (ε_r) and loss tangent (tanδ) of ceramics (1–x)[0.85$Na_{0.5}Bi_{0.5}TiO_3$ – 0.15$Ba_{0.8}Ca_{0.2}TiO_3$] – x$BiMg_{0.5}Ti_{0.5}O_3$, (a) x = 0.5 (b) x = 0.6 (c) x = 0.7..... 119

Figure 5.5 Plots of temperatures corresponding to low temperature (T_1) and high temperature (T_2) dielectric anomalies (1–x)[0.85$Na_{0.5}Bi_{0.5}TiO_3$ – 0.15$Ba_{0.8}Ca_{0.2}TiO_3$] – x$BiMg_{0.5}Ti_{0.5}O_3$, x = 0 – 0.7 (1 kHz)..... 119

Figure 5.6 Temperature-dependant relative permittivity (ε_r) and loss tangent (tanδ) of ceramics (1–x)[0.85$Na_{0.5}Bi_{0.5}TiO_3$ – 0.15$Ba_{0.8}Ca_{0.2}TiO_3$] – x$BiMg_{0.5}Ti_{0.5}O_3$, x = 0.05 – 0.5 (1 kHz). 120

Figure 5.7 P-E hysteresis loop of (1–x)[0.85$Na_{0.5}Bi_{0.5}TiO_3$ – 0.15$Ba_{0.8}Ca_{0.2}TiO_3$] – x$BiMg_{0.5}Ti_{0.5}O_3$, x = 0.05 – 0.5. 122

Figure 5.8 S-E hysteresis loop of (1–x)[0.85$Na_{0.5}Bi_{0.5}TiO_3$ – 0.15$Ba_{0.8}Ca_{0.2}TiO_3$] – x$BiMg_{0.5}Ti_{0.5}O_3$, x = 0.05 – 0.5. 122

Figure 5.9 SEM images of (1–x)[0.85$Na_{0.5}Bi_{0.5}TiO_3$ – 0.15$Ba_{0.8}Ca_{0.2}TiO_3$] – x$BiMg_{0.5}Ti_{0.5}O_3$, (a) x = 0.3, (b) x = 0.4 and (c) x = 0.5. 123

Fig 5.10. Absolute/geometrical densities of the ceramics(1–x)[0.85$Na_{0.5}Bi_{0.5}TiO_3$ – 0.15$Ba_{0.8}Ca_{0.2}TiO_3$] – x$BiMg_{0.5}Ti_{0.5}O_3$, $0 \leq x \leq 0.6$. 124

Figure 5.11 X-ray powder diffraction patterns of (1–x)[0.85$Na_{0.5}Bi_{0.5}TiO_3$ – 0.15$Ba_{0.8}Ca_{0.2}TiO_3$] – x$BiMg_{0.5}Ti_{0.5}O_3$ + 3wt.% Bi_2O_3 ($0.3 \leq x \leq 0.6$). 126

Figure 5.12 Temperature-dependent relative permittivity (ε_r) and loss tangent (tanδ) of (1–x)[0.85$Na_{0.5}Bi_{0.5}TiO_3$ – 0.15$Ba_{0.8}Ca_{0.2}TiO_3$] – x$BiMg_{0.5}Ti_{0.5}O_3$ + 3wt.% Bi_2O_3, (a) x = 0.3 (b) x = 0.4 (c) x = 0.5 and (d) x = 0.6. 128

Figure 5.13 Maximum relative permittivity, room temperature relative permittivity and temperature of maximum relative permittivity versus mol fraction $BiMg_{0.5}Ti_{0.5}O_3$, of ceramics, (1–x)[0.85$Na_{0.5}Bi_{0.5}TiO_3$ – 0.15$Ba_{0.8}Ca_{0.2}TiO_3$] – x$BiMg_{0.5}Ti_{0.5}O_3$ + 3wt.% Bi_2O_3 (x = 0.3 – 0.6). 128

Figure 5.14 X-ray diffraction patterns of, (1–x)[$(Na_{0.5}Bi_{0.5}TiO_3)_{1-y}$ – $(Ba_{0.8}Ca_{0.2}TiO_3)_y$] – x$BMg_{0.5}Ti_{0.5}O_3$ [(x,y) = (0.4, 0.05), (0.4, 0.3), (0.4, 0.3), (0.4, 0.4)]. 132

Figure 5.15 Temperature dependence of relative permittivity (ε_r) and tanδ of (1–x)[$(Na_{0.5}Bi_{0.5}TiO_3)_{1-y}$ – $(Ba_{0.8}Ca_{0.2}TiO_3)_y$] – x$BMg_{0.5}Ti_{0.5}O_3$, (a) (x, y) = (0.4, 0.05), (0.4, 0.3), (b) (0.3, 0.3), (c) (0.4, 0.3) and (d) (0.4, 0.4)..... 134

Figure 6.1 Illustration of the location of the compositions (1–x)[0.85 $Na_{0.5}Bi_{0.5}TiO_3$ – 0.15$Ba_{0.8}Ca_{0.2}TiO_3$] – x$LiNbO_3$, x = 0 – 0.15 in the relevant ternary system. 139

Figure 6.2 (a) X-ray powder diffraction patterns of ceramic system (1–x)[0.85 $Na_{0.5}Bi_{0.5}TiO_3$ – $0.15Ba_{0.8}Ca_{0.2}TiO_3$] – $xLiNbO_3$, x = 0 – 0.15 and (b) A broad view of 111, 002/200 peaks, (T = Tetragonal, C = Cubic). 141

Figure 6.3 Lattice parameters as a function of x mol % $LiNbO_3$ (LN) of, (1–x)[0.85 $Na_{0.5}Bi_{0.5}TiO_3$ – $0.15Ba_{0.8}Ca_{0.2}TiO_3$] – $xLiNbO_3$ (x = 0 – 0.08)..... 142

Figure 6.4 Temperature-dependent relative permittivity (ε_r) and tanδ of (1–x)[$0.85Na_{0.5}Bi_{0.5}TiO_3$ – $0.15Ba_{0.8}Ca_{0.2}TiO_3$] – $xLiNbO_3$ (a) x = 0, (b) x = 0.005 (c) x = 0.01 (d) x = 0.015 (e) x = 0.02 (f) x = 0.03.(data set continued in Figure 6.5) 144

Figure 6.5 Temperature-dependent relative permittivity (ε_r) and tanδ of (1–x)[$0.85Na_{0.5}Bi_{0.5}TiO_3$ – $0.15Ba_{0.8}Ca_{0.2}TiO_3$] – $xLiNbO_3$, (a) x = 0.04, (b) x = 0. 05, (c) x = 0.06 (d) x = 0.07, (e) x = 0.1, (f) x = 0.15. 145

Figure 6.6 Temperature-dependent relative permittivity (ε_r) of (1–x)[0.85 $Na_{0.5}Bi_{0.5}TiO_3$ – $0.15Ba_{0.8}Ca_{0.2}TiO_3$] – $xLiNbO_3$, (a) x = 0.005 – 0.03 and (b) x = 0.04 – 0.15) (at 1kHz), Note dielectric losses were high in x = 0.15. 146

Figure 6.7 plots of $\ln(1/\varepsilon - 1/\varepsilon_m)$ versus $\ln(T - T_m)$ for ceramic system, (1–x)[$0.85Na_{0.5}Bi_{0.5}TiO_3$ – $0.15Ba_{0.8}Ca_{0.2}TiO_3$] – $xLiNbO_3$, ($0 \leq x \leq 0.15$)..... 147

Figure 6.8 SEM micrographs of (1–x)[$0.85Na_{0.5}Bi_{0.5}TiO_3$ – $0.15Ba_{0.8}Ca_{0.2}TiO_3$] – $xLiNbO_3$ (a) x = 0.01 and (b) x = 0.02, ceramics..... 148

Figure 6.9 Variation of piezoelectric constant (d_{33}) with x mol fraction of LN for (1–x)[$0.85Na_{0.5}Bi_{0.5}TiO_3$ – $0.15Ba_{0.8}Ca_{0.2}TiO_3$] – $xLiNbO_3$, x = 0 – 0.02..... 149

Figure 6.10 Logarithm of dc resistivity as a function of 1/T of (1–x)[0.85 $Na_{0.5}Bi_{0.5}TiO_3$ – 0.15$Ba_{0.8}Ca_{0.2}TiO_3$] – x$LiNbO_3$, x = 0 – 0.04..... 150

Figure 7.1 (a) X-ray diffraction patterns of ceramic series (1–x)[0.85$Na_{0.5}Bi_{0.5}TiO_3$ – 0.15$Ba_{0.8}Ca_{0.2}TiO_3$] – x$NaNbO_3$, ($0 \leq x \leq$ 0.8).and (b) a broad view of 111 and 002/200 peak..... 154

Figure 7.2 The value of *a* lattice parameter of the ceramic system (1–x)[0.85$Na_{0.5}Bi_{0.5}TiO_3$ – 0.15$Ba_{0.8}Ca_{0.2}TiO_3$] – x$NaNbO_3$, ($0 \leq x \leq 0.45$) as function of x mol % NN. 155

Figure 7.3 a) Temperature-dependent relative permittivity (ε_r) and tanδ of (1–x)[0.85$Na_{0.5}Bi_{0.5}TiO_3$ – 0.15$Ba_{0.8}Ca_{0.2}TiO_3$] – x$NaNbO_3$, (a) x = 0, (b) x = 0.02, (c) x = 0.05, (d) x = 0.1, (e) x = 0.2 and (f) x = 0.3. (data set continued in Figure 7.4) 157

Figure 7.4 Temperature-dependent relative permittivity (ε_r) and tanδ of (1–x)[0.85$Na_{0.5}Bi_{0.5}TiO_3$ – 0.15$Ba_{0.8}Ca_{0.2}TiO_3$] – x$NaNbO_3$, (a) x = 0.4, (b) x = 0.45, (c) x = 0.5 and (d) x = 0.6. 158

Figure 7.5 Temperature-dependent relative permittivity (ε_r) of (1–x)[0.85$Na_{0.5}Bi_{0.5}TiO_3$ – 0.15$Ba_{0.8}Ca_{0.2}TiO_3$] – x$NaNbO_3$, (a), x = 0.02 – 0.1 and (b) x = 0.2 – 0.5 (at 1 kHz). 158

Figure 7.6 Plots of $\ln(1/\varepsilon - 1/\varepsilon_m)$ versus $\ln(T - T_m)$ for, x = 0.02 – 0.5. 160

Figure 7.7 Plots of (a) Relative density and (b) Geometric density as a function of x mol% $NaNbO_3$. 161

Figure 7.8 SEM micrographs of a) x = 0.05, b) x = 0.1, c) x = 0.3, and d) x = 0.4. 161

Figure 7.9 Resistivity of ceramics, x = 0.1 and 0.3 as a function of inverse absolute temperature. 162

Figure 8.1 XRD patterns of $(1–x)Ba_{0.6}Sr_{0.4}Zr_{0.2}Ti_{0.8}O_3 – xBiMg_{0.5}Ti_{0.5}O_3$ ($0 \leq x \leq 0.8$) at ambient temperature. 165

Figure 8.2 Lattice parameters and volume of unit cell versus mol fraction $BiMg_{0.5}Ti_{0.5}O_3$ (BMT)..... 166

Figure 8.3 Temperature-dependent relative permittivity and tanδ of (1-x)$Ba_{0.6}Sr_{0.4}Zr_{0.2}Ti_{0.8}O_3 – xBiMg_{0.5}Ti_{0.5}O_3$, (a) x = 0, (b) x = 0.1, (c) x = 0.2 (d) x = 0.3, (e) x = 0.4 and (f) x = 0.5. (data set continued in Figure 8.4) 168

Figure 8.4 Temperature-dependent relative permittivity and tanδ of (1-x)$Ba_{0.6}Sr_{0.4}Zr_{0.2}Ti_{0.8}O_3 – xBiMg_{0.5}Ti_{0.5}O_3$, (a) x = 0.6 and (b) x = 0.7..... 169

Figure 8.5. Temperature of maximum relative permittivity versus mole fraction BMT for $(1–x)Ba_{0.6}Sr_{0.4}Zr_{0.2}Ti_{0.8}O_3 – xBiMg_{0.5}Ti_{0.5}O_3$, x = 0.1 – 0.6..... 169

Figure 8.6 plots of linear fit of experimental data, ln $(1/\varepsilon – 1/\varepsilon_m)$ V.s ln $(T – T_m)$ of $(1–x)Ba_{0.6}Sr_{0.4}Zr_{0.2}Ti_{0.8}O_3 – xBiMg_{0.5}Ti_{0.5}O_3$, x = 0, 0.1 and 0.4 (1 kHz)..... 171

Figure 8.7 plots of log resistivity versus 1/T(K) of $(1–x)Ba_{0.6}Sr_{0.4}Zr_{0.2}Ti_{0.8}O_3 – xBiMg_{0.5}Ti_{0.5}O_3$, x = 0 – 0.4..... 172

Figure 8.8 P-E response for ceramics compositions, $(1–x)Ba_{0.6}Sr_{0.4}Zr_{0.2}Ti_{0.8}O_3 – xBiMg_{0.5}Ti_{0.5}O_3$, x = 0 – 0.5..... 173

Figure 8.9 SEM micrographs of $(1–x)Ba_{0.6}Sr_{0.4}Zr_{0.2}Ti_{0.8}O_3 –xBiMg_{0.5}Ti_{0.5}O_3$, (a) x = 0, (b) x = 0.2, (a) x = 0.3 and (d) x = 0.5..... 174

Figure 9 (a) Bar plots representing temperature-stable relative permittivity of selected studied compositions (Navy blue bar) and tanδ ≤ 0.02 (red bar) of $0.7[0.85Na_{0.5}Bi_{0.5}TiO_3 – 0.15Ba_{0.8}Ca_{0.2}TiO_3] – 0.3BiMg_{0.5}Ti_{0.5}O_3$, $0.93[0.85Na_{0.5}Bi_{0.5}TiO_3 – 0.15Ba_{0.8}Ca_{0.2}TiO_3] – 0.07LiNbO_3$, $0.7[0.85Na_{0.5}Bi_{0.5}TiO_3 – 0.15Ba_{0.8}Ca_{0.2}TiO_3] – 0.3NaNbO_3$, $0.6[0.85Na_{0.5}Bi_{0.5}TiO_3 – 0.15Ba_{0.8}Ca_{0.2}TiO_3] – 0.4NaNbO_3$, $0.9[0.85Na_{0.5}Bi_{0.5}TiO_3 – 0.15Ba_{0.8}Ca_{0.2}TiO_3] – 0.1LiNbO_3$, $0.7Ba_{0.6}Sr_{0.4}Zr_{0.2}Ti_{0.8}O_3 – 0.3BiMg_{0.5}Ti_{0.5}O_3$ and $0.8Ba_{0.6}Sr_{0.4}Zr_{0.2}Ti_{0.8}O_3 – 0.2BiMg_{0.5}Ti_{0.5}O_3$(top to bottom) and 182

Figure 9 (b) Temperature-stable dielectrics from early literature $0.85[0.685Na_{0.5}Bi_{0.5}TiO_3 – 0.4K_{0.5}Bi_{0.5}TiO_3] – 0.15K_{0.5}Na_{0.5}NbO_3$, (Dittmer, 2012), $0.82[0.0.94Na_{0.5}Bi_{0.5}TiO_3 – 0.06BaTiO_3] – 0.18K_{0.5}Na_{0.5}NbO_3$ (Dittmer, 2011), $0.5BaTiO_3 – 0.25BaZn_{0.5}Ti_{0.5}O_3 – 0.25BiScO_3$ (Ba-deficient) (Raengthon, 2012), $0.45Ba_{0.8}Ca_{0.2}TiO_3 – 0.55BiMg_{0.5}Ti_{0.5}O_3$ (Zeb, 2014), $0.5\ Ba_{0.8}Ca_{0.2}TiO_3 – 0.5\ BiMg_{0.5}Ti_{0.5}$ (Zeb, 2013), $0.45Ba_{0.8}Ca_{0.2}TiO_3 – 0.35BiMg_{0.5}Ti_{0.5}O_3 – 0.2NaNbO_3$ (Zeb, 2014), $0.7Na_{0.5}Bi_{0.5}TiO_3 – 0.3NaNbO_3$ (Bridger, 2010) and $0.8[0.82(0.94Na_{0.5}Bi_{0.5}TiO_3 – 0.06BaTiO_3) – 0.18K_{0.5}Na_{0.5}NbO_3] – 0.2CaZrO_3$ (Acosta, 2012) top to bottom)..... 182

Abbreviations and Symbols

BT – $BaTiO_3$

NBT – $Na_{0.5}Bi_{0.5}TiO_3$

BCT – $Ba_{0.8}Ca_{0.2}TiO_3$

BMT – $BiMg_{0.5}Ti_{0.5}O_3$

NN – $NaNbO_3$

LN – $LiNbO_3$

BSZT – $Ba_{0.6}Sr_{0.4}Zr_{0.2}TiO_3$

BZST – BMT = (1–x) $Ba_{0.6}Sr_{0.4}Zr_{0.2}TiO_3$ – $xBiMg_{0.5}Ti_{0.5}O_3$

NBT – BCT = (1–x) $Na_{0.5}Bi_{0.5}TiO_3$ – $xBa_{0.8}Ca_{0.2}TiO_3$

NBT – yBCT– xBMT = (1–x)[$(Na_{0.5}Bi_{0.5}TiO_3)_{1-y}$ – $(Ba_{0.8}Ca_{0.2}TiO_3)_y$] – $xBiMg_{0.5}Ti_{0.5}O_3$

NBT – 0.85BCT – xLN = (1–x)[$0.85Na_{0.5}Bi_{0.5}TiO_3$ – $0.15Ba_{0.8}Ca_{0.2}TiO_3$)] – $xLiNbO_3$

NBT – 0.85BCT – xNN = (1–x)[$0.85Na_{0.5}Bi_{0.5}TiO_3$ – $0.15Ba_{0.8}Ca_{0.2}TiO_3$)] – $xNaNbO_3$

PZ – $PbZrO_3$

PT – $PbTiO_3$

PZT – $PbZr_xTi_{1-x}O_3$

MPB – Morphotrophic phase boundary

P-E – Polarization electric field

S-E - Strain electric field

SEM – Scanning electron microscopy

TEM – Transmission electron microscopy

XRD – X-ray diffraction

EDX – Energy dispersive X-ray spectroscopy

ε_r – relative permittivity

ε_0 – permittivity of free space

T_C – Curie temperature

Chapter 1

1.1 Introduction

Currently there is strong impetus to develop lead-free dielectrics, which can operate at high temperatures (T > 200 ºC) for use in capacitors for power electronics and electronic systems located in harsh environments (Chen et al., 2015, Zeb et al., 2014). Pushing the temperature envelope to a much higher level is required due to the increased integration of power electronics and associated heat dissipation issues.

Applications for new high temperature control and sensing systems operating in harsh environments include automotive engines, aerospace applications, electrically powered cars, defence and down-hole drilling (Dittmer et al., 2011a).

Traditional barium titanate based high relative permittivity dielectrics are limited to upper working temperatures of 125 ºC, 150 ºC and 175 ºC for X7R, X8R and X9R capacitors respectively (Zeb et al., 2014). The demand is to reach 300 °C.

Although lead-based perovskite dielectrics can operate to higher temperatures (~ 250 °C) than barium titanate, concerns over the toxicity of lead oxide prompted current research into lead-free alternatives.

A number of lead-free ceramics with temperature-stable permittivity have been explored. These are mostly based on perovskite relaxor dielectrics. Examples include: $Na_{0.5}K_{0.5}NbO_3$ – $LiTaO_3$ – $BiScO_3$ (Zhu et al., 2011), $K_{0.5}Bi_{0.5}TiO_3$ – $BiScO_3$ (Kruea-In et al., 2012), $Ba_{0.8}Ca_{0.2}TiO_3$ – $BiMg_{0.5}Ti_{0.5}O_3$ (Zeb and Milne, 2013d), $Ba_{0.8}Ca_{0.2}TiO_3$ – $BiMg_{0.5}Ti_{0.5}O_3$ – $NaNbO_3$ (Zeb and Milne, 2013b, Zeb et al., 2014), $BaTiO_3$ – $Bi(Mg_{0.5}Zr_{0.5})O_3$ (Zeb and Milne, 2013c, Zeb and Milne, 2014b), $K_{0.5}Bi_{0.5}TiO_3$ – $Ba(Ti_{0.8}Zr_{0.2})O_3$ (Zeb and Milne, 2013a), $BiMg_{0.5}Ti_{0.5}O_3$ –

$BaTiO_3$ (Zhang et al., 2011, Xiong et al., 2011), $BiZn_{0.5}Ti_{0.5}O_3$ – $BaTiO_3$ (Huang and Cann, 2008), $BaTiO_3$ – $LiTaO_3$ (Wang et al., 2013), $BaTiO_3$ – $K_{0.5}Na_{0.5}NbO_3$ – Li, Ti, Si, O (Hu et al., 2013), $Na_{0.5}Bi_{0.5}TiO_3$ – $K_{0.5}Bi_{0.5}TiO_3$ – $K_{0.5}Na_{0.5}NbO_3$ (Dittmer et al., 2012), $BiScO_3$ – $BaTiO_3$ – $K_{0.5}Bi_{0.5}TiO_3$ (Lim et al., 2009), $BaTiO_3$ – $BiScO_3$ – $BiZn_{0.5}Ti_{0.5}O_3$ (Raengthon et al., 2012, Huang et al., 2007), $Na_{0.5}Bi_{0.5}TiO_3$ – $BaTiO_3$ – $K_{0.5}Na_{0.5}NbO_3$ (Dittmer et al., 2011a), $BaTiO_3$ – $BiZn_{0.5}Ti_{0.5}O_3$ – $Na_{0.5}NbO_3$ (Raengthon et al., 2013b).

The challenge remains to maintain stable (within ± 15 %) relative permittivity from high (≥ 300 °C) to low (-55 °C) temperatures in a single material, allied to low dielectric losses.

The thesis also considers piezoelectric properties. Efforts have been made globally to develop lead-free ceramics as alternatives to lead zirconate titanate. Much of the past lead-free piezoelectric research has been focussed on barium titanate, $BaTiO_3$ (BT) and sodium bismuth titanate, $Na_{0.5}Bi_{0.5}TiO_3$ (NBT) families.

In this group, work on ceramic composition (1–x)NBT – xBT [NBT – BT] has so far received the most attention because of excellent dielectric and piezoelectric properties near a MPB at around x ~ 0.06. Takenaka et al. reported a piezoelectric constant d_{33} ~ 125 pC/N, room temperature relative permittivity, ε_r ~ 580, electromechanical coupling factor k_{33} ~ 55 %, dielectric loss tanδ ~ 0.03 and maximum dielectric temperature, T_m ~ 288 ºC near the morphotrophic phase boundary (MPB) composition at x = 0.06 (Rödel et al., 2009). However, despite relatively good properties, a number of issues were highlighted, for example a relatively low depolarization temperature (~ 100 ºC) and problems in the control of volatile species during thermal processing.

1.2 Aims and Objectives

The focus of this study was to

- Develop novel lead-free temperature-stable dielectrics for high temperature (> 200 ºC) capacitors and also understand the factors controlling the phase formation during fabrication.
- Modify a well-known $Na_{0.5}Bi_{0.5}TiO_3$ – $BaTiO_3$ [NBT – BT] system by incorporating Ca^{2+} with a view to improve its properties to a more temperature-stable dielectrics.
- Study the effect of Bi_2O_3 excess on the properties of $Na_{0.5}Bi_{0.5}TiO_3$ – $Ba_{0.8}Ca_{0.2}TiO_3$ [NBT – BCT].
- Modify, NBT – BCT with $LiNbO_3$, $BiMg_{0.5}Ti_{0.5}O_3$ and $NaNbO_3$ respectively and also fabricate binary solid solutions, $Ba_{0.6}Sr_{0.4}Zr_{0.2}TiO_3$ – $BiMg_{0.5}Ti_{0.5}O_3$ [BSZT – BMT], assessing for high performance temperature-stable materials.
- Examine the phase formation of the fabricated ceramics, using X-ray powder diffraction, $\varepsilon_r(T)$ plots, Scanning Electron Microscopy (SEM) and Transmission Electron Microscopy (TEM) techniques.
- Investigate polarization – electric field (P-E) and bipolar strain electric field response (S-E) of selected ceramics.
- Study the electrical resistivity of the fabricated ceramics.

Chapter 2

Background science and literature review

2.1 Dielectrics

Dielectrics are the special class of nonconductive materials that can be polarized when subjected to an external electric field (Moulson and Herbert, 2003). Dielectrics of high relative permittivity, good temperature stability, low dielectric loss (Dittmer et al., 2011a, Du et al., 2008), and high resistivity find applications in high temperature capacitors where high charge storage density is required (Dittmer et al., 2011a). Porosity levels, chemical inhomogenity, lattice defects, strongly affect the performance of dielectrics (Moulson and Herbert, 2003).

Relative permittivity of a dielectrics is described by Equation 2.1, as the ratio between the magnitude of charge stored on either surface of electroded dielectrics when an external electric field is applied, to the charge stored on a set of similar electrodes separated by vacuum.

$\varepsilon_r = \varepsilon/\varepsilon_0 = C_{die}/C_{vac} = 1 + \chi_e$ ……Equation 2.1

ε = permittivity of the medium.

ε_0 = permittivity of free space (8.85×10^{-12} F/m).

C_{die} = Capacitance of parallel plate capacitor separated by a dielectric.

C_{vac} = Capacitance of parallel plate capacitor separated by vacuum.

χ_e = Electric susceptibility of dielectric.

Relative permittivity and dielectric loss tangent, tanδ, plotted as a function of temperature can be utilized as one of the most useful tools for the identification of phase transitions (ferroelectric-ferroelectric, ferroelectric-antiferroelectric and

ferroelectric-paraelectric) in ceramics. In addition, frequency dispersion of the dielectric plot helps to identify the relaxor behaviour of ferroelectrics (Jaffe, 1971).

2.1.1 Dielectric loss or tanδ

When a dielectric is subjected to an alternating voltage (ac), it has both real (in phase or resistive leakage) and imaginary (out of phase or dielectric absorption) components; the phase difference between the two is the cause of power loss, Figure 2.1. In an ideal case, power loss in dielectrics will be zero if the phase change between the voltage and the current (V and I) is 90º (Nishino, 1996).

The loss tangent tanδ, is the ratio of the out of phase component to the in phase component of ac voltage, depends upon temperature and frequency of the applied field (Jaffe, 1971) Equation 2.2.

$\tan\delta = \varepsilon''/\varepsilon'$ ……Equation 2.2

where ε" is the imaginary part of complex permittivity, $\varepsilon^* = \varepsilon' - j\varepsilon''$ ($j = \sqrt{-1}$) and ε' is the real permittivity.

Dielectric loss plotted as a function of temperature helps to identify the depolarization temperature and phase transition in ceramics (Jaffe, 1971).

If a dielectric material is placed in an ac field, then the current I, leads the voltage, V, if the two are exactly out of phase by 90^0 then the power loss is zero (ideal case), Figure 2.1a. Whenever the voltage increases, the current decreases and drops to zero when the capacitor is fully charged. The capacitor starts discharging when voltage begins to drop, whereas in response the current increases. For ideal case, the power loss $P = V.I = VI\cos\theta$ is zero. However the phase change between V and I is always less than 90^0 for most real dielectrics, giving dielectric loss due to resistive leakage current, Figure 2.1b.

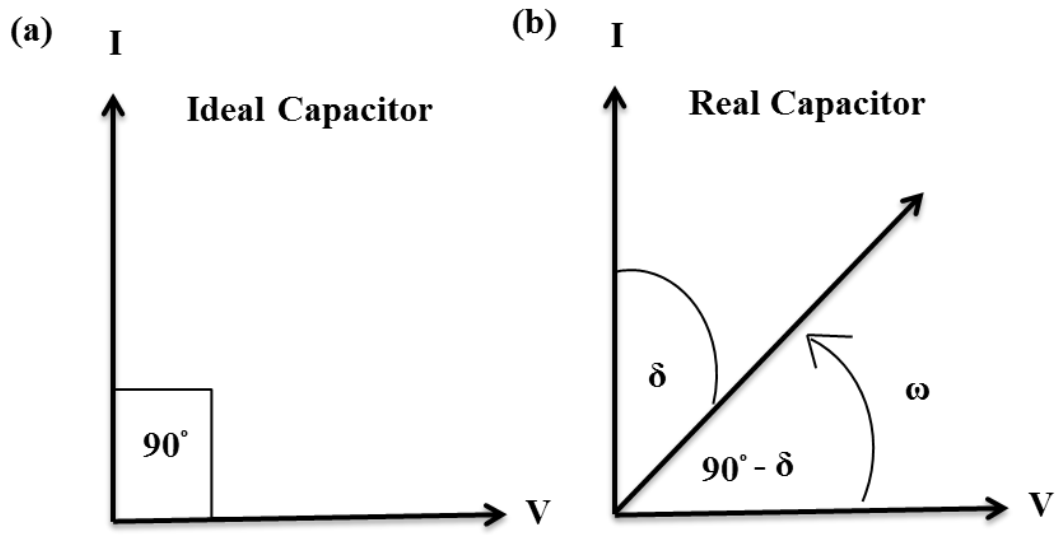

Figure 2.1 Phasor diagram of (a) ideal and (b) real capacitor. Modified as (Moulson, 2003 Wolfe, 2015)

2.1.2 Dipole moment μ

Two equal but opposite point charges separated by small distance, d, comprises an electric dipole, Figure 2.2. The dipole moment μ is given by Equation 2.3.

$\mu = qd$ ……Equation 2.3

where q is the magnitude of either of the two charges (+ve, or -ve) and d is the separation between the two charges. Polarization, P, is defined as the dipole per unit volume (Ponnusamy, 2007).

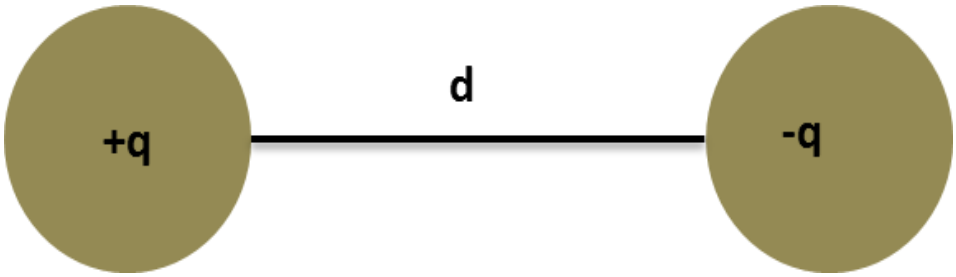

Figure 2.2 Schematic representation of dipole moment.

The measure of extent of how easily a dielectric material can be polarized by an applied electric field is termed the dielectric suseptability (χ_e), which is a constant of proportionality and determines the electrical permittivity of the material.

The expression for a linear dielectric, where polarization is proportional to the electric field is given by Equation 2.4.

$\chi_e = P/\varepsilon_0 E$ ……Equation 2.4

Where, χ_e is electric susceptibility of material, P is electric polarization, and E is the applied field.

The dielectric displacement D is given by

$D = Q/A$ (SI unit = C/m^2) ……Equation 2.5

where Q is the charge stored on the capacitor of electrode area A. It can be expressed in terms of electric polarization (P), dielectric susiptability (χ_e) and electric field intensity (E), (Jaffe, 1971).

$D = \varepsilon_0 E + P = \varepsilon_0 E + \chi_e \varepsilon_0 E = \varepsilon_0 E(1+ \chi_e) = \varepsilon_0 \varepsilon_r E$ ……Equation 2.6

The permittivity of the dielectric, ε, is defined by

$\varepsilon = \varepsilon_0(1 + \chi_e)$ ……Equation 2.7

Where, $1+ \chi_e = \varepsilon_r$, and hence relative permittivity ε_r is equal to $\varepsilon/\varepsilon_0$.

2.1.3 Capacitors

A charge storage capacitor consists of an insulating material between two electrodes. High relative permittivity ceramics can offer large capacitance with compact size. Ferroelectric materials are often used as the dielectric in capacitors because of the wide ranging values of relative permittivity (Dittmer et al., 2011a).

Dielectrics are used between the plates of capacitor to increase its capacitance, relative to a non-filled capacitor, Figure 2.3. For a parallel plate

capacitor of cross-section area A separated by distance d, connected to a potential difference source of voltage V, the charge Q stored on either plate of capacitor is .

$Q = CV$ ($C = Q/V$) ……Equation 2.8

and $C = A\varepsilon_0/d$ ……..Equation 2.9

This is the capacitance of the capacitor in presence of free space or vacuum between the plates of capacitors.

When a dielectric of permittivity ε is introduced between the plates of capacitors, Figure 2.3, then

$C_{die} = A\varepsilon/d = A\varepsilon_0\varepsilon_r/d = \varepsilon_r C$ ($\varepsilon = \varepsilon_0\varepsilon_r$) ……Equation 2.10

Thus $C_{die} > C$ by ε_r, this is because the net E-field ($E_{net} = E_{appl} - E_{diel}$) decreased due to the opposing dielectric field ($V = Ed$ and $C = Q/V$) (Prakash, 2008-09).

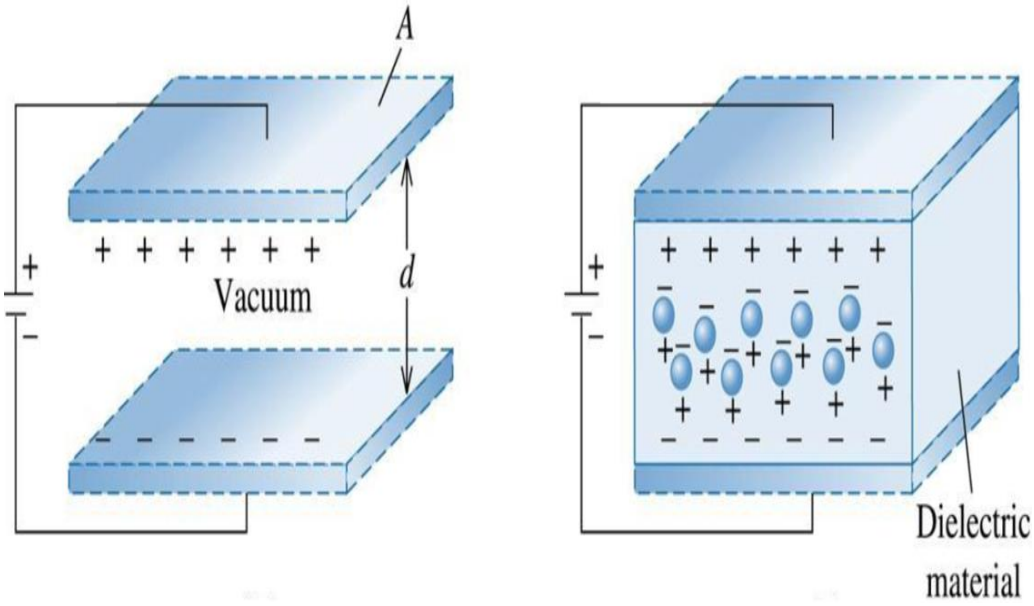

Figure 2.3 Schematic diagram of air filled and dielectric filled capacitor.(Levi, 2009)

2.2 Electric Polarization

As stated above, polarization P is the dipole moment per unit volume of a dielectric material, which is either caused by an electric field (or applied stress).

Polarization is the net effect of the dipole moment in each unit cell of a crystal and is a measure of ferroelectricity in a material, and can be calculated from P-E hysteresis loop measurements (Jaffe, 1971, Kingery, 1976, Moulson and Herbert, 2003). It can be categorized into four types which are listed below.

2.2.1 Space charge polarization

Space charge polarization is the effect of charges that either stick to the interfaces of grain boundaries or are trapped at dielectric surfaces and cannot discharge through electrodes on interaction with applied electric field, Figure 2.4. Such charge polarization involves limited mobility of charge carrier, until stopped at the grain boundaries.

It loses its response to the applied electric field beyond 10^3 Hz, resulting in a decrease in the value of relative permittivity, Figure 2.8 (Moulson and Herbert, 2003, Jaffe, 1971)

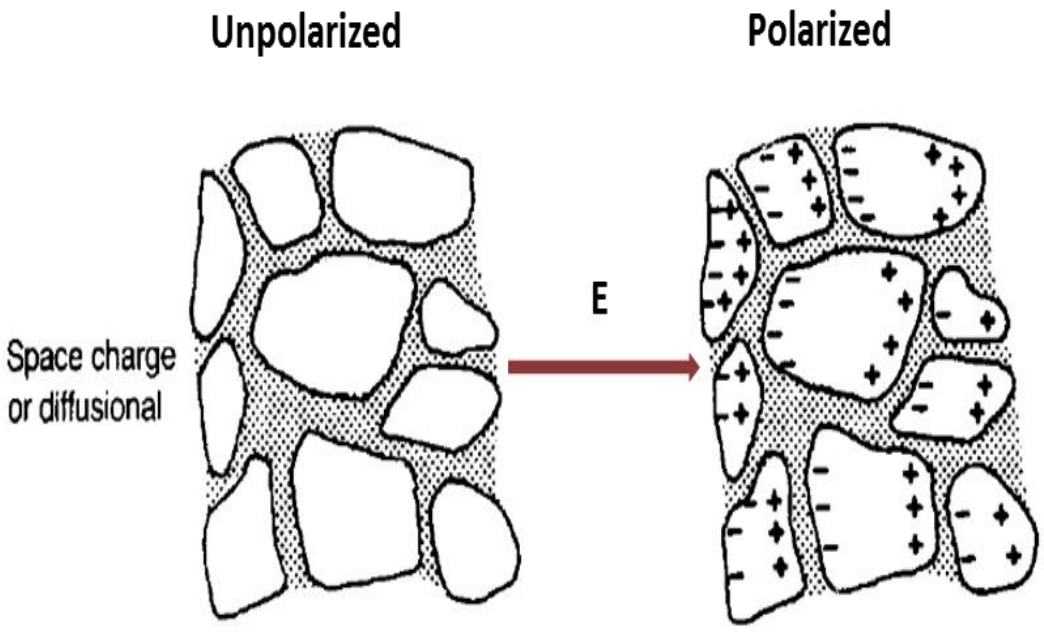

Figure 2.4 Space charge polarization. Modified after (Moulson and Herbert, 2003)

2.2.2 Dipolar or orientational polarization

A slight twist or torque is produced in dipoles due to applied electric field, Figure 2.5. It is common in liquids and gases in nature. The direction of dipole (E-field frequency dependent), can be changed by application of E-field. Dipoles cannot follow the changing high ac frequency quickly, but rather lag behind the ac field, this effect is called relaxation.

Dipolar polarization loses its response to the frequency of electric field beyond 10^{10} Hz, which results in the further decrease of relative permittivity of material (Moulson and Herbert, 2003, Jaffe, 1971), Figure 2.8.

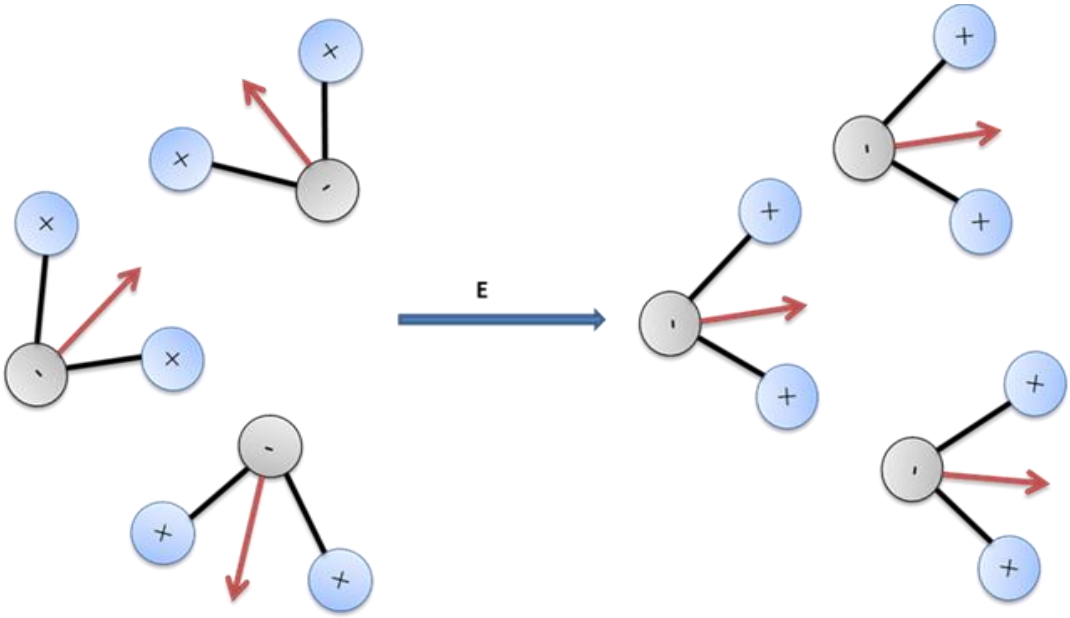

Figure 2.5 Dipolar polarization mechanism. Modified as (DoITPoMS, Access date 19th Sep 2015)

2.2.3 Ionic polarization

Ionic polarization is due to a small relative drift of cations (+ve charge) and anions (-ve charge) in ionic crystals. In the unstrained conditions, the centres of positive and negative charges coincide and hence the net polarization is zero. When

ionic crystals are brought under stress, or exposed to electric field, the charges drift slightly relative to one another and hence the crystal is polarized, Figure 2.6.

Ionic polarization is attributed to the phenomena of resonance. It loses its response to applied electric field beyond a frequency of 10^{13} Hz, which causes a further decrease in relative permittivity, Figure 2.8 (Jaffe, 1971, Moulson and Herbert, 2003).

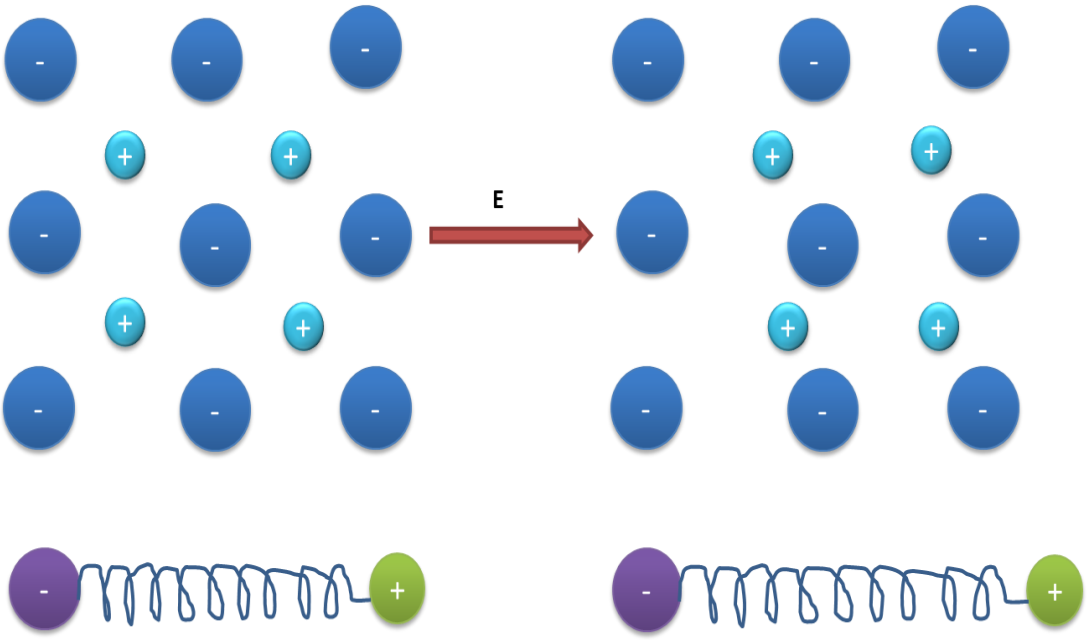

Figure 2.6 Ionic polarization mechanism. Modified as (DoITPoMS, Access date 19th Sep 2015)

2.2.4 Electronic polarization or atomic polarization

When an electric field is applied to an atom, there is a relative displacement of electrons cloud with respect to the nucleus and hence the atom gets polarized, Figure 2.7.

Atomic polarization exists in all materials and is attributed to the phenomena of resonance. It loses its response to electric field at a frequency beyond 10^{15} Hz (Moulson and Herbert, 2003, Jaffe, 1971, Lines and Glass, 2001), Figure 2.8.

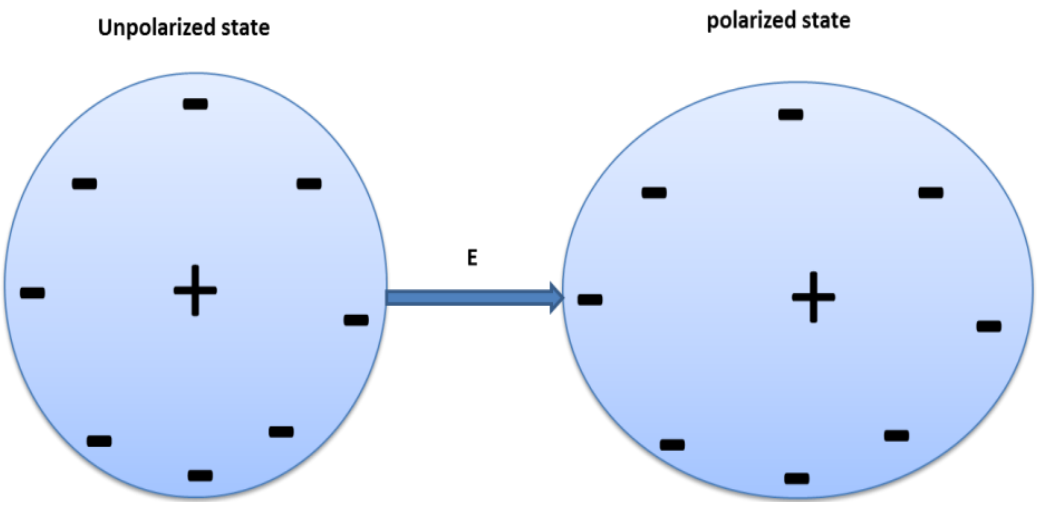

Figure 2.7 Electronic polarization in the unstressed and stressed conditions. Modified as (DoITPoMS, Access date 19th Sep 2015)

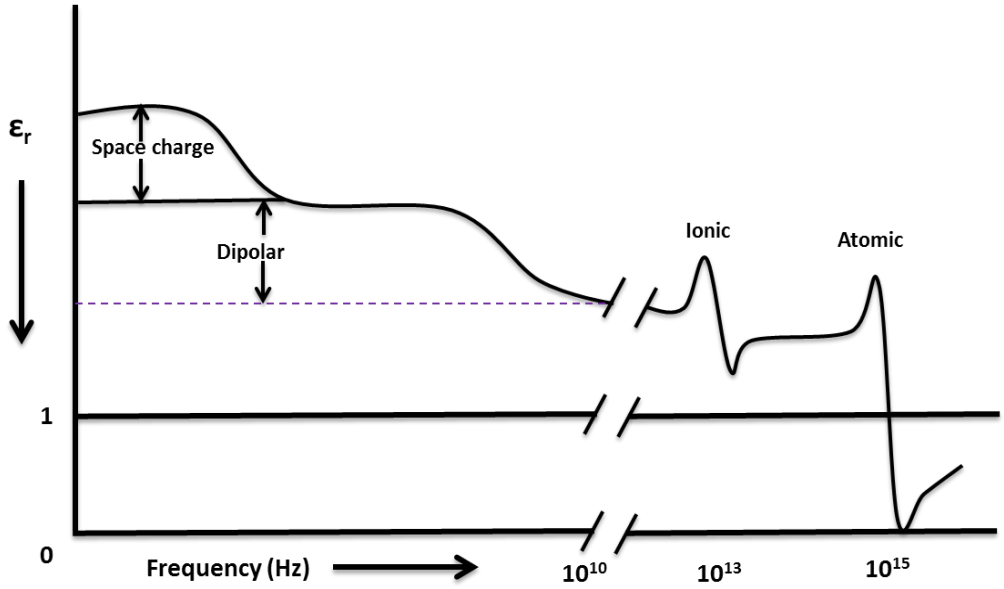

Figure 2.8 Variation in relative permittivity with a.c frequency. Modified as (Moulson and Herbert, 2003)

2.3 Ferroelectricity

Ferroelectricity was first discovered in a single crystal Rochelle salt in 1921 and polycrystalline $BaTiO_3$ in 1940. Ferroelectrics are a special class of dielectrics. They are non-centrosymmetric crystals which possess a property of spontaneous polarization, the direction of which can be reversed by application of an electric field (Haertling, 1999, Elissalde and Ravez, 2001, Jiles, 2001), Figure 2.9.

Out of the four general groups of ferroelectrics (tungsten bronze, oxygen octahedral ABO_3 perovskite, pyrochlore, and bismuth layered), the perovskite group ABO_3 is the most important category. Barium titanate, lead zirconate titanate, lead titanate, and sodium potassium niobate belong to this group (Haertling, 1999).

Spontaneous polarization exists in ferroelectrics even at zero E-field as the centres of positive and negative charges do not coincide with each other below the Curie point T_C. Spontaneous polarization and electric field reversible polarization is the basic criteria for ferroelectricity (Megaw, 1952, Jaffe, 1971).

The performance of ferroelectric materials is strongly affected by external factors like temperature and applied electric field frequency (Elissalde and Ravez, 2001).

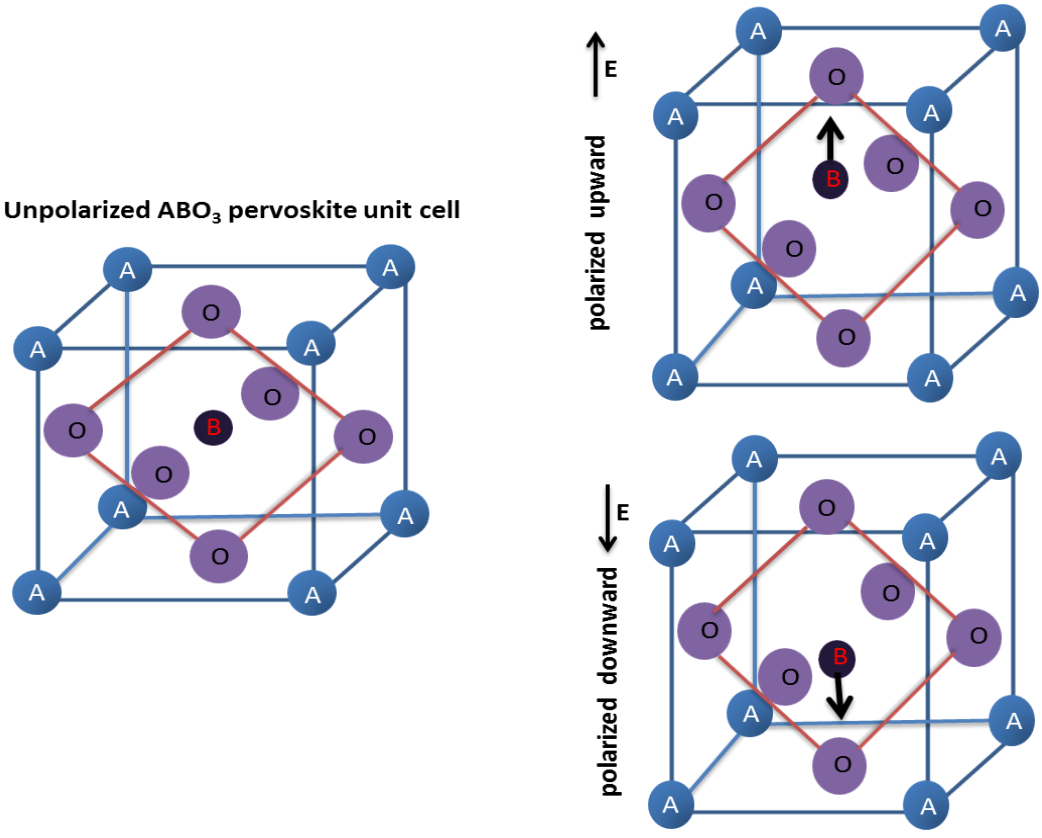

Figure 2.9 Polarization mechanism in ABO_3 Perovskite unit cell.

2.4 Perovskites ABO_3

The origin of ferroelectricity lie in ion displacements in the unit cell. This can best be explained by reference to the crystal structure of perovskites, of general formula ABO_3 for example $BaTiO_3$. The polarization mechanism in ABO_3 ferroelectric perovskite unit cell is shown in Figure 2.9.

The perovskite cubic unit cell is non-ferroelectric (paraelectric) and contains A cations (12-fold co-ordination number) on each corner, B cations (6-fold co-ordination number) at its centre and anion O (6-fold co-ordination number) at each of its six faces (Jaffe, 1971) Figure 2.10.

The structure can be considered as being based on a cubic close packing arrangement of A and O ions with B ions, with a quarter of octahedral ‘voids being occupied by smaller B site ions. In cubic $BaTiO_3$ the Ti ions lie at the centre of the cube, forming TiO_6 octahedra represented by the shaded volume. There is no net charge displacement in the unit cell and hence no spontaneous polarization.

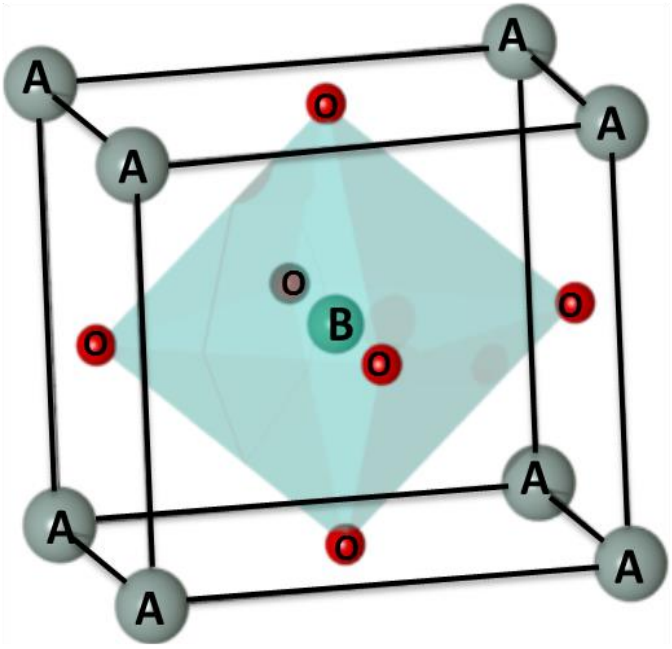

Figure 2.10 Cubic perovskite ABO_3 structure unit cell. Modified as (Rödel et al., 2009). The shaded volume represents oxygen octahedra.

The perovskite structure is very flexible and can accommodate cations of different valance number easily, for example $A^{1+}B^{5+}O^{2-}_3$, $A^{2+}B^{4+}O^{2-}_3$ or $A^{3+}B^{3+}O^{2-}_3$. The structure tolerance factor t, of perovskite, which is the ratio that governs the relationship between the ionic radii of the unit cell, can be changed due to different radii (R_A, R_B and R_O) of cations and anions (Megaw, 1957, Goldschmidt, 1926) Equation 2.11.

$$t = (R_A+R_O)/\sqrt{2}(R_B+R_O) \qquad \text{Equation 2.11}$$

The perovskite structure is stable in the range ($0.9 < t < 1.1$), for ideal cubic perovskite structures $t \approx 1.0$. Larger deviation from $t = 1$, generally prevents the crystallization of the compound, in the form of ABO_3 perovskite structure.

The $BaTiO_3$ structure is cubic and paraelectric above ~ 130 °C. Below ~130 °C, the structure changes from cubic to tetragonal crystal systems, with the Ti ion moving off centre toward one of the apical oxygen that make up the TiO_6 octahedra. This creates a net displacement of negative and positive charge in the unit cell, giving a permanent unit cell dipole and spontaneous polarization characteristic of a ferroelectric. For example, the polarization mechanism in $BaTiO_3$ unit cell during phase transition from high temperature cubic phase to low temperature tetragonal phase with off centred Ti ion is shown in Figure 2.11. The off centred Ti-ion creates elongation in any of the six possible crystallographic directions towards corner oxygen ions and hence creates a dipole. If all the Ti-ions are displaced along one particular direction then the unit cell is unstable and generates electrostatic and mechanical stresses. The regions of crystal have different unit cells Ti ion displacements to minimize electrostatic and mechanical stress and hence domains are generated. Domains are the local regions in crystal with common dipole orientation.

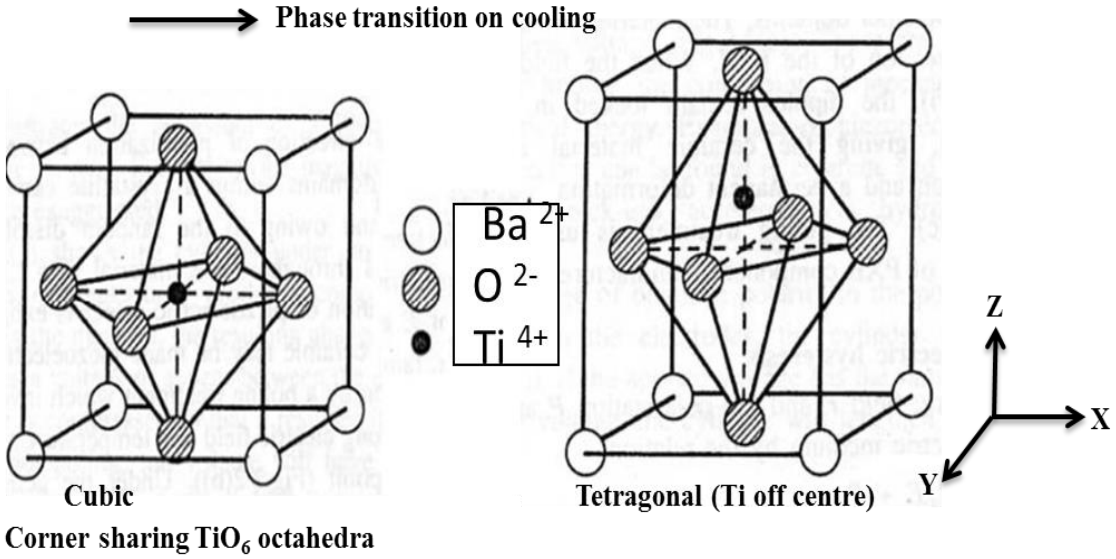

Figure 2.11 Unit cells of Cubic and Tetragonal $BaTiO_3$ showing the corner sharing TiO_6 octahedra and off centred Ti ion. (Taken from Steven J. Milne Lecture PEME1730)

The cubic to tetragonal phase transition can result in six possible directions dipole moment associated with Ti being displaced toward any one of the 6 oxygen ions. These displacement directions are the <100> directions in crystallographic notation.

At lower temperatures other polymorphs form. The primary cell alters to monoclinic (unit cell is larger than the primary cell and is orthorhombic) with Ti moving in <110> directions below around 0 °C and at even lower temperatures a rhombohedral unit cell forms with Ti displacements along <111>, Figure 2.12.

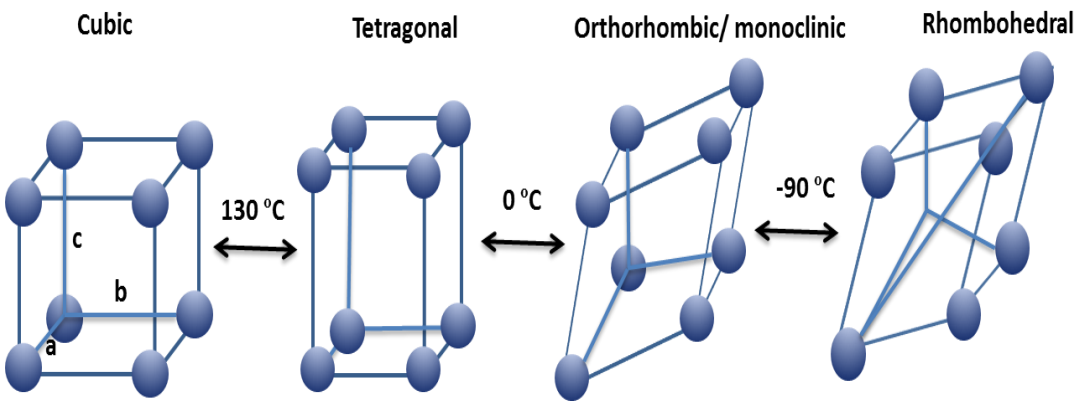

Figure 2.12 Unit cell phase transformations in barium titanate. Modified as (Jaffe, 1971)

It is noted that the perovskite unit cell has a simple lattice type, with a lattice point (repeat motif in structure) corresponding to the formula unit. The 14 possible combinations of unit cell shape (crystal system) and lattice types which cover all possible crystal structures are shown in Figure 2.13.

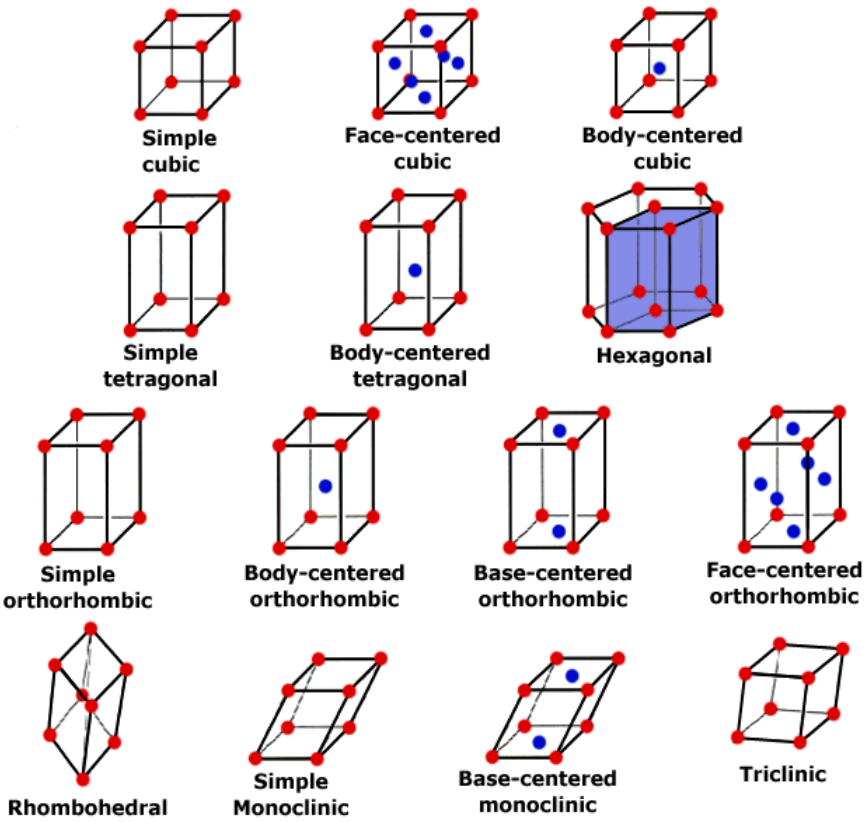

Figure 2.13 The seven crystal systems and fourteen Bravias lattices. (Pietrovito . A, 2015)

2.5 Ferroelectric domains and polarisation-electric field response (P-E)

The homogeneous regions of the ferroelectric crystal, where all the dipoles are oriented along one particular direction, constitute domains. In a single crystal all the domains are oriented along one particular direction, whereas in polycrystalline materials they are directed in different directions.

In tetragonal $BaTiO_3$ 90° domains, form on cooling from the paraelectric phase to minimize mechanical stress whereas 180° domains form to minimize electrostatic stress (Jaffe, 1971, Haertling, 1999, Cao and Randall, 1996, Streiffer et al., 1998). Figure 2.14, show a schematic representations of 90º and 180º domains.

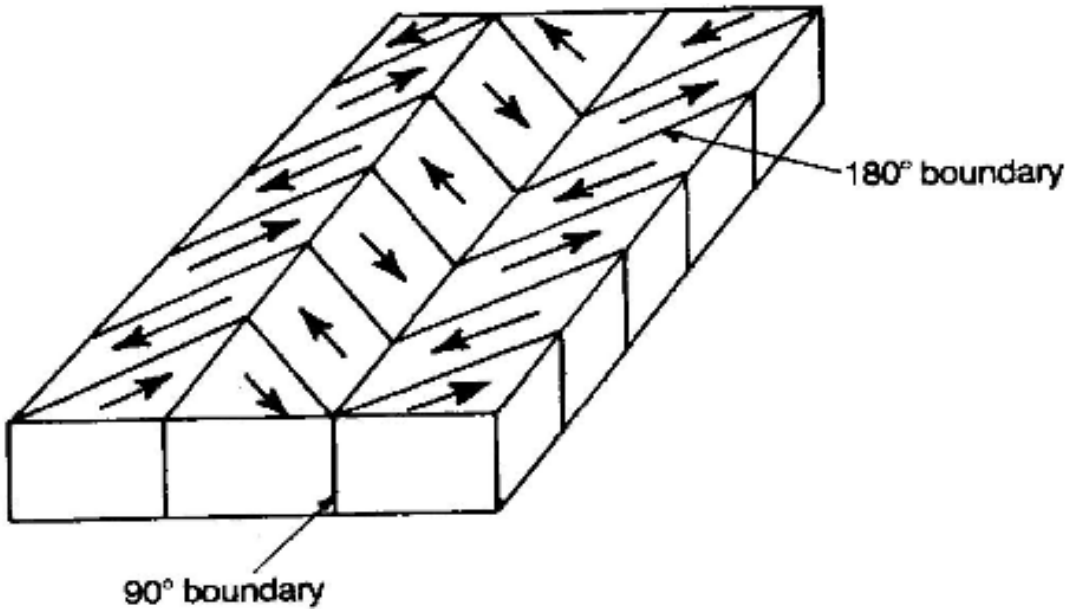

Figure 2.14 A schematic representations of 90º and 180º domains. (Moulson and Herbert, 2003)

The walls separating domains are called domain walls (Kittel, 1951), which exits between 90° domains, as well as 180° domains (Merz, 1954).

Ferroelectricity in materials can be directly evidenced from polarization-electric field hysteresis loop (Jaffe, 1971, Xu et al., 2015).

For example, a normal ferroelectric like P-E hysteresis loop is shown in Figure 2.15. The vertical axes represents polarization and the horizontal axes represents the applied electric field (Jaffe, 1971).

Under normal conditions the net electric polarization is nearly zero due to random orientation of domain dipoles, Figure 2.15 (1). These dipoles orient themselves in particular direction in accordance with the applied static electric field, until the saturation point (A, B), at which the polarization reaches its peak value (P_s) Figure 2.15.

The direction of domain dipoles in poled ferroelectrics can be reversed when the direction of applied electric field is reversed (Jaffe, 1971). The material starts to depolarize gradually on reversal of direction of applied field. When the E-field becomes zero, there still exists a spontaneous polarization in ferroelectrics, called remanent polarization (P_r = OE), Figure 2.15 (2). On further decreasing the E-field the material is completely depolarized at a certain value, called coercive field $E_{c,}$ (points C and D), Figure 2.15 (Haertling, 1999, Jaffe, 1971). At a certain negative maximum of electric field, the material is completely polarized in opposite direction, Figure 2.15 (4).

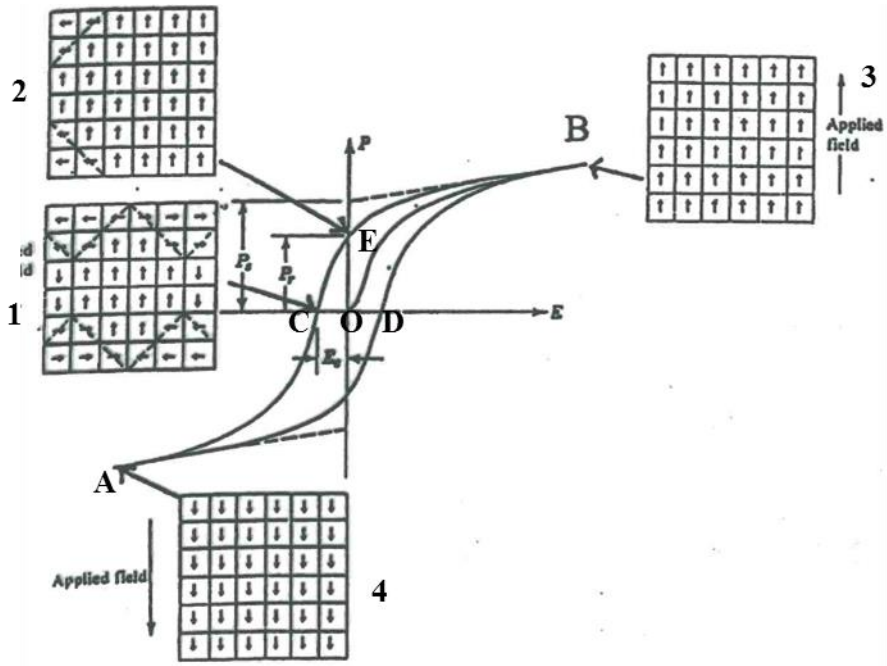

Figure 2.15 A typical ferroelectric polarization-electric field hysteresis loop. (Taken from Steven J. Milne lecture PEME 1710)

Single crystals show strong ferroelectricity in one particular direction, whereas polycrystalline materials show weak ferroelectricity in the unstrained conditions. Domains in ferroelectrics can be switched along any particular allowed crystallographic direction by application of electric field (Haertling, 1999).

Ferroelectrics are mainly used as high dielectric constant capacitors, ultrasonic transducers, pyroelectric security sensors, ultrasonic motors, electro-optical light valves and many more (König et al., 2009).

P-E hysteresis loops of different shapes and sizes can be used as a fingerprint to identify the type of material, for example, a linear P-E response show a dielectric capacitor characteristic, a highly nonlinear saturated loop with low coercive field indicate a memory ferroelectric, a non-linear slim P-E loop evidence a relaxor ferroelectric and a double P-E loop indicate a nonmemory antiferroelectric materials (Haertling, 1999).

2.6 Curie Weiss law

Ferroelectric materials retain ferroelectricity below Curie point temperature, T_C, at which the relative permittivity reaches its maximum value. Above the Curie point the relative permittivity suddenly decreases due to transformation to paraelectric phase and follows Curie Weiss law (Bokov and Ye, 2007, Jaffe, 1971), Equation 2.12,

$\varepsilon_r - 1 = C/T\text{-}T_C$ ……Equation 2.12

Where ε_r is relative permittivity, C is Curie constant.

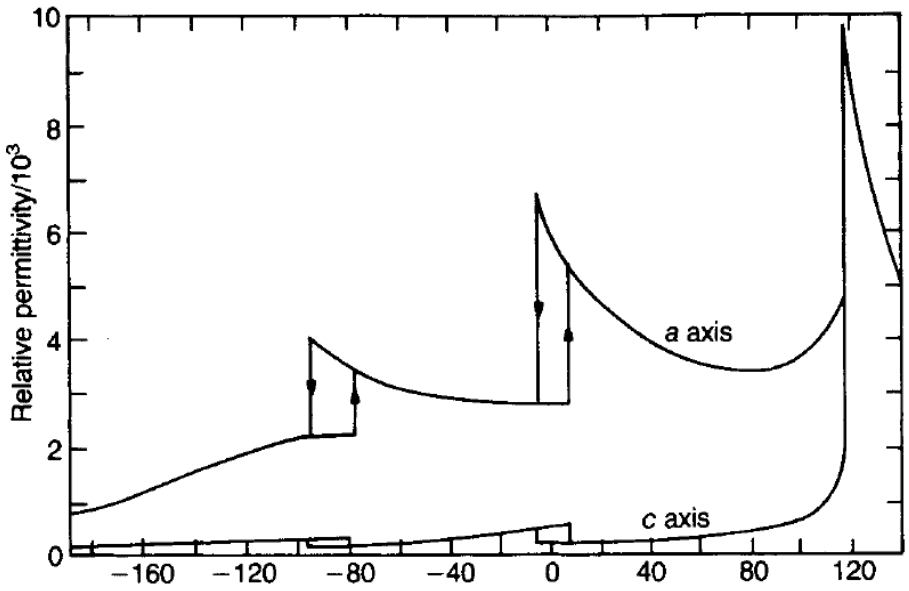

Figure 2.16 Temperature-dependent relative permittivity plot of single crystal $BaTiO_3$. (Jaffe, 1971, Moulson and Herbert, 2003)

At the Curie point, the crystal structure of ferroelectrics changes from ferroelectric state to paraelectric state, at which electric polarization drops to zero.

However there also exist some ferroelectric-ferroelectric transitions (for example, rhombohedral-tetragonal, orthorhombic-tetragonal, rhombohedral-orthorhombic) below Curie point in some ferroelectrics (Jaffe, 1971), Figure 2.16.

2.7 Relaxor ferroelectrics

Relaxors are a special class of ferroelectrics with haphazardly oriented short range nano-sized domains that can be switched by the application of external electric field. These domains exist down to very low temperature (Li et al., 2009, Bokov and Ye, 2007, Ke et al., 2009). Majority of relaxors belongs to a family of lead-based pervoskites, such as $Pb(Mg_{1/3}Nb_{2/3}Ta_{1/2}O_3)$, $Pb(Sc_{1/2}Ta_{1/2}O_{3)}$ and $(PbLaZrTi)O_3$.

Relaxor ferroelectrics are divided into two main categories, which are classical relaxors with only short range ordering, for example $PbMg_{1/3}Nb_{2/3}O_3$ (PMN) Figure 2.17, and semi-classical relaxor ferroelectrics with both short and long range ordering (Kumar, 2012). In PMN single crystals, a significant diffuse peak appears below the Burns temperature ($T < T_B$) on cooling, which was attributed to the existence of correlated polar nano domains PNRs, which are small groups of electric dipoles in nanometre size. The size of PNRs increased with decreasing temperature until freezing temperature, resulting in a diffuse dielectric peak, Figure 2.17.

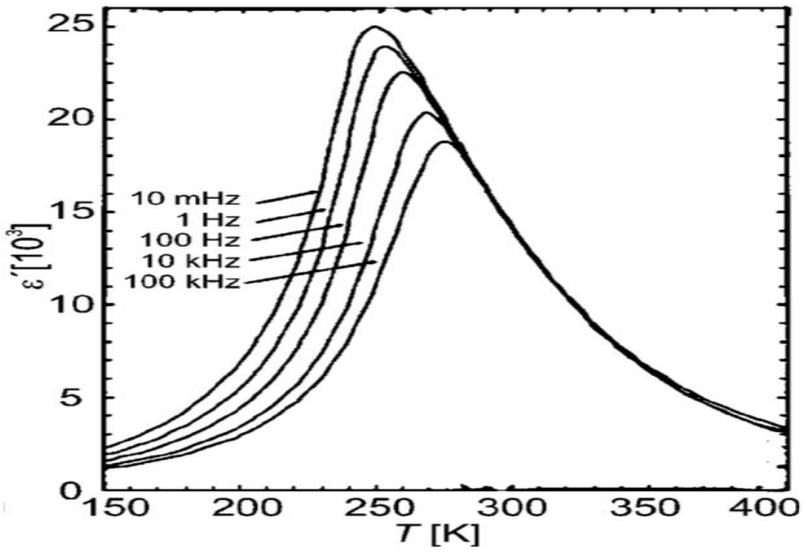

Figure 2.17 The temperature dependence of the real part of the dielectric permittivity measured at different frequencies for single crystal of relaxor compound $Pb(Mg_{1/3}Nb_{2/3}O_3)$. (Shvartsman, 2012)

In relaxors, long range ordered symmetry and macrodomains, which exist in normal ferroelectrics are absent, instead order is restricted to the nanoscale due to symmetry breaking defects. The origin of symmetry breaking defect might be charge disorder due to: off-valent cation substitutions and so called random electric fields; partial B-site lattice substitution of ions that remain at the centre of BO_6 octahedra and therefore prevent long range dipole formation; partial substitution of ions of differing radii, creating stress fields; intermediate scale ordering of octahedral cations of different radii and charge (Stringer et al., 2007).

Compared to normal ferroelectrics, relaxor ferroelectrics exhibit unique properties, such as frequency dispersion of relative permittivity, diffuse relative permittivity peaks, slim hysteresis loop and no macroscopic symmetry change associated with the permittivity peak (Smolensky, 1984, Lu and Calvarin, 1995, Ke et al., 2009, Li et al., 2009, Kreisel et al., 2002). The temperature below which polar nanoregions, PNRs, begin to form is termed as the Burn's temperature, T_B. On further cooling Neutron diffraction has confirmed the number and size of PNRs increase and hence total polarization increases. However this is accompanied by an increase in the energy barrier for PNR re-orientation (coupling) and at a particular temperature, T_m, a peak in relative permittivity is observed, due to the dominant effect of the energy parameter. As temperature continues to fall, 'freezing' of PNRs occurs. Some relaxors transform spontaneously into normal ferroelectrics at $T << T_m$, in other cases poling may induce ferroelectric behaviour (Ke et al., 2009).

The frequency dependence of T_m can be considered to arise because of the dynamics of PNR re-orientation, i.e. re-orientation under an electric field is easier to achieve at low frequencies, and hence T_m is lower.

Owing to the applications in capacitors, sensors and actuators, much attention is given to $PbMg_{1/3}Nb_{2/3}O_3$ based relaxor perovskites. However due to the

toxicity of lead-based ceramics, researchers change their direction of research towards lead free relaxor materials like $Ba(Ti,ZrO_3)$, $BaTiO_3 - BiScO_3$ and $K_{0.5}Na_{0.5}TiO_3 - SrTiO_3$ (Kruea-In et al., 2012).

The compositional disorder in ionic crystals is believed to be the origin of the relaxor behaviour of perovskites (Yu and Ye, 2008, Uchino, 1994).

2.8 Piezoelectricity

A special group of non-centrosymmetric crystalline materials, discovered by J.Curie and P.Curie in 1880, that develop charges, when squeezed or stressed, is piezoelectricity (Haertling, 1999). According to Caddy, piezoelectricity is the "electric polarization produced by mechanical strain in crystals belonging to certain classes, the polarization being proportional to the strain and changing sign with it (Haertling, 1999).

Charge per unit area (dipole moment) induced on piezoelectric materials is a linear function of mechanical stress, called direct piezoelectric effect or generator effect, Equation 2.15 and Figure 2.18a.

$$D = P = Q/A = dT \qquad \text{Equation 2.15}$$

Where, d is a piezoelectric charge constant, Q being charge and A is a charge build upon surface and T is applied stress.

Also strain is produced in piezoelectric material when electric field is applied, which is directly related to the magnitude of applied electric field (E). This effect is called converse piezoelectric effect or motor effect, Figure 2.18b.

$$S = dE \qquad \text{Equation 2.16}$$

Where S is strain and d is piezoelectric charge constant (Haertling, 1999, Jaffe, 1971).

The piezoelectric charge constant d is the ratio of charge stored per unit area to the applied mechanical stress (direct piezoelectric effect) or the ratio of strain to the applied electric field (converse piezoelectric effect). It is expressed in the units of pC/N or pm/V. Since the transfer of mechanical energy into electrical energy and vice versa, as a result of the piezoelectric effect, occurs in all x, y, and z direction, which gives rise to the use of tensors to denote directions. Thus the piezoelectric charge constant will be different in different directions and hence is a tensor. If the direction of applied stress and electric polarization is the same, the piezoelectric constant is represented by d_{33} and if at right angle by d_{31}. For soft materials its value is higher, whereas a converse for hard materials.

Of the 32 crystallographic point groups, 20 show piezoelectricity and of these 10 are non-centrosymmetric and will exhibit ferroelectricity (Cady, 1946).

High dielectric constant, discovery of ferroelectricity in $BaTiO_3$ and poling, are the three basic steps in the discovery and understanding of piezoelectricity (Jaffe, 1971).

Commercial piezoelectric ceramics are used mainly for, generation of voltages, electromechanical actuations, frequency control and generation and detection of acoustic and ultrasonic energy (Moulson and Herbert, 2003).

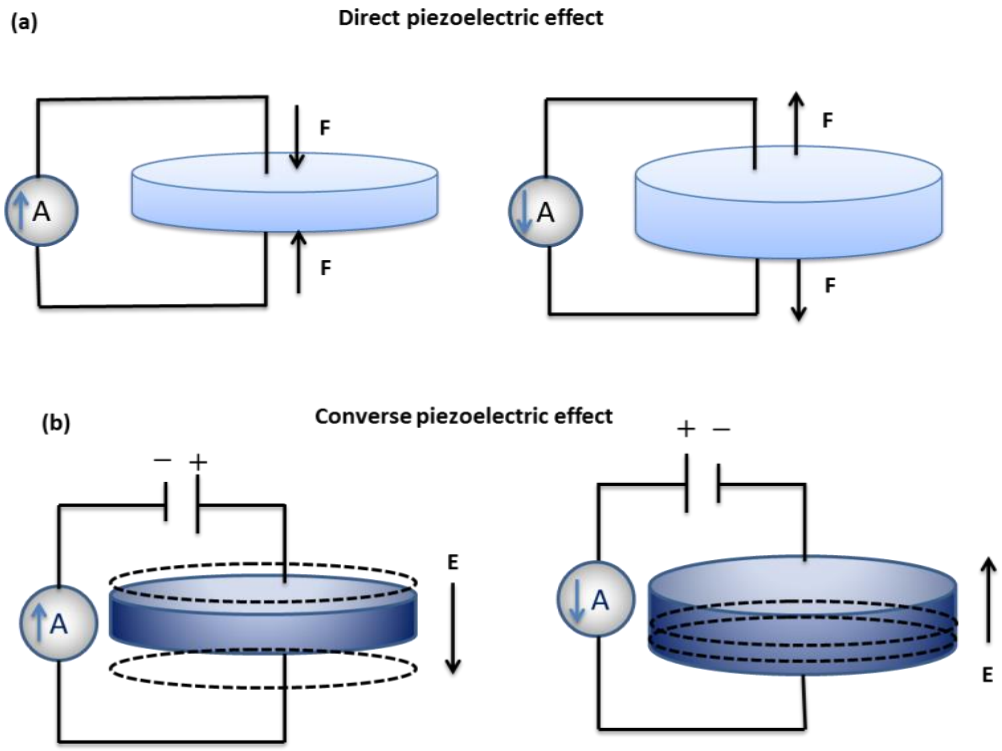

Figure 2.18 (a) Direct piezoelectric effect and (b) converse piezoelectric effect. Modified as (Moulson and Herbert, 2003)

The electrical energy supplied to the material is partly converted into useful work and the rest being wasted or dissipated inside the material. This can be expressed in terms of electromechanical constant k, which is the square root of the ratio of input electrical energy converted into mechanical energy to the input electrical energy due to the applied electric field (converse piezoelectric effect), or the ratio of the square root of input mechanical energy converted to electrical energy to the input mechanical energy or stress (direct piezoelectric effect) is called electromechanical coupling factor k, (Jaffe, 1971), Equation 2.17,

$$k = \sqrt{\frac{\text{electrical energy converted into mechanical energy}}{\text{input electrical inergy}}} \qquad \text{Equation 2.17}$$

Typical value of 'k' is always less than 1, for Rochelle salt k = 0.9 at 24 ºC, 0.10 for quartz and 0.5 to 0.7 for $BaTiO_3$ (Jaffe, 1971).

2.9 Electrostriction

Electrostriction is the basic electromechanical effect observed in all insulator or dielectrics in which the electric field/polarization-induced strain (S) is a direct function of the square or even powers of electric field (E)/polarization (P) (Li et al., 2014, Jaffe, 1971), Equation 2.18,

$$S = ME^2 = QP^2 \qquad \text{Equation 2.18}$$

where Q and M are electrostrictive coefficients, which can be determined from strain–polarization (S-P) and strain-electric field (S-E), for materials with high dielectric response where strain can be measured accurately (Li et al., 2014).

The strain induced by an electrostrictive effect is generally small and its sign is independent of the polarity of the electric field in contrast to the strain induced in piezoelectricity, in which the sign of deformation is dependent on the polarity of the applied electric field (Li et al., 2014).

More attention on electrostriction was focused in 1980s, during a systematic study of relaxor ferroelectrics with pervoskite structure, for example $Pb(Mg_{1/3}Nb_{2/3})O_3$ (PMN) and $Pb(Zn_{1/3}Nb_{2/3})O_3$(PZN) single crystal/ceramics, in which high electrostrictive effect was observed due to high dielectric response (Li et al., 2014).

Relaxors are superior to ferroelectric materials in many ways for example, low hysteresis in S-E response, no remanent strain, low ageing effect and no polling required.

Compared to classical ferroelectrics, electrostrictive materials are believed to be potential candidates for actuator use (Li et al., 2014).

2.10 Lead zirconate titanate, PZT

A high piezoelectric response in many ceramics, especially PZT is attributed to the presence of morphotrophic phase boundary (MPB), which separate the regions of different symmetries (e.g. rhombohedral-tetragonal), that can be crossed through a change in composition (Aksel and Jones, 2010). At a MPB the polarizability and piezoelectric properties increase due to mixed phase co-existence (e.g. rhombohedral-tetragonal) (Shrout and Zhang, 2007).

In the $PbZrO_3$ (PZ) and $PbTiO_3$ (PT) solid solution the most favourable piezoelectric properties were observed for the MPB composition $PbZr_{0.55}Ti_{0.45}O_3$ (PZT) between tetragonal and rhombohedral structures (Jaffe, 1971, Aksel and Jones, 2010). MPB is basically a vertical line on the phase diagram separating two crystal structures, that is only dependent on composition fluctuation, but independent or nearly independent of temperature as in the $PbZrO_3$ - $PbTiO_3$ solid solution system (Moulson and Herbert, 2003).

To date, there is still a controversy over the MPB in lead zirconate titanate (PZT), reports indicate an intermediate monoclinic phase, and the presence of a MPB is not always a necessary component of lead-free replacement materials for up grading piezoelectric properties (Aksel and Jones, 2010).

The phase diagram of lead titanate and lead zirconate system is shown in Figure 2.19.

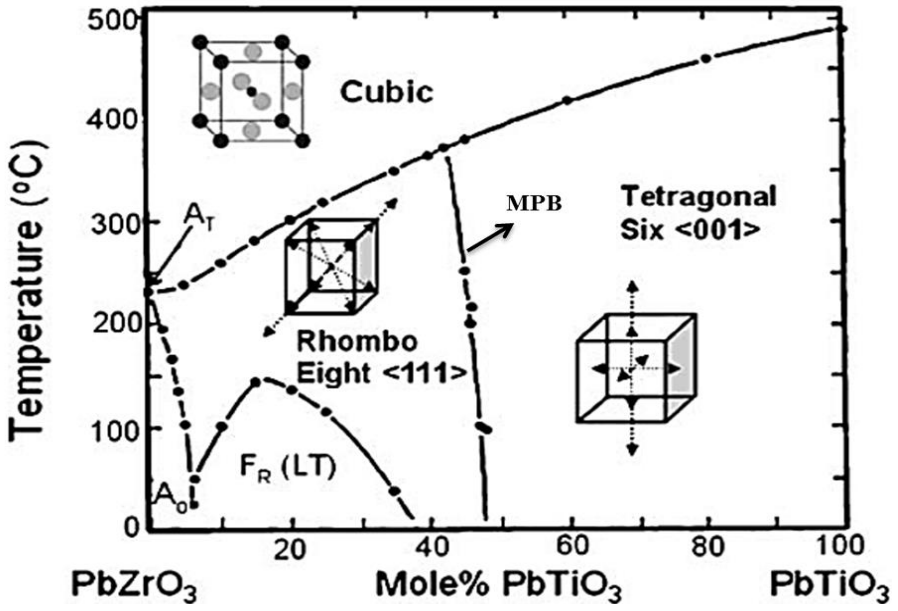

Figure 2.19 Phase Diagram of the PZT system. (Shrout and Zhang, 2007)

2.11 Poling

Poling, a process of aligning a randomly distributed domains in a single crystal or polycrystalline material into one particular direction when subjected to dc electric field and was first discovered in barium titanate by R.B Gray in 1945 (Haertling, 1999). The direction of polarization is directed along the direction of applied field (Jaffe, 1971), Figure 2.20.

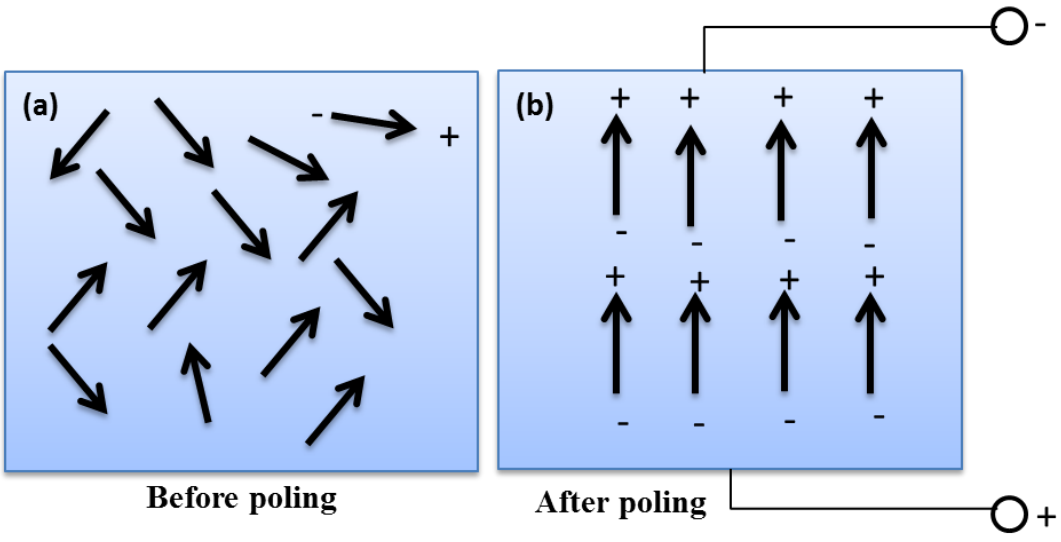

Figure 2.20 Representation of (a) unpoled and (b) poled ceramics.

2.12 Lead zirconate titanate based piezoelectrics

Lead zirconate titanate $Pb(Zr_{(1-x)}Ti_x)O_3$ (PZT) based ceramics have been market dominant piezoelectrics over several decades due to their excellent piezoelectric properties (Panda, 2009). The high piezoelectric properties of PZT were attributed to the presence of a morphotrophic phase boundary (MPB) between tetragonal and rhombohedral symmetries. Near the MPB, the relative permittivity, piezoelectric coefficients and coupling factors are optimized (Rödel et al., 2009).

The dielectric, microstructure and piezoelectric properties of PZT can be altered by modifying it with either donor dopants of higher charge number than Pb^{2+}, Zr^{4+} or Ti^{4+}, for example La^{3+}, B^{3+} (A-site), Nb^{5+}, Ta^{5+}, Sb^{5+} (B-site) or acceptor dopants of lower charge number than Pb^{2+}, Zr^{4+} or Ti^{4+}, for example K^{+1} (A-site) Sc^{3+}, Mg^{+2} (B-site) (Qiu and Hng, 2002).

The donor dopants act as ‘softener’, which causes a decrease in coercive field, an increase in relative permittivity and piezoelectric constant. In contrast, the acceptor dopants which act as a ‘hardener’ have the reverse effect on piezoelectric and dielectric properties of PZT (Zhang et al., 1983).

The saturation polarization, remanent polarization and coercive field reported for A-site La-doped (donor) PZT (52/48) were ~ 25.58 $\mu C/cm^2$, ~ 8.99 $\mu C/cm^2$ and 6.0 kV/cm respectively (Prabu et al., 2013). The coercive field observed for the donor doped PZT (Ni, Sb) was ~ 1 kV/mm and remanent polarization ~ 40 $\mu C/cm^2$ (Kounga et al., 2008). A high piezoelectric coefficient ~ 779 pm/V is reported for, 0.02 Sr, K, Nb, doped PZT 53/47, (Donnelly et al., 2007).

Undoubtedly PZT and modified PZT ceramics have shown superior dielectric and piezoelectric properties, however there have been concerns of European Union (EU) environmental legislation of waste electrical and electronic

equipment (WEEE) directive and the restriction of hazardous substance (RoHS) over the toxicity of lead oxide (PbO) during thermal processing and waste disposal (Qiao et al., 2012, Rödel et al., 2009, Directive, 2003).This has turned the focus of research from lead-based materials towards environmental friendly lead-free ferroelectrics (Rödel et al., 2009).

Among lead-free ferroelectrics, $BaTiO_3$ (BT), $Na_{0.5}Bi_{0.5}TiO_3$ (NBT), $K_{0.5}Bi_{0.5}TiO_3$ (KBT) and $K_{0.5}Na_{0.5}NbO_3$ (KNN) have been researched intensively (Panda, 2009, Leontsev and Eitel, 2010, Aksel and Jones, 2010). Of these $BaTiO_3$ based ceramic are widely used in capacitors and piezoelectric materials for commercial purposes (Zhang et al., 2011).

2.13 Barium titanate - based compositions

Barium titanate based solid solutions offer variety of properties (dielectric, piezoelectric and ferroelectric), for example a range of piezoelectric coefficient (d_{33}) values are reported, subject to different sintering temperatures, domain engineering of fine grained BT ceramics with high 90º domain wall densities and [110] grain-oriented BT: values range from ~ 191 to 788 pC/N, (Wada et al., 2010, Gao et al., 2011). However its low Curie temperature (~ 130 ºC), limits its dielectric and piezoelectric applications to temperature well below 130 ºC (Panda, 2009).

Electronic systems used as control units, for example in deep oil well exploration, aerospace, electric automobiles and nuclear reactors are required to operate under harsh environmental conditions ($T \geq 200$ ºC) (Dittmer et al., 2012). Dielectric capacitors are essential parts of the electronic devices used in these systems. The BT-based X7R – X9R commercial dielectric materials operate well below 200 ºC, but are unsuitable for the new applications in harsh environments (Buttay et al., 2011).

Dielectric capacitors, operating under harsh environment (≥ 200 ºC) is a growing research topic. New capacitor materials must be found which sustain high and stable relative permittivity (ε_r ± 15 %) to > 200 ºC and ideally to > 300 ºC. Efforts are underway to discover ceramics with high performance for harsh operating conditions. Different dopants/modifications have been incorporated into BT to develop new ceramics of desired properties.

The modification of BT with different compounds/ceramics resulted in good temperature-stable dielectric, piezoelectric and ferroelectric properties. For example nanocomposites of $BaTiO_3 – K_{0.5}Na_{0.5}NbO_3$ doped with 0.7 wt.% Li – Ti– Si – O sintering flux resulted in relative permittivity ~ 3960 at 25 ºC, a long range temperature stable plateau of relative permittivity from -55 to 150 ºC with temperature coefficient of capacitance no more than 12 %, which is of interest with reference to X8R capacitor (Hu et al., 2013).

A stable relative permittivity (~ 1500 – 3000) with tanδ < 2 % in the temperature range ~ 200 – 400 ºC varying no more than ±15 %, was observed for the system $BiMg_{0.5}Ti_{0.5}O_3 – xBaTiO_3$ ceramics (Zhang et al., 2011).

Xiong et al. reported stable dielectric properties (ε_r ~ 1000), fluctuating no more than ±15 %, in the temperature range -70 – 160 ºC for niobium doped $(1–x)BiMg_{0.5}Ti_{0.5}O_3 – xBaTiO_3$ system (Xiong et al., 2011).

Zeb et al. reported an extended flat plateau of relative permittivity (~835 ± 40) in the temperature range 65 – 550 ºC for the ceramic system $Ba_{0.8}Ca_{0.2}TiO_3 – BiMg_{0.5}Ti_{0.5}O_3$ (50/50), Figure 2.21, ε_r ~ 950 ± 10 % for, $0.45Ba_{0.8}Ca_{0.2}TiO_3 – (0.55 – x)\ BiMg_{0.5}Ti_{0.5}O_3 – xNaNbO_3$ (x = 0) in temperature range 80 – 600 ºC, Figure 2.22 and ε_r ~ 1030 ± 15 % in the temperature range 25 – 400 ºC for $Ba_{0.8}Ca_{0.2}TiO_3 – xBiZn_{0.5}Ti_{0.5}O_3$ (x = 0.3), Figure 2.23. (Zeb and Milne, 2013b, Zeb and Milne, 2013d, Zeb and Milne, 2014a).

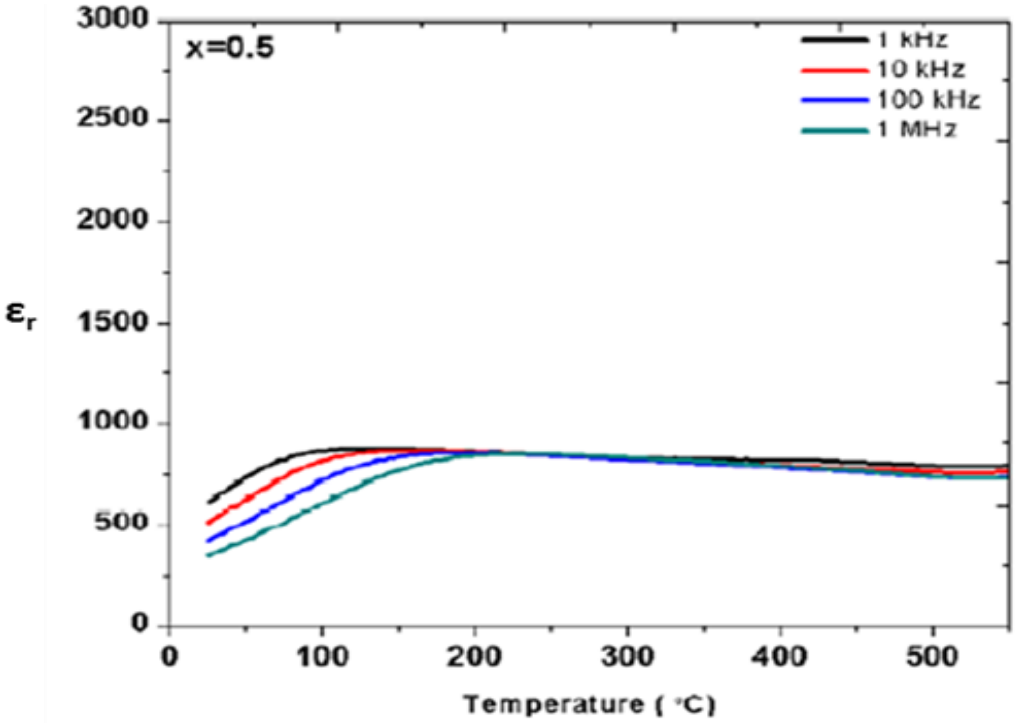

Figure 2.21 Temperature-dependent relative permittivity at frequencies 1 kHz – 1 MHz for $(1–x)Ba_{0.8}Ca_{0.2}TiO_3 – xBi(Mg_{0.5}Ti_{0.5})O_3$, (x = 0.5). (Zeb, 2011)

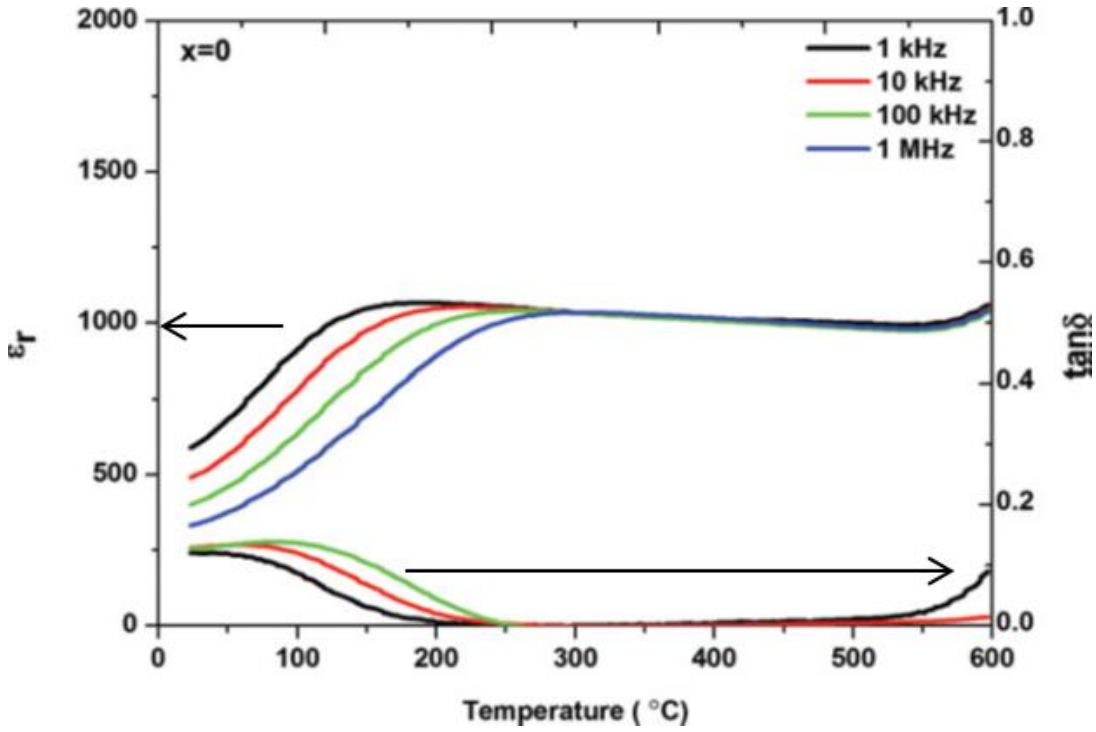

Figure 2.22 Temperature-dependent relative permittivity and tanδ at frequencies 1 kHz – 1 MHz for for $0.45Ba_{0.8}Ca_{0.2}TiO_3 – (0.55 – x)$ $Bi(Mg_{0.5}Ti_{0.5})O_3 – xNaNbO_3$, (x = 0).(Zeb, 2013)

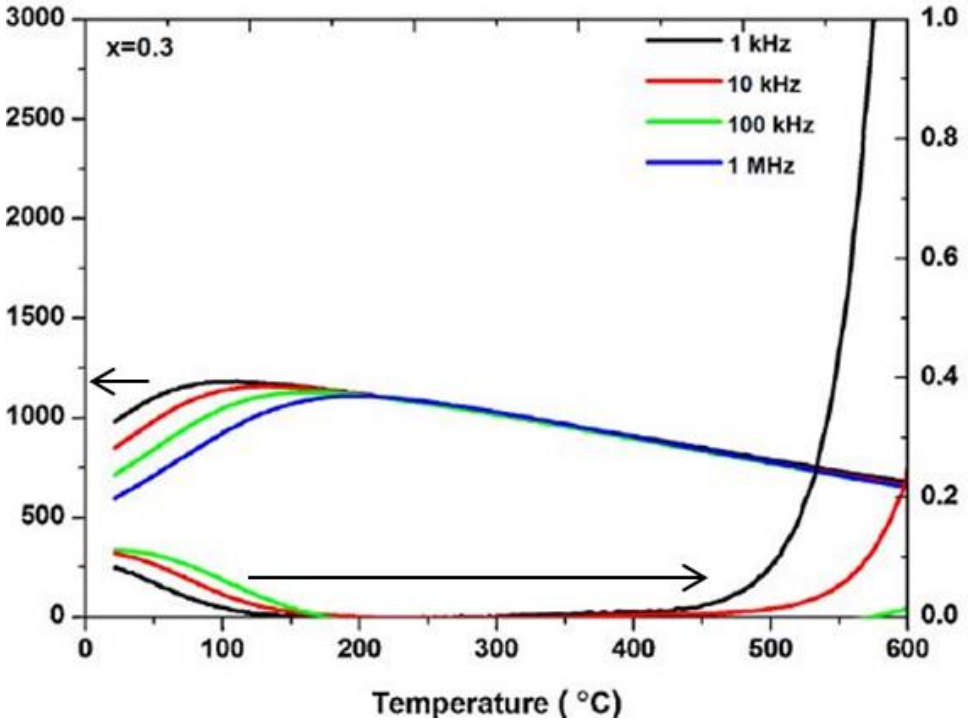

Figure 2.23 Temperature-dependent relative permittivity and tanδ at frequencies 1 kHz – 1 MHz for $Ba_{0.8}Ca_{0.2}TiO_3 – xBiZn_{0.5}Ti_{0.5}O_3$, (x = 0.3).

Raengthon et al. reported a ternary compound $BaTiO_3 – BiZn_{0.5}Ti_{0.5}O_3 – NaNbO_3$ with extended temperature independent dielectric properties (ε_r ~ 450 – 700 ± 15%) in the temperature gradient ~ -100 – 200 ºC, that makes it feasible for X9R capacitor application (Raengthon et al., 2013a), Figure 2.24.

Ogihara et al. reported that the ceramic $0.7BaTiO_3 – 0.3BiScO_3$ might be a potential candidate for high energy storage capacitor maintaining relatively good relative permittivity, nearly independent of temperature over a wide range of temperature (~ 50 – 400 ºC) (Ogihara et al., 2009), Figure 2.25. Furthermore, Raengthon et al. reported ceramics $BaTiO_3 – BiZn_{0.5}T_{0.5}O_3 – BiScO_3$ with temperature stable dielectric properties (ε_r > 1000) in the temperature range ~ 100 – 500 ºC (Raengthon et al., 2012), Figure 2.26.

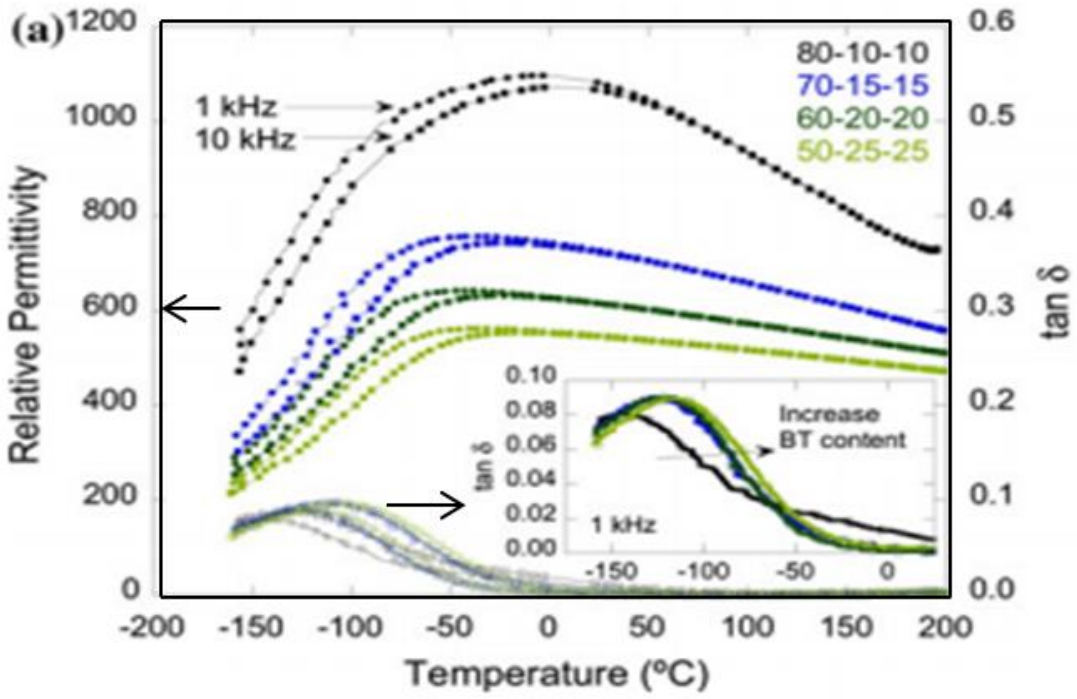

Figure 2.24 Temperature-dependent relative permittivity and tanδ at 1 kHz and 10 kHz, for $BaTiO_3$ – $BiZn_{0.5}Ti_{0.5}O_3$ – $NaNbO_3$. (Raengthon, 2013)

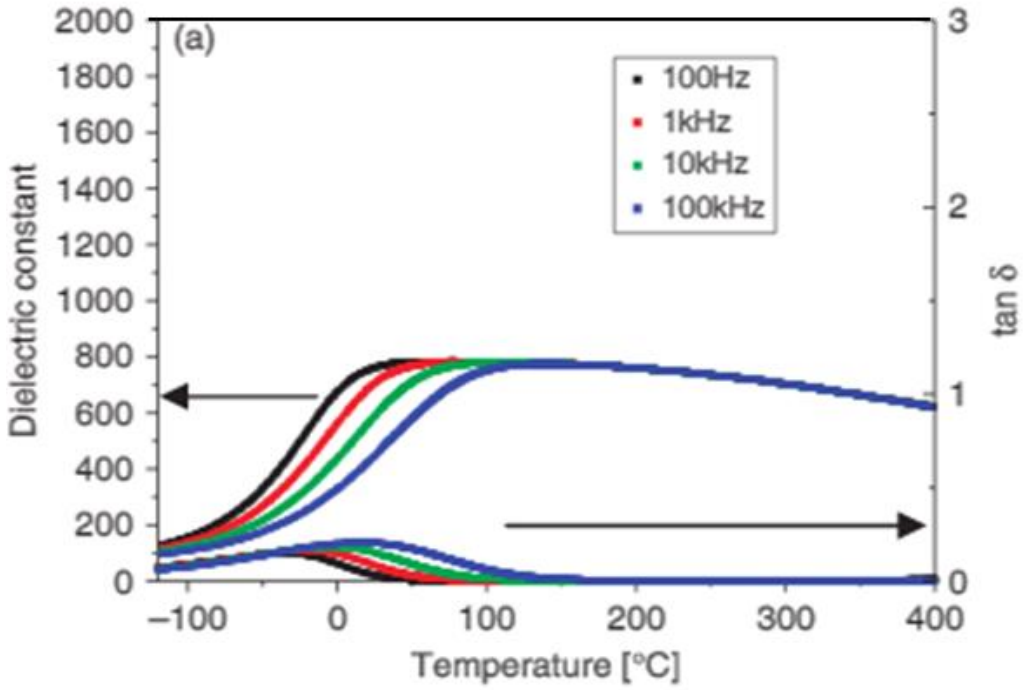

Figure 2.25 Temperature-dependent relative permittivity and tanδ at 1 kHz – 1 MHz for $0.7BaTiO_3$ – $0.3BiScO_3$. (Ogihara, 2009)

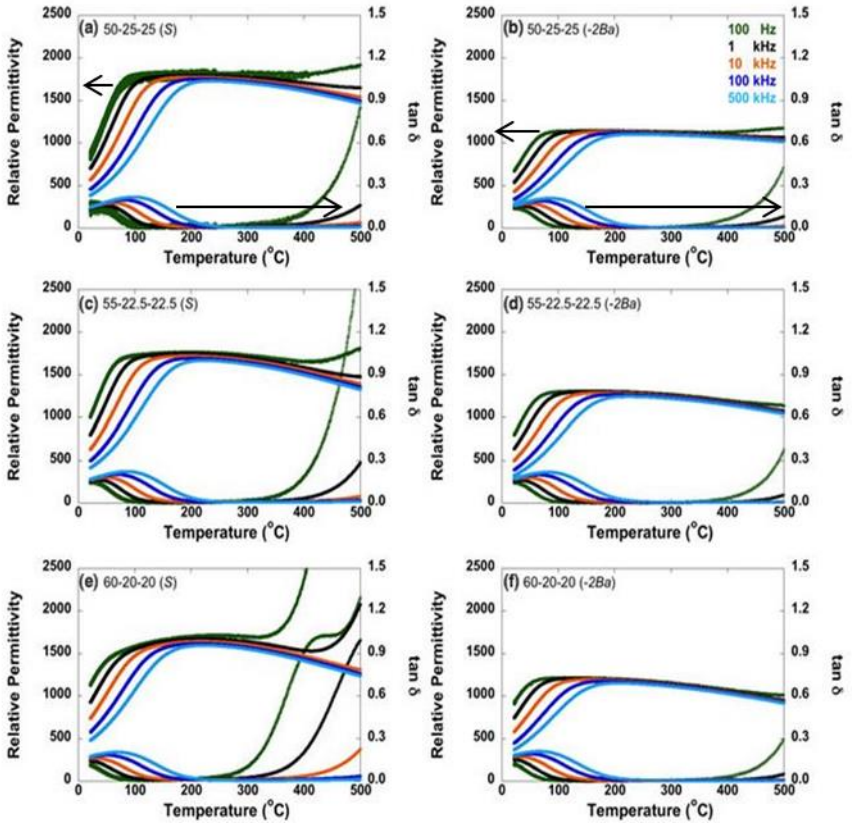

Figure 2.26 Temperature-dependent relative permittivity and tanδ of stoichiometric (S) and 2 mol% Ba deficient (-2Ba) (a and b) $50BaTiO_3 – 25BiZn_{0.5}Ti_{0.5}O_3 – 25BiScO_3$ (c and d) $55BaTiO_3 – 22.5BiZn_{0.5}Ti_{0.5}O_3 – 22.5BiScO_3$ and (e and f) $60BaTiO_3 – 20BiZn_{0.5}Ti_{0.5}O_3 – 20BiScO_3$ ceramics. (Raengthon et al. 2012)

2.14 Sodium bismuth titanate based solid solutions

Sodium bismuth titanate $Na_{.5}Bi_{0.5}TiO_3$ [NBT], was discovered by Smolensky et al, in 1960. At room temperature, a rhombohedral R3c space group is reported by Jones and Thomas in 2002 (Aksel and Jones, 2010).

Rietveld neutron diffraction powder analysis of the compound NBT were carried out by Jones et al. in the temperature range -268 – 540 ºC to study the phase transition temperatures of compound NBT. The sequence of phase transition temperature have shown a rhombohedral structure in the temperature range -268 – 255 ºC, a mixed rhombohedral – tetragonal phases in the temperature range 255 –

400 ºC, a tetragonal phase from 400 ºC to 500 ºC, a mixed tetragonal - pseudocubic phases in the temperature range 500 – 540 ºC and a prototype cubic phase beyond 540 ºC (Jones and Thomas, 2002).

A high resolution transmission electron microscopy (TEM) study on NBT have shown a complex structure with the formation of nanometre size tetragonal platelets, which are homogeneously distributed within the rhombohedral R3c matrix (Dorcet and Trolliard, 2008). In addition the *in situ* TEM study performed on NBT, revealed a destabilization of R3c rhombohedral phase near 200 ºC and a modulated phase, which is due to the intergrowth of orthorhombic sheets within rhombohedral R3c matrix in the temperature range ~ 230 – 300 ºC. The orthorhombic sheets, which act as twin boundaries between two R3c ferroelectric domains increases with increasing temperature due to micro twining process until 300 ºC, after which they switched immediately into a tetragonal phase (Dorcet et al., 2008, Trolliard and Dorcet, 2008, Dorcet et al., 2009).

In addition a high resolution powder x-ray diffraction patterns of NBT have shown a monoclinic phase from ~ 25 ºC to ~ 250 ºC (Aksel et al., 2011).

A high Curie temperature (T_C ~ 320 ºC), remanent polarization (P_r ~ 38 $\mu C/cm^2$) (Panda, 2009) and relatively good piezoelectric constant d_{33} ~ 73 pC/N (Aksel and Jones, 2010) make NBT a promising lead-free piezoelectric. However NBT in its pure form has some drawbacks, for example a high coercive field (Ec ~ 7.3 kV/mm), high electrical conductivity due to volatility of bismuth oxide during processing, difficulty in poling, low depolarization temperature and relatively high sintering temperatures (Panda, 2009, Rödel et al., 2009). There have been still controversies and complexity about the crystal structure of NBT, research is still in progress to further investigate its structure.

The incorporation of different additives reduces the coercive field of NBT and improves the piezoelectric properties. NBT has a mixture of Bi^{+3} and Na^{+1} ions on the A-site. The co-doping with Li^{+1} and K^{+1}, on A-site increased d_{33} to 146 pC/N, coupling factor k to 36 % but reduced E_c to 3.7 kV/mm (Aksel and Jones, 2010). Different dopants have different effects on the properties of NBT, for example, 6 mol % La_2O_3 increased d_{33} from ~ 64 to 92 pC/N, and 2 mol % $NaNbO_3$ to 88 pC/N (Panda, 2009).

NBT is now used in binary solid solutions, for example $Na_{0.5}Bi_{0.5}TiO_3$ – $K_{0.5}Bi_{0.5}TiO_3$ [NBT – KBT], $Na_{0.5}Bi_{0.5}TiO_3$ – $BaTiO_3$ [NBT– BT], $Na_{0.5}Bi_{0.5}TiO_3$ – $K_{0.5}Na_{0.5}NbO_3$ [NBT - KNN], $Na_{0.5}Bi_{0.5}TiO_3$ – $BiFeO_3$ [NBT – BFO], and ternary solid solutions $Na_{0.5}Bi_{0.5}TiO_3$ – $BaTiO_3$ – $KNaNbO_3$ [NBT – BT – KNN], to get desired piezoelectric and ferroelectric properties (Aksel and Jones, 2010). Figure 2.27, shows a pervoskite unit cell of NBT.

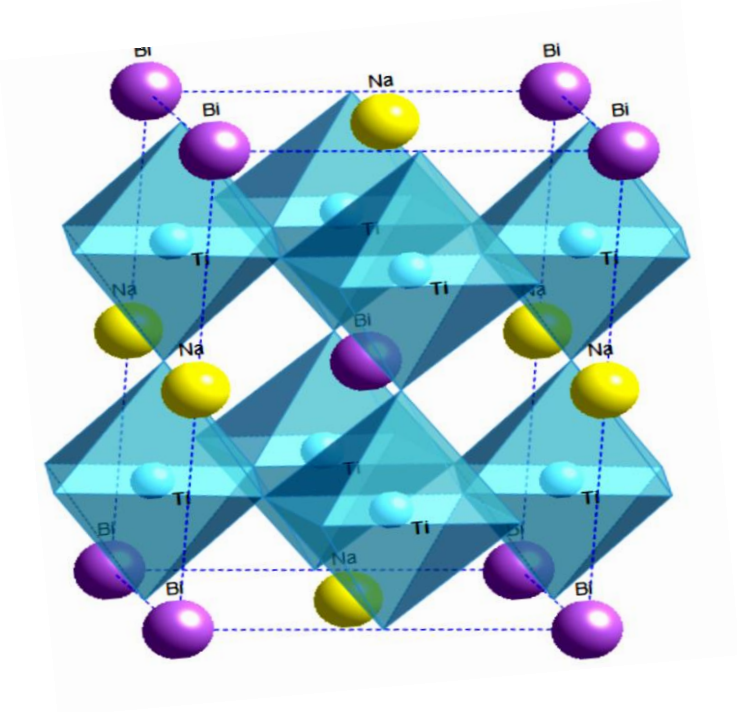

Figure 2.27 NBT Pervoskite pseudo-cubic structure, Oxygen (O) at each six edges of octahedra, not shown for clear view of B-cation). (Aksel., 2010)

Takenaka et al. observed a morphotrophic phase boundary between a rhombohedral NBT and a tetragonal BT solid solution at 6 – 7 mol% BT, with enhanced room temperature dielectric constant (ε_r ~ 580), electromechanical coupling coefficient (k_{33} ~ 55 %) (Rödel et al., 2009) and piezoelectric constant d_{33} ~ 125 pC/N (Leontsev and Eitel, 2010). The piezoelectric constant of this MPB composition was further improved to d_{33} ~ 208 pC/N by lithium modification. The MPB composition has relatively high T_C of ~ 288 ºC and depolarization temperature T_d ~ 150 ºC (Leontsev and Eitel, 2010).

A high piezoelectric coefficient d_{33} ~ 192 pC/N is reported for the MPB composition of $Na_{0.5}Bi_{0.5}TiO_3 – xBi_{0.5}K_{0.5}TiO_3$ (16 – 20 %) (Aksel and Jones, 2010, Leontsev and Eitel, 2010, Zhang et al., 2008b). The MPB composition has high T_C ~ 280 – 300 ºC and low depolarization T_d ~ 140 ºC (Leontsev and Eitel, 2010). The $d_{33,}$ k_p, P_r values reported for 22 mol% of KBT composition, were 192 pC/N, 32.5 %, 19.5 $\mu C/cm^2$ respectively (Aksel and Jones, 2010). According to these authors, sintering conditions of the solid solution of NBT – KBT play an important role in its piezoelectric properties. The volatility of bismuth, potassium and sodium limits its sintering temperature.

Zhang et al. reported an increase in $d_{33,}$ from 155 pC/N to 192 pC/N, when the sintering temperature was increased from 1110 ºC to 1150 º at an MPB composition (Aksel and Jones, 2010, Zhang et al., 2008b). The addition of 4 at.% Li to the MPB composition enhanced d_{33} to ~176 pC/N and k_{33} to 60 % (Rödel et al., 2009). A mixed orthorhombic – tetragonal phase is observed in the ceramics $K_{0.5}Na_{0.5}NbO_3 – xNa_{0.5}Bi_{0.5}TiO_3$ (x = 0.02 and x = 0.03), resulting in high d_{33} ~ 195 pC/N and electromechanical coupling factor of 43 % (Aksel and Jones, 2010).

Dittmer et al. reported a temperature stable relative permittivity from ~ 43 to 319 ºC (±10 % tolerance) for the ternary ceramics NBT – 0.06BT – xKNN (x =

0.18). A high relative permittivity ε_r ~ 2150 at 150 ºC and high resistivity of the order of 10^8 Ω m was observed for the composition, x = 0.18 (Dittmer et al., 2011a), Figure 2.28.

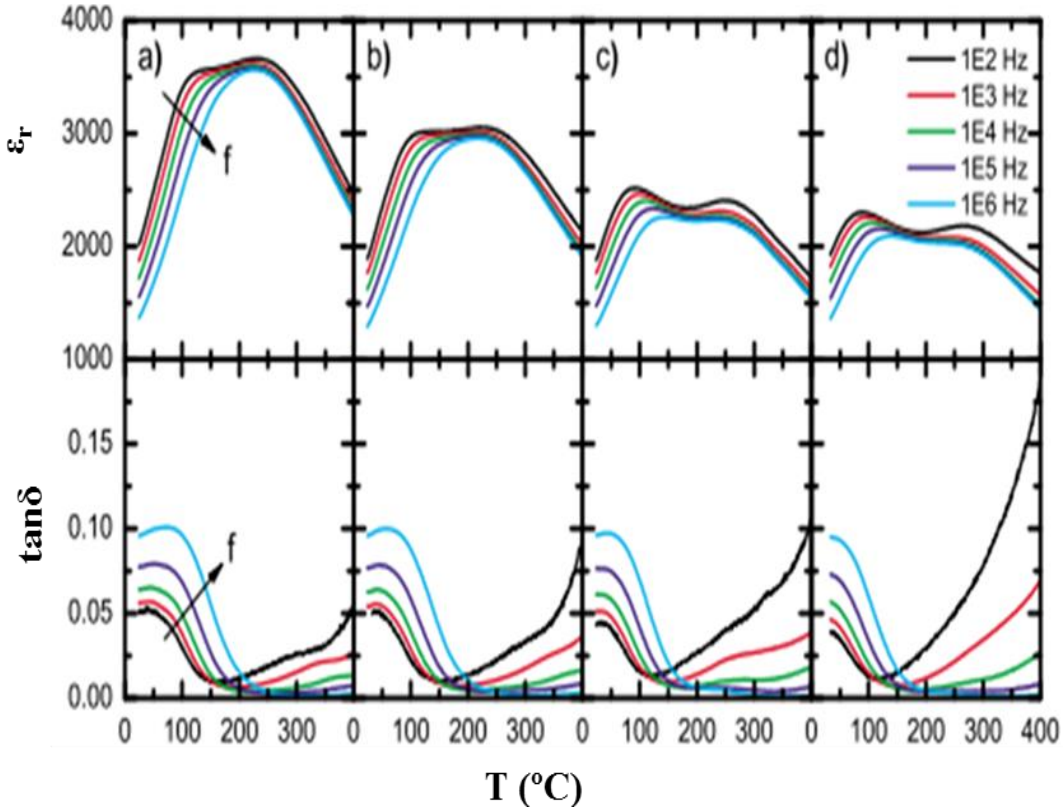

Figure 2.28 Temperature-dependent relative permittivity and tanδ of (1–x)[0.94 $Na_{0.5}Bi_{0.5}TiO_3$ – 0.06$BaTiO_3$] – x$K_{0.5}Na_{0.5}NbO_3$ (a) x = 0.09 (b) x = 0.12, (c) x = 0.15, and (d) x = 0.18 (Dittmer 2011)

Temperature-stable dielectric properties were reported for ceramics NBT – 0.4BKT – xKNN) with x = 0.15 at less than 10 % variation in relative permittivity of about 2100 in the temperature range ~ 54 ºC – 400 ºC which can be used for capacitor applications (Dittmer et al., 2012), Figure 2.29.

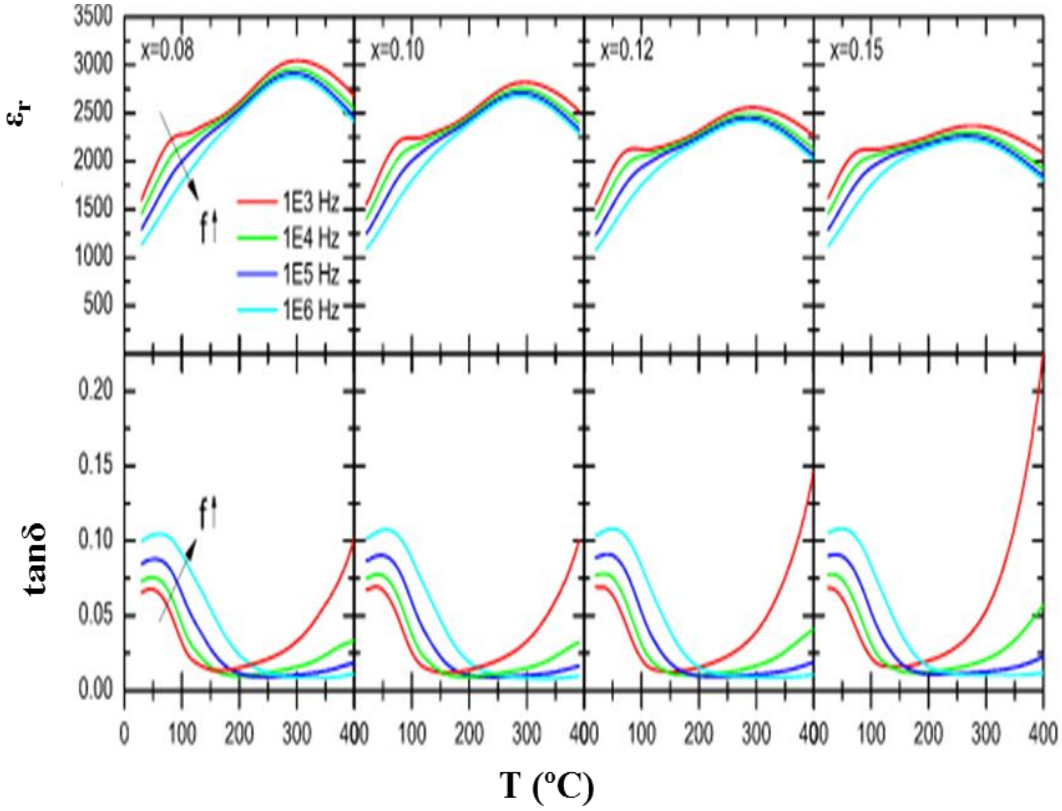

Figure 2.29 Temperature-dependent relative permittivity and loss factor for (1 – x) [0.6$Na_{0.5}Bi_{0.5}TiO_3$ – 0.4$Bi_{0.5}K_{0.5}TiO_3$] – x$K_{0.5}Na_{0.5}NbO_3$ of x = 0.08, 0.10, 0.12, 0.15) up to 400 °C. (Dittmer, 2012)

2.15 Summary

There have been many developments in the dielectric material over the past few decades. Many lead-free material systems have been investigated of which some displayed comparable properties to PZT, however there is still no single system with versatile applications similar to PZT. The historically significant BT continued to be a fundamental system of research, but its properties are limited to a temperature below 130 ºC, which makes it inferior to PZT. A high Curie temperature compound, sodium bismuth titanate (NBT), lacks enough high piezoelectric properties due to low depolarization temperature (below 200 ºC). However, modifications to BT and NBT resulted in better piezoelectric and dielectric properties in many cases, for example, NBT – BT, NBT – KBT.

The dielectric and piezoelectric properties of many lead-free ceramics are limited to a temperature well below 200 ºC. There is a requirement for current growing modern technology to explore a novel lead-free ceramics that can operate at temperatures well above 200 ºC without any degradation to its dielectric and piezoelectric properties.

For the ceramic system $BiMg_{0.5}Ti_{0.5}O_3 - xBaTiO_3$, the temperature-stable relative permittivity: $\varepsilon_r \sim (1500 - 3000) \pm 15$ % observed in the temperature range ~200 – 400 ºC. For Nb-doped, $(1–x)BiMg_{0.5}Ti_{0.5}O_3 - xBaTiO_3$, $\varepsilon_r \sim 1000 \pm 15$ % from -70 to160 ºC. For $0.5Ba_{0.8}Ca_{0.2}TiO_3 - 0.5BiMg_{0.5}Ti_{0.5}O$, $\varepsilon_r \sim 835 \pm 40$ in the temperature range 65 – 550 ºC. For $Ba_{0.8}Ca_{0.2}TiO_3 - BiMg_{0.5}Ti_{0.5}O - xNaNbO_3$, $\varepsilon_r \sim 950 \pm 10$ % from 80 to 600 ºC. For $Ba_{0.8}Ca_{0.2}TiO_3 - xBiZn_{0.5}Ti_{0.5}O_3$ (x = 0.3), $\varepsilon_r \sim 1030 \pm 15$ % in the temperature range 25 – 400 ºC and for NBT – 0.06BT – xKNN (x = 0.18) $\varepsilon_r \sim 2150 \pm 10$ % in the temperature range ~ 43 – 319 ºC.

In this study efforts will be made to develop lead-free ceramics with relatively good dielectric and piezoelectric properties, which are temperature independent over an extended region well beyond 200 ºC. Furthermore, the effects of Bi excess will also be studied on some of the NBT-based solid solutions.

2.16 Background science to processing and characterization techniques

2.16.1 Calcination

Calcination is a heat treatment process of a ceramic powder below its melting point and is used to promote diffusion of ions of a constituent's reagents to form a compound and remove volatile materials, such as carbonates. Diffusion takes place due to the movement of ions within the material.

The key factors that allow diffusion of atoms or ions or molecules within the material are lattice vacancies in the vicinity of neighbouring atoms and the supply of sufficient energy to break bonds with neighbouring atoms. When the temperature increases the vibrational energy of atoms or ions or molecules starts to increase, resulting in more rapid diffusion.

The minimum energy required to start a chemical reaction among the constituent's atoms/ions/molecules to form a compound is the activation energy E_a. In calcination a chemical reaction will take place beyond its activation energy (Callister, 2000).

2.16.2 Sintering

Sintering is used for densification of a compacted powder pellet (green pellet) to form a dense ceramic composed of interlocking grains. In sintering mechanisms mass transport phenomena take place through surface diffusion, volume diffusion, grain boundary diffusion, and grain growth, evaporation and condensation (Shimosaka et al., 2003) Figure 2.30 (a) & (b).

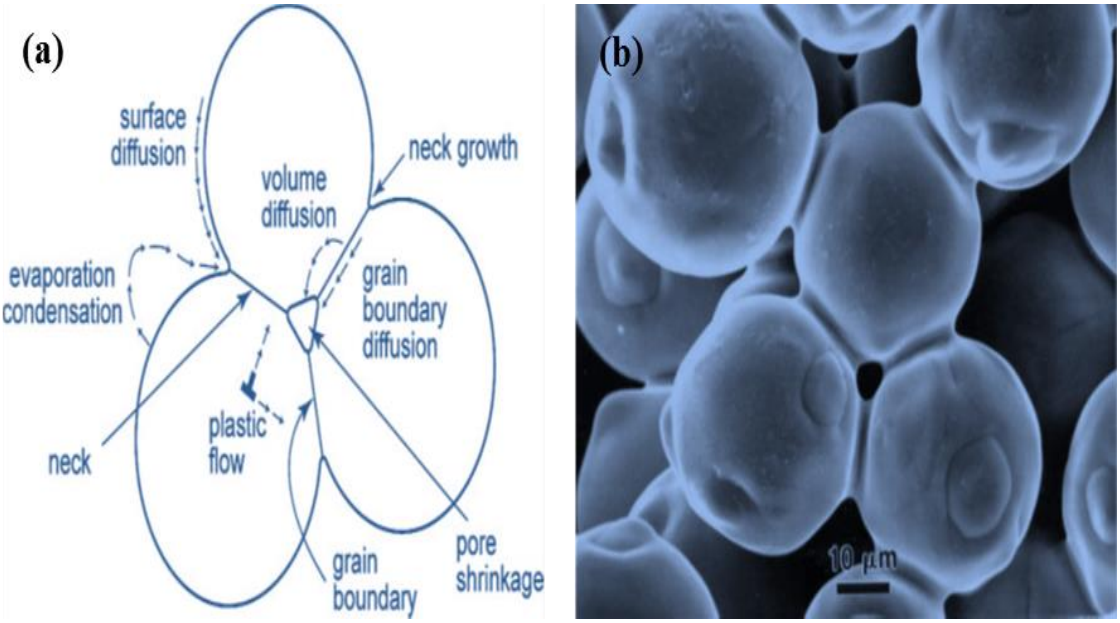

Figure 2.30 (a) A schematic diagram showing three spherical particles and the various mass transport paths that provide neck growth and in some cases pore shrinkage (b) neck formation in spherical particles. (German, 2010)

The process of sintering is strongly dependent upon the nature of the material, its melting point, particle size and other processing variables. Sintering produces a contraction (shrinkage), where the densification of compact powder takes place, leading to strengthening. Sintering reduces surface energy by replacing solid-gas interfaces with lower energy solid-solid grain boundary interfaces.

Coarsening, or grain growth, also occurs during sintering (German, 2010). Large grain sizes can be the result of secondary grain growth, where smaller particles inter diffuse with larger particles.

The key factor for coarsening and densification is the magnitude of pore to particle size ratio and its change during densification. Surface diffusion is one of the main mass transport mechanisms during the intermediate stage of sintering, whereas boundary and volume diffusion contributes mainly at the final stage of sintering (Shi,1999)

2.16.3 X-ray diffraction

X-rays, are highly energetic electromagnetic radiations of wavelength of the order ~1 Å, lying between ultraviolet and gamma rays in the electromagnetic spectrum and were discovered by a German physicist Rontgen in 1895 (Cullity and Stock, 2001). In crystallography, X-ray diffraction is one of the powerful tools for phase identification of minerals, ceramics, chemical compounds, engineering materials and identification of crystal structures of known materials. Inter planer d-pacing, theoretical density, and crystallite size can be determined from XRD patterns (Cullity and Stock, 2001, Hammond, 2009).

X-rays can either be generated by the deceleration of highly energetic charges (electrons), or from the inner shell transitions of electrons of complex atoms Figure 2.31 (a) & (b). The former are called white or continuous x-rays, and the later, a characteristic x-rays (West, 1999, Cullity and Stock, 2001).

Monochromatic X-rays are more often used for diffraction purpose. A high energy beams ($E \geq 30$ kV), strikes a metal target, more often copper, and knocked out some K-shell electrons, produce vacancies. These vacancies in the K-shell are filled by a jump of electrons from either higher shells (L, M, N …) by losing energy, equal to the energy difference between the two shells ($\Delta E = hf = hC/\lambda$) in the form of X-rays, Figure 2.31 (a). The jump of L-shell electron to K-shell, generates K_α characteristics X-rays (λ = 1.5418 Å), and a jump of M-shell electron to K-shell, produces K_β characteristic x-rays (λ = 1.3922 Å). K_α radiations are more intense compared to K_β radiations, and are used in diffraction research, Figure 2.31 (b).

Since the transition has a slightly different energies for the two possible spin states of L-shell electron which makes the transition, relative to the spin of K-shell vacant orbital, K_α exists in doublets , $K_{\alpha1}$ ($\lambda \sim 1.54051$ Å) and $K_{\alpha2}$ ($\lambda \sim 1.54433$ Å).

The $K_{\alpha 2,}$ on right half of diffraction peak is striped out by software X-pert high score plus. Nickel (Ni) filter is used to eliminate K_{β} radiation and obtain near monochromatic $K_{\alpha,}$ X-rays for diffraction (West, 2013).

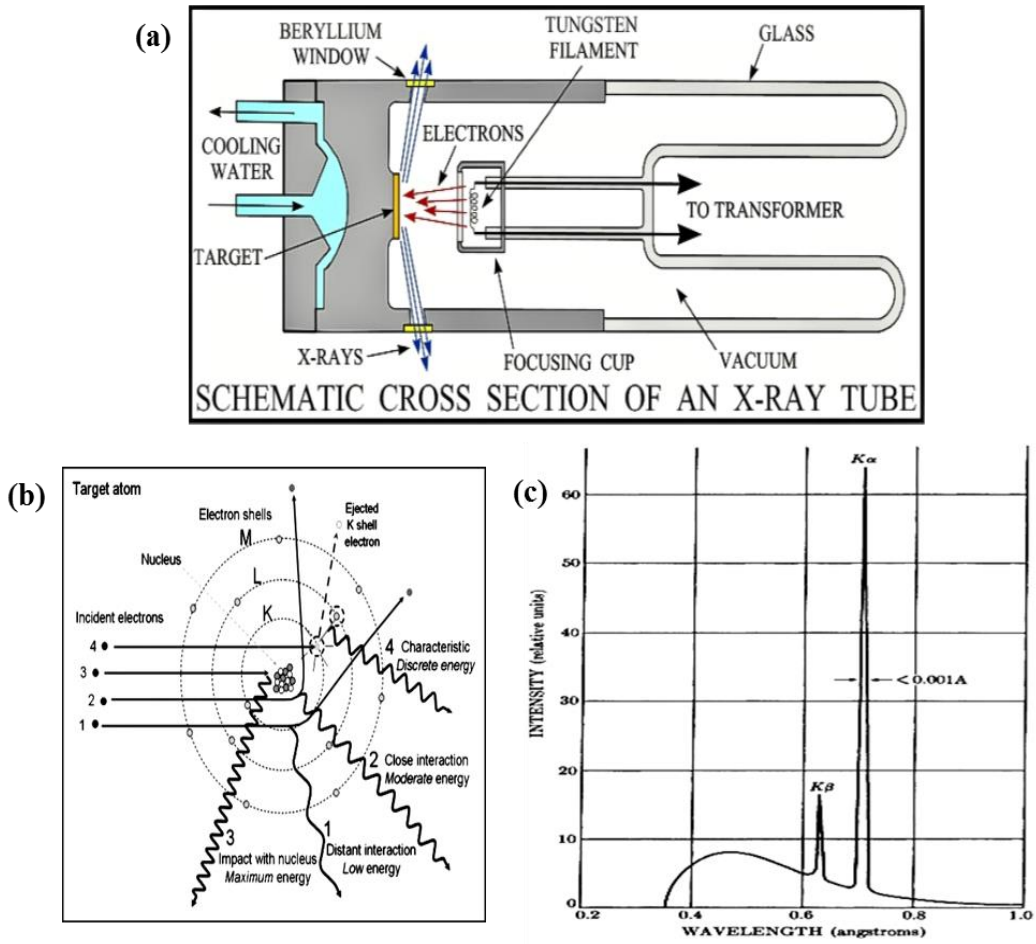

Figure 2.31 (a) Generation of X-rays (Poppe et al., 2001), (b) Characteristic X-rays generation (Seibert, 2004) and (c) Intensity V.s wavelength of X-rays (Moulson and Herbert, 2003)

X-ray peaks are due to the diffraction of in phase waves. Light waves travel straight in air, and bend when they strike an obstacle or aperture comparable to the size of wavelength of light, which we call diffraction phenomena of waves. It is the superposition of two or more similar type of waves that either result in maxima (in phase waves) or minima (out of phase waves), Figure 2.32.

X-rays cannot be diffracted by a standard optical diffraction grating due to their small wavelengths, compared to interspacing between the lines of a diffraction grating. X-rays can be diffracted by crystal lattice because of comparable d-spacing between atoms (~ 1 Å) to the wave length of X-rays. Bragg's derived a mathematical relation to find inter-planer spacing and Miller indices, from the x-ray diffraction pattern of the sample (Cullity and Stock, 2001).

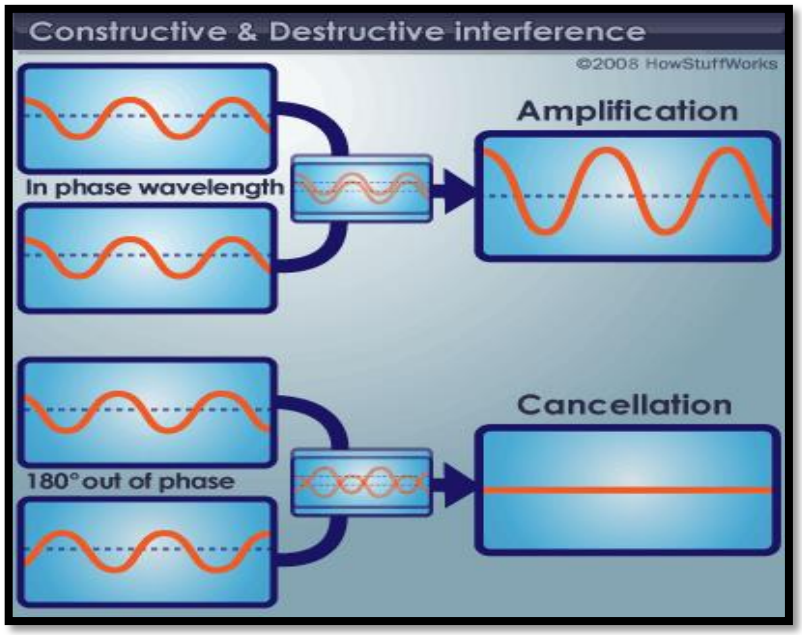

Figure 2.32 Interference of electromagnetic waves. (Horton, 2008)

Bragg approached the diffraction of X-rays by treating crystals as the combination of equally spaced parallel planes which act as semi-transparent mirror. Some of the X-rays falling on the crystal are reflected such that the angle of incidence is equal to angle of reflection, whereas the rest of X-rays are either transmitted through crystal or absorbed by crystal. The reflected X-rays either interfere constructively if in phase (path-difference = $n\lambda$, n = 1, 2, 3….) or destructively if out of phase (path-difference = $(n+1/2)\lambda$, n = 1, 2, 3….). Partial destructive interference occurs for intermediate path differences.

Bragg diffraction can be well understood by considering two parallel in phase rays 1 and 2 that falls on crystal planes A and B, separated by interplanar spacing d as shown in Figure 2.33.

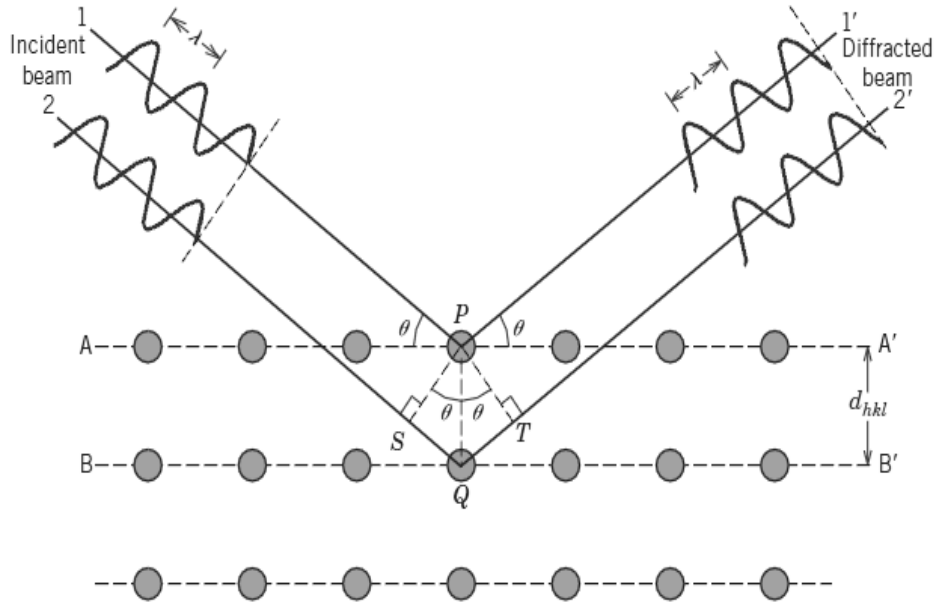

Figure 2.33 X-Ray diffraction and Bragg's law. (Callister, 2000)

The two waves after reflection from crystal planes interfere constructively if the path difference between the waves is nλ, where, n = 0, 1, 2 ….. . Ray 2 travels further a distance SQ + QT than ray 1.

From right angle triangle ΔPQS

$\sin\theta = QS/PQ = QS/d$ $(QS = d\sin\theta)$ Equation 2.19

Similarly, from right angle ΔPQT,

$QT = d\sin\theta$ Equation 2.20

Now the total path difference between the two interfering rays is

$SQ + QT = d\sin\theta + d\sin\theta = 2d\sin\theta$ Equation 2.21

Since the two waves are in phase with each other thus for nth order maxima

$SQ + QT = n\lambda$ Equation 2.22

$n\lambda = 2d\sin\theta$ Equation 2.23

Where n is an integer, λ is the wavelength of the X-rays, d is the interplanar spacing generating the diffraction and, θ is the diffraction angle. λ and d both are usually measured in angstroms Å (1 Å = 10^{-10} m).

For first order maxima n = 1

$\lambda = 2d\sin\theta$ ($\sin\theta = \lambda/2d$) Equation 2.24

Sharp peaks in XRD patterns are the ideal condition, however broad or diffuse peaks are also observed in many cases which might be either due to incomplete reaction or particle size or lattice strain or instrumental error. The Sherrer formula can be used to find crystallize size

$t = k\lambda/\beta\cos\theta$ Equation 2.25

Where, t = crystallize size.

λ = wavelength of incident x-rays.

β = integral breadth of the peak.

k = shape factor ~ 1.

From equation 2.25, sharp XRD peaks will be possible by using materials with smaller cell size (nano size particles).

2.16.4 Scanning electron microscopy

SEM is a modern technique for studying surface topography of organic and inorganic materials from nano to micro scale (Goldstein, 2003, West, 1999). Particle/grain size, qualitative or semi-quantitative chemical analysis, can be obtained, using high magnification (10 × – 1000 ×) and high resolution (1 – 5 nm) (Goodhew, 2000).

The idea of scanning electron microscopy was floated by H.Stizing in 1927, while the first image was developed by H.Knoll in 1935 (Hawkers et al, 2007).

Highly accelerated electrons are focused on the specimen, which may scan across or raster the surface of the specimen to produce its image (Joseph Goldstein, 2003). This energetic beam of electrons interacts with the specimen, resulting in backscattered electrons, secondary electrons, Auger electrons, characteristic X-rays and some other photons of various energies (Joseph Goldstein, 2003, Pye et al.,2005).

Using transmission electron microscopy, signals generated from SAED (selected area electron diffraction) of the specimen are used for surface analysis and crystallographic analysis. The X-rays generated yield compositional information. Back scattered and secondary electrons are of much interest in all the generated signals, as these are generated as a result of difference in surface topography.

The secondary electrons are responsible for the image formation of the specimen. The characteristic x-rays generated from the sample gives both qualitative and quantitative elemental information to ~ 1 μm depth and beam diameter. Large depth-of-field of SEM is used for three dimensional imaging of the specimen (Joseph Goldstein 2003).

The secondary electron based SEM was developed in New Jersey RCA laboratories during world war two. The first SEM images of Oatley and his colleagues, were obtained in 1951, and were commercialized in 1958 (Egerton, 2005).

2.16.4.1 Principle of SEM

The SEM comprises electromagnetic lenses system, electron gun, and electron collector, visual and recording cathode ray tubes (Pye et al., 2005), Figure 2.34 (a).

Electrons generated by means of field emission or thermionic emission are accelerated towards the specimen by the application of high voltage (Reimer, 1998). The primary beam of electrons, suffers two types of scattering, elastic and inelastic on interaction with the specimen.

In an elastic scattering the electron interacts with the nucleus without losing energy, whereas in an inelastic scattering electron loses its energy by emitting continuous X-rays, or ejecting secondary electrons from the specimen. These signals are collected by the detector and image of the specimen is produced (Pye et al., 2005).

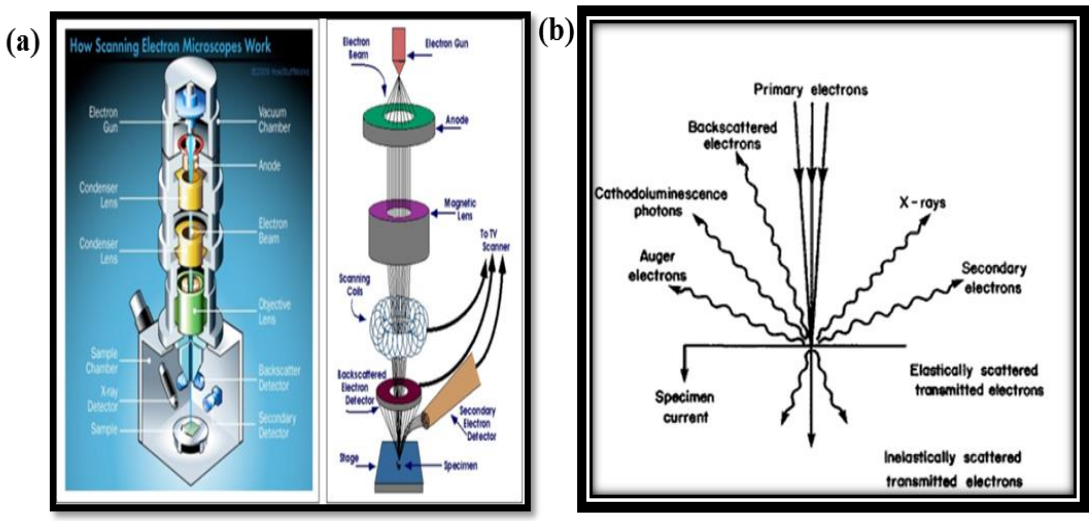

Figure 2.34 (a) A schematic diagram of electron microscope (Atteberry, 2014) and (b) Interaction of electrons with specimen. (Reimer, 1998)

The magnification, resolution and depth of focus of SEM, mainly depends upon the working distance (WD), which is the separation between the sample and the detector. Depth of focus is increased, whereas resolution is decreased by long WD, while examining a complex sample at low magnification. For high resolution a much smaller specimen is required so that working distance can be minimized between the sample and the detector. Large size samples are usually porous and can

pollute the vacuum of the tube on discharge of gas present inside the pores (Patrick Echlin, 2009).

In all microscopy the limit of resolution, which is the smallest separation between two points is found, using Rayleigh criterion Equation 2.26.

$\delta = 0.61\ \lambda/\mu\sin\beta$ Equation 2.26

Where λ = wave length associated with electrons.

μ = refractive index of the material.

β = semi-angle of collection from magnifying lenses.

δ = least observable distance.

The resolving power of microscope is a direct function of wave length associated with highly accelerated electrons (Reed, 2005).

Chapter 3

Experimental methods

The methods of processing of raw materials into ceramics is a key factor for determining the final properties. Processing techniques strongly effect the particle size, density, chemical homogeneity and porosity of the ceramics, which in turn effects dielectric, ferroelectric and piezoelectric properties of the materials.

The main stages of the conventional fabrication process are: sourcing the specified raw materials; preparation of the desired composition of precursor powders; calcination to promote solid state reaction; powder compaction to form the desired shape; sintering to induce densification; post-sintering machining, if appropriate.

The first part of this chapter is based upon the fabrication methods used for developing lead-free piezoelectric ceramics, for example milling, calcination and sintering.

The second part of this chapter explains the characterization techniques used for determination of the properties of the powder and ceramics. X-Ray diffraction, scanning electron microscopy (SEM), transmission electron microscopy (TEM) electrical testing (dielectric, ferroelectric, piezoelectric measurements).

3.1 Powder fabrication methods

3.1.1 Powders preparation

The starting powders, including details of the supplier and the chemical purity are shown in Table 3.1.

Before weighing, all the raw materials were dried in an oven at 200 ºC for 24 h to remove moisture owing to the hygroscopic nature of some precursors and then cooled to room temperature in desiccators to improve chemical stoichiometry while weighing.

Table 3.1 Chemical purity and supplier of raw powders.

Raw powders	Suppliers	Purity	CAS No.
$BaCO_3$	Alfa Aesar	≥ 99 %	513-77-9
$CaCO_3$	Sigma Aldrich	≥ 99 %	471-34-1
Na_2CO_3	Sigma Aldrich	≥ 99.5 %	497-19-8
Bi_2O_3	Aldrich	99.9 %	1304-76-3
Li_2CO_3	Alfa Aesar	99 %	554-13-2
TiO_2	Sigma Aldrich	99.9 %	1317-80-2
Nb_2O_5	Alfa Aesar	99.9 %	1313-96-8
MgO	Alfa Aesar	99.95 %	1309-48-4
Isopropanal	Sigma Aldrich	99.5 %	67-64-1

All powders were then weighed according to the stoichiometric ratios for each batch, using a Sartorius electronic balance within the precision limit of ± 0.001g.

3.1.2 Sample preparation methods

A conventional ball milling technique was used throughout this research work for mixing and removing agglomerates and reduction of particle size.

3.1.2.1 Conventional ball milling

Conventional/Traditional ball milling is a process which is mainly used for the reduction of particle size, mixing of components and to break agglomerates (depending on agglomerate strength). Milling therefore should lead to improved reaction during calcination and sintering (Jaffe, 1971).

Different materials may be used as grinding media, including ceramic or steel balls, or pebbles. The media must be more harder than the materials to be ground to minimize contamination from wear debris. The particle size achieved by milling is a direct function of the dimensions of the grinding media.

For ultimate comminution a series of milling steps using progressively finer grinding media can be employed. An internal cascading effect reduces the reagent material to a fine powder. During rotation of the bottle the grinding media collide with one another (fall upon one another) and with the walls of the bottle resulting in the crushing of coarse powders between them. This in turn will reduce particle size, agglomerations of the powders and produce a relatively homogeneous mixture. This is one of the most common technique used in industries for preparation of large powder batches.

The volume of the grinding material should be of the order of one third of the milling media for efficient action (Moulson and Herbert, 2003).

The reagent powders, Y-stabilized ZrO_2 grinding media and isopropanol were placed in a cylindrical container on rotating rods, rotating about a horizontal axis. The cylindrical plastic bottle (~ 400 cm^3) was partially filled (one third of volume of bottle) with Y-stabilized ZrO_2 grinding media (l = 0.719 cm, d = 0.706 cm, V = 0.281 cm^3); isopropanal (IPA), was placed on rotating rods of the machine, Figure 3.1. The volume ratio of media to powder was 2:1. Batches of 50 g of

powders along with grinding media were added to the bottle and immersed in IPA to fill 1/2 of the bottle and then milled for 20 - 24 h.

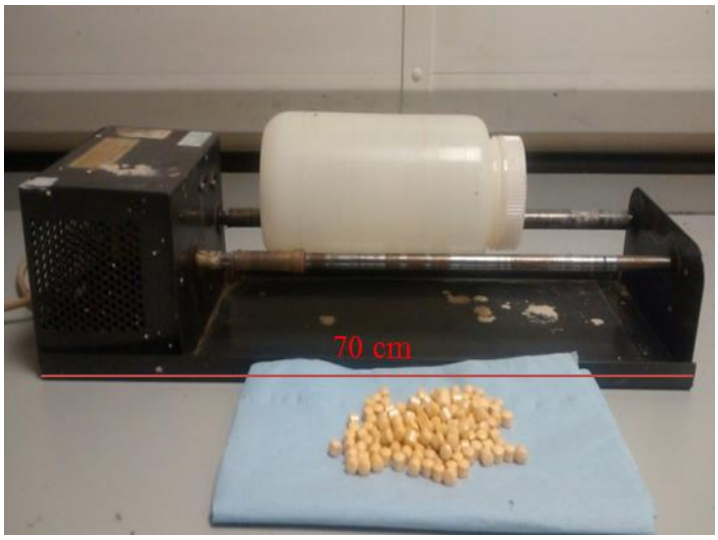

Figure 3.1 A photograph of ball milling machine and the grinding media.

3.1.2.2 Drying of Milled powder

After milling process the mixture was poured into Pyrex glass (Fisher Brand), Figure 3.2. The solvent was removed by distillation (b.pt IPA ~ 80 ºC) in about 5 – 6 h. The powder was sieved using 300 µm mesh.

Figure 3.2 A photograph of solvent distillation reflux kit.

3.1.3 Calcination

In our experimental work, the milled powders were placed inside a high purity alumina crucible (Fisher Scientific limited CWC-500-090E, Purity 99.8%), covered with an alumina lid (to minimize the volatility of precursor) and then heated (calcined) in a box furnace. The powders of the solid solutions discussed in the following chapters 4, 5, 6, 7 and 8 were calcined at 850 ºC for 4 h at a heating and cooling rate of 300 ºC /h.

3.1.4 Shaping of powder into ceramics

The calcined powder were sieved, remilled overnight with incorporation of 1 – 2wt.% binder (Ciba Glascol HA4), dried and sieved again. The binder helps in adhesion of particles and gives strength for resisting stresses on removal from the steel die and during handling. In the first step a uniaxial press was used to shape the powder into pellets Figure 3.3 (a), followed by cold isostatic pressing (selected samples), in which a uniform pressure is exerted by hydraulic fluid from all directions. Pellets were enclosed in Fisher Brand medium FB69293 polymers, Figure 3.3 (b).

In this work, powders (0.5 – 0.9 g) were compacted into green pellets (10 – 15 mm diameter) using pressure 75 – 100 MPa and then cold isostatic pressed (Stansted fluid powder isopress), Figure 3.3 (b) for uniform compaction and higher green density of ceramics at 200 MPa (5 – 15 min).

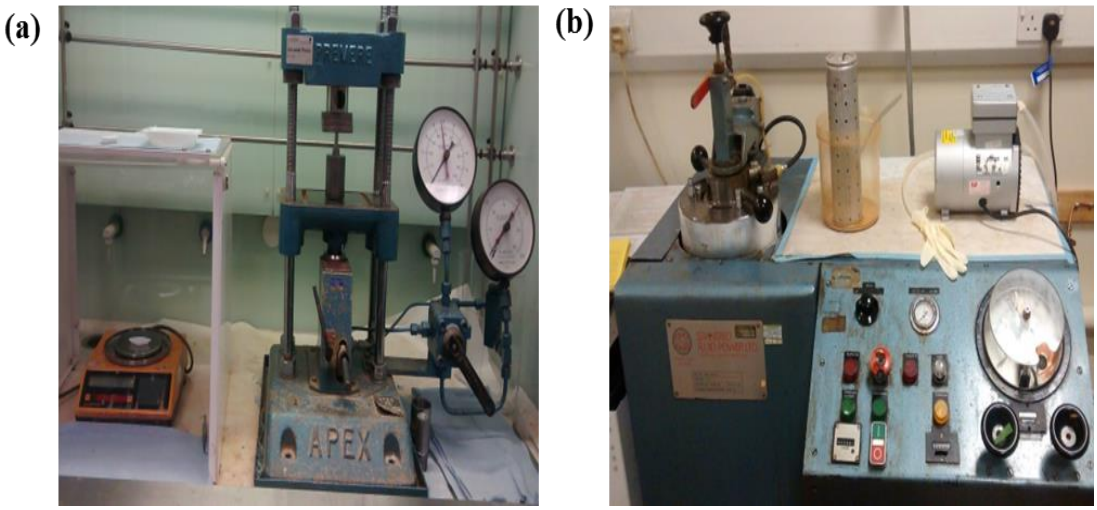

Figure 3.3 Photographs of (a) Uniaxial press and electronic balance and (b) Cold isostatic press, Vacuum pump and ceramics in evacuated white gloves.

3.1.5 Sintering

In this study green ceramics (non-sintered pellets) were placed in alumina crucibles with a powdered bed of the calcined powder of same composition (without binder) and covered with more powder from the top to bury the whole ceramics. The crucibles were covered with lids and placed in a heating furnace. The powder bed and the covered crucible prevents the volatilization of elements from the ceramics and also prevents reaction of elements from outside the ceramics.

The ceramics were heated slowly (50 ºC/h) to 550 ºC (1 h dwell) in the early stage to remove the binder and minimize the pores development in the ceramics. In the second stage of sintering the ceramics were heat treated (from 550 ºC) at 300 ºC/h until the desired temperature and dwelled to the required time. The ceramics were then cooled to room temperature at cooling rate of 300 ºC/h. Different sintering temperatures were tried for some compositions. A typical sintering profile of relatively fine shape ceramics is shown in Figure 3.4. The difference between the dimensions and weights of sintered and green ceramics in future will be beneficial, especially for weight loss.

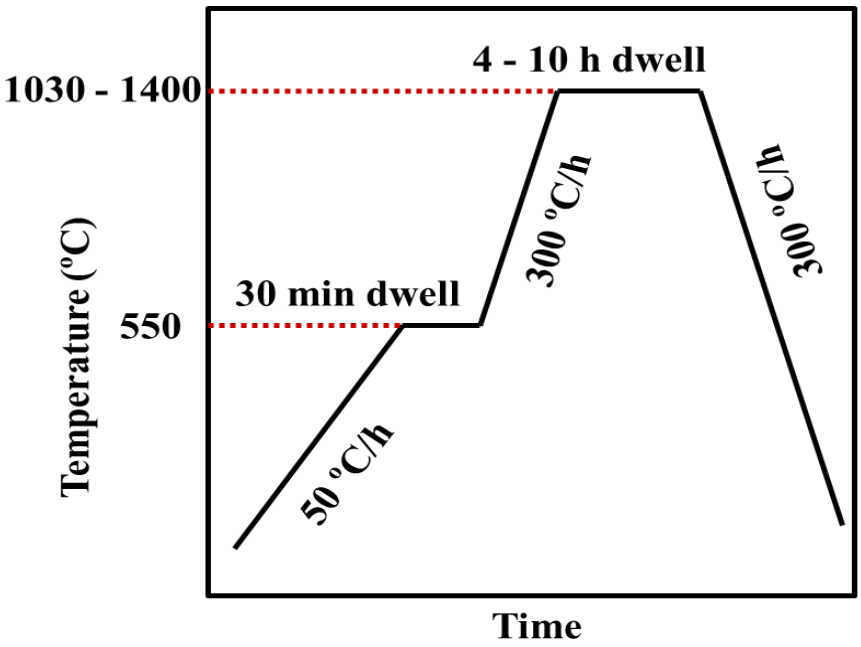

Figure 3.4 Heating profile for sintering ceramics reported in Chapters, 4 - 8.

The sintering temperature ranges and dwell times of the ceramics explored in this study are displayed in Table 3.2.

Table 3. 2 Sintering temperature and dwell times for ceramics discussed in chapter 4, 5, 6, 7, and 8.

$(1–x)Na_{0.5}Bi_{0.5}TiO_3 – xBa_{0.8}Ca_{0.2}TiO_3$ and 3wt.%Bi_2O_3-modified	
Samples	**Sintering temperatures/dwell times**
x = 0 – 0.2	1160 ºC/6 h
x = 0.2 – 0.5	1170 ºC/6 h
x = 0.5 – 0.7	1190 ºC/6 h
x = 1 (standard)	1400 ºC /6 h
$(1–x)[0.85Na_{0.5}Bi_{0.5}TiO_3 – 0.15Ba_{0.8}Ca_{0.2}TiO_3] – xBiMg_{0.5}Ti_{0.5}O_3$ and 3 wt. % Bi-modified	
x = 0.05 – 0.1	1160 ºC /4 h
x = 0.1 – 0.5	1100 ºC /4 h
x = 0.6 – 0.7	1050 ºC /4 h
$(1–x)[0.85Na_{0.5}Bi_{0.5}TiO_3 – 0.15Ba_{0.8}Ca_{0.2}TiO_3] – xLiNbO_3$	
x = 0.005 – 0.15	1070 ºC /10 h
$(1–x)[0.85Na_{0.5}Bi_{0.5}TiO_3 – 0.15Ba_{0.8}Ca_{0.2}TiO_3] – xNaNbO_3$	
x = 0.02 – 0.8	1170 ºC /10 h
$(1–x)Ba_{0.6}Sr_{0.4}Zr_{0.2}Ti_{0.8}O_3 – xBiMg_{0.5}Ti_{0.5}O_3$	
x = 0	1400 ºC /6 h
x = 0.1 – 0.8	1150 -1170 ºC /10 h

3.1.6 Finishing and grinding of ceramics

After sintering process the ceramics were ground using MD Piano 600 and 1200 (stainless steel strips)/Silicon carbide papers (Buehler carbimet Grit 600 – 1200) and using Motopal 2000 to remove any possibly reacted elements from outer surfaces of the ceramics, Figure 3.5.

The pellets were washed with acetone and dried in a furnace at 200 ºC for ~ 1 h to eliminate the possibility of any moisture absorbed during grinding. Geometric densities were calculated from masses and dimensions of the pellet. Theoretical densities were calculated from refined X-rays peak positions using a software FPsuit and a unit cell parameters. The formula, $\rho = 1.66\Sigma A/V$ (A = atomic mass number and V = volume of unit cell) was used for calculation of theoretical densities of the studied compositions. Relative density was calculated from the ratio of geometrical density to theoretical density.

Figure 3.5 A photograph of grinding/polishing machine Motopal 2000.

Ceramics processing steps are summarized in the flow chart, Figure 3.6

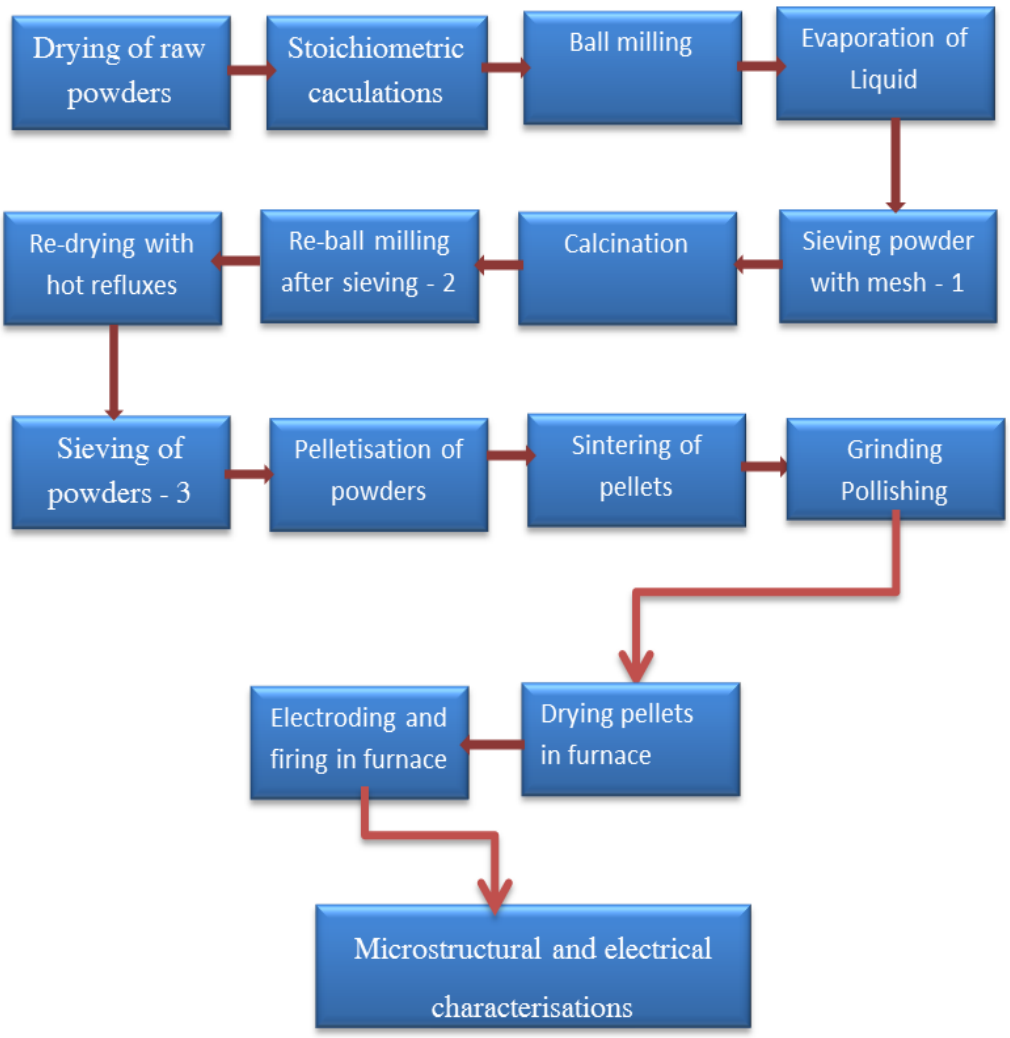

Figure 3.6 Flow chart of ceramic processing steps leading to characterizations.

3.2 Characterization techniques

3.2.1 X-ray powder diffraction examinations

In this research XRD was mainly used to identify the possible crystal structure of ceramics using Bruker D8. Powders of crushed ceramics were scanned using Cu K_α radiation ($\lambda \sim 1.5406$ Å), with room temperature scan parameters of: 0.05 $^\circ 2\theta$ step size; 0.033 $^\circ 2\theta\ s^{-1}$ rate and range of angles from 20 – 70 $^\circ 2\theta$.

XRD data was collected and analyzed using instrumental software: ' PANalytical X' Pert High score plus. This software allowed the analysis of peak positions and Hanawalt searches, with reference patterns ICDD (international centre for diffraction data) database. The unit cell parameters were measured using a software ' FP Suite ' with R_{wp} (weighted R profile) < 5 %. In this study the majority of the compositions were mainly pseudocubic (Pm3m), tetragonal (P4mm), rhombohedral (R3c), orthorhombic (Amm2) or some mixed phases.

3.2.2 Scanning electron microscopy (SEM)

In this study, SEM was used to see grain morphology and grain size from fractured /polished surfaces of the specimen using LEO 1530 Gemini FEGSEM (Field Emission Gun Scanning Electron Microscope) and Hitachi SU 8230 cold FESEM (Field Emission Scanning Electron Microscope) with secondary electron mode with voltage settings 2 kV – 3 kV and a working distance of 3 – 7 mm. samples were coated to 5 nm with Pt/Pd using AGAR High Resolution Sputter Coater, to minimize the charging effect of samples.

3.2.3 Transmission electron microscopy (TEM)

In Transmission Electron Microscopy (TEM) the focused beam of electrons transmits through a very thin specimen (< 500 nm), unlike SEM in which electrons

are reflected from the specimen surface. Magnification down to atomic scale can be achieved using either imaging or diffraction modes. Images are developed from diffracted electrons (dark field) and undiffracted electrons (bright field electrons) due to elemental or microstructural differences [Chescoe, (1990)].

In this work, selected ceramics pellets were ground to ~ 60 μm by using different grits and dimpled at the centre, using Dimple Grinder (Gatan, USA), followed by Precision Ion Beam polishing System (PIPS, Gatan, USA).

A Philips CM200 Field Emission Gun Transmission electron microscope (FEGTEM) with super twin objective lenses and cryoshielding was used to study domain structure and chemical segregations. Dr Mike Ward, a research officer at LEMAS, University of Leeds conducted all operations of TEM facilities.

3.2.4 Electrical measurements

Ground/polished ceramics, after drying in oven, were silver painted to ~ 0.05 layers (Agar Scientific). The electroded ceramics were then fired to 550 ºC for 10 minutes and cooled to room temperature. The edges of the pellets were cleaned from the silver paint after firing using carbide papers, to avoid short circuiting of the ceramics during electrical testing. In this work circular ceramics with fine flat surfaces of thickness 1 – 1.5 mm and diameter 8 – 10 mm were used for electrical testing.

3.2.4.1 Dielectric analysis

Relative permittivity and tanδ, of ceramic samples were measured using an Agilent HP4192A LF impedance analyzer, Figure 3.7, with varying frequencies, and calculated using Equation 3.11,

$$\varepsilon_r = C.t/A\varepsilon_0 \qquad \text{Equation 3.11}$$

Where ε_r is the relative permittivity, *C* is the capacitance, A is area of cross-section, t is thickness of ceramics and ε_0 (~ 8.854×10^{-12} F/m) is the permittivity of free space.

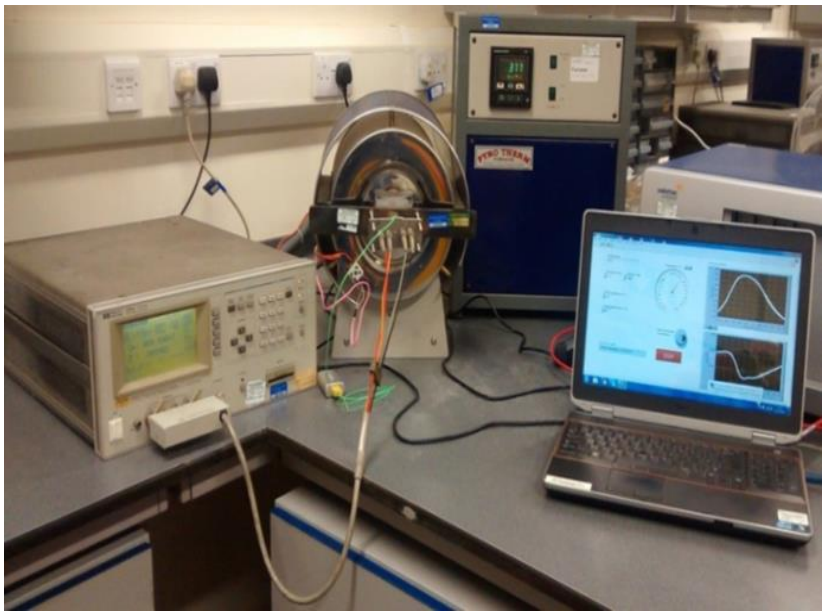

Figure 3.7 A photograph of the equipment used for dielectric measurements.

In this research work high temperature measurements were made using Pyrotherm tube furnace from room temperature to 450 ºC at 3 ºC/min using Eurotherm 847 programmable controller, whereas low temperature measurements were made from -70 ºC to room temperature by using environmental chamber (TJR; Tenney Environmental-SPX, white deer, PA) and an impedance analyzer 4194A (Hewlett Packard). The ε_r –T plots on cooling is presented in Chapters, 4 – 8. The normalized relative permittivity was found by using formula $\Delta\varepsilon/\varepsilon_{mid} = (\varepsilon_{max} - \varepsilon_{mid})/\varepsilon_{mid} = (\varepsilon_{min} - \varepsilon_{mid})/\varepsilon_{mid}$, where ε_{max} and ε_{min} are the ± deviation from the mid value [$\varepsilon_{mid} = (\varepsilon_{max} + \varepsilon_{min})/2$].

3.2.4.2 Resistivity measurements

The resistance of a unit area per unit length ($\rho = RA/L$), called resistivity was measured in the temperature range 250 ºC – 550 ºC, at a fixed voltage, 80 V, using a Keithley 617 programmable electrometer (Cleveland, OH).

3.2.5 Piezoelectric measurements

Polarization-electric field and bipolar strain-electric field were measured at voltage ≥ 40 kV, by using LC precision analyzer (Radiant technology Inc., Albuquerque). These operations were performed by Aurang Zeb, a PhD student in the same research group, the University of Leeds.

3.2.5.1 Poling

Electrodes (silver paint) were applied to ceramic samples, 1 mm thick and 8 mm diameter. The edges of the samples were abraded with 1200 grit SiC paper to reduce the risk of dielectric break down. The samples were immersed in a silicone oil bath to minimize conduction and regulate heat dissipation. To regulate temperature control, the silicone oil bath was placed on a hot plate with magnetic-stirrer facility. Care was taken to avoid any possible thermal shock to the materials.

An electric field was applied (3 kV – 8 kV) to the ceramic samples (for 10 – 15 minutes), care was taken to ensure that the current was not so high as to cause excessive thermal heating of the material near the contacts. The samples were removed carefully after delay of 5 – 10 minutes between the time the potential difference across the sample read zero and shorting the sample before removal from the apparatus.

After DC poling, the piezoelectric charge co-efficient d_{33} was analyzed using Piezotest Piezometer PM300, which provide oscillating force and induces charge per unit applied force (d_{33}), for few selected samples (chapter 6).

In our work samples were poled at 80 ºC and subjected to an applied electric field ~ 30 – 60 kV/cm at a ramp rate of 50 V/s. All the operations with poling were made by Aurang Zeb, a PhD student in the same research group, the University of Leeds.

Chapter 4

Examination of $(1–x)Na_{0.5}Bi_{0.5}TiO_3 – xBa_{0.8}Ca_{0.2}TiO_3$ ceramics

4.1 Introduction

This chapter examines the dielectric, ferroelectric, piezoelectric, and microstructural properties of standard as well as 3wt.% Bi_2O_3 modified ceramics: $(1–x)Na_{0.5}Bi_{0.5}TiO_3 – xBa_{0.8}Ca_{0.2}TiO_3$, abbreviated as [(1–x)NBT – xBCT] ($0 \leq x \leq 1.0$).

In the first part of this chapter a series of solid solutions $(1–x)Na_{0.5}Bi_{0.5}TiO_3 – xBa_{0.8}Ca_{0.2}TiO_3$ [(1–x)NBT – xBCT] ($0 \leq x \leq 1.0$) were synthesised by a mixed oxide route. Ceramics in the system $(1–x)Na_{0.5}Bi_{0.5}TiO_3 – xBa_{0.8}Ca_{0.2}TiO_3$ demonstrate a phase boundary between cubic and tetragonal at $0.1 < x < 0.2$. All the ceramics with $x \geq 0.2$ have shown tetragonal symmetry.

There was a gradual convergence in the temperatures of a frequency-dependent inflection and peak in relative permittivity-temperature plots with increasing x, for $x = 0.3 – 0.5$, such that for $0.5 \leq x \leq 0.7$ normal relaxor-like behaviour was observed with no reflection in $\varepsilon_r – T$ plots. Compositions $x = 0.8$ and 0.9 showed broad $\varepsilon_r –T$ peaks with no frequency dispersion (i.e non relaxor), whilst $x = 1$ ($Ba_{0.8}Ca_{0.2}TiO_3$) gave a sharper peak more typical of a ferroelectric.

Constriction in the polarisation-electric field hysteresis loops for the phase boundary composition $x = 0.1$ may suggest an electric field-induced phase transition, as reported for other $Na_{0.5}Bi_{0.5}TiO_3$ based piezoelectrics. The bipolar

electromechanical strain was ~ 0.25 % at 40 kV/cm and high-field effective value of piezoelectric charge coefficient (d_{33}* = strain/applied electric field), d_{33}* ~ 640 pm/V for x = 0.1.

The grain size was in the range of ~ 2 – 5 μm. TEM micrographs revealed contrast patterning consistent with a ferroelectric domain structure in x = 0.1 and 0.2 (the only samples examined) with no clear evidence of core-shell segregation. The dc resistivities were in the range of ~ 10^7 – 10^3 Ω m in the temperature range 250 – 500 ºC.

4.1.1 Results

The calculated wt.% contribution of precursors for different batches in the ceramic series $(1–x)Na_{0.5}Bi_{0.5}TiO_3 – xBa_{0.8}Ca_{0.2}TiO_3$ are shown in Table 4.1.

Table 4. 1 The calculated wt.% contribution of precursors in ceramic system $(1–x)Na_{0.5}Bi_{0.5}TiO_3 – xBa_{0.8}Ca_{0.2}TiO_3$, $(0 \leq x \leq 1)$.

Sample	wt.% $BaCO_3$	wt.% $CaCO_3$	wt.% Na_2CO_3	wt.% Bi_2O_3	wt.% TiO_3
x = 0	0	0	11.89	52.27	35.83
x = 0.05	3.51	0.45	11.21	49.27	35.56
x = 0.08	5.60	0.71	10.80	47.50	35.39
x = 0.10	7.00	0.89	10.54	46.32	35.29
x = 0.12	8.34	1.06	10.33	45.15	35.18
x = 0.15	10.38	1.32	9.87	43.41	35.02
x = 0.20	13.72	1.74	9.22	40.55	34.75
x = 0.30	20.30	2.60	7.95	34.95	34.23
x = 0.40	26.66	3.39	6.71	29.51	33.72
x = 0.50	32.85	4.17	5.51	24.24	33.24
x = 0.60	38.85	4.93	4.35	19.11	32.76
x = 0.70	44.70	5.67	3.22	14.13	32.30
x = 0.80	50.38	6.39	2.09	9.29	31.85
x = 0.90	55.88	7.09	1.04	4.58	31.41
x = 1.0	61.25	7.77	30.98	0	0

4.1.2 XRD analysis of $(1–x)Na_{0.5}Bi_{0.5}TiO_3 – xBa_{0.8}Ca_{0.2}TiO_3$

X-ray diffraction patterns of annealed powder of ceramics system $(1–x)Na_{0.5}Bi_{0.5}TiO_3 – xBa_{0.8}Ca_{0.2}TiO_3$ system $(0 \leq x \leq 1)$ are shown in Figure 4.1.

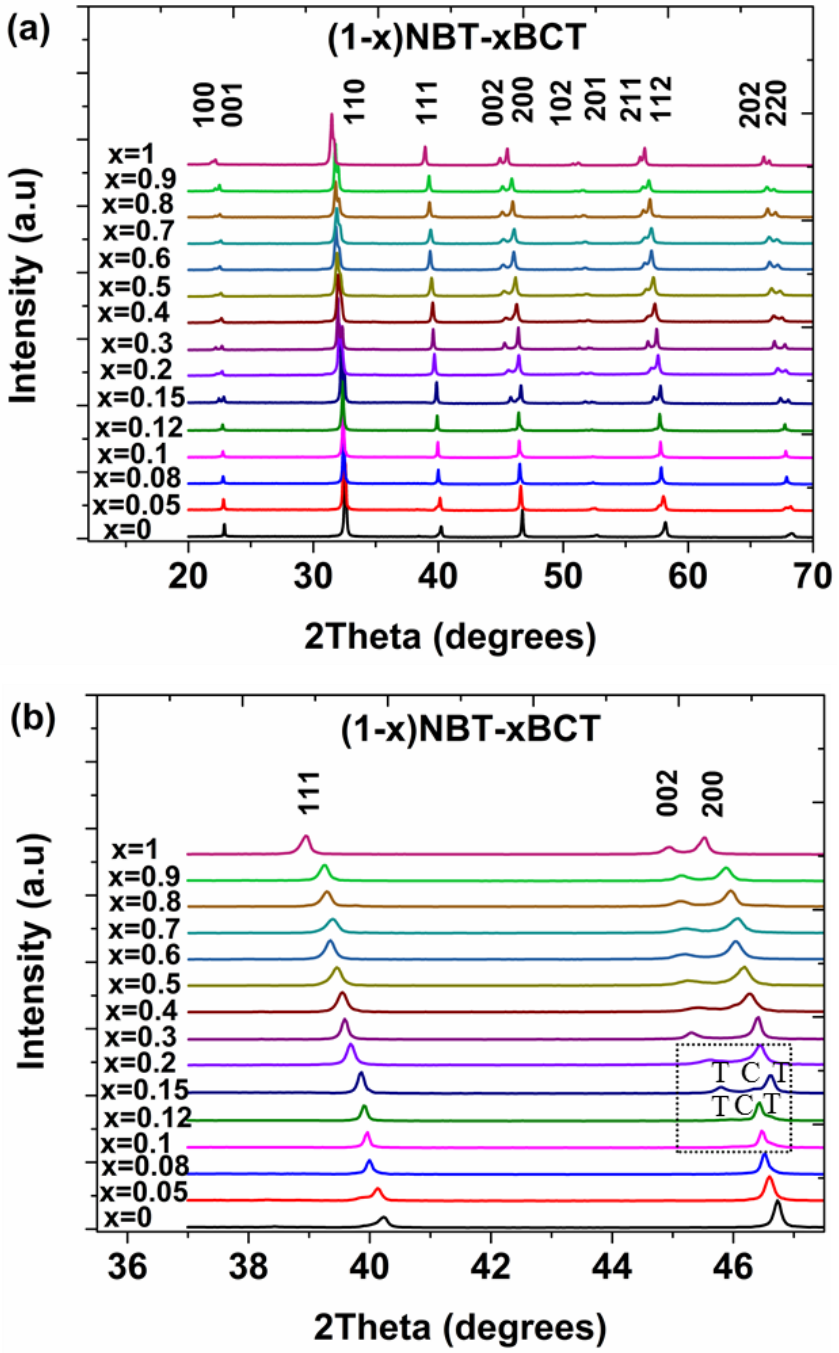

Figure 4.1 (a) XRD patterns of the ceramic system $(1–x)Na_{0.5}Bi_{0.5}TiO_3 – xBa_{0.8}Ca_{0.2}TiO_3$, $(0 \leq x \leq 1)$.and (b) A broad view of 111, 002/200 peaks, the shaded region shows a mixed phase region (T = Tetragonal and C = Cubic).

The ceramic compositions, x = 0 – 1.0 showed a pure single-perovskite phase with no evidence of secondary phases, Figure 4.1a, indicating a complete diffusion of BCT into NBT. From XRD patterns NBT (x = 0) appeared cubic, but with slight broadening and asymmetry to the 111_c peak consistent with poorly resolved peak splitting of a lower symmetry structure: rhombohedral and monoclinic systems have been reported for NBT (Aksel et al., 2011). Hereafter the NBT pattern is referred to as cubic or pseudocubic (pc).

The XRD patterns of the $0.05 \leq x < 0.12$ sample was similar to NBT, but with a sharpening of the 111pc peak and an increase in a_{pc} lattice parameters, Figure 4.2. Close inspection suggested very faint extra tetragonal peaks at x = 0.1. The mixed phase tetragonal + cubic/(pc) XRD pattern was more obvious in composition x = 0.15. For compositions $x \geq 0.2$, only tetragonal peaks were evident. Thus a mixed phase region of cubic and tetragonal phases is limited to a narrow range of compositions, $0.1 < x < 0.2$.

Within the tetragonal phase field, the lattice parameters *a* and *c* increased linearly with increasing x. The *c/a* ratio was ~ 1.008 – 1.012 and showed little variation with composition, Figure 4.2. High temperature phase analysis in this region of the (1–x)NBT – xBCT system would be required before labelling the region as a true MPB. The morphotrophic phase boundary in the (1–x)NBT – xBT system occurs at a slightly more NBT- rich composition $0.06 \leq x \leq 0.1$ (Cheng et al., 2013) than for the present Ca-modified system. Tetragonal symmetry was observed for all compositions with $x > 0.15$ for the (1–x)NBT – xBCT system.

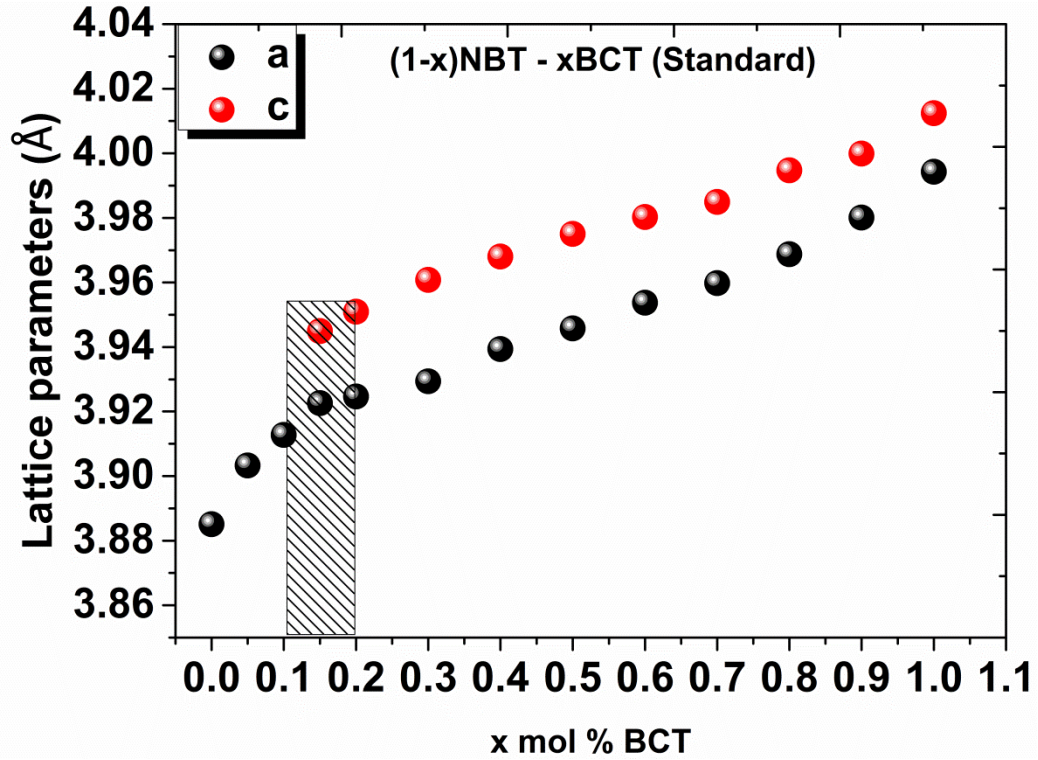

Figure 4.2 Variation in lattice parameters of ceramic system (1–x)$Na_{0.5}Bi_{0.5}TiO_3$ – x$Ba_{0.8}Ca_{0.2}TiO_3$, ($0 \leq x \leq 1$), the shaded region shows a mixed phase region.

4.1.3 Dielectric Measurements

Cooling plots of relative permittivity (ε_r) and tan delta (tanδ) versus temperature for (1–x)NBT – xBCT, ($0 \leq x \leq 1$) at 1 kHz – 1 MHz from room temperature to 450 ºC are shown in Figure 4.3 – 4.5.

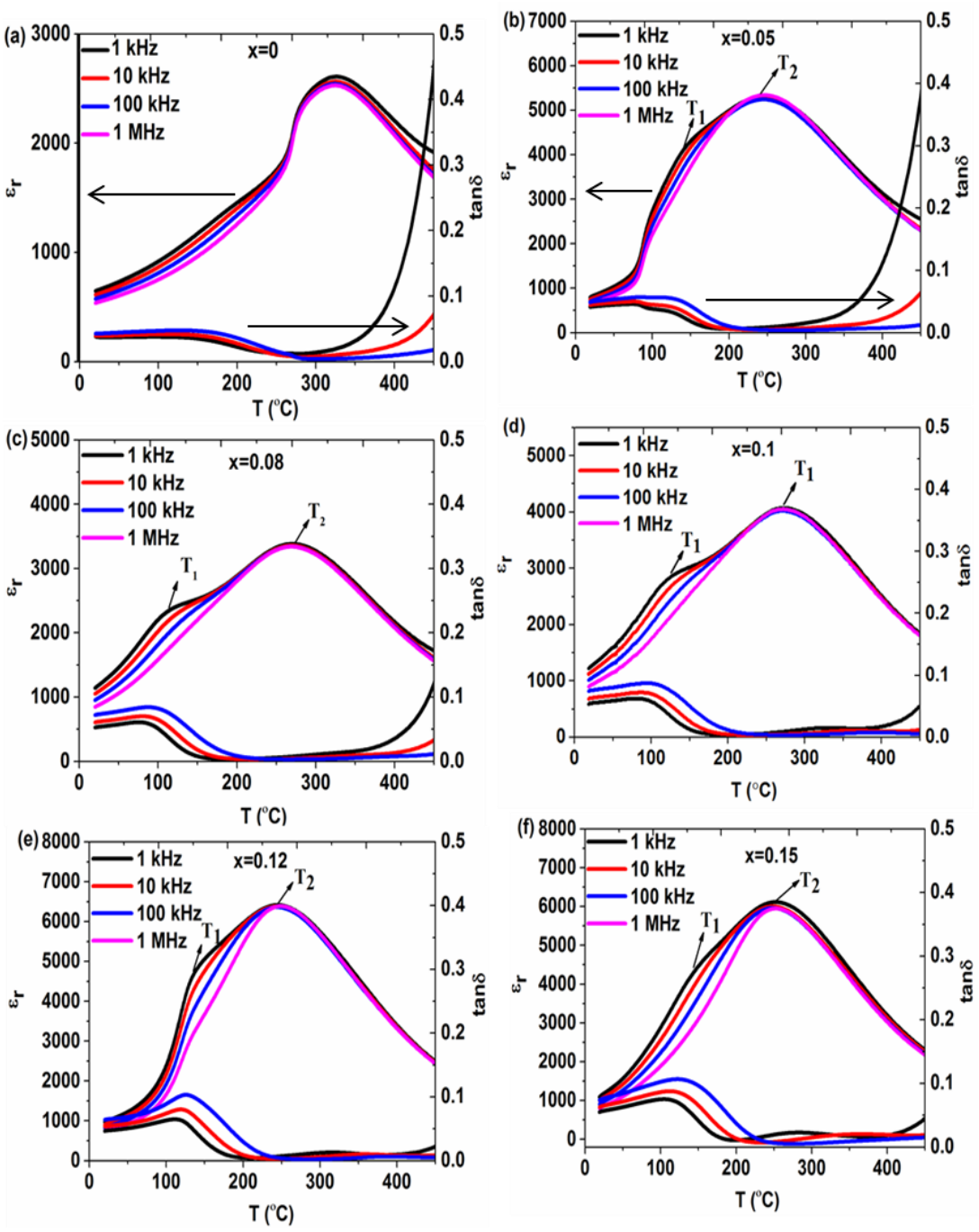

Figure 4.3 Temperature-dependent relative permittivity (ε_r) and loss tangent (tanδ) of $(1–x)Na_{0.5}Bi_{0.5}TiO_3 – xBa_{0.8}Ca_{0.2}TiO_3$, (a) x = 0, (b) x = 0.05, (c) x = 0.08, (d) x = 0.1, (e) x = 0.12 and (f) x = 0.15. (data set continued in Figure 4.4)

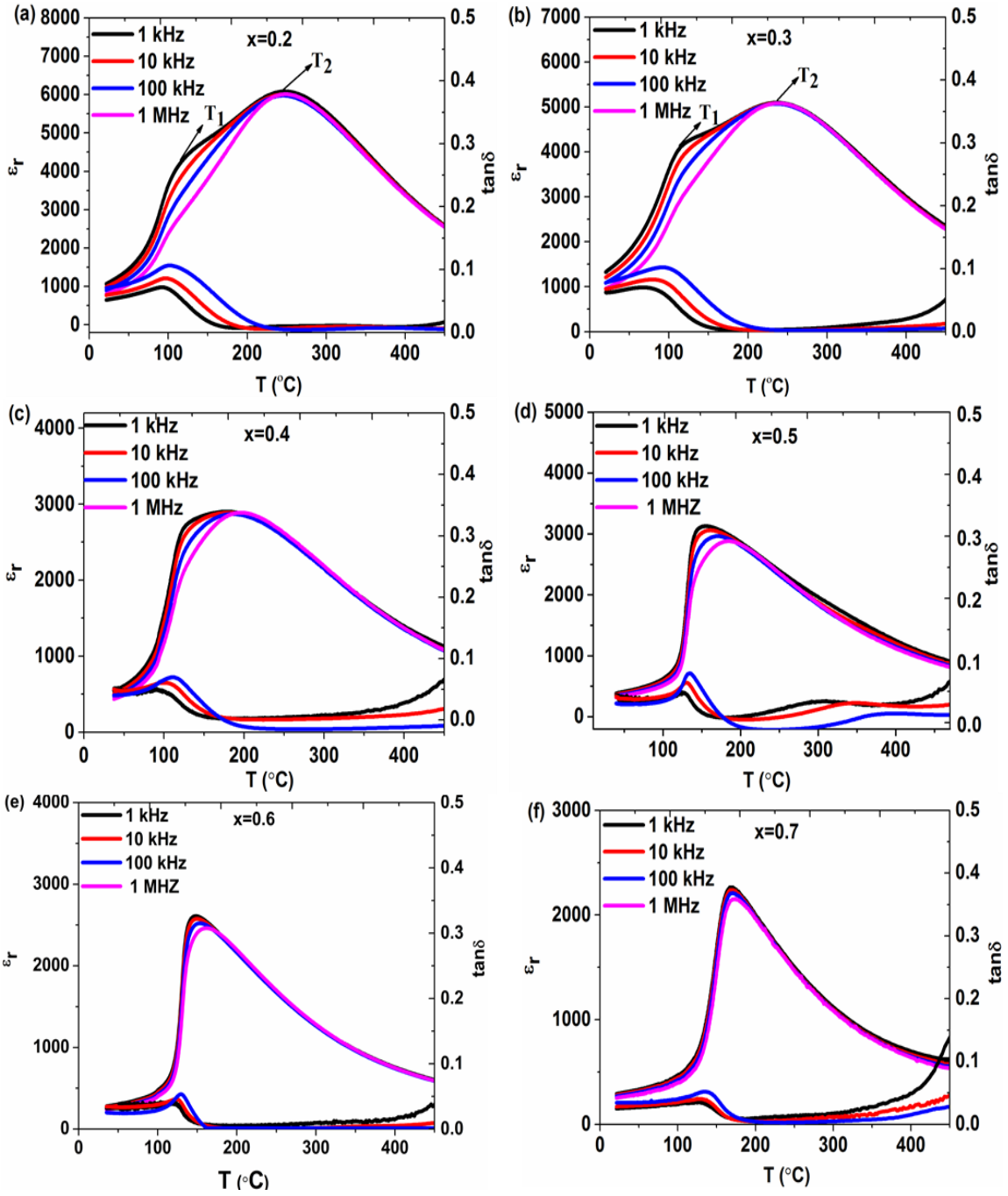

Figure 4.4 Temperature-dependent relative permittivity (ε_r) and loss tangent (tanδ) of $(1–x)Na_{0.5}Bi_{0.5}TiO_3 – xBa_{0.8}Ca_{0.2}TiO_3$, (a) x = 0.2, (b) x = 0.3, (c) x = 0.4, (d) x = 0.5, (e) x = 0.6 and (f) x = 0.7. (data set continued in Figure 4.5)

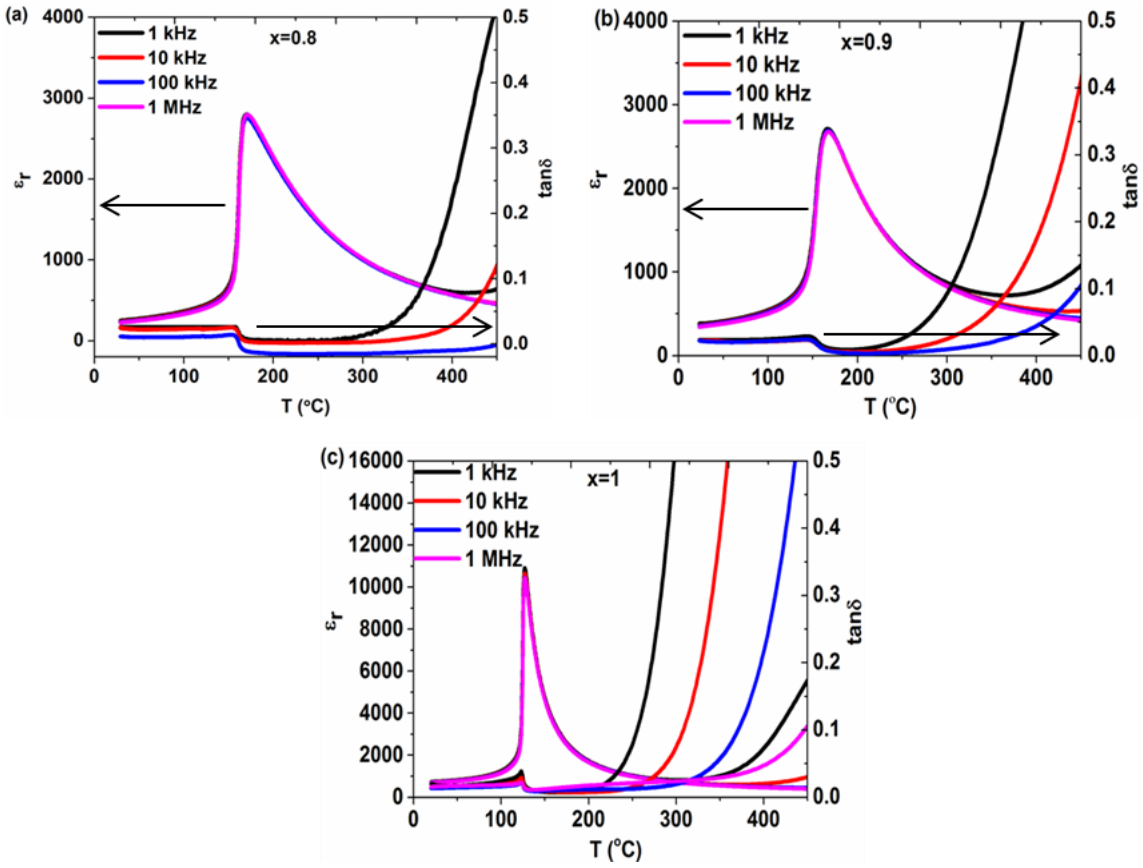

Figure 4.5 Temperature-dependent relative permittivity (ε_r) and loss tangent (tanδ) of (1–x)$Na_{0.5}Bi_{0.5}TiO_3$ – x$Ba_{0.8}Ca_{0.2}TiO_3$, (a) x = 0.8, (b) x = 0.9 and (c) x = 1

For the NBT end member (x = 0) an inflection in ε_r occurred at ~ 240 °C (temperature of onset of inflection on heating, 1 kHz) with a frequency dispersion below that temperature and a broad dielectric peak occurred at ~ 330 °C, in close agreement with previous reports (Yang et al., 2011). There is debate as to the origin of the lower temperature anomaly in the parent NBT – BT and NBT – KBT systems, with TEM suggesting a biphasic structure (Dorcet et al., 2008, Zeb and Milne, 2014b). It is noted the inflection is most pronounced at the lower frequencies, which may be symptomatic of sluggish coupling dynamics between localised dipoles.

The incorporation of BCT at the level $0.05 \geq x \geq 0.6$ led to a more pronounced frequency-dependent inflection than for NBT, and a decrease of the

inflection temperature onset (heating) to ~ 100 °C, there was also a decrease in the main peak temperature, to ~ 160 °C. A progressive convergence in temperatures of the main peak (T_2) and inflection (T_1) in ε_r –T plots occurred between x > 0.05 to x = 0.4, mainly due to a decrease in the temperature T_2 of the main peak, Figure 4.3–4.4, such that a normal relaxor response with broad frequency dependent ε_r peak was observed for samples x = 0.5 and 0.6, Figure 4.4. The associated frequency-dispersion in tanδ (at $T \sim T_m$) was also characteristic of a relaxor behaviour (Lee et al., 2001).

A change in ε_r –T plots from frequency dependent relaxor to diffuse, non-frequency dependent peaks occurred at x > 0.7 with a gradual sharpening of the ε_r peak and a lowering in peak temperature consistent with normal ferroelectric character as x increased to 1.0. It is presumed that the present (1– x)NBT – xBCT ceramics have a complex A-site cations structure, with distribution of Bi^{3+}, Ba^{2+}, Ca^{2+}, Na^{1+} which leads to disruption of long range ferroelectric domains; instead a relaxor-like structure of polar nano domains is anticipated, but a detailed TEM study lay outside the scope of this thesis. Trends in dielectric parameters are summarised in Table 4.2. Similar type trends in T_1 and T_2 were observed in NBT modified BT ceramics system (Tadashi Takenaka, 1991).

Table 4.2 Summary of dielectric properties of (1–x)$Na_{0.5}Bi_{0.5}TiO_3$ – x$Ba_{0.8}Ca_{0.2}TiO_3$.

x	ε_r (25 ºC)	ε_{max}	T_1 (ºC) 1kHz	T_2 (ºC) 1kHz	tanδ ≤ 0.02 (T-range) 1kHz
0	670	2620	240	330	210–330 ºC
0.05	850	5320	130	250	150–320 ºC
0.08	1190	3390	110	280	130–370 ºC
0.1	1300	4070	140	270	140–410 ºC
0.12	1000	6420	130	250	160–440 ºC
0.15	1190	6120	130	250	170–410 ºC
0.2	700	6080	110	250	150–450 ºC
0.3	1400	5100	100	240	190–400 ºC
0.4	520	2920	---	170	180–370 ºC
0.5	350	3090	---	160	150–250 ºC
0.6	310	2610	---	150	130–420 ºC
0.7	300	2270	---	170	150–320 ºC
0.8	250	2800	---	170	160–320 ºC
0.9	400	2760	---	170	160–240 ºC
1	730	10900	---	130	30–220 ºC

4.1.3.1 Modified Curie Weiss law

In this study the typical relaxor behaviour of (1–x)NBT – xBCT is characterised by diffuse ferroelectric phase transition and strong frequency dispersion with two dielectric anomalies (x ≤ 0.3). The relative permittivity of typical ferroelectrics above the paraelectric transition temperature obey the Curie

Weiss law ($1/\varepsilon = (T - T_0)/C$, where T_0 is the Curie Weiss temperature and C is the Curie Weiss constant. A modified expression has been suggested for relaxors: $(1/\varepsilon - 1/\varepsilon_m) = (T - T_m)^{\gamma}/C$, $(1 \leq \gamma \leq 2)$, where C and γ are material constants (Guo et al., 2004, Uchino, 1994). For classical ferroelectrics $\gamma = 1$; for typical relaxors $\gamma = 2$ (Guo et al., 2004, Uchino, 1994).

Dielectric data for the (1–x)NBT – xBCT samples are considered in terms of the modified Curie Weiss law in Figure 4.6. The value of γ reached a maximum of ~ 2 for x = 0.1. The substitution of $Ba^{2+}$and Ca^{2+} for Na^{1+} and Bi^{3+} in the A-site of the perovskite structure may cause cation ordering due to the large difference in ionic radii.

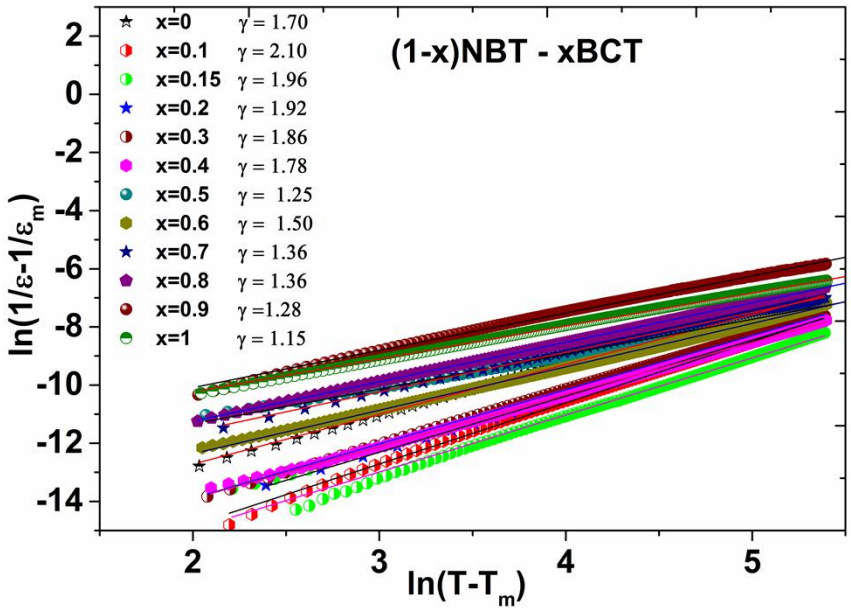

Figure 4.6 $\ln(1/\varepsilon - 1/\varepsilon_m)$ as a function of $\ln(T - T_m)$ of ceramic series (1–x)$Na_{0.5}Bi_{0.5}TiO_3$ – x$Ba_{0.8}Ca_{0.2}TiO_3$, x = 0 – 1.0.

4.1.4 Ferroelectric and piezoelectric properties

Polarisation-electric field loops are shown in Figure 4.7. The NBT end member x = 0 showed no evidence of ferroelectric domain switching at the fields tested < 40 kV/cm. The BCT end-member (x = 1) gave a well-saturated ferroelectric hysteresis loop. Intermediate solid solution compositions except x = 0.1 gave broad

ellipsoid P-E loops typical of lossy dielectrics. A non-conventional P-E loop similar to a distinctive pinched P-E loop was observed for sample x = 0.1, with a coercive field ~ $+E_c$ = 14 kV/cm. This composition lies very close to the pseudocubic-tetragonal phase boundary, Figure 4.1.

One other Ca-modified NBT – BT composition is reported in the literature, containing a higher Ca content 30 at%, but these samples showed no such constriction in P-E loops (Yang et al., 2011). However similar P-E behaviour is reported in the parent (1–y)NBT – yBT system for compositions close to its morphotrophic phase boundary. Guo et al. observed pinching in room-temperature P-E loops for a y = 0.07 composition in poled samples, and ascribed this behaviour to a coexistence of ferroelectric and anti-ferroelectric phases (Guo et al., 2011).

Tan et al. subsequently showed by electric field in situ TEM that phase stability around the MPB in NBT – BT was dependent on applied electric field (Ma et al., 2012).

In the NBT – KBT system electric field in situ synchrotron X-ray diffraction demonstrated that the position of the pseudocubic-tetragonal phase boundary is dependent on the magnitude of the applied electric field, as well as on the rate of increase in the field (Royles et al., 2011, Royles et al., 2010).

Thus in the present (1–x)NBT – xBCT system, the constriction in P-E loop for composition x = 0.1 is most likely also to be a consequence of a field induced phase transition, rather than alternative explanations such as ageing due to pinning of domain walls (Daniels et al., 2009, Yun et al., 2009b, Yun et al., 2009a).

Bipolar strain-field measurements, Figure 4.8, indicated a relatively large electromechanical strain of ~ 0.25 % for the x = 0.1 sample, (E_{max} = 40 kV/cm) with an effective d_{33}* value (S_{max}/E_{max}) of ~ 640 pm/V. Trends in the values of remnant polarization (P_r), saturated polarization (P_s), coercive field (E_C), maximum strain

(S_{max}), maximum electric field (E_{max}) and effective values of d_{33} (S_{max}/E_{max}), determined from P-E and S-E loops are shown in Table 4.3.

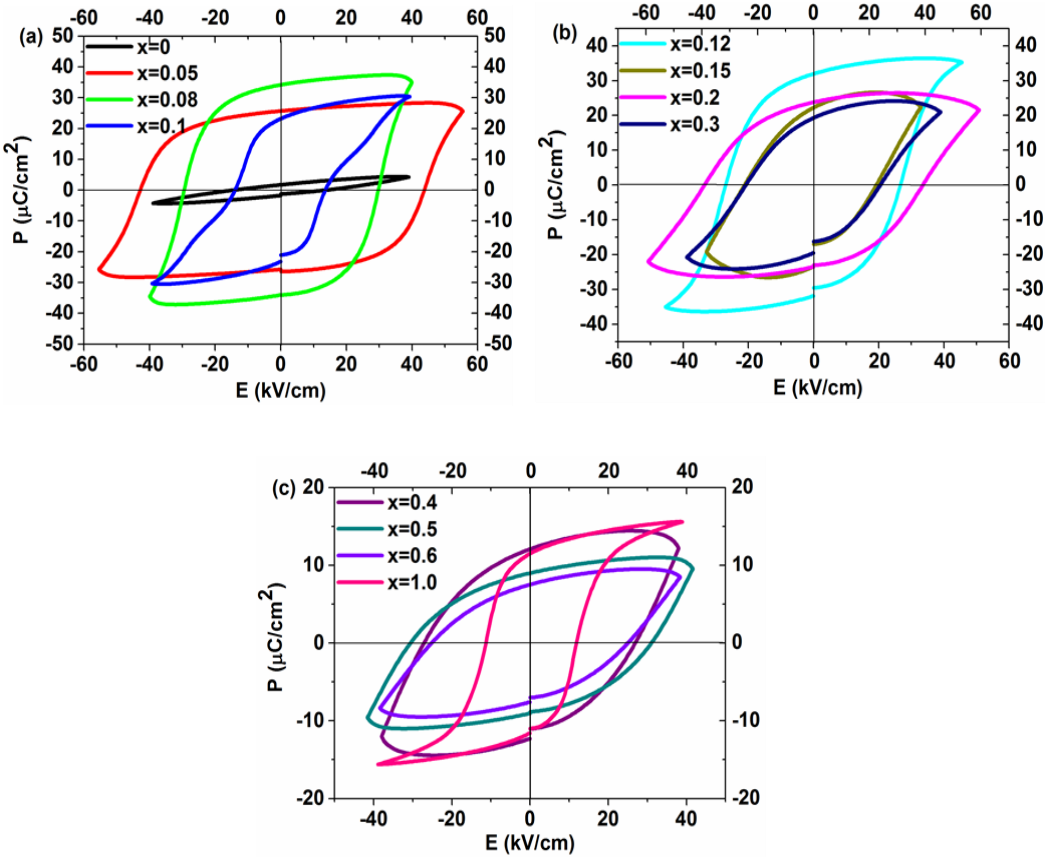

Figure 4.7 P-E hysteresis loops of $(1–x)Na_{0.5}Bi_{0.5}TiO_3 – xBa_{0.8}Ca_{0.2}TiO_3$, (a) x = 0 – 0.1(b) x = 0.12 – 0.3 and (c) x = 0.4 – 1.0.

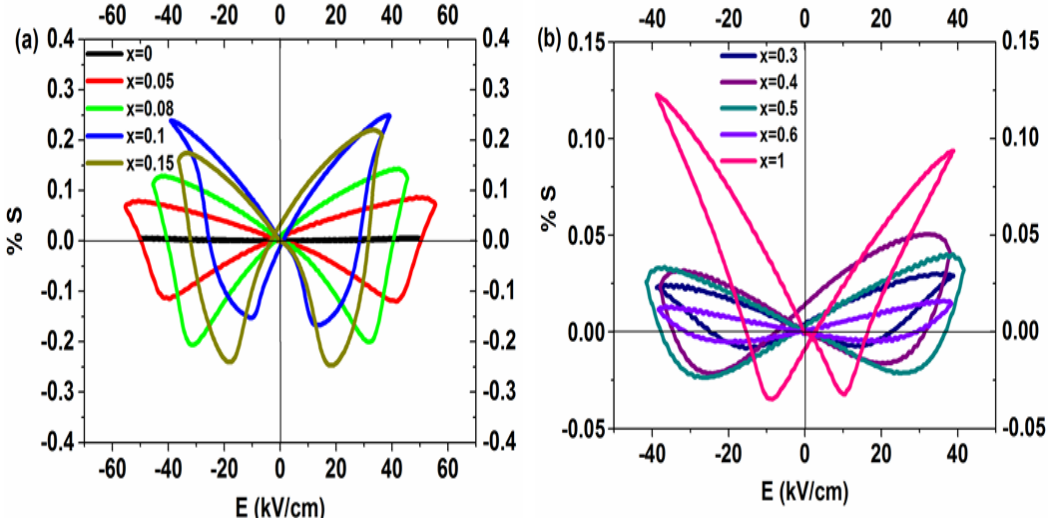

Figure 4.8 Bipolar strain S versus electric field of $(1–x)Na_{0.5}Bi_{0.5}TiO_3 – xBa_{0.8}Ca_{0.2}TiO_3$, (a) x = 0 – 0.15 and (b) x = 0.3 – 1.

Table 4.3 Piezoelectric and ferroelectric properties of $(1–x)Na_{0.5}Bi_{0.5}TiO_3 – xBa_{0.8}Ca_{0.2}TiO_3$ ceramics

Sample (x)	P_r ($\mu C/cm^2$)	Ec (kV/cm)	P_s ($\mu C/cm^2$)	S_{max} (%)	E_{max} (kV/cm)	$d_{33}^* = S_{max}/E_{max}$ (pm/V)
0	2	16	5	0.01	48	20
0.05	26	43	28	0.09	50	180
0.08	35	30	37	0.14	44	320
0.1	32	14	31	0.25	39	640
0.12	32	27	35	0.15	33	450
0.15	24	21	25	0.21	39	540
0.2	23	34	24	0.2	49	410
0.3	19	20	23	0.03	39	80
0.4	12	27	14	0.05	38	130
0.5	9	31	11	0.04	41	100
0.6	7	25	10	0.02	38	50
1	12	12	16	0.12	39	308

4.1.5 Microscopic analysis of ceramics

The microstructure of fractured sintered ceramics samples was analysed using scanning electron microscopy (SEM). Geometrical densities of the ceramics are shown in Figure 4.9. Spherical shaped grains with grain sizes ~ 2 – 5 μm were observed, Figure 4.10.

The grains were of spherical like shape for compositions $x \leq 0.9$, with a slight variations in grain sizes for different compositions. The variations in grain size can also affect the dielectric behaviour. A decrease in crystallite size can give

broad dielectric peaks, whereas an increase in crystallite size gives sharp permittivity peaks similar to observed in $BaTiO_3$ and $PbTiO_3$ ceramics (Martirena and Burfoot, 1974, Chattopadhyay et al., 1995). Geometrical densities of the compositions were in the range 5.6 - 4.8 g/cm$^{3)}$ (~ 89 - 95 % of theoretical density).

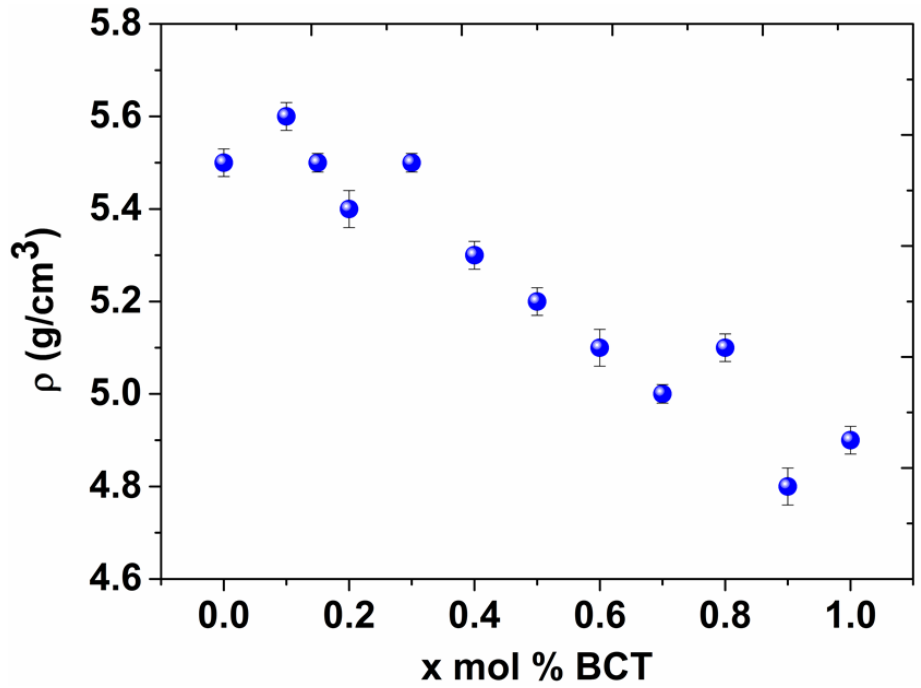

Figure 4.9 Geometrical densities of (1–x)$Na_{0.5}Bi_{0.5}TiO_3$ – x$Ba_{0.8}Ca_{0.2}TiO_3$.

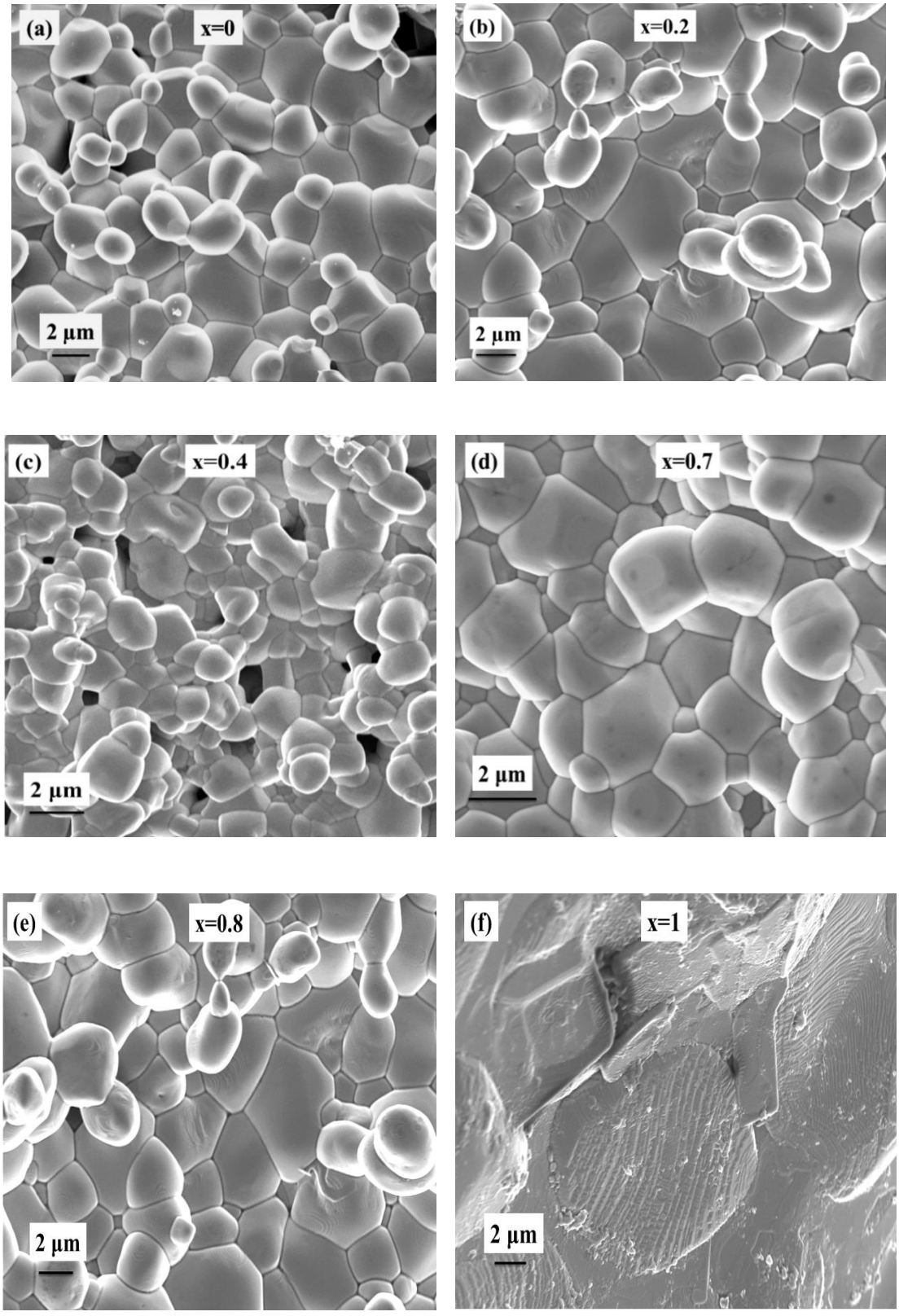

Figure 4.10 SEM micrographs of standard $(1–x)Na_{0.5}Bi_{0.5}TiO_3 – xBa_{0.8}Ca_{0.2}TiO_3$ system (a) x = 0, (b) x = 0.2, (c) x = 0.4, d) x = 0.7, (e) x = 0.8 and (f) x = 1.0.

4.1.6 Transmission electron microscopy

Microstructure analysis of ceramics was performed using transmission electron microscopy (TEM) and energy dispersive X-ray spectroscopy (EDX). TEM images of the ceramic compositions (1–x)NBT – xBCT, x = 0.1 and 0.2 are shown in Figure 4.11. The circled line shows some small grains within the large grain, indicating some biphasic structure, which was not observed in XRD. This may be due to incomplete reaction.

Contrast lamellae were observed in compositions x = 0.1 and 0.2. The dark and light contrast lines might indicate the presence of ferroelectric domains or might be due to stressed regions or faults in the sample. When comparing the dark field image to the corresponding X-ray elemental maps, no change in the homogeneity was observed for x = 0.1 and x = 0.2. Hence no core shell segregation was observed from elemental mapping, Figure 4.12 and Figure 4.13.

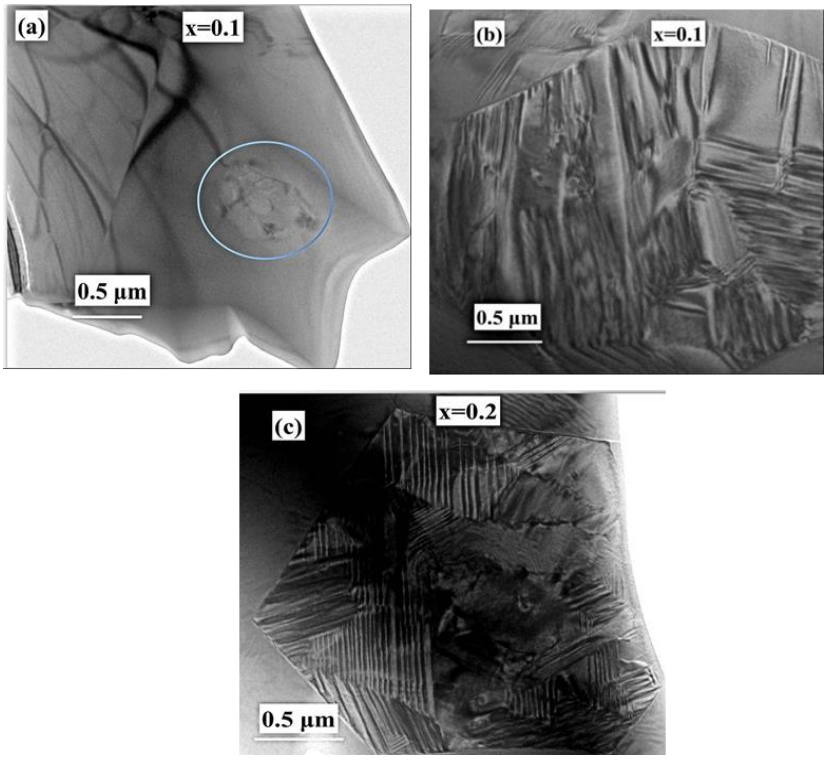

Figure 4.11 TEM images of (1–x)$Na_{0.5}Bi_{0.5}TiO_3$ – x$Ba_{0.8}Ca_{0.2}TiO_3$.system, (a–b) x = 0.1 and (c) x = 0.2.

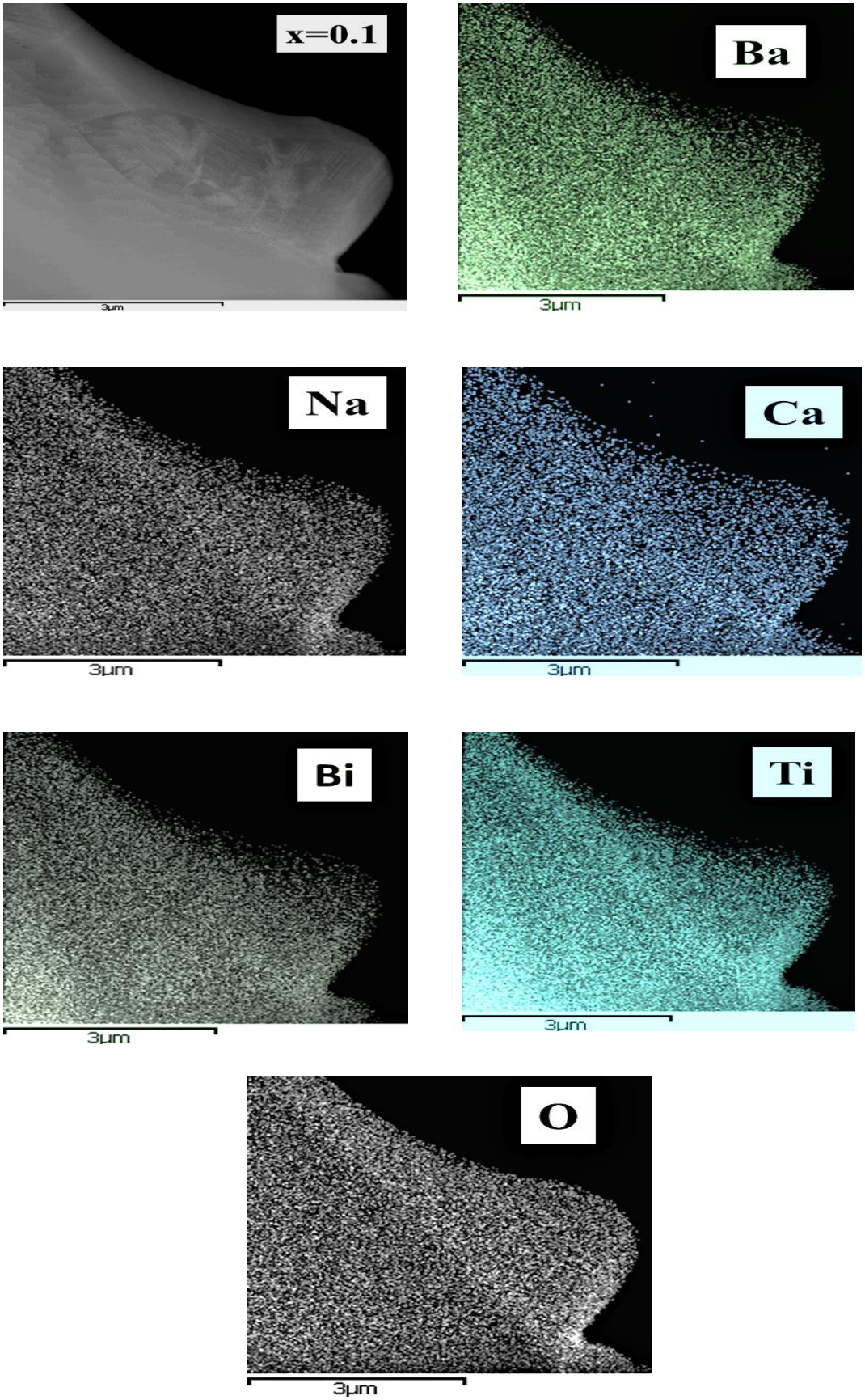

Figure 4.12 TEM elemental maps of (1–x)$Na_{0.5}Bi_{0.5}TiO_3$ – x$Ba_{0.8}Ca_{0.2}TiO_3$, x = 0.1 with dark field Ba, Bi, Ca, Na, Ti, and O EDX maps.

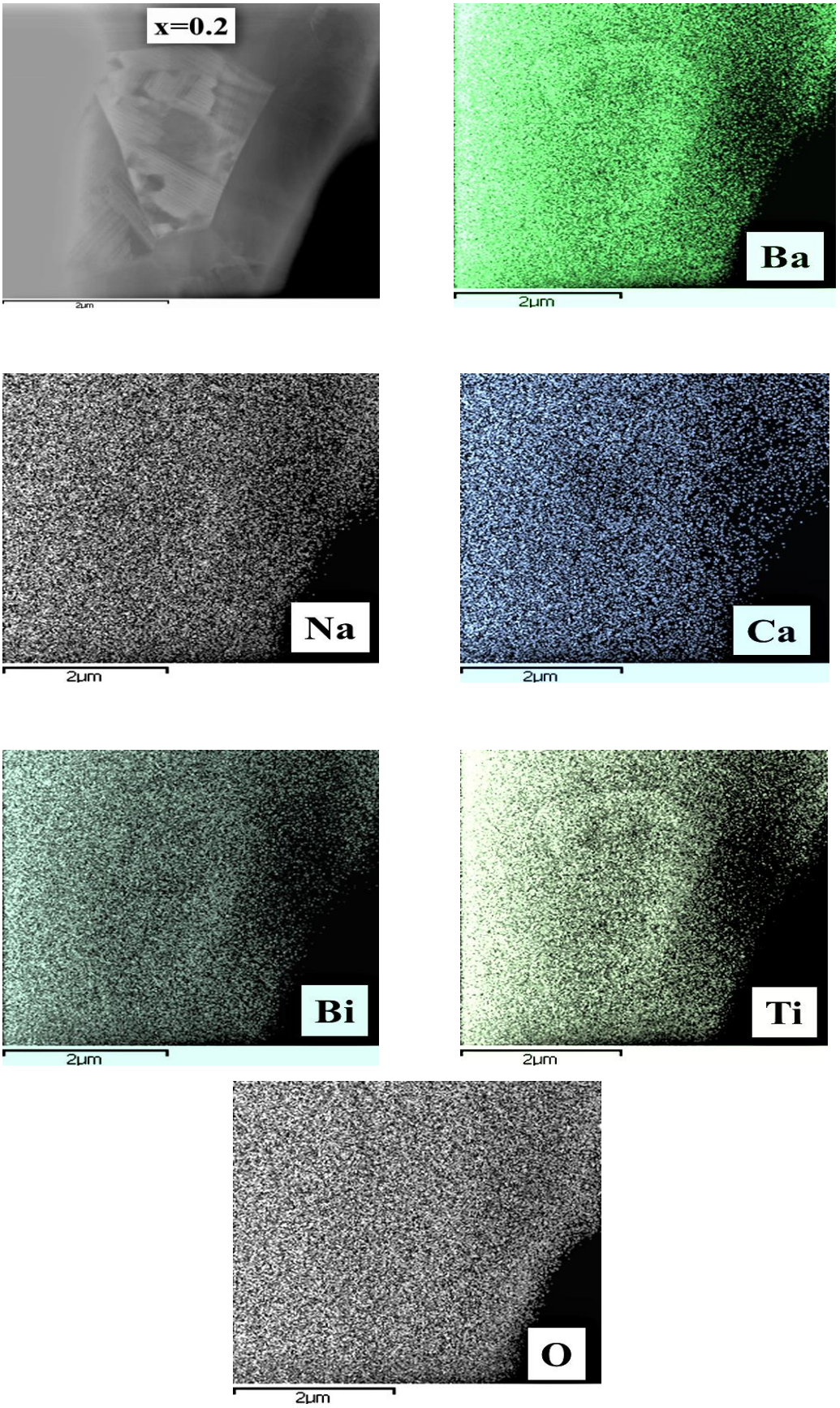

Figure 4.13 TEM elemental maps of (1–x)$Na_{0.5}Bi_{0.5}TiO_3$ – x$Ba_{0.8}Ca_{0.2}TiO_3$, x = 0.2 with dark field Ba, Bi, Ca, Na, Ti, and O EDX maps.

4.1.7 Resistivity study

The values of dc resistivity for x = 0, 0.05, 0.1 were recorded as a function of temperature in the range of 250 °C – 500 °C at a fixed voltage of 80 V, using a Keithley 617 programmable electrometer (Cleveland, OH), Figure 4.14. The resistivity dropped from approx. ~ 10^7 – 10^6 Ω m at 250 ºC to 10^3 Ω m at 500 ºC: these values lie within the range of resistivity observed by Dittmer et al. and Zeb et al. (Dittmer et al., 2012, Zeb and Milne, 2014a) for high temperature dielectrics.

The values of activation energy E_a for the electrical conductivity in the temperature rang 250 – 500 ºC observed from Arrhenius plots, were 0.54 eV (x = 0), 0.62 eV (x = 0.05) and 0.58 eV (x = 0.1). These values of activation energy might be attributed to the oxygen ion migration in perovskites (Zeb and Milne, 2014a, Selvamani et al., 2012, Islam, 2000, Raengthon and Cann, 2012).

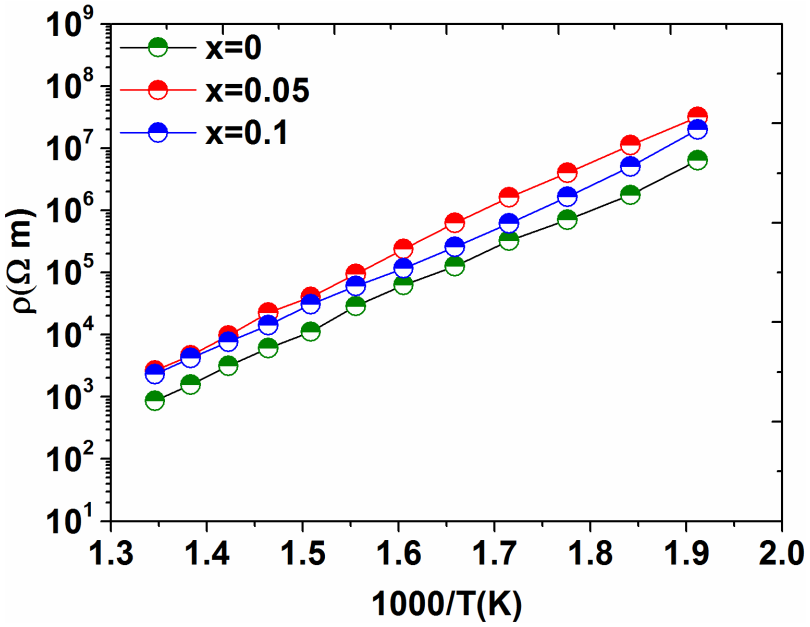

Figure 4.14 Resistivity as a function of inverse absolute temperature for (1–x)$Na_{0.5}Bi_{0.5}TiO_3$ – x$Ba_{0.8}Ca_{0.2}TiO_3$, x = 0 - 0.1.

4.1.8 Conclusions

Phase analysis of $(1–x)Na_{0.5}Bi_{0.5}TiO_3 – xBa_{0.8}Ca_{0.2}TiO_3$ ceramics by X-ray powder diffraction demonstrated a phase boundary between pseudocubic and tetragonal phases, separated by a narrow two-phase region at $0.1 < x \leq 0.2$.

Dielectric measurements revealed a frequency dependent anomaly at temperatures below the main broad peak in $\varepsilon_r – T$ plots for compositions $x \leq 0.4$ which merged with the main ε_r peak as the $Ba_{0.8}Ca_{0.2}TiO_3$ content increased to x = 0.5, giving a standard relaxor response, which changed to a diffuse but non-relaxor response at x = 0.7/0.8.

A constriction to the P-E loop for composition at x = 0.1 at the compositional phase boundary may be symptomatic of an electric field-induced phase transition. A high-field electromechanical strain of ~ +0.25 % (at 40 kV/cm) was recorded for composition x = 0.1, equivalent to a d_{33}* value of ~ 640 pm/V.

A SEM study have shown spherical shape grains, with slight variations in grain sizes (2 – 5 μm) for compositions, $x \leq 0.9$. TEM analysis indicated a domain structure in the ceramics x = 0.1 and 0.2 with no evidence of core shell segregation. The resistivity decreased from $\sim 10^7 – 10^6$ Ω m at 250 ºC temperature down to ~ 10^3 Ω m at 500 ºC.

.

4.2 Effects of bismuth oxide excess on properties of (1–x)$Na_{0.5}Bi_{0.5}TiO_3$ – x$Ba_{0.8}Ca_{0.2}TiO_3$ ceramics

4.2.1 Summary

Few investigations have been made on the effects of Bi_2O_3 excess to NBT-based ceramics. It is known that Bi_2O_3 vaporizes at elevated temperatures during sintering due to its low melting point (830 ºC). It is commonly used as modifier to enhance dielectric and piezoelectric properties of ceramics or as a sintering aid to decrease sintering temperatures (Zhang et al., 2008a).

The study of earlier literature (Xu, 2009, Wang, 2005) has shown complex effects of Bi_2O_3 excess which can be divided into three possible categories: 1) the compensation for loss of bismuth oxide at elevated temperature, but which has no effect on piezoelectric properties; 2) excess Bi_2O_3 persists at grain boundaries, which will degrade the piezoelectric properties due to the presence of non-ferroelectric phase at grain boundaries; 3) The occupancy of A-site (and oxygen) vacancies by excess Bi_2O_3 which will improve the piezoelectric properties due to facilitation of domain wall movement (Wang et al., 2005b).

The effects of 1wt.%, 1.5wt.% and 5wt.% Bi_2O_3 excess, on some compositions were studied, which has no significant influence on the dielectric properties of the ceramics, specially on loss factor (tanδ). The 5wt.% Bi_2O_3 excess composition resulted in the formation of secondary phases. However significant effect on tanδ was observed for 3wt.% Bi_2O_3 compositions.

In this study the effects of 3wt.% Bi_2O_3 modification on the crystal structure, morphology and electric properties of solid solutions (1–x)$Na_{0.5}Bi_{0.5}TiO_3$ – x$Ba_{0.8}Ca_{0.2}TiO_3$ ($0 \leq x \leq 0.9$), synthesised by a mixed oxide route were explored

using scanning electron microscopy (SEM), X-ray diffraction (XRD), dielectric and ferroelectric testing.

The effects of the addition of 3wt.% excess Bi_2O_3 on the crystal structure of (1–x)NBT – xBCT were examined from XRD patterns, no significant difference was observed compared to standard XRD patterns, except for slight promotion of mixed phase region towards higher x ($0.12 < x \leq 0.2$). The dielectric loss, especially at higher temperatures was significantly suppressed for Bi_2O_3-modified ceramics compared to the standard ceramics.

From P-E measurements, there was less evidence of loss, and generally better saturation and sharper P-E loops were observed for Bi_2O_3-modified compositions. Piezoelectric parameters were similar (or slightly improved) to unmodified formulations.

SEM micrographs have shown a significant decrease in grain size (~ 1 – 2 μm) compared to the standard compositions (~ 2 – 5 μm). The resistivity dropped from ~10^8 – ~10^7 Ω m at 250 ºC temperature down to ~10^4 Ω m at 500 ºC. These values of resistivity were higher than for standard (1–x)NBT – xBCT ceramics which were ~ 10^7 – ~ 10^6 Ω m at 250 ºC.

4.2.2 Compositional analysis

A ceramic fabrication technique reported in section 4.1.1 of this chapter were used to prepare a series of solid solutions $(1–x)Na_{0.5}Bi_{0.5}TiO_3 – xBa_{0.8}Ca_{0.2}TiO_3$ + 3wt.% Bi_2O_3 abbreviated as [(1–x)NBT – xBCT + 3wt.% Bi_2O_3] for $0 \leq x \leq 0.9$. For all samples with 3wt % excess Bi_2O_3, sintering conditions were as for standard non-excess samples i.e for x = 0 to 0.15, 1160 °C for 6 h. For x = 0.2 to x = 0.5 ,1170 °C for 6 h, and for x = 0.6 to 0.9, 1190°C for 6 h. Sample x = 1 (BCT) 1400 °C for 6 h.

Sintered pellet densities were ~ 5.6 – 5.0 g/cm^3 (~ 90 – 95% of theoretical density), comparable to the standard samples.

4.2.3 Examination of powders of crushed ceramics using XRD

XRD patterns of (1–x)NBT – xBCT + 3wt.% Bi_2O_3 ceramics are given in Figure 4.15. All the ceramic patterns showed a single perovskite structure with no evidence of secondary phases, consistent with standard (1–x)NBT – xBCT system. The only difference was a slightly increased extent of the single phase cubic region, $0 \leq x \leq 0.12$ as opposed to $0 \leq x \leq 0.1$ for standard ceramics. The mixed phase region was from x = 0.12 – 0.2, thereafter single phase tetragonal occurred, Figure 4.15b. The values of *a* and *c* are plotted in Figure 4.16. The *c* values were lower than for standard samples giving a lower *c/a* ratio ~ 1.002 – 1.005, for excess samples compared to ~1.008 – 1.012 for standard samples, Figure 4.16.

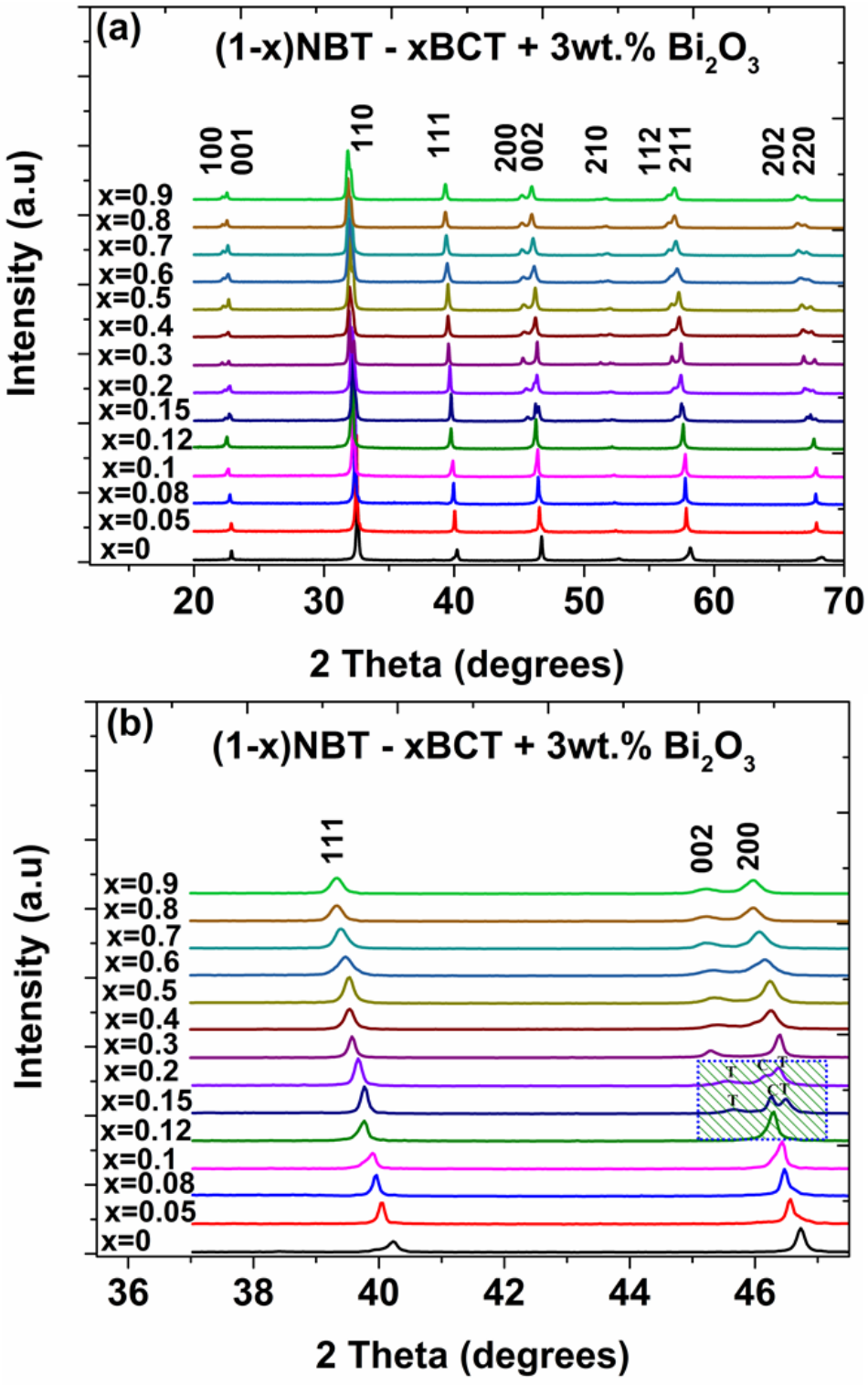

Figure 4.15 (a) XRD patterns of (1–x)$Na_{0.5}Bi_{0.5}TiO_3$ – x$Ba_{0.8}Ca_{0.2}TiO_3$ + 3wt.% Bi_2O_3 ceramic system and (b) A broad view of 111, 002/200 XRD peaks, the shaded region shows a mixed phase region (T = Tetragonal and C = Cubic) (See Figure 4.1a-b for standard samples).

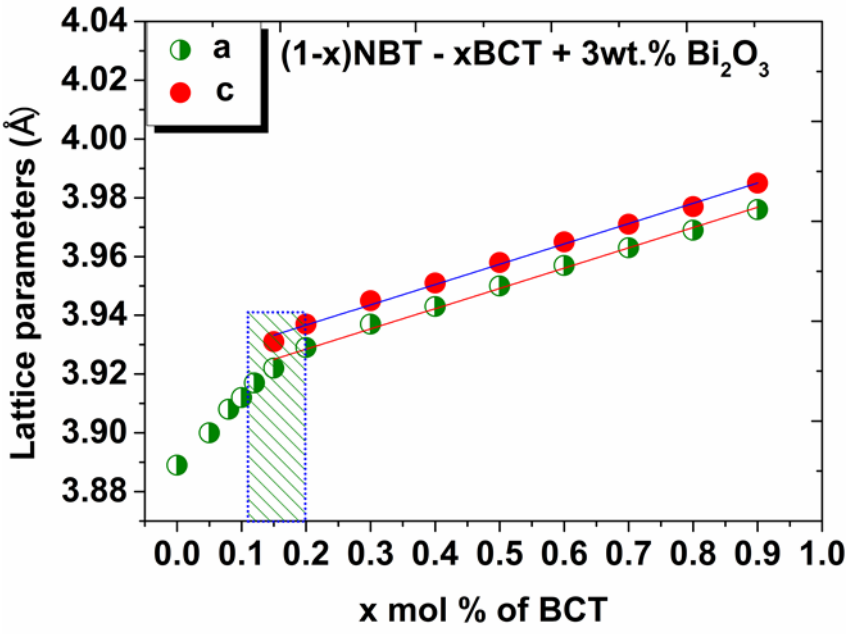

Figure 4.16 Variation of lattice parameters of ceramic series (1–x)$Na_{0.5}Bi_{0.5}TiO_3$ – x$Ba_{0.8}Ca_{0.2}TiO_3$ + 3wt.% Bi_2O_3 , the shaded region show a mixed phase region.

4.2.4 Dielectric characterization

The temperature dependence of relative permittivity (ε_r) and loss tangent (tanδ) for bismuth oxide-modified (1–x)NBT – xBCT ceramics at various frequencies (1 kHz – 1 MHz) from ambient temperature to 450 ºC are displayed in Figure 4.17 – 4.19. The heating and cooling rate was kept 3 ºC/min during all the measurements.

The general appearance of ε_r – T plots was similar to standard samples. However there was a greater separation of T_1 and T_2 in the excess samples for most values of x; exception being x = 0.1. In standard ceramics the values of temperature corresponding to the first dielectric peak, T_1 were slightly higher ($x \leq 0.3$), whereas the temperature corresponding to the maximum relative permittivity peak T_2 were slightly lower for $x \leq 0.08$, and comparable for $x \geq 0.1$, Figure 4.17 – 4.19. This was most apparent in case of T_1 for x = 0.2 and 0.3. The temperature difference between

the temperature of lower dielectric anomaly at T_1 and a high dielectric anomaly at T_2, for standard and Bi_2O_3 excess NBT – BCT ceramic is shown in Figure 4.20. For most BCT levels, x, the tanδ values at high temperatures, > 350 ºC were reduced by the use of excess Bi_2O_3, Figure 4.17 – 4.19 (Table 4.2 and Table 4.4 for comparison). A summary of dielectric properties of (1– x)NBT – xBCT + 3wt.% Bi_2O_3 is presented in Table 4.4. A comparison of dielectric properties of no excess (standard) and 3wt.% Bi_2O_3 ceramics are given in Table 4.5.

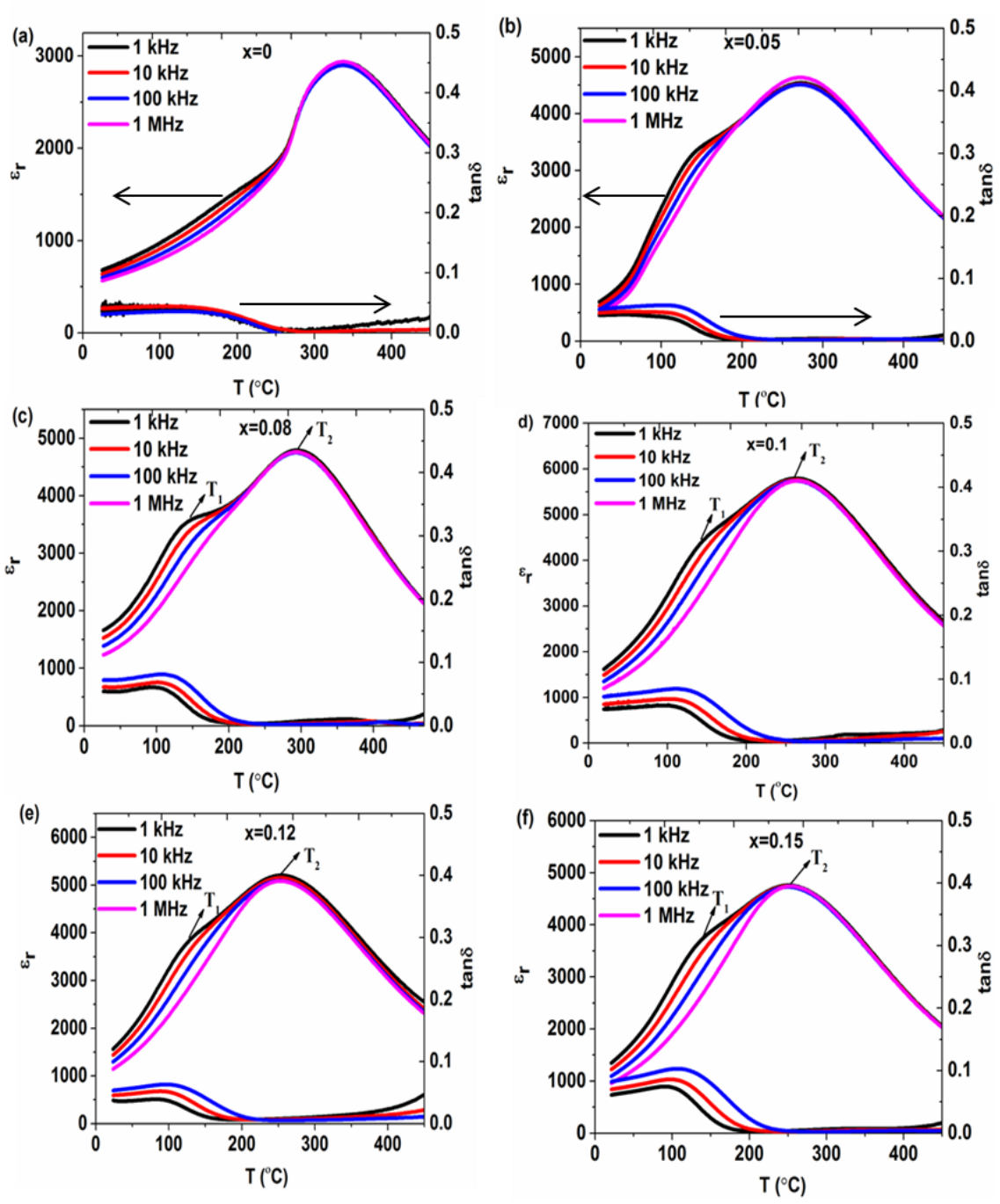

Figure 4.17 Temperature-dependent relative permittivity (ε_r) and loss tangent (tanδ) of ceramics, $(1–x)Na_{0.5}Bi_{0.5}0TiO_3 – xBa_{0.8}Ca_{0.2}TiO_3$ + 3wt.% Bi_2O_3, for (a) x = 0, (b) x = 0.05, (c) x = 0.08, (d) x = 0.1, (e) x = 0.12 and (f) x = 0.15. (data set continued in Figure 4.17)

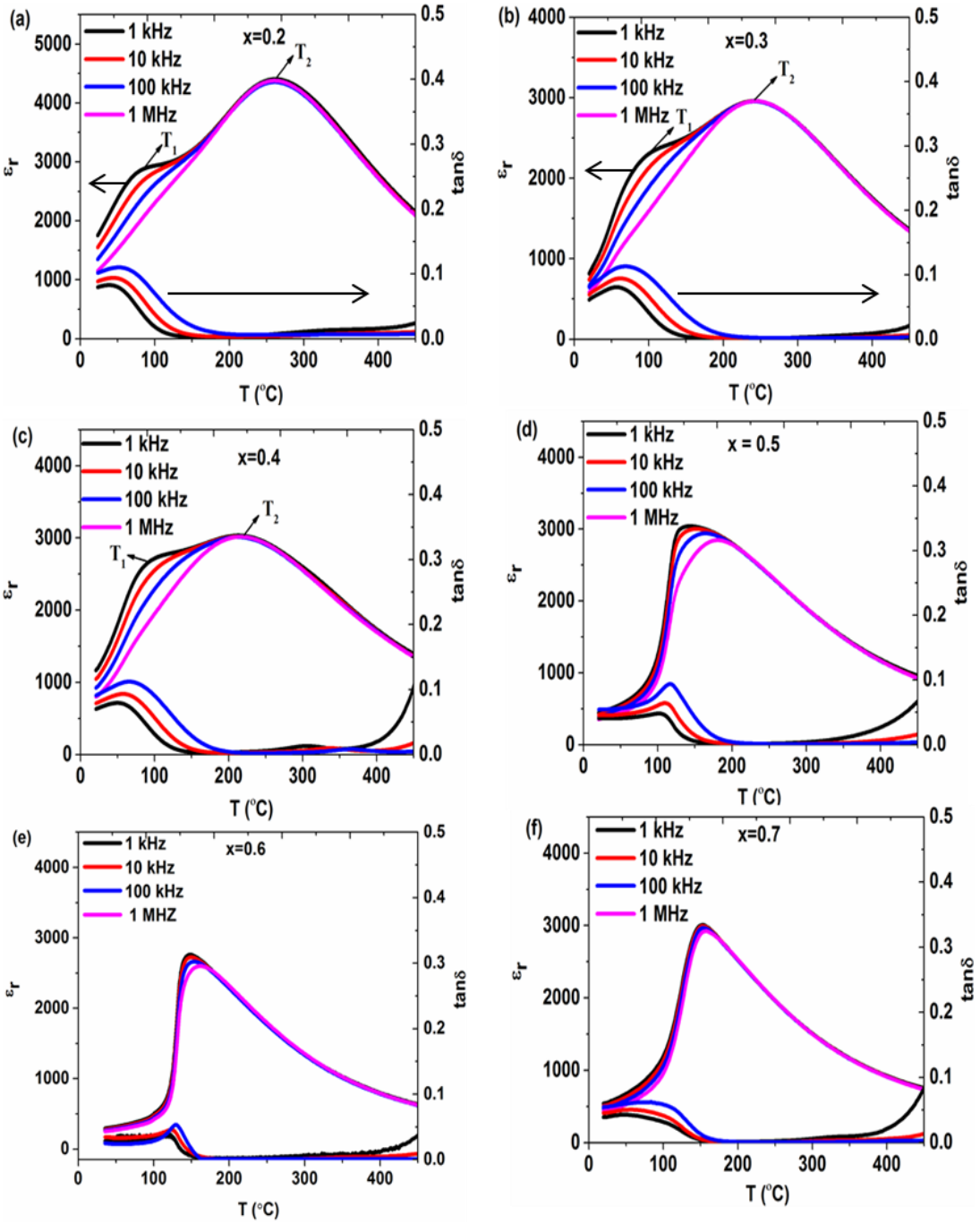

Figure 4.18 Temperature-dependent relative permittivity (ε_r) and loss tangent (tanδ) of ceramics, $(1–x)Na_{0.5}Bi_{0.5}TiO_3 – xBa_{0.8}Ca_{0.2}TiO_3$ + 3wt.% Bi_2O_3, for (a) x = 0.2, (b) x = 0.3, (c) x = 0.4, (d) x = 0.5, (e) x = 0.6 and (f) x = 0.7. (data set continued in Figure 4.18)

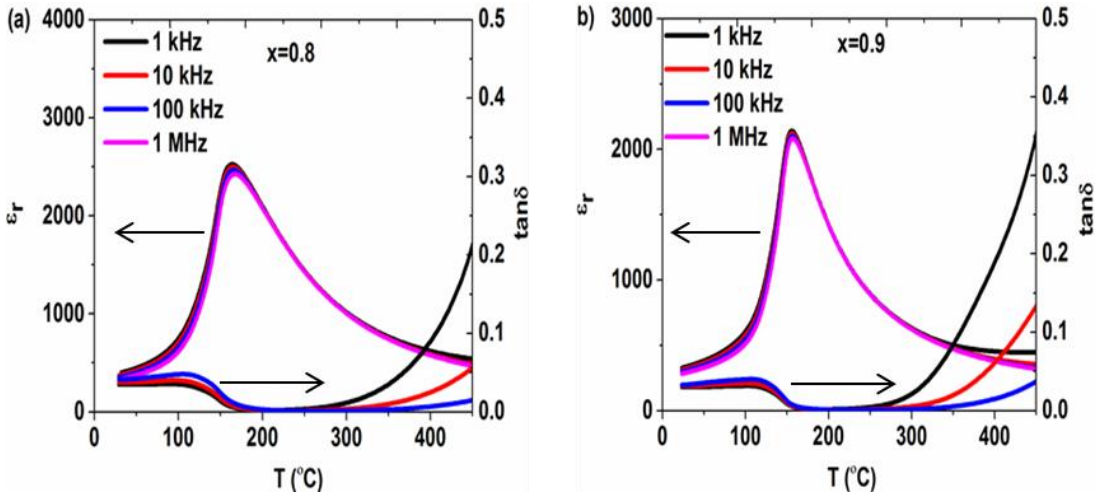

Figure 4.19 Temperature-dependent relative permittivity (ε_r) and loss tangent (tanδ) of ceramics, (1–x)$Na_{0.5}Bi_{0.5}TiO_3$ – x$Ba_{0.8}Ca_{0.2}TiO_3$ + 3wt.% Bi_2O_3, for (a) x = 0.8 and (b) x = 0.9.

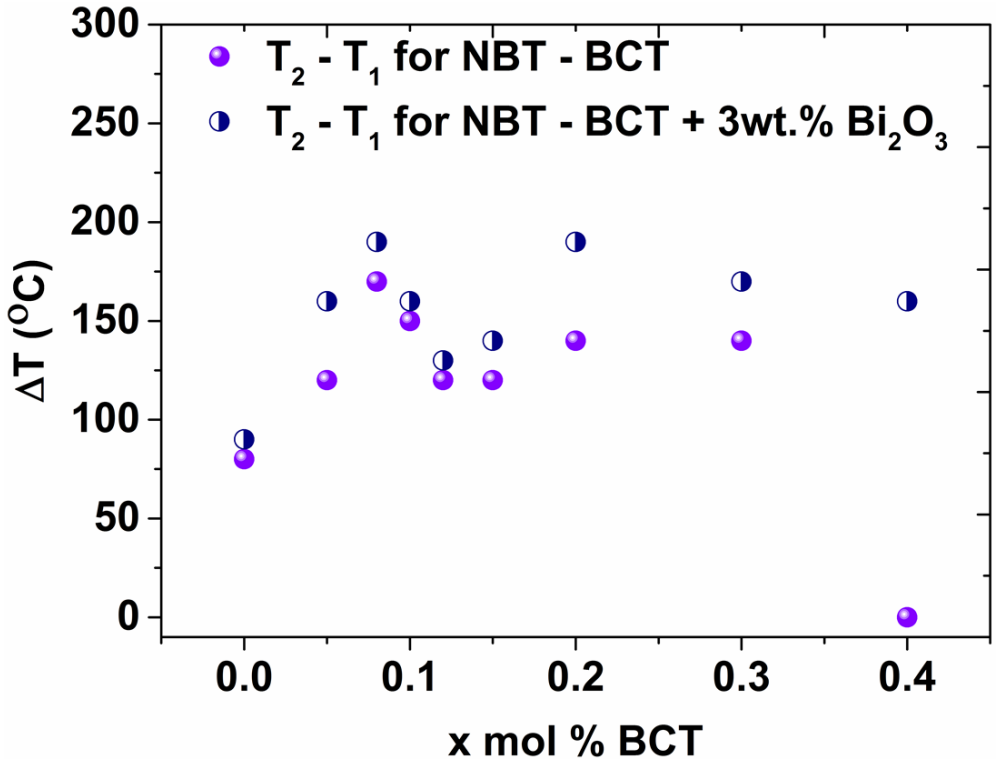

Figure 4.20 Temperature difference between lower temperature anomaly at T_1 and high temperature anomaly at T_2/T_m for both standard and 3wt.% Bi_2O_3 excess (1–x)$Na_{0.5}Bi_{0.5}TiO_3$ – x$Ba_{0.8}Ca_{0.2}TiO_3$ ceramics, (x = 0 – 0.4).

Table 4.4 Dielectric properties of (1–x)$Na_{0.5}Bi_{0.5}TiO_3$ – x$Ba_{0.8}Ca_{0.2}TiO_3$ + 3wt.% Bi_2O_3 ceramics.

Sample (x)	ε_r (25 ºC)	ε_{max}	T_1 (ºC)	$T_2 = T_m$ (ºC)	tanδ≤0.02 (T-range) 1kHz
0	680	2930	250	340	200–420 ºC
0.05	710	4540	110	270	140–450 ºC
0.08	1660	4790	100	290	150–450 ºC
0.1	1640	5790	110	270	160–450 ºC
0.12	1590	5200	120	250	130–390 ºC
0.15	1400	4760	110	250	150–450 ºC
0.2	1790	4400	70	260	100–440 ºC
0.3	910	2960	70	240	120–450 ºC
0.4	1230	3030	60	220	110–400 ºC
0.5	460	3040		140	130–380 ºC
0.6	300	2760		150	120–410 ºC
0.7	550	2890		170	120–400 ºC
0.8	310	2520		160	140–320 ºC
0.9	330	2140		160	140–300 ºC

4.2.4.1 Modified Curie Weiss law

The plots of $\ln(1/\varepsilon - 1/\varepsilon_m)$ as a function $\ln(T - T_m)$ for the 3wt.% Bi_2O_3 + (1–x)BNT – xBCT ceramics series are shown in Figure 4.21. A linear relationship was observed for all modified ceramics as observed in the standard ceramics discussed in section 4.1.4.1 of this chapter.

The slope of the fitting curve was used to determine the value of γ. The values of diffuseness constant γ were in the range of ~ 1.4 – 2 for the modified ceramics. Values of diffuseness constant γ for both standard and modified (1–x)NBT – xBCT ceramics are shown in Table 4.5. Normal ferroelectric like behaviour was observed for compositions x > 0.7 (γ ~ 1.4 – 1.5).

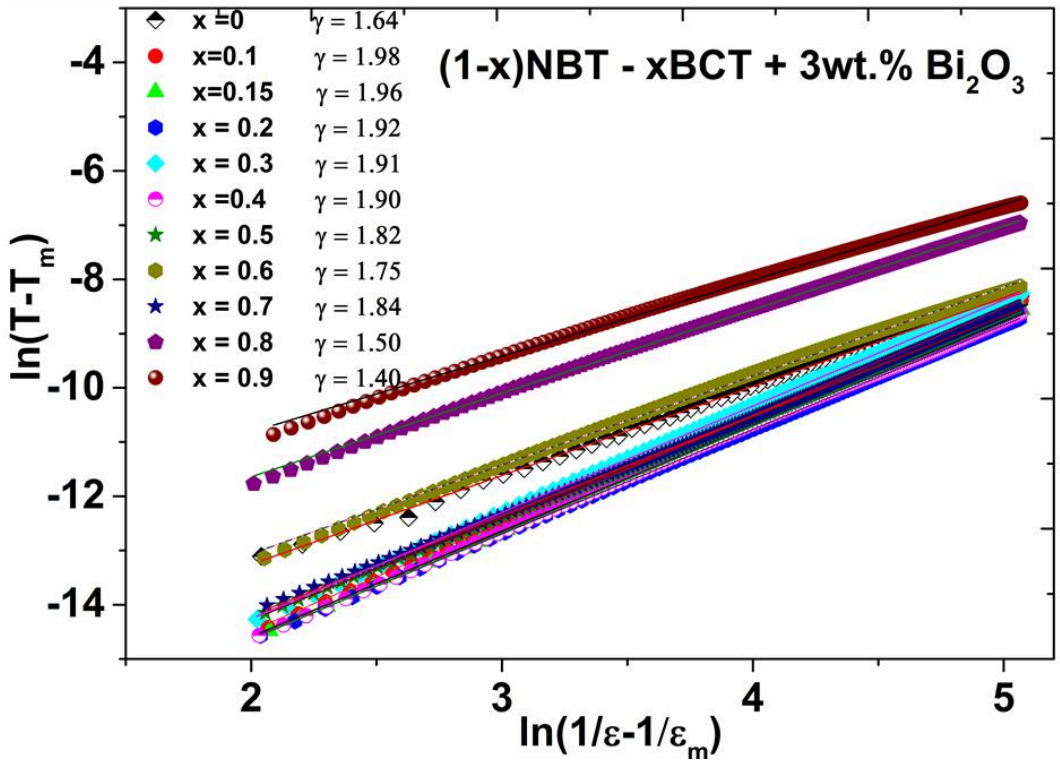

Figure 4.21 $\ln(1/\varepsilon - 1/\varepsilon_m)$ as a function of $\ln(T - T_m)$ for $(1–x)Na_{0.5}Bi_{0.5}TiO_3 – xBa_{0.8}Ca_{0.2}TiO_3$ + 3wt.% Bi_2O_3 ceramics, x = 0 – 0.9.

Table 4.5 Summary of the comparison of standard and 3wt.% Bi_2O_3 -modified $(1–x)Na_{0.5}Bi_{0.5}TiO_3 – xBa_{0.8}Ca_{0.2}TiO_3$.ceramics.

x	Low temperature Inflection T_1(°C)		Maximum-relative permittivity temperature T_2 (°C)		Maximum relative permittivity $\varepsilon_{r\,max}$		Diffuseness constant (γ)	
	Standard	**Modified**	**Standard**	**Modified**	**Standard**	**Modified**	**Standard**	**Modified**
0	240	250	330	340	2620	2930	1.7	1.6
0.05	130	110	250	270	5320	4540	---	---
0.08	110	100	280	290	3390	4790	---	---
0.1	120	110	270	270	4070	5790	2.1	2.0
0.12	130	120	250	250	6420	5200	---	---
0.15	130	110	250	250	6120	4760	2.0	2.0
0.2	110	70	250	260	6080	4400	1.9	1.9
0.3	100	70	240	240	5100	2960	1.9	1.9
0.4	-----	60	170	220	2920	3030	1.8	1.9
0.5	-----	-----	160	140	3090	3040	1.3	1.8
0.6	-----	-----	150	150	2610	2760	1.5	1.8
0.7	-----	-----	170	170	2270	2890	1.4	1.8
0.8	-----	-----	170	160	2800	2520	1.4	1.5
0.9	-----	-----	170	160	2760	2140	1.3	1.4

4.2.5 Ferroelectric and piezoelectric properties

Room temperature ferroelectric measurements were made at various voltages 2 – 5 kV/cm (1 Hz) for modified compositions $x \leq 0.15$ (only x = 0 to 0.15 pellets had been fabricated at the time of accessing the P-E and S-E testing equipment). The polarization-electric field (P-E) response of $(1–x)Na_{0.5}Bi_{0.5}TiO_3 – xBa_{0.8}Ca_{0.2}TiO_3$ + 3wt.% Bi_2O_3 is shown in Figure 4.22.

The P-E loops were less rounded than for standard samples. Constricted P-E loops were observed for x = 0.1 and 0.12 in the mixed phase region similar to x = 0.1 in the standard ceramic system. The remnant polarization P_r values for modified ceramics were comparable to the standard ceramics, except for x = 0.1 – 0.12, whereas coercive field E_C was less for most samples Table 4.7. The remnant polarization (estimated P_r ~ 8 μC/cm^2), observed for another studied 3 at% Bi-excess composition $(Ba_{0.9}Ca_{0.1})_{0.9}(Na_{0.5}Bi_{0.5})_{0.1}TiO_3$ was less to our both standard and Bi-modified sample (x = 0.1) , whereas coercive field E_C (estimated ~ 23 kV/cm) was higher to our study (x = 0.1) (Yun, 2009).

Typical S-E butterfly loops were observed for all modified compositions, Figure 4.23. The effective d_{33}^* values increased with increasing x until x = 0.12, reaching a maximum, d_{33}^*~ 720 pm/V at x = 0.12 (on the boundary between cubic and mixed phase Figure 4.15. These effective d_{33}^* values for most bismuth oxide modified samples were higher than for the unmodified (1–x)NBT – xBCT system,

Furthermore a decrease in coercive field was observed for the modified system, x = 0 – 0.12, except x = 0.15. This decrease in some sample compositions might be attributed to the decrease in oxygen vacancies compared to the standard system. The oxygen vacancies have clamping effect on domain wall motion which limits the reversal of spontaneous polarization of ferroelectric domains under applied electric field (Xu et al., 2008).

A comparison of values of effective piezoelectric constant d_{33}^* and coercive field E_c for modified and unmodified ceramics is shown in Figure 4.24. Trends in the values of remnant polarization (P_r), saturated polarization (P_s), coercive field (E_C), maximum strain (S_{max}), maximum electric field (E_{max}) and effective values of d_{33} (S_{max}/E_{max}), determined from P-E and S-E loops are shown in Table 4.6. A

comparison of ferroelectric and piezoelectric properties of standard and bismuth modified ceramics is presented in Table 4.7.

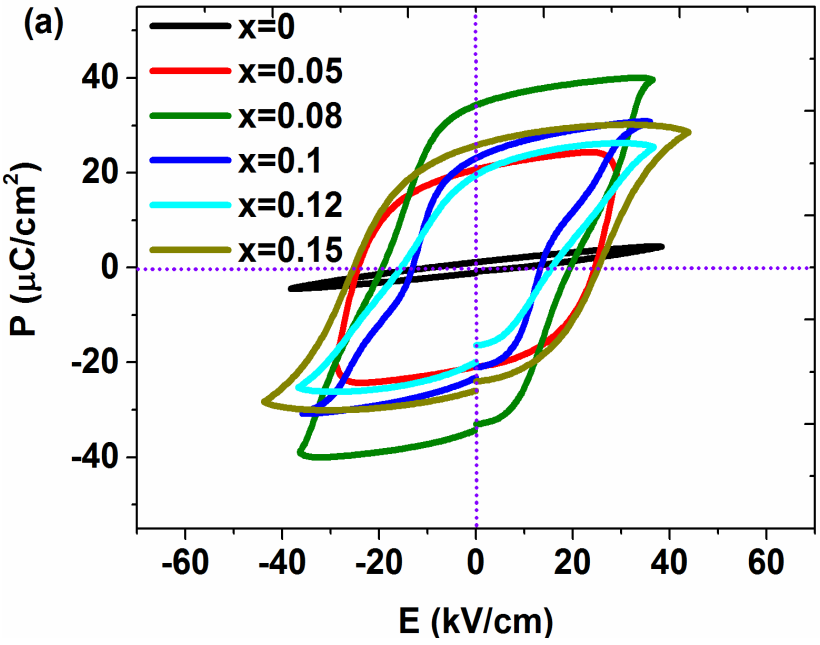

Figure 4.22 P-E hysteresis loop for compositions (1–x)$Na_{0.5}Bi_{0.5}TiO_3$ – x$Ba_{0.8}Ca_{0.2}TiO_3$ + 3wt.% Bi_2O_3, 0 ≤ x ≤ 0.15.

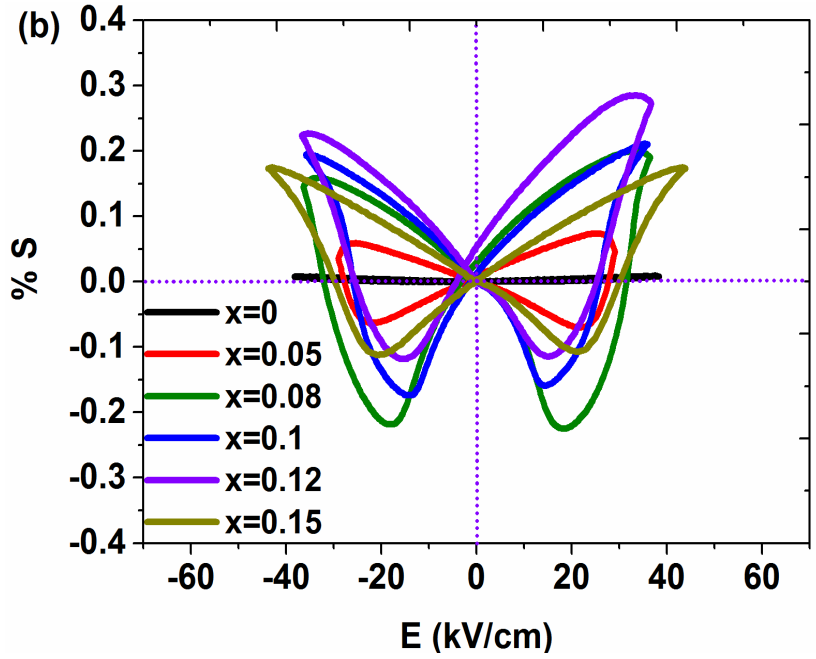

Figure 4.23 Bipolar strain S versus electric field for compositions (1–x)$Na_{0.5}Bi_{0.5}TiO_3$ – x$Ba_{0.8}Ca_{0.2}TiO_3$ + 3wt.% Bi_2O_3, 0 ≤ x ≤ 0.15.

Table 4.6 Ferroelectric and Piezoelectric properties of ceramics system, (1–x)$Na_{0.5}Bi_{0.5}TiO_3$ – x$Ba_{0.8}Ca_{0.2}TiO_3$ + 3wt.% Bi_2O_3.

x mol %	P_r ($\mu C/cm^2$)	E_C (kV/cm)	P_S ($\mu C/cm^2$)	S_{max}	E_{max} (kV/cm)	$d_{33}=S_{max}/E_{max}$ (Pm/V)
0	2	10	5	0.01	38	30
0.05	25	24	25	0.08	26	270
0.08	35	19	40	0.2	35	570
0.1	24	13	31	0.21	36	590
0.12	20	15	25	0.26	36	720
0.15	26	25	29	0.12	43	420

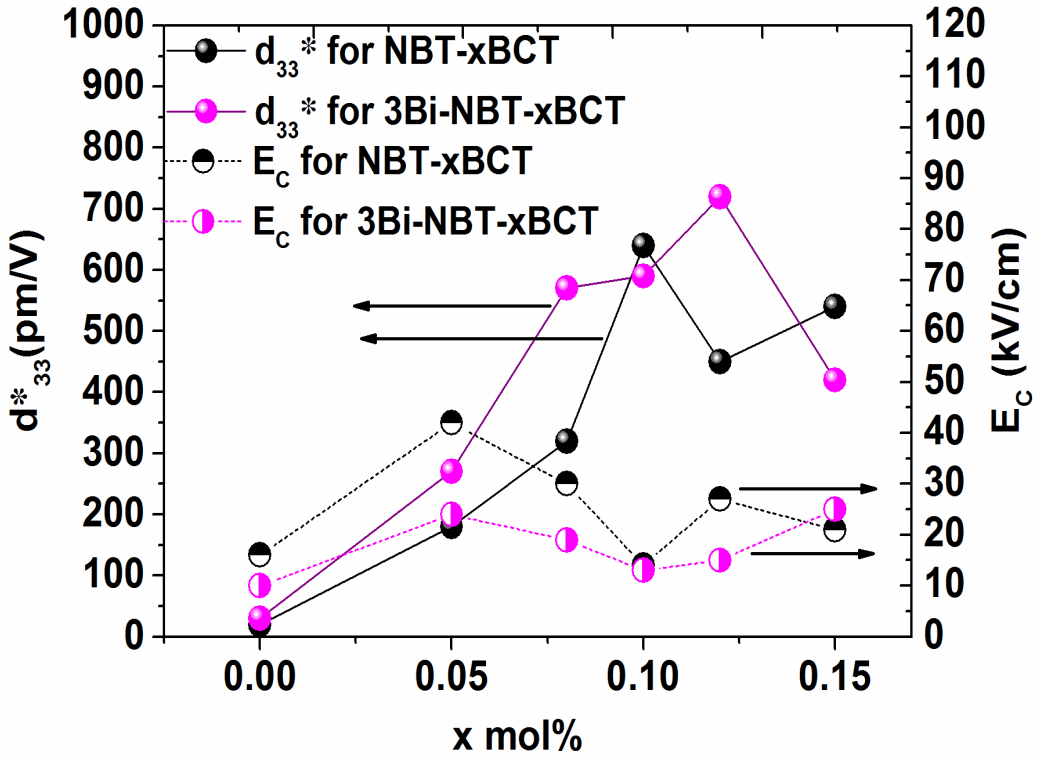

Figure 4.24 Plots showing comparison of values of effective piezoelectric constant d_{33}^* and coercive field E_C for unmodified (black and semi black spheres) and 3wt.% Bi_2O_3 modified (pink and semi pink spheres) (1–x)$Na_{0.5}Bi_{0.5}TiO_3$ – x$Ba_{0.8}Ca_{0.2}TiO_3$ system.

Table 4.7 A comparison of ferroelectric and piezoelectric properties of bismuth oxide excess and standard (1–x)$Na_{0.5}Bi_{0.5}TiO_3$ – x$Ba_{0.8}Ca_{0.2}TiO_3$ ceramics.

Sample (x)	P_r (μC/cm^2)		E_C (kV/cm)		$d_{33}=S_{max}/E_{max}$ (Pm/V)	
	Standard	Modified	Standard	Modified	Standard	Modified
0	2	2	16	10	20	30
0.05	26	25	43	24	180	270
0.08	35	35	30	19	320	570
0.1	32	24	14	13	640	590
0.12	32	20	27	15	450	720
0.15	24	26	21	25	540	420

4.2.6 Microstructural analysis

The microstructures of the (1–x)NBT – xBCT + 3wt.% Bi_2O_3 system were analysed using SEM. The micrographs showing fracture surfaces of samples x = 0.05, 0.2, 0.3, 0.5, 0.7, 0.9 are shown in Figure 4.25. A dense microstructure was observed for nearly all the studied samples. The grain growth was suppressed significantly by introducing excess of Bi_2O_3 compared to unmodified (1–x)NBT – xBCT ceramics, which is similar to the effect observed by Wang et al , Zhang et al and Sehirlioglu et al, (Wang et al., 2005b, Zhang et al., 2008a, Sehirlioglu et al., 2009).

The grain size observed was ranged between ~ 1 – 2 μm, which is less than the standard ceramics for which the grain size was ~ 3 – 5 μm. The geometrical densities of the ceramics are shown in Figure 4.26. The densities for the bismuth oxide excess compositions were comparable to the standard ceramics (~ 90 – 96 % of theoretical density).

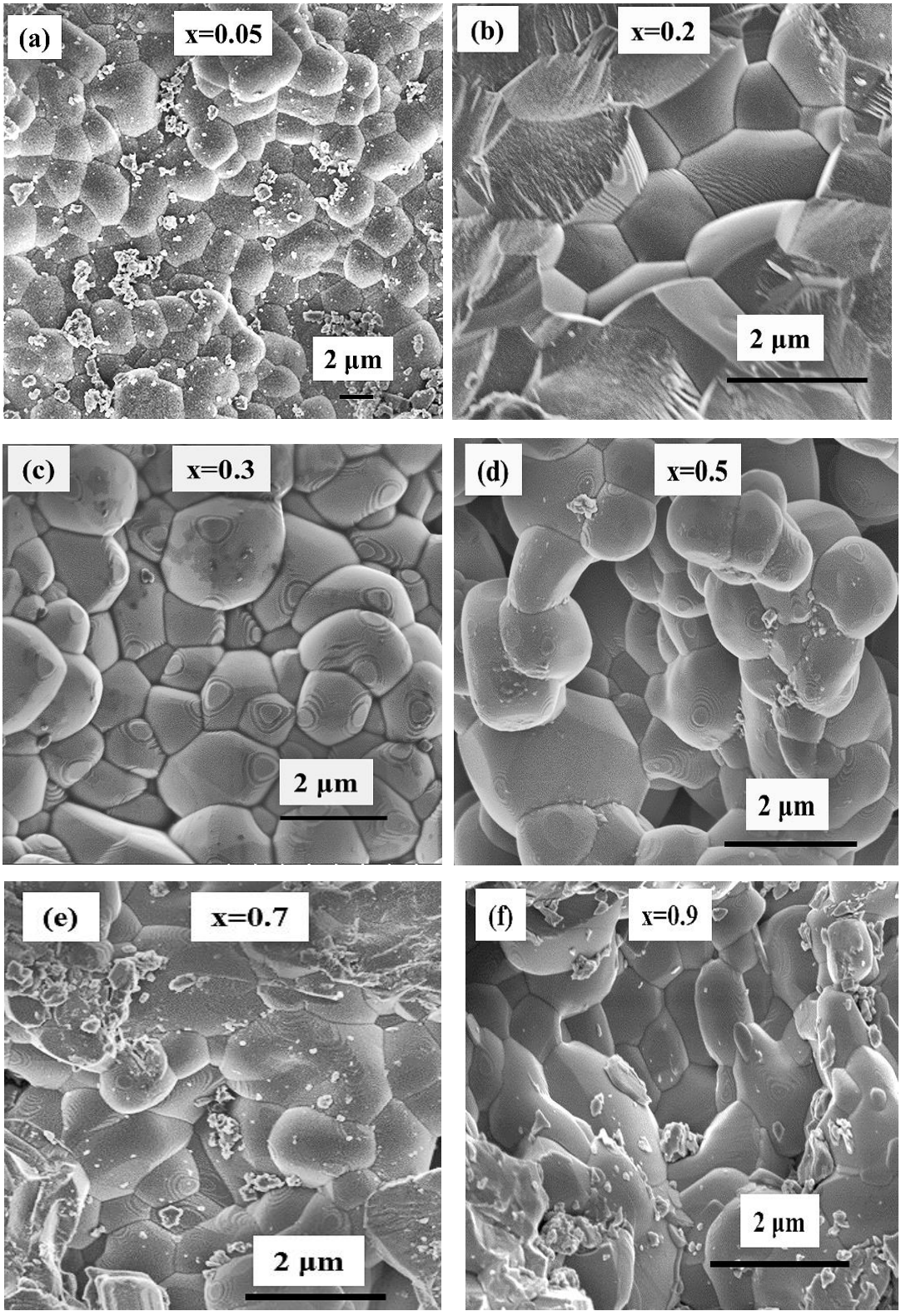

Figure 4.25 SEM micrographs of (1–x)$Na_{0.5}Bi_{0.5}TiO_3$ – x$Ba_{0.8}Ca_{0.2}TiO_3$ + 3wt.% Bi_2O_3, for (a) x = 0.05 (b) x = 0.2 (c), x = 0.3 (d), x = 0.5 (e), x = 0.7 and (f) x = 0.9.

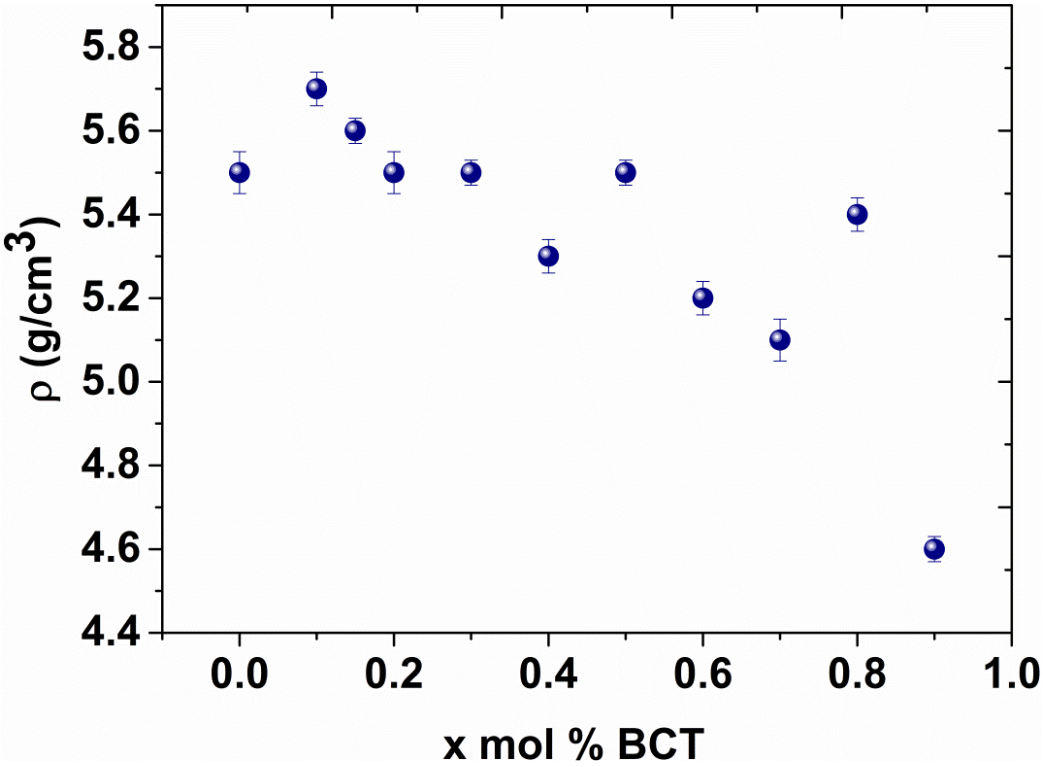

Figure 4.26 Geometrical densities of ceramics system, (1–x)$Na_{0.5}Bi_{0.5}TiO_3$ – x$Ba_{0.8}Ca_{0.2}TiO_3$ + 3wt% Bi_2O_3.

4.2.7 Resistivity study

Values of dc resistivity are presented as Arrhenius plots in Figure 4.27, for temperatures from 250 ºC to 500 ºC. The dc resistivity ranged from ~10^6 Ω m to ~10^8 Ω m at 250 °C down to ~10^4 at 500 °C, which were higher by about ten times to the values of dc resistivities for the standard (1–x)BNT – xBCT (~ 10^7 – 10^6 Ω m) at 250 ºC) discussed in the early section 4.1.8 of this chapter.

The activation energies measured from linear fit of Arrhenius plots were 0.55 eV (x = 0), 0.64 eV (x = 0.05) and 0.61 eV (x = 0.1) , within expected error (~ 0.01), comparable to standard formulations.

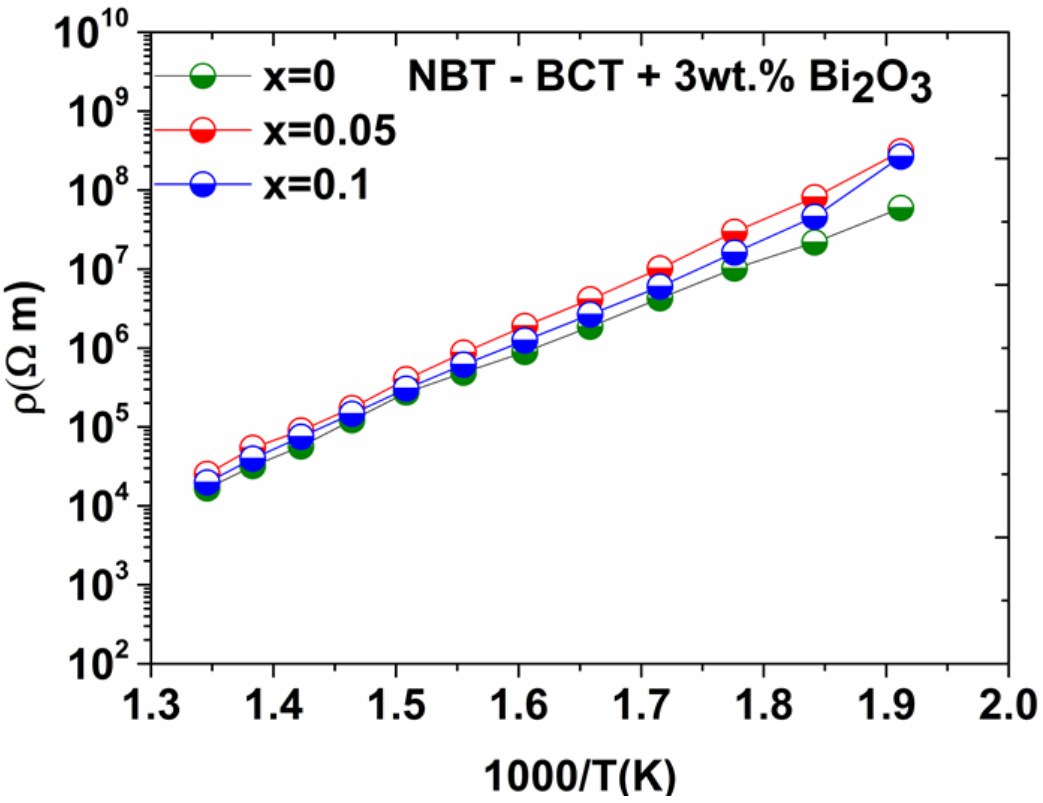

Figure 4.27 Resistivity as a function of inverse absolute temperature for (1–x)$Na_{0.5}Bi_{0.5}TiO_3$ – x$Ba_{0.8}Ca_{0.2}TiO_3$ + 3wt.% Bi_2O_3, x = 0 – 0.1.

4.2.8 Overall Conclusions

Ceramics in the system (1–x)NBT – xBCT and (1–x)NBT – xBCT + 3wt.% Bi_2O_3 were fabricated by mixed oxide route. The samples $x < 0.12$ displayed a single cubic phase, $0.12 \leq x \leq 0.2$ a mixed cubic + tetragonal phase and $x > 0.2$ a pure tetragonal phase at room temperature. The 3wt.% Bi_2O_3 excess has no remarkable effect on the crystal structure, except for slight promotion of mixed phase region into higher concentration level $x > 0.12$ to 0.2, in contrast to the standard ceramics for which $x > 0.1$ to 0.2.

The lattice parameters *a* and *c* increased linearly with x for both + (1–x)NBT – xBCT +3wt.% Bi_2O_3 and (1–x)NBT – xBCT ceramics, but the values of *c* for bismuth modified ceramics were slightly smaller than for standard ceramics. This might be attributed to either grain size effect or some strain phenomena.

For the modified ceramics the relative permittivity increased from ~ 2930 (x = 0) to to ~ 5970 (x = 0.1) and then started to decrease with increasing x for most samples, whereas, for standard ceramics ~ 2620 (x = 0) increased to 6420 (~ x = 0.12) and then decreased for most samples.

Typical relaxor like behaviour with frequency dispersion at T_m was observed in permittivity plots for (1– x)NBT – xBCT, x ~ 0.4 – 0.6. Plots were more typical of a ferroelectric with no relaxor transition for $x > 0.7$. The dielectric loss for (1–x)NBT – xBCT + 3wt.% Bi_2O_3 was lower than for standard ceramics at high temperature which might be due to compensation of oxygen vacancies by excess bismuth oxide. A high effective d_{33}^* ~ 720 pm/V was observed for modified sample x = 0.12, whereas 640 pm/V for x = 0.1 standard sample. The grain size was less (~ 1 – 2 μm) for the bismuth excess ceramics in contrast to the standard ceramics (~ 2 – 5 μm). A high dc resistivity ~10^8 Ω m at 250 $^{\circ}$C was observed for (1– x)NBT –

xBCT + 3wt.% Bi_2O_3 ceramics, whereas for standard this value was ~10^8 Ω m at 250 $^{\circ}$C.

Chapter 5

Study of the properties of $(1–x)[(Na_{0.5}Bi_{0.5}TiO_3)_{1-y} – (Ba_{0.8}Ca_{0.2}TiO_3)_y] – xBiMg_{0.5}Ti_{0.5}O_3$ ternary system

5.1 Introduction

This chapter is divided into three sections. In the first section, the dielectric, ferroelectric and microstructural properties of standard ceramic compositions system $(1–x)[0.85Na_{0.5}Bi_{0.5}TiO_3 – 0.15Ba_{0.8}Ca_{0.2}TiO_3] – xBiMg_{0.5}Ti_{0.5}O_3$ ($0 \leq x \leq 0.7$, $y = 0.15$), abbreviated as (1–x)[NBT – 15BCT] – xBMT, as synthesized by a mixed oxide route are reported.

X-ray powder diffraction analysis of crushed sintered ceramics has shown a perovskite single phase for samples, $x = 0 – 0.5$. Secondary phases of Bi_2O_3 appeared for, $x > 0.5$. The ceramic compositions, $x > 0.05$ were consistent with cubic/pseudocubic symmetry, whereas the base composition $x = 0$ ($0.85NBT – 0.15BCT$) (as reported in chapter 4) and $x = 0.05$, lies in the vicinity of mixed phase region between tetragonal BCT and cubic/pseudocubic NBT phases at room temperature.

The base composition $0.85Na_{0.5}Bi_{0.5}TiO_3 – 0.15Ba_{0.8}Ca_{0.2}TiO_3$ was selected from mixed tetragonal + cubic phases region, with a view to develop novel materials with relatively good dielectric and piezoelectric properties in analogy to the properties reported for other modified mixed phase region ceramics, for example $Na_{0.5}Bi_{0.5}TiO_3 – BaTiO_3 – K_{0.5}Bi_{0.5}TiO_3$, $Na_{0.5}Bi_{0.5}TiO_3 – K_{0.5}Bi_{0.5}TiO_3$-$K_{0.5}Na_{0.5}NbO_3$ and many more.

Relative permittivity-temperature plots have shown broad/diffuse dielectric peaks (at T_2) for the compositions $x \geq 0$, which increased in temperature with increasing x. Lower temperature inflection in $\varepsilon_r(T)$ with strong frequency dispersions at ≤ 10 kHz was observed at T_1 ~ 100 ºC (x = 0.05), T_1 ~ 70 ºC (x = 0.1) and T_1 ~ 60 ºC (x = 0.2). Maximum relative permittivity decreased from ~ 4040 (x = 0.05) to ~1060 (x = 0.5.

Sample composition x = 0.3 was a normal relaxor, whereas samples x > 0.3 were temperature-stable relaxors.

Temperature-stable relative permittivity was observed for sample, x = 0.3, 1720 ± 15 %, in the temperature range 120 – 450 ºC+ and $\tan\delta \leq 0.02$ in the temperature range 150 ºC to 360 ºC.

No evidence of domain switching was observed from the P-E loops for samples x > 0. The maximum bipolar strain (S ~ 0.11 %) was observed for the composition x = 0.1. SEM micrographs have shown grain sizes ~ 3 – 7 μm.

The weight percent contribution of each precursor of the ceramics system $(1–x)\ [0.85Na_{0.5}Bi_{0.5}TiO_3 – 0.15Ba_{0.8}Ca_{0.2}TiO_3] – xBiMg_{0.5}Ti_{0.5}O_3$ are presented in Table 5.1.

Table 5.1 Calculated wt.% of each precursor in (1–x)[0.85 $Na_{0.5}Bi_{0.5}TiO_3$ – 0.15$Ba_{0.8}Ca_{0.2}TiO_3$] – x$BiMg_{0.5}Ti_{0.5}O_3$ ceramics system.

precursors	x = 0.05	x = 0.1	x = 0.2	x = 0.3	x = 0.4	x = 0.5	x = 0.6
Bi_2O_3	78.08	76.63	73.62	70.47	67.17	63.70	60.06
Na_2CO_3	0.39	0.77	1.61	2.47	3.37	4.32	5.32
$BaCO_3$	0.41	0.83	1.69	2.60	3.55	4.54	5.60
$CaCO_3$	0.05	0.10	0.21	0.33	0.45	0.58	0.71
TiO_2	14.547	15.33	17.11	18.98	20.93	22.99	25.15
MgO	6.61	6.33	5.76	5.16	4.53	3.87	3.17

5.1.1 X-ray examination

X-ray powder diffraction patterns of crushed sintered pellets of ceramic series (1–x)[0.85$Na_{0.5}Bi_{0.5}TiO_3$ – 0.15$Ba_{0.8}Ca_{0.2}TiO_3$] – x$BiMg_{0.5}Ti_{0.5}O_3$ ($0 \leq x \leq 0.7$), revealed mixed type cubic/pseudocubic + tetragonal phases for, x = 0, (0.85NBT – 0.15BCT), and 0.05, whereas samples, x > 0.05 were consistent with a perovskite cubic/pseudocubic structure, Figure 5.1a - b. Secondary peaks of similar d-spacing to Bi_2O_3 began to appear at $x \geq 0.6$. (ICDD 04-015-6853) along with some unidentified phases. This might be due to incomplete solid-state reaction, or because the true solid-solution formula deviates from the prepared formulation or because the solid solution limit is x ~ 0.5.

Figure 5.2, Illustrates a segment of the pseudo-ternary phase diagram of (1–x)[0.85$Na_{0.5}Bi_{0.5}TiO_3$ – 0.15$Ba_{0.8}Ca_{0.2}TiO_3$] – x$BiMg_{0.5}Ti_{0.5}O_3$ ($0 \leq x \leq 0.7$) system, showing the locations of the studied compositions. All the studied compositions are the derivatives of the base composition 0.85$Na_{0.5}Bi_{0.5}TiO_3$ – 0.15$Ba_{0.8}Ca_{0.2}TiO_3$.,

which lies in the vicinity of the MPB between tetragonal BCT and cubic/ pseudocubic NBT end members,(as discussed in chapter 4).

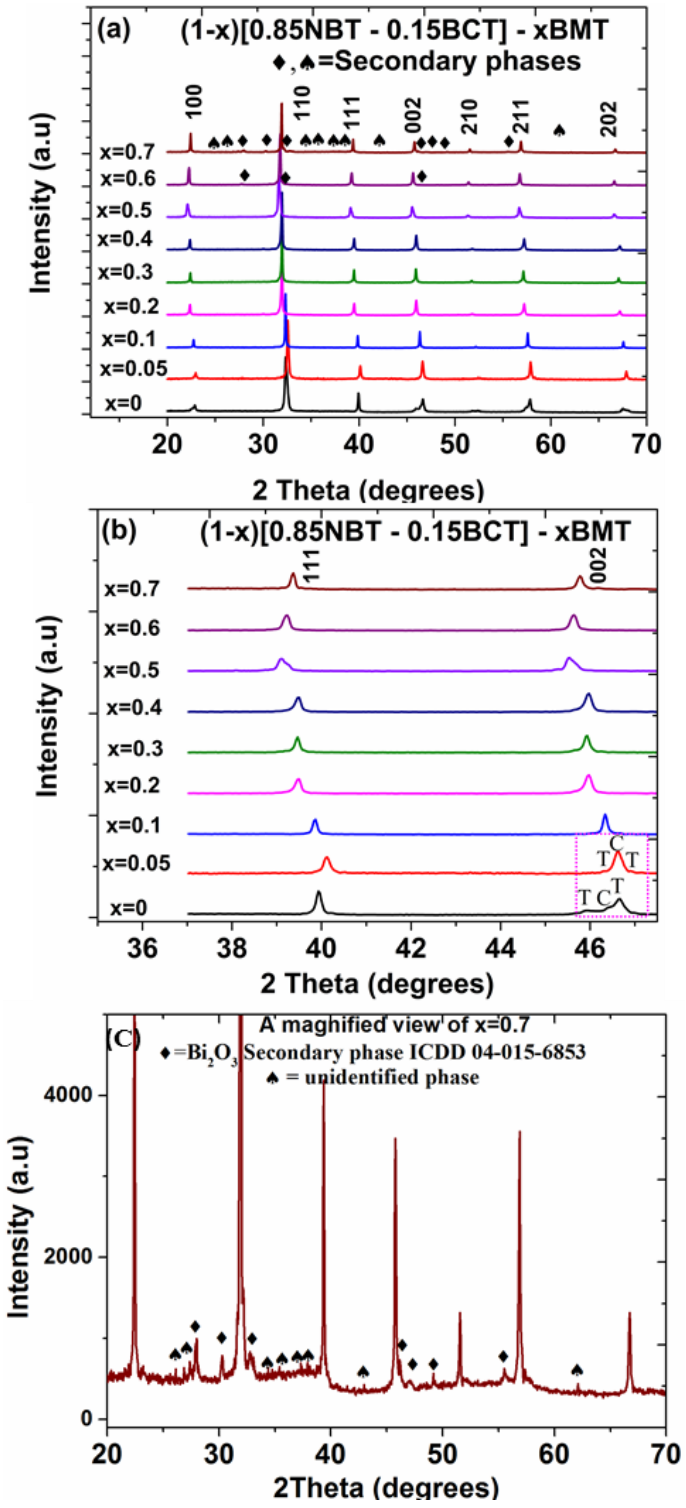

Figure 5.1(a) XRD patterns of (1–x)[0.85 $Na_{0.5}Bi_{0.5}TiO_3$ – 0.15$Ba_{0.8}Ca_{0.2}TiO_3$] – x$BiMg_{0.5}Ti_{0.5}O_3$, ($0 \leq x \leq 0.7$) and (b) a zoomed view of 111, 002/200 peaks (T = tetragonal, C = cubic) (c) A magnified view of XRD pattern of x = 0.7, showing secondary phases.

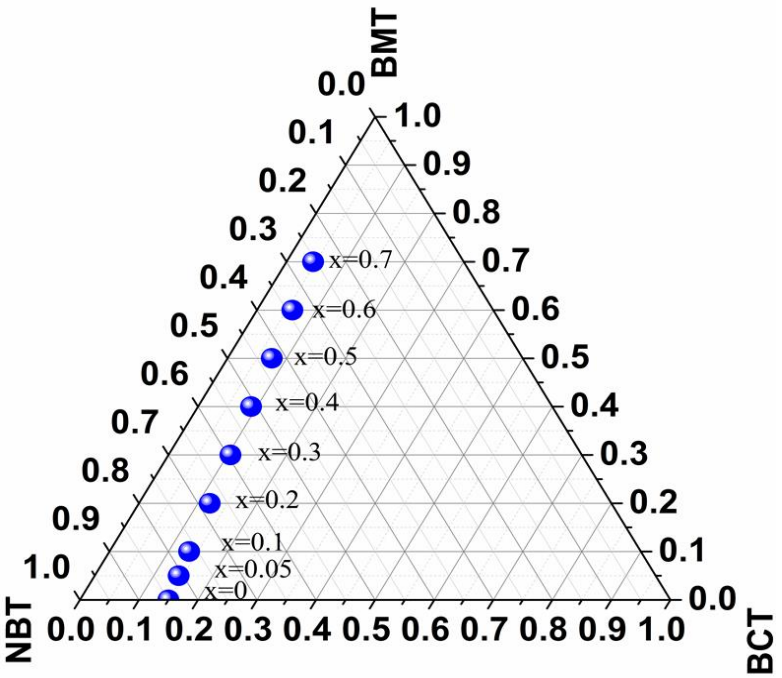

Figure 5.2 Illustration of the location of compositions (1–x)[0.85$Na_{0.5}Bi_{0.5}TiO_3$ – 0.15$Ba_{0.8}Ca_{0.2}TiO_3$] – x$BiMg_{0.5}Ti_{0.5}O_3$, ($0 \leq x \leq 0.7$) in the ternary system.

5.1.2 Dielectric analysis

Plots of temperature-dependent relative permittivity (ε_r), and tanδ, from ambient temperature to 450 °C (1 kHz – 1 MHz), have shown a broad dielectric peak at temperature T_2 with discontinuity at lower temperature T_1. The lower temperature hump/shoulder with strong frequency dispersion for ≤ 10 kHz were detected at T_1 ~ 100 ºC (x = 0.05), T_1 ~ 70 ºC (x = 0.1) and T_1 ~ 60 ºC (x = 0.2), Figure 5.3 - 5.4. Similar type lower temperature inflections were observed in other NBT-based ceramics, (Xu et al., 2015, Wang et al., 2005a), and also in our (1–x)NBT – xBCT ceramics as discussed in chapter 4.

A shift of the lower anomaly at temperature T_1 was observed towards lower temperature, whereas the dielectric maxima at T_2 shifted towards higher temperature as x increased, $x \leq 0.2$, Figure 5.5. The lower anomaly at T_1 disappeared at $x \geq 0.3$, converging into plateau giving temperature-stable permittivity over a wide range.

Maximum relative permittivity decreased from ~ 4040 (x = 0.05) to ~ 1060 (x = 0.5), whereas its corresponding temperature T_m/T_2 increased from 270 ºC (x = 0.05) to 290 ºC (x = 0.2) and then decreased to 220 ºC (x > 0.3), Figure 5.3-5.4.

Ceramics $x \geq 0.3$ have a wide operating temperature range spanning ~ 450 ºC+ with ±15 % variation in relative permittivity at 1 kHz. The variations in relative permittivity at 1 kHz, with ± tolerance were calculated using formula $\Delta\varepsilon/\varepsilon_{mid}$, [$\Delta\varepsilon = \varepsilon_{max} - \varepsilon_{mid} = \varepsilon_{min} - \varepsilon_{mid}$, $\varepsilon_{mid} = (\varepsilon_{max} + \varepsilon_{min})/2$, ε_{max} and ε_{min} is the ± deviation from ε_{mid}], Table 5.2.

Temperature-stable relative permittivity observed for sample, x = 0.3, ε_r ~ 1720 ± 15 %, in the temperature- range 120 – 450 ºC+ and $\tan\delta \leq 0.02$, temperature–range, 150 – 360 ºC. For x = 0.4, ε_r ~ 940 ± 15 %, in temperature–range 120 – 450 ºC+ and $\tan\delta \leq 0.02$ temperature –range 130 – 350 ºC and. For x = 0.5, ε_r ~ 930 ± 15 %, in temperature–range, 125 – 400 ºC and $\tan\delta \leq 0.02$, temperature–range 140 – 320 ºC.

This small difference in relative permittivity over a wide operational range is a notable feature since Electronic Industries Alliance (EIA) permits ±15 % deviations for commercially available X7R – X9R (-55 – 200 ºC) capacitors, which are designated for high temperature applications. Similar type of temperature-stable permittivity plateaus were observed in $Na_{0.5}Bi_{0.5}TiO_3$ – $NaNbO_3$, $BaTiO_3$ – $BiMg_{0.5}Ti_{0.5}O_3$, $BiZn_{0.5}Ti_{0.5}O_3$ – $BiMg_{0.5}Ti_{0.5}O_3$, $BiScO_3$ – $BiZn_{0.5}Ti_{0.5}O_3$ and $BaTiO_3$ – $BiZn_{0.5}Ti_{0.5}O_3$ – $BiScO_3$ (Xu et al., 2015, Xiong et al., 2011, Huang et al., 2007, Huang and Cann, 2008, Raengthon et al., 2012).

The dielectric loss (tanδ) increased at high temperature with increasing x, Figure 5.6. The samples x > 0.5 presented higher losses in contrast to $x \leq 0.5$, which

might be attributed to the presence of secondary phases. This factor plus the tanδ peak at $T \sim T_1$ gave a restricted temperature range of low $\tan\delta \leq 0.02$ Table 5.2.

A typical relaxor character with broad relative permittivity peak was observed for, $x = 0.3$, whereas samples $x > 0.3$ were temperature stable relaxors. Relative permittivity peak with the frequency dispersion at $T \leq T_m$, is one of the common feature of relaxor ferroelectrics (Tang et al., 2004). Also no frequency dispersion was observed at T_m, which might be attributed to paraelectric-relaxor phase transition. Recently it has been proposed for $Na_{0.5}Bi_{0.5}TiO_3 – BaTiO_3$ system that T_m is related to the relaxation of tetragonal polar nanoregions (PNRs) emerged from rhombohedral polar nanoregions (Shi et al., 2014, Jo et al., 2011). The increase in diffuse peak with increasing content of BMT might be attributed to the cations disordering on lattice sites. Similar diffuse phase peak was also observed in other NBT-based ceramics (Dittmer et al., 2011b, Dittmer et al., 2012, Dittmer et al., 2011a).

Summary of the dielectric properties of the ceramics is presented in Table 5.2.

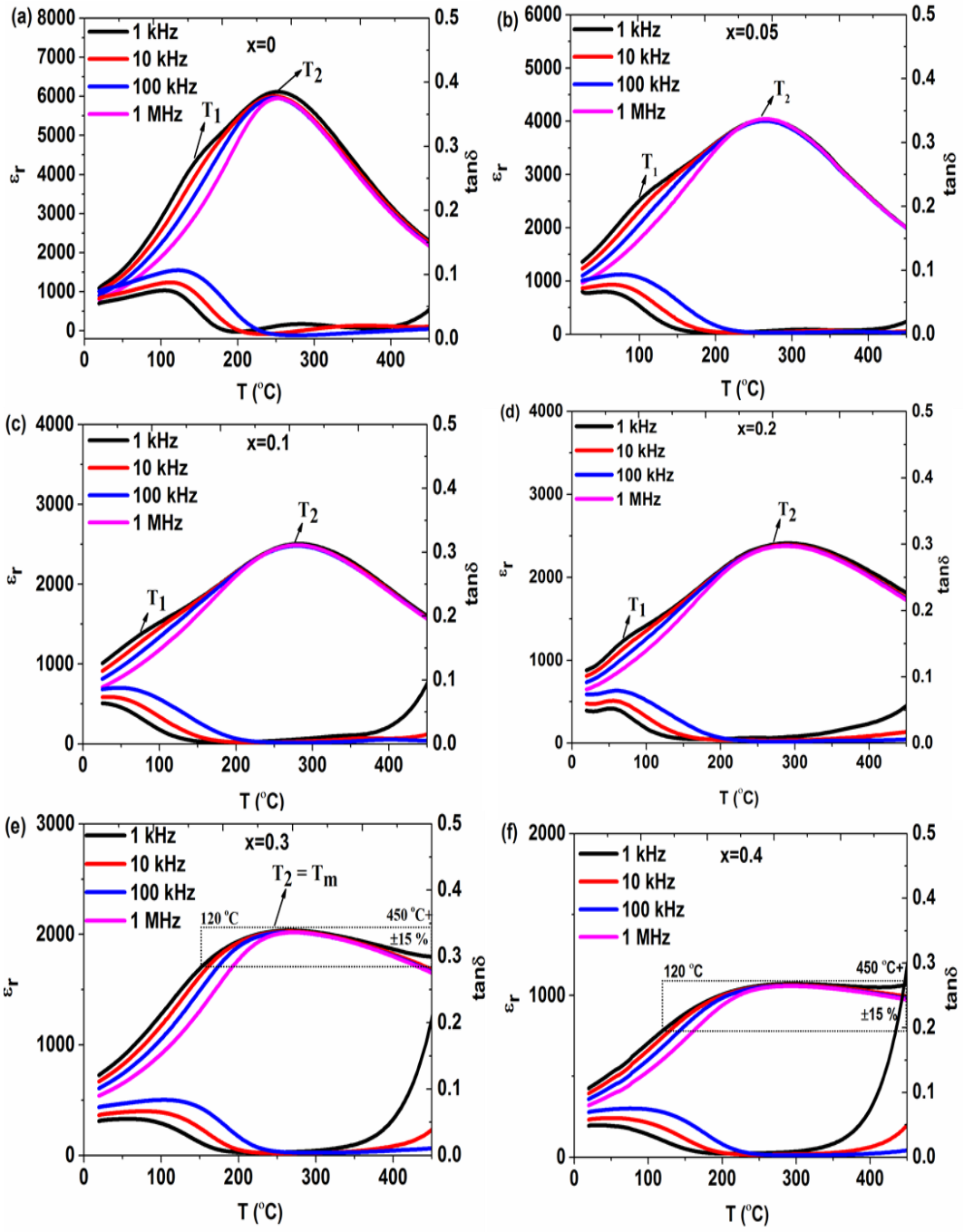

Figure 5.3 Temperature-dependant relative permittivity (ε_r) and loss tangent (tanδ) of ceramics $(1–x)[0.85Na_{0.5}Bi_{0.5}TiO_3 – 0.15Ba_{0.8}Ca_{0.2}TiO_3] – xBiMg_{0.5}Ti_{0.5}O_3$, (a) x = 0 (b) x = 0.05 (c) x = 0.1(d) x = 0.2 (e) x = 0.3 (f) x = 0.4 (data set continued in Figure 5.4)

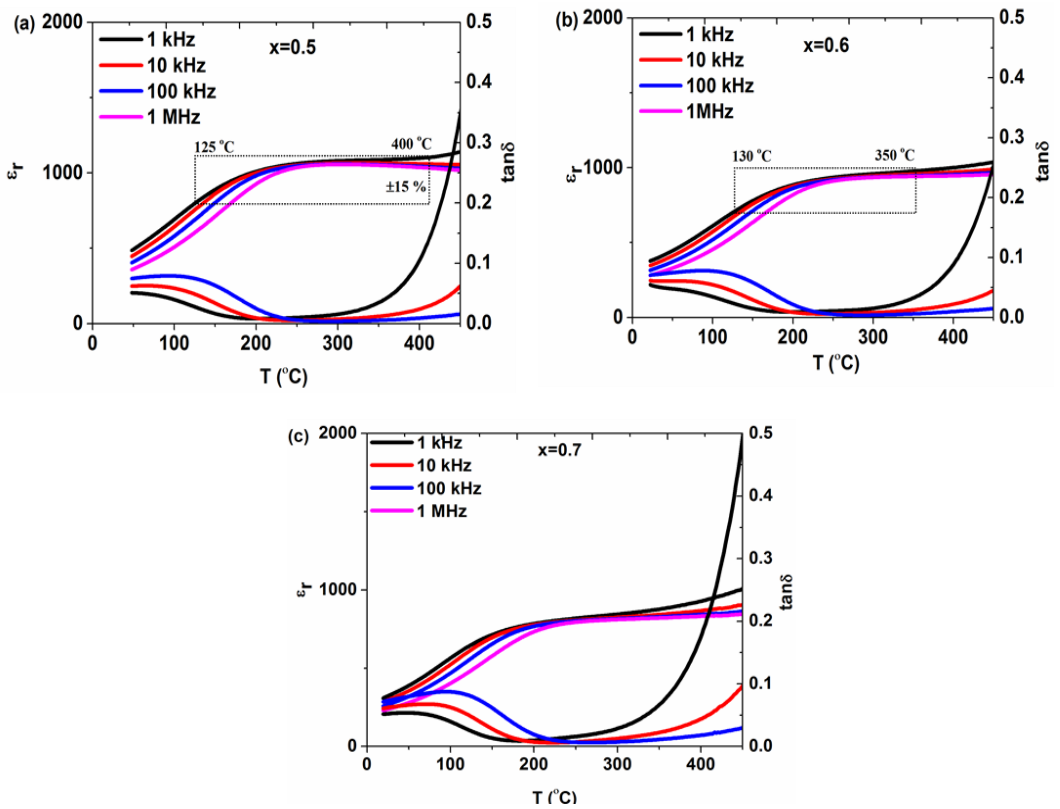

Figure 5.4 Temperature-dependant relative permittivity (ε_r) and loss tangent (tanδ) of ceramics (1–x)[0.85$Na_{0.5}Bi_{0.5}TiO_3$ – 0.15$Ba_{0.8}Ca_{0.2}TiO_3$] – x$BiMg_{0.5}Ti_{0.5}O_3$, (a) x = 0.5 (b) x = 0.6 (c) x = 0.7.

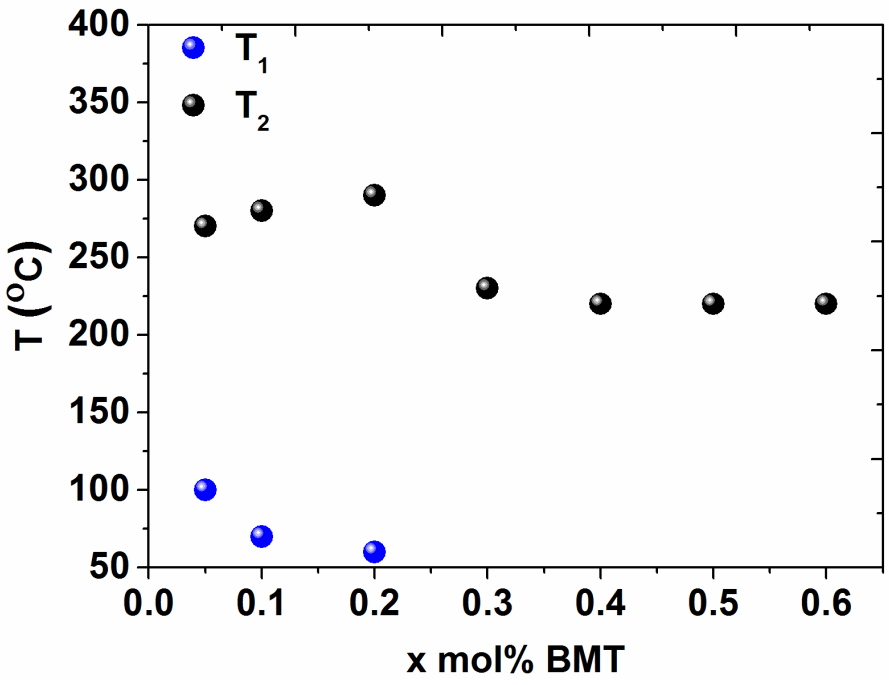

Figure 5.5 Plots of temperatures corresponding to low temperature (T_1) and high temperature (T_2) dielectric anomalies (1–x)[0.85$Na_{0.5}Bi_{0.5}TiO_3$ – 0.15$Ba_{0.8}Ca_{0.2}TiO_3$] – x$BiMg_{0.5}Ti_{0.5}O_3$, x = 0 – 0.7 (1 kHz).

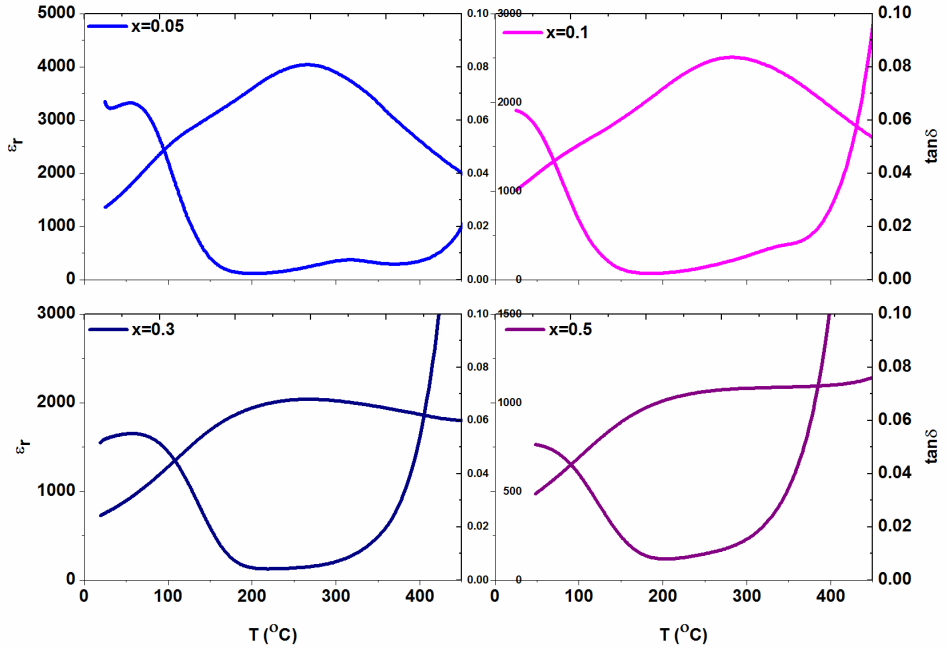

Figure 5.6 Temperature-dependant relative permittivity (ε_r) and loss tangent (tanδ) of ceramics (1–x)[0.85$Na_{0.5}Bi_{0.5}TiO_3$ – 0.15$Ba_{0.8}Ca_{0.2}TiO_3$] – x$BiMg_{0.5}Ti_{0.5}O_3$, x = 0.05 – 0.5 (1 kHz).

Table 5.2 Dielectric properties of (1–x)[0.85$Na_{0.5}Bi_{0.5}TiO_3$ – 0.15$Ba_{0.8}Ca_{0.2}TiO_3$] – x$BiMg_{0.5}Ti_{0.5}O_3$, (0 ≤ x ≤ 0.7) system.

Sample (x)	ε_{max} (1kHz)	T_1 (°C)	T_2 (°C) (1kHz)	ε_{mid} (1kHz)	ε_{mid}±15% (1kHz) T-range (°C)	tanδ ≤0.02 (1kHz) T-rage (°C)
x = 0	6120	240	330	------	------	-------
x = 0.05	4040	100	270	------	-------	130 – 430
x = 0.1	2510	70	280	------	-------	100 – 390
x = 0.2	2430	60	290	------	-------	100 – 430
x = 0.3	1980	-----	230	1720	120 – 450	150 – 360
x = 0.4	1070	-----	220	940	120 – 450	130 – 350
x = 0.5	1060	-----	220	930	125 – 400	140 – 320
x = 0.6	960	-----	220	830	130 – 350	130 – 320

5.1.3 Ferroelectric and piezoelectric measurements

Polarization–electric field hysteresis loops measured at room temperature (1 Hz) for ceramics compositions $0 \leq x \leq 0.5$ is shown in Figure 5.7. The composition x = 0, (0.85NBT – 0.15BCT) (as discussed in chapter 4), displayed a typical ferroelectric hysteresis loop. The sample x = 0, (0.85NBT – 0.15BCT), exhibited a maximum polarization ~ 32 μC/cm^2 (at ~ 40kV/cm), remnant polarization P_r ~ 26 μC/cm^2 and maximum bipolar strain (S ~ 0.18%) (as discussed in Chapter 4).

Both coercive field (E_C) and remnant polarization (P_r) decreased for x > 0; resulting in the slim P-E loops. Similar type of slim loops were observed in other lead-free dielectrics. Examples include (Sr,Na,Bi)TiO_3, $Na_{0.5}Bi_{0.5}TiO_3$ – $KNbO_3$ – $SrTiO_3$, $Na_{0.5}Bi_{0.5}TiO_3$ – $BaTiO_3$ – $SrTiO_3$ (Bai et al., 2015, Xu et al., 2015, Shi et al., 2014, Ang and Yu, 2006).

S-E hysteresis loops undergo a strong deviation from typical ferroelectrics with maximum strain values were ~ 0.04 – 0.11 %, Figure 5.8. The samples, x > 0, showed only electrostriction. From the study of the early literature, large electrostriction effect might be attributed to either ferroelectric material just above their Curie temperatures due to reinforcement of unstable ferroelectric phase by the electric field or relaxor ferroelectrics having phase transition temperature close to room temperature(Haertling, 1999).

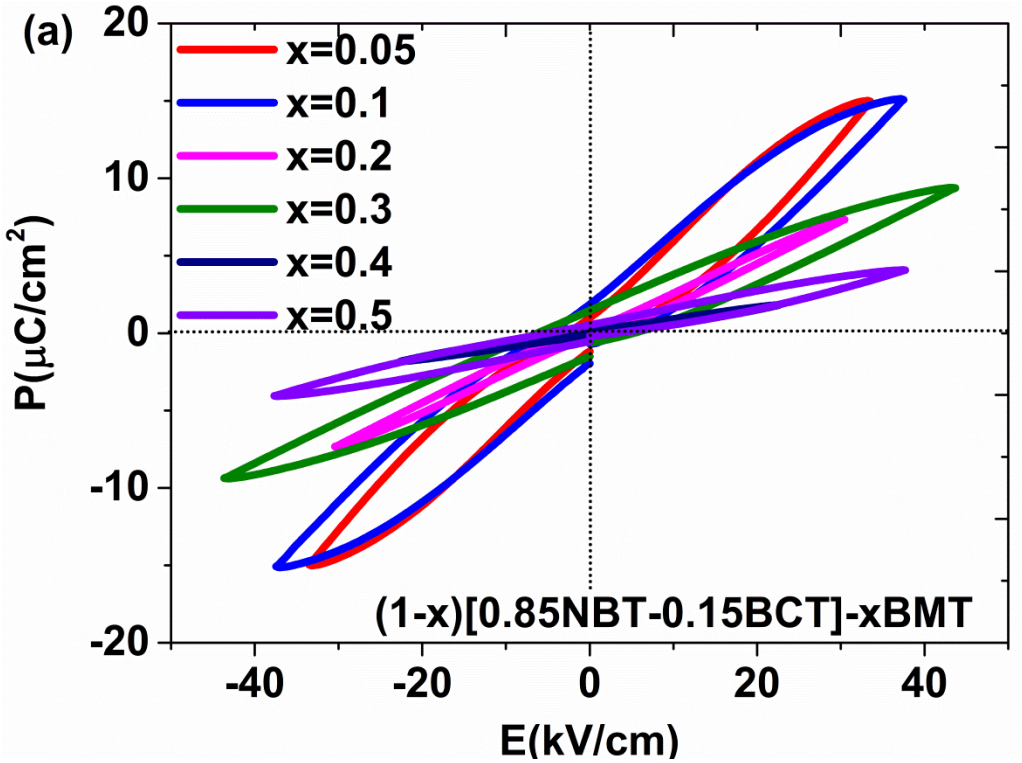

Figure 5.7 P-E hysteresis loop of (1–x)[0.85$Na_{0.5}Bi_{0.5}TiO_3$ – 0.15$Ba_{0.8}Ca_{0.2}TiO_3$] – x$BiMg_{0.5}Ti_{0.5}O_3$, x = 0.05 – 0.5.

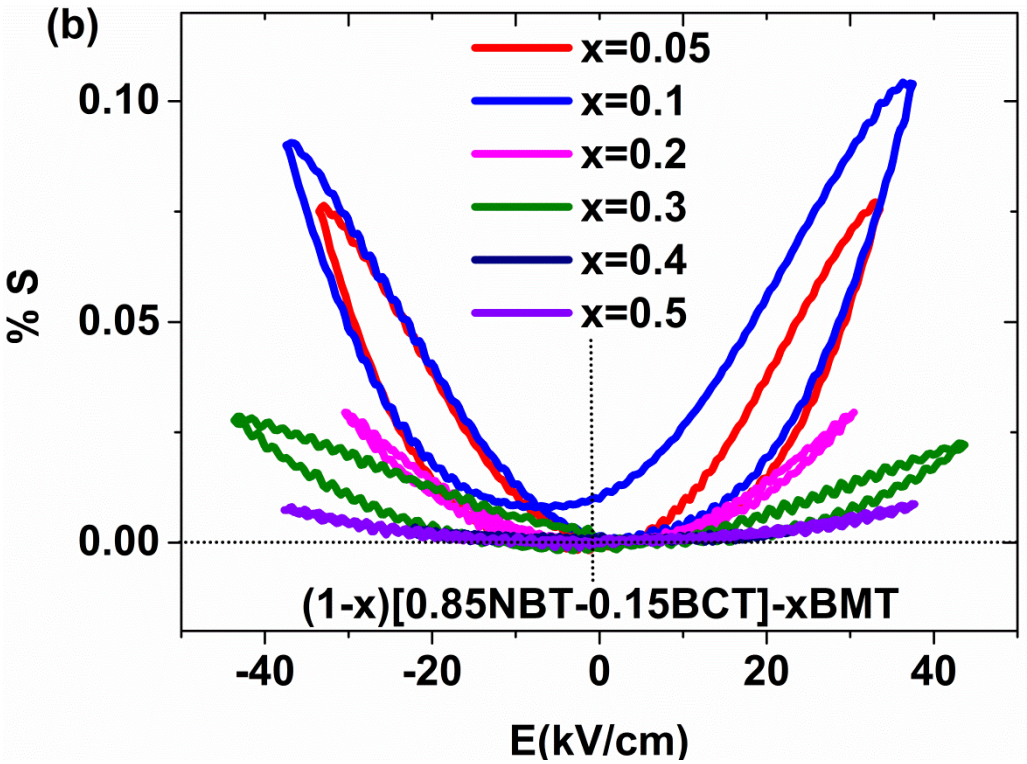

Figure 5.8 S-E hysteresis loop of (1–x)[0.85$Na_{0.5}Bi_{0.5}TiO_3$ – 0.15$Ba_{0.8}Ca_{0.2}TiO_3$] – x$BiMg_{0.5}Ti_{0.5}O_3$, x = 0.05 – 0.5.

5.1.4 Microstructural study

Microstructures of selected thermally etched polished samples x = 0.3, 0.4, 0.5 is shown in Figure 5.9. The grain sizes were in the range of ~ 3 – 7 μm. No significant difference in the grain morphology and grain size was observed. The geometrical densities of the ceramics increased with increasing x, Figure 5.10. The geometrical densities were in the range of ~ 5.5 – 6.2 g/cm^2 (~ 92 – 97 % of theoretical density).

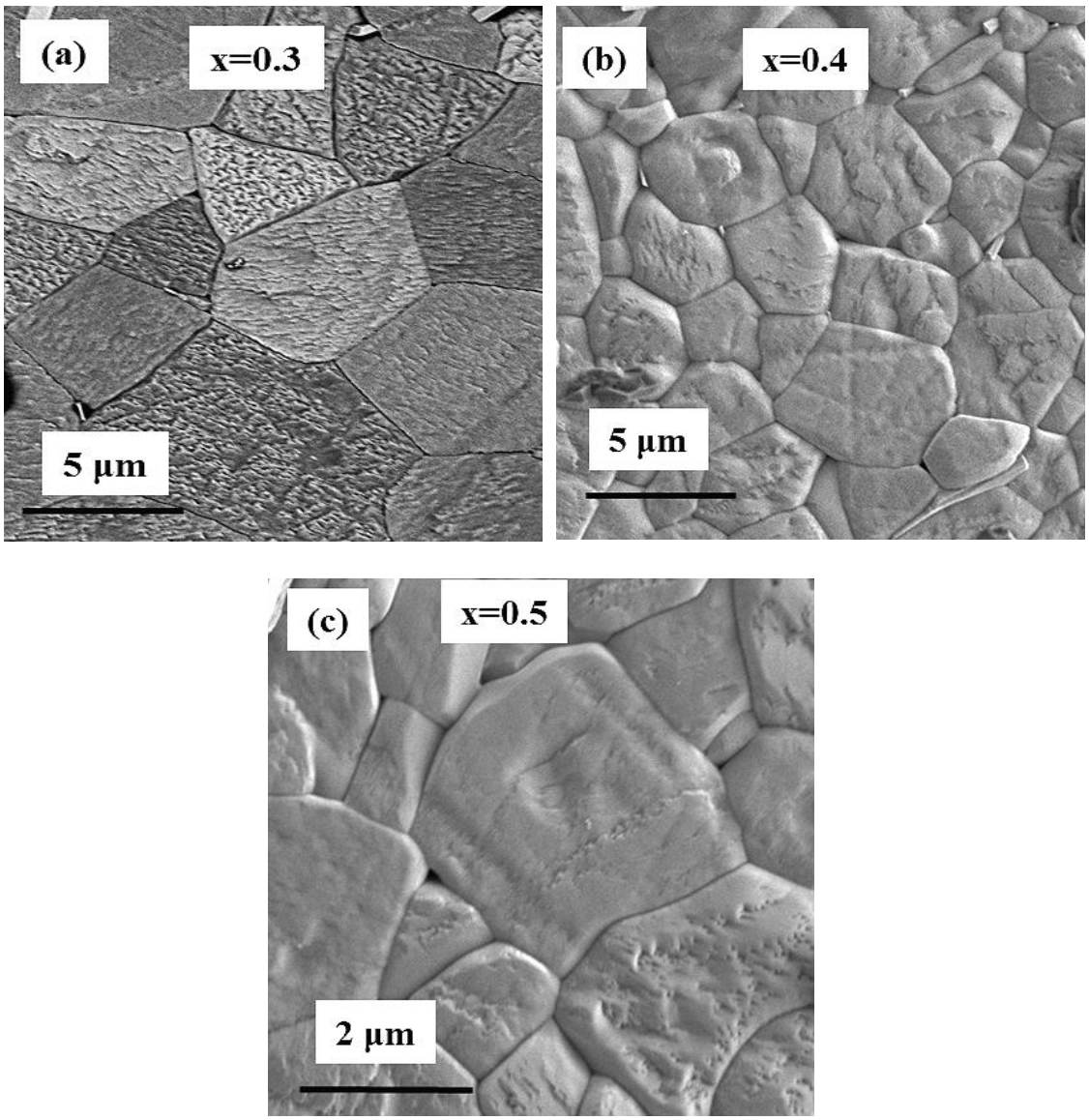

Figure 5.9 SEM images of (1–x)[0.85$Na_{0.5}Bi_{0.5}TiO_3$ – 0.15$Ba_{0.8}Ca_{0.2}TiO_3$] – x$BiMg_{0.5}Ti_{0.5}O_3$, (a) x = 0.3, (b) x = 0.4 and (c) x = 0.5.

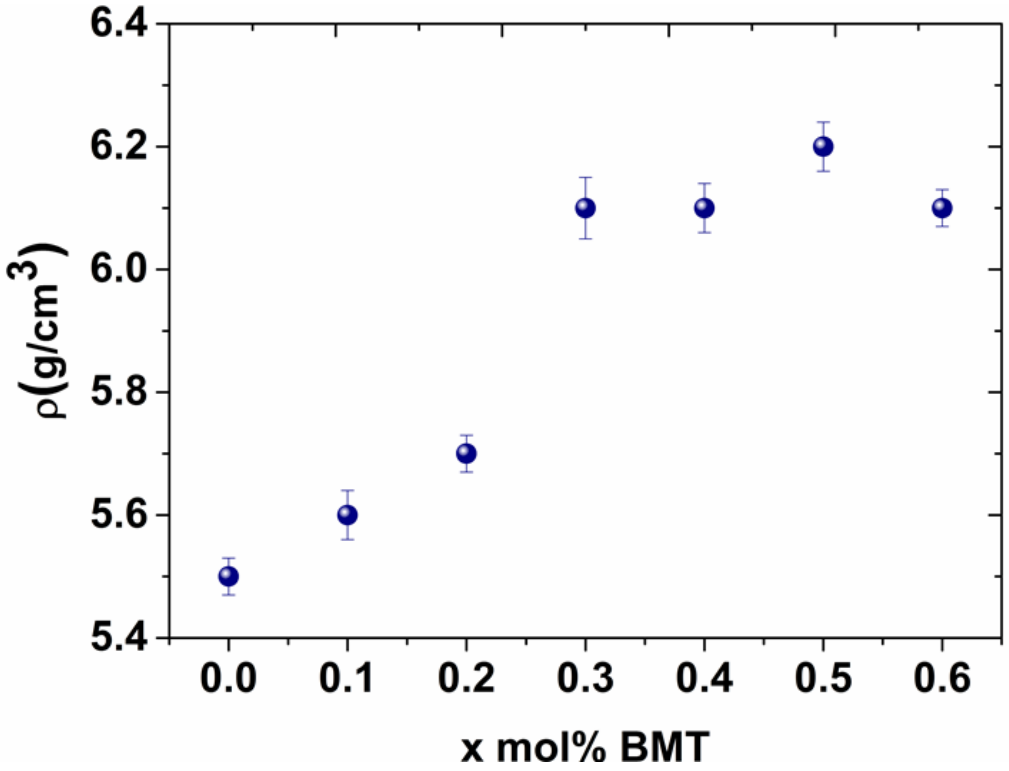

Fig 5.10. Absolute/geometrical densities of the ceramics(1–x)[0.85$Na_{0.5}Bi_{0.5}TiO_3$ – 0.15$Ba_{0.8}Ca_{0.2}TiO_3$] – x$BiMg_{0.5}Ti_{0.5}O_3$, $0 \leq x \leq 0.6$.

5.1.5 Conclusions:

The ceramics system $(1–x)[0.85Na_{0.5}Bi_{0.5}TiO_3 – 0.15Ba_{0.8}Ca_{0.2}TiO_3] – xBiMg_{0.5}Ti_{0.5}O_3$, $(0 \leq x \leq 0.7)$, manufactured by mixed oxide route were investigated for high temperature capacitor applications. Pure perovskite phase was observed for samples, $x = 0 – 0.5$. Compositions $(x > 0.05)$ have shown cubic or pseudocubic symmetry, whereas the compositions, $x = 0 – 0.05$ lies in the mixed phase region between tetragonal BCT and cubic/pseudocubic NBT at room temperature.

A broad dielectric peak with frequency dispersed lower hump was detected for the compositions, $x \leq 0.2$. The lower dielectric inflection shifted towards lower temperature with increasing x, $(x \leq 0.2)$, and disappeared at $x \geq 0.3$. A single broad/diffuse peak with frequency dispersion at $T \leq T_m$, for $x \geq 0.3$, indicate a typical relaxor character for the ceramics. Temperature-stable relative permittivity observed for samples, x = 0.3, 1720 ± 15 %, in the temperature range 120 – 450 ºC+ and $\tan\delta \leq 0.02$, T–range, 150 – 360 ºC.

P-E hysteresis loops have shown maximum polarization ~ 32 μC/cm^2 (40 kV/cm) and remnant polarization P_r ~ 26 μC/cm^2. From S-E loops, a maximum bipolar strain (S ~ 0.18%), was observed for the composition x = 0, (as discussed in chapter 4). No negative strain was observed for x > 0, indicating electrostrictive characteristic. SEM micrographs have shown no significant change in grain sizes and grain morphology with compositions.

5.2 Examination of the effects of 3wt.% Bi_2O_3 on (1–x)[0.85$Na_{0.5}Bi_{0.5}TiO_3$ – 0.15$Ba_{0.8}Ca_{0.2}TiO_3$] – x$BiMg_{0.5}Ti_{0.5}O_3$

In this second section of the chapter the dielectric properties of 3wt.% bismuth oxide excess (1–x)[0.85NBT – 0.15BCT] – xBMT ($0.3 \leq x \leq 0.6$) abriviated to 0.85NBT – 0.15BCT – xBMT + 3wt.% Bi_2O_3, ceramics compositions were studied.

Figure 5.11, shows room temperature X-ray powder diffraction patterns for the 0.85NBT – 0.15BCT – xBMT + 3wt.% Bi_2O_3 ($0.3 \leq x \leq 0.6$) ceramics. Single phase perovskite cubic/pseudocubic structure was evedinced for compositions $x \leq 0.5$, whereas secondary phases of Bi_2O_3 (ICDD 01-074-2351) appeared for $x \geq 0$. by analogy to the standard ceramics, Figure 5.1 and Figure 5.11. No significant change in the XRD patterns, was observed for bismuth modified and unmodified ceramics $x \geq 0.3$.

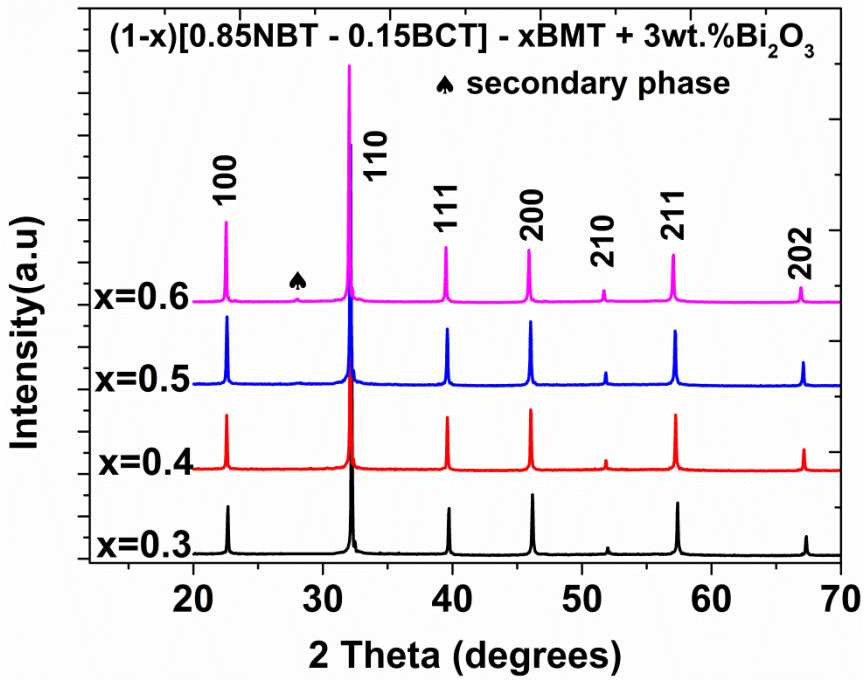

Figure 5.11 X-ray powder diffraction patterns of (1–x)[0.85$Na_{0.5}Bi_{0.5}TiO_3$ – 0.15$Ba_{0.8}Ca_{0.2}TiO_3$] – x$BiMg_{0.5}Ti_{0.5}O_3$ + 3wt.% Bi_2O_3 ($0.3 \leq x \leq 0.6$).

5.2.1 Relative permittivity

The incorporation of excess bismuth oxide slightly pushed the temperature-stable region of relative permittivity towards higher temperature gradients, in contrast to the standard ceramics Table 5.3. Relative permittivity decreased and tanδ increased at high temperatures with increasing x, in analogy to standard ceramics. However the values of maximum relative permittivity were higher and tanδ were lower (at T > 300 ºC) for the bismuth oxide modified ceramics, Figure 5.3 and Figure 5.12. Similar type of effects were observed by Simoes et al, and Zhou et al, (Simões et al., 2005, Zhou et al., 2013).

In addition, temperatures corresponding to the maximum relative permittivity for modified ceramics were slightly higer than for unmodified ceramics Table 5.3. Similar type of trends were observed for other bismuth oxide excess $BiFeO_3$ – $BaTiO_3$ ceramics (Zhou et al., 2013). Maximum dielectric temperature decreased with incorporation of $BiMg_{0.5}Ti_{0.5}O_3$, as observed in $Bi_{0.5}K_{0.5}TiO_3$ – $BaTiO_3$ ceramics (Chung et al., 2009).

Trends in maximum/room temperature relative permitivities and temperatures corresponding to the maximum dielectric permitivities are shown in Figure 5.13. A summary of the comparison of dielectric properties for the standard and 3 wt. % Bi_2O_3, 0.85NBT – 0.15BCT – xBMT ceramics is presented in Table 5.3.

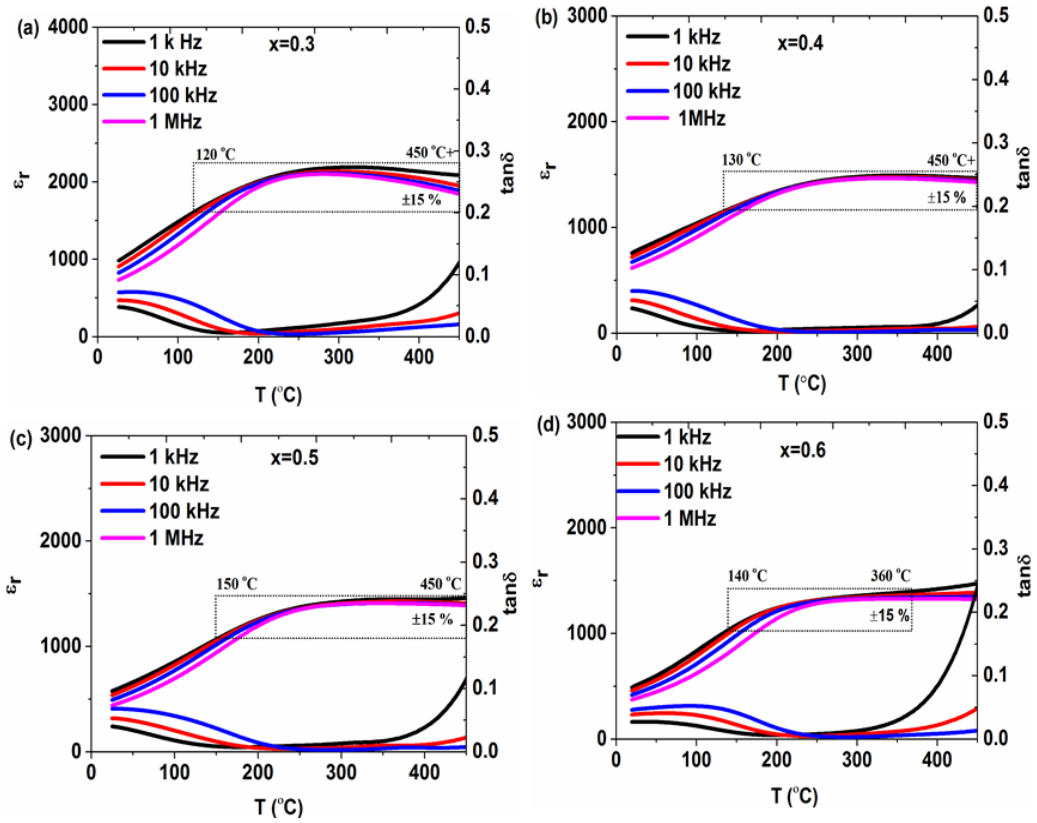

Figure 5.12 Temperature-dependent relative permittivity (ε_r) and loss tangent (tanδ) of (1–x)[0.85$Na_{0.5}Bi_{0.5}TiO_3$ – 0.15$Ba_{0.8}Ca_{0.2}TiO_3$] – x$BiMg_{0.5}Ti_{0.5}O_3$ + 3wt.% Bi_2O_3, (a) x = 0.3 (b) x = 0.4 (c) x = 0.5 and (d) x = 0.6.

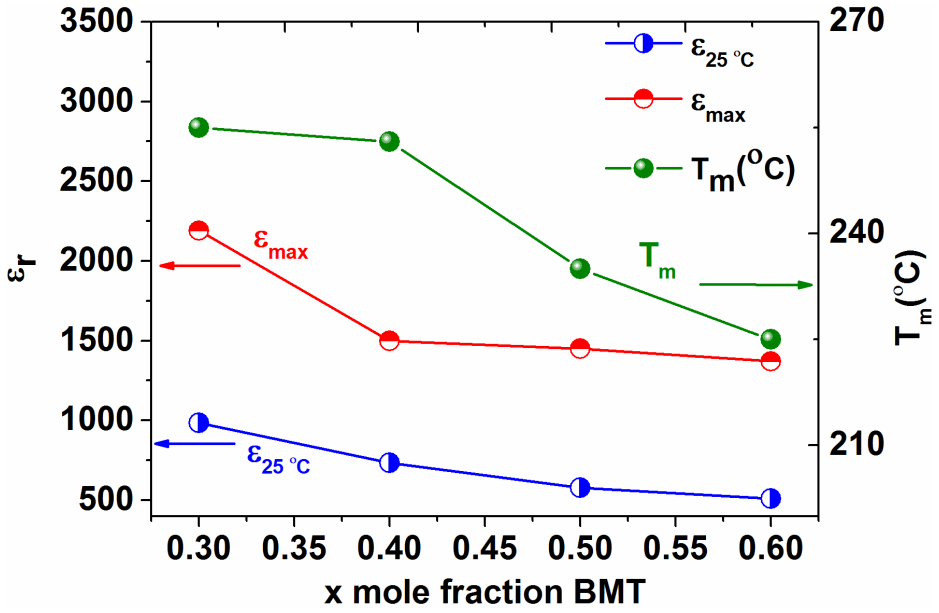

Figure 5.13 Maximum relative permittivity, room temperature relative permittivity and temperature of maximum relative permittivity versus mol fraction $BiMg_{0.5}Ti_{0.5}O_3$, of ceramics, (1–x)[0.85$Na_{0.5}Bi_{0.5}TiO_3$ – 0.15$Ba_{0.8}Ca_{0.2}TiO_3$] – x$BiMg_{0.5}Ti_{0.5}O_3$ + 3wt.% Bi_2O_3 (x = 0.3 – 0.6).

Table 5.3 Comparison of dielectric properties of unmodified and 3wt.% Bi_2O_3-modified $(1–x)[0.85Na_{0.5}Bi_{0.5}TiO_3 – 0.15Ba_{0.8}Ca_{0.2}TiO_3] – xBiMg_{0.5}Ti_{0.5}O_3$ ceramics.

Sample	T_m (ºC)		ε_{max}		ε_{mid} ± 15 % and (T ºC -range) (1kHz)	
x	**unmodified**	**modified**	**unmodified**	**modified**	**unmodified**	**modified**
0.3	230	255	1980	2200	120 – 450 (1720 ± 15)	120 – 450 (1900 ±15)
0.4	220	250	1070	1480	120 – 450 (940 ± 15)	130 – 450 (1300 ±15)
0.5	220	240	1060	1430	125 – 400 (930 ± 15)	150 –450 (1240 ±15)
0.6	220	230	960	1360	130 – 350 (830 ± 15)	140 – 360 (1180 ±15)

5.2.2 Conclusions from 3wt.% Bi_2O_3 modified ceramics

Ceramic compositions $(1–x)[0.85Na_{0.5}Bi_{0.5}TiO_3 – 0.15Ba_{0.8}Ca_{0.2}TiO_3] – xBiMg_{0.5}Ti_{0.5}O_3$ ($0.3 \leq x \leq 0.6$) with no bismuth oxide excess and 3wt.% Bi_2O_3 were prepared by conventional ball milling tecnique.

XRD patterns of standard ceramics revealed a mixed Tetragonal + Cubic/Pseudocubic phases for x = 0 – 0.05 and a cubic/pseudocubic phase for x > 0.05, whereas a cubic/pseudocubic phase for 3wt.% Bi_2O_3-modified ceramics ($x \geq 0.3$).

Maximum relative permittivity decreased, whereas the the loss factor tanδ at higher temperatures increased with increasing x, for standard and Bi_2O_3-modified 85NBT – 15BCT – xBMT samples ($x \geq 0.3$). However the values of maximum relative permittivity for the Bi_2O_3-modified ceramics were higher and tanδ were lower at higher temperatures, in contrast to the standard ceramics. The temperatures corresponding to maximum relative permittivity T_m, for bismuth oxide modified ceramics were higher than for the unmodified ceramics ($x \geq 0.3$). The temperature gradient of stable-relative permittivity (ε_{mid} ± 15 %) for Bi_2O_3-modified compositions were shifted slightly towads higher temperature regions, in contrast to the standard ceramics. Temperature-stable permittivity (at 1 kHz) observed for samples , x = 0.3, 1900 ± 15 % in the temperature-range 120 – 450 ºC+ and $tan\delta \leq 0.02$, temperature-range, 100 – 300 ºC, x = 0.4, 1300 ± 15 % in the temperature-range 130 – 450 ºC+ and $tan\delta \leq 0.02$, temperature-range, 70 – 420 ºC, x = 0.5, 1250 ± 15 % in the temperature-range 150 – 450 ºC+ and $tan\delta \leq 0.02$, temperature-range, 90 – 370 ºC, and x = 0.6, 1180 ± 15 % in the temperature-range 140 – 360 ºC+ and $tan\delta \leq 0.02$, temperature-range, 100 – 320 ºC

5.3 Examination of $(1–x)[(Na_{0.5}Bi_{0.5}TiO_3)_{1-y} – (Ba_{0.8}Ca_{0.2}TiO_3)_y] – xBiMg_{0.5}Ti_{0.5}O_3$

The third section of this chapter examines the lead-free ceramics composition $(1–x)[(Na_{0.5}Bi_{0.5}TiO_3)_{1-y} – (Ba_{0.8}Ca_{0.2}TiO_3)_y] – xB_{0.5}Mg_{0.5}TiO_3$ [(x,y) = (0.4, 0.05), (0.3, 0.3), (0.4, 0.3), (0.4, 0.4)]. The aim of this study is to investigate, any change in relative permitivity and temperature gradients of stable-relative permittivity varying by no more than ±15 % using different concentrations of BCT (y) and BMT (x). These compositions were chosen from the base compositions (1–y)NBT – yBCT ($0 \leq y \leq 1.0$), as discussed in chapter 4.

5.3.1 X-ray powder diffraction examination

Figure 5.14, shows the room temperature perovskite XRD patterns of crushed sintered pellets of $(1–x)[(Na_{0.5}Bi_{0.5}TiO_3)_{1-y} – (Ba_{0.8}Ca_{0.2}TiO_3)_y] – xBMg_{0.5}Ti_{0.5}O_3$ [(x,y) = (0.4, 0.05), (0.3, 0.3), (0.4, 0.3), (0.4, 0.4). The compositions (x, y) > 0 appeared cubic/pseudocubic with no detection of secondary phases.

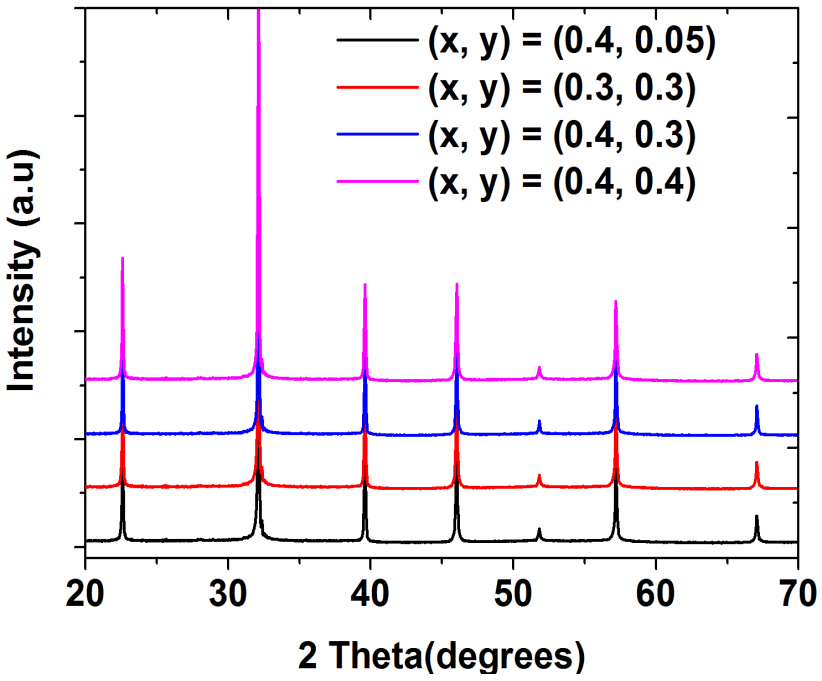

Figure 5.14 X-ray diffraction patterns of, $(1–x)[(Na_{0.5}Bi_{0.5}TiO_3)_{1-y} – (Ba_{0.8}Ca_{0.2}TiO_3)_y] – xBMg_{0.5}Ti_{0.5}O_3$ [(x,y) = (0.4, 0.05), (0.4, 0.3), (0.4, 0.3), (0.4, 0.4)].

5.3.2 Relative permittivity analysis

Examination of relative permittivity and loss tangent as a function of temperature are displayed in Figure 5.15, for number of frequencies (1 kHz – 1 MHz) over a temperature range 25 – 450 ºC.

The maximum relative permittivity observed for samples, (x, y = 0.4, 0.05), ε_{max} ~1680. For (x, y = 0.3, 0.3), ε_{max} ~ 1760. For (x, y = 0.4, 0.3), ε_{max} ~ 1570 and. For (x, y = 0.4, 0.4). ε_{max} ~ 1100. Lower losses were observed at high temperatures for (x, y = 0.3, 0.3) and (x, y = 0.4, 0.3), compared to the unmodified and bismuth oxide modified 0.85NBT– 0.15BCT – xBMT ceramics, Figure 5.3 and 5.13. No significant shift of T_m was observed with different x, y concentrations compared to the unmodified and Bi_2O_3-modified 0.85NBT– 0.15BCT – xBMT ceramics discussed in sections 5.1 and 5.2 of this chapter. However the relative permitivities

were higer compared to the ceramics discussed in section 5.1 and comparable to the bismuth oxide modified ceramics discussed section 5.2.

Slight variations in temperature-stable platuea of permitivity (ε_{rmid} ± 15 %), were observed compared to the studied compositions in sections 5.1 and 5.2. Temperature-stable relative permittivity observed for samples, (x, y) = (0.4, 0.05), 1470 ± 15 % over a temperature range 130 – 450 ºC+ and tanδ ≤ 0.02 in temperature-range 150 – 350 ºC, (x, y) = (0.3, 0.3), 1540 ± 15 % over a temperature range 110 – 450 ºC+ and tanδ ≤ 0.02 in temperature-range 90 – 430 ºC, (x, y) = (0.4, 0.3), 1370 ± 15 % over a temperature range 120 – 450 ºC+ and tanδ ≤ 0.02 in temperature-range 80 – 430 ºC and (x, y) = (0.4, 0.4), 950 ± 15 % over a temperature range 90 – 450 ºC+ and tanδ ≤ 0.02 in temperature-range 140 – 320 ºC. The dielectric properties of $(1–x)[(Na_{0.5}Bi_{0.5}TiO_3)_{1-y} – (Ba_{0.8}Ca_{0.2}TiO_3)_y] – xB_{0.5}Mg_{0.5}TiO_3$ [(x,y) = (0.4, 0.05), (0.3, 0.3), (0.4, 0.3), (0.4, 0.4) are presented in Table 5.4.

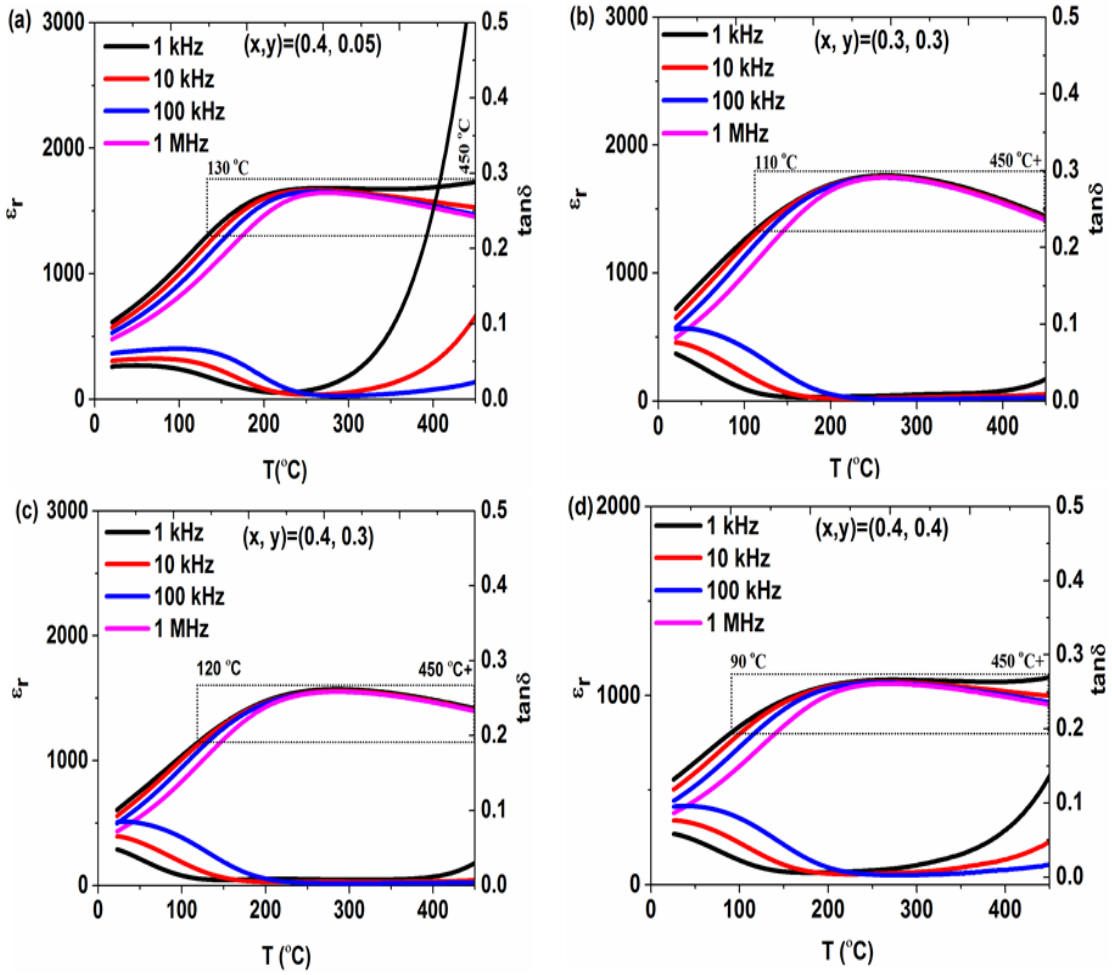

Figure 5.15 Temperature dependence of relative permittivity (ε_r) and tanδ of $(1–x)[(Na_{0.5}Bi_{0.5}TiO_3)_{1-y} – (Ba_{0.8}Ca_{0.2}TiO_3)_y] – xBMg_{0.5}Ti_{0.5}O_3$, (a) (x, y) = (0.4, 0.05), (0.4, 0.3), (b) (0.3, 0.3), (c) (0.4, 0.3) and (d) (0.4, 0.4).

Table 5.4 A summary of dielectric properties of $(1–x)[(Na_{0.5}Bi_{0.5}TiO_3)_{1-y} – (Ba_{0.8}Ca_{0.2}TiO_3)_y] – xBMg_{0.5}Ti_{0.5}O_3$ [(x,y) = (0.4, 0.05), (0.3, 0.3), (0.4, 0.3), (0.4, 0.4)] ceramics.

Sample (x, y)	T_m (ºC) (1kHz)	ε_{max} (1kHz)	ε_{mid} ± 15 % and T-range (ºC)	tanδ ≤ 0.02, (T-range) (1kHz)
0.4, 0.05	270	1680	130 – 450 ºC (1470 ± 15)	150 – 350 ºC
0.3, 0.3	270	1760	110 – 450 ºC (1540 ± 15)	90 – 430 ºC
0.4, 0.3	280	1570	120 – 450 ºC (1370 ± 15)	80 – 430 ºC
0.4, 0.4	280	1100	90 – 450 ºC (950 ± 15)	140 – 320 ºC

5.3.3 Conclusions from effects of ceramics with different x, y concentrations

Ceramics compositions $(1–x)[(Na_{0.5}Bi_{0.5}TiO_3)_{1-y} – (Ba_{0.8}Ca_{0.2}TiO_3)_y] – xBMg_{0.5}Ti_{0.5}O_3$ (x,y) = (0.4, 0.05), (0.4, 0.3), (0.4, 0.3), (0.4, 0.4) were prepared by conventional solid state route. Cubic/pseudocubic phase was obseved for the selected cermics. Relaxor behaviour with temperature-stable permittivity and a frequency dispersion below dielectric maximum temperature was obseved for the studied compositions.

Temperature-stable relative permittivity revealed for samples, (x, y) = (0.4, 0.05), ~1470 ± 15 % over a temperature range ~130 – 450 ºC+ and tanδ ≤ 0.02 in temperature-range ~150 – 350 ºC, (x, y) = (0.3, 0.3), ~1540 ± 15 % over a temperature range ~110 – 450 ºC+ and tanδ ≤ 0.02 in temperature -range ~ 90 – 430 ºC, (x, y) = (0.4, 0.3), ~1370 ± 15 % over a temperature range ~120 – 450 ºC+ and tanδ ≤ 0.02 in temperature-range ~ 80 – 430 ºC and (x, y) = (0.4, 0.4), 950 ± 15 % over a temperature range 90 – 450 ºC+ and tanδ ≤ 0.02 in temperature -range 140 – 320 ºC. Different x,y concentrations have shown no significat effect on temperature-stability of dielectrics.

Chapter 6

Dielectric properties of ternary system $(1–x)[0.85Na_{0.5}Bi_{0.5}TiO_3 – 0.15Ba_{0.8}Ca_{0.2}TiO_3] – xLiNbO_3$

6.1 Introduction

The main focus of this chapter is to study the dielectric and structural properties of the ternary solid solutions $(1–x)[0.85Na_{0.5}Bi_{0.5}TiO_3 – 0.15Ba_{0.8}Ca_{0.2}TiO_3] – xLiNbO_3$, $(0 \leq x \leq 0.15)$, abbreviated as, 0.85NBT – 0.15BCT – xLN.

X-ray powder diffraction patterns of the crushed sintered pellets revealed a single-perovskite phase for the compositions, $(0 \leq x \leq 0.08)$. Secondary phases possibly $NaBaCaNb_5TiO_{15}$ were detected for samples x = 0.1 and 0.15. A mixed cubic + tetragonal structure was observed for ceramics, $0 \leq x \leq 0.02$ and a cubic symmetry for $x \geq 0.03$.

Relative permittivity-temperature plots showed broad dielectric peaks for x = 0 – 0.02. Temperature-stable wide plateau of relative permittivity (ε_r varying by no more than ±15 %) were observed for samples, x = 0.07 – 0.1. For example at x = 0.07 , $\varepsilon_r = 1530 \pm 15$ % from 30 ºC to 420 ºC, and $\tan\delta \leq 0.02$ from 90 ºC to 400 ºC.

A relatively high piezoelectric charge coefficient of poled sample measured with Berlincourt apparatus, $d_{33} \sim 148$ pC/N was recorded for x = 0 and 155 pC/N for x = 0.02, comparable to widely reported $Na_{0.5}Bi_{0.5}TiO_3$ - $BaTiO_3$ lead-free piezoceramics (NBT – BT). A high dc resistivity ~ 10^9 Ω m was observed for x =

0.04 at 250 ºC, important for any dielectric being considered as a high temperature capacitor material.

6.2 Batch calculations

The weight percent contributions of each precursor in preparation of different batches of $(1- x)[0.85Na_{0.5}Bi_{0.5}TiO_3 - 0.15Ba_{0.8}Ca_{0.2}TiO_3] - xLiNbO_3$, $(0 \leq x \leq 0.1)$ are shown in Table 6.1.

Table 6.1 Calculations of wt.% of raw powders of ceramics series $(1–x)[0.85 Na_{0.5}Bi_{0.5}TiO_3 – 0.15Ba_{0.8}Ca_{0.2}TiO_3] – xLiNbO_3$, $(0 \leq x \leq 0.1)$.

x	wt.% $BaCO_3$	wt.% $CaCO_3$	wt.% Bi_2O_3	wt.% Na_2CO_3	wt.% TiO_2	wt.% Li_2CO_3	wt.% Nb_2O_5
x=0.005	10.33	1.33	43.25	9.84	34.88	0.08	0.29
x=0.01	10.31	1.31	43.09	9.80	34.75	0.16	0.58
x=0.015	10.29	1.30	42.91	9.76	34.62	0.24	0.88
x=0.02	10.28	1.30	42.70	9.73	34.49	0.33	1.17
x=0.03	10.13	1.29	42.45	9.65	34.23	0.49	1.76
x=0.04	10.12	1.28	42.10	9.58	33.96	0.65	2.35
x=0.05	10.02	1.27	41.77	9.50	33.69	0.82	2.95
x=0.06	9.91	1.26	41.44	9.43	33.43	0.99	3.55
x=0.07	9.82	1.25	41.12	9.35	33.16	1.15	4.153
x=0.08	9.80	1.24	40.77	9.27	32.89	1.32	4.76
x=0.1	9.63	1.22	40.09	9.12	32.34	1.66	5.98

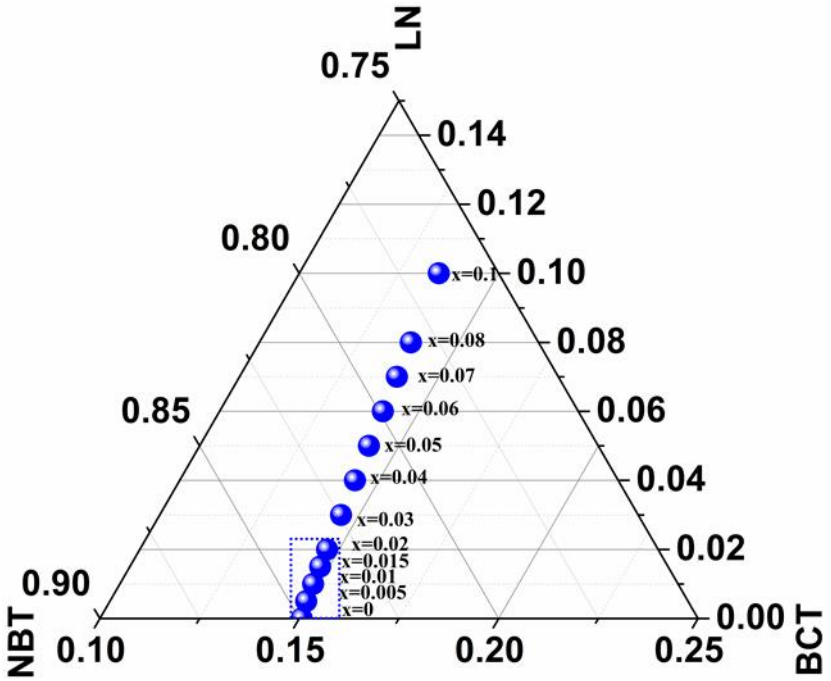

Figure 6.1 Illustration of the location of the compositions (1–x)[0.85 $Na_{0.5}Bi_{0.5}TiO_3$ – 0.15$Ba_{0.8}Ca_{0.2}TiO_3$] – x$LiNbO_3$, x = 0 – 0.15 in the relevant ternary system.

Figure 6.1 illustrates a segment of the relevant ternary compositional diagram showing the locations of the studied compositions of (1–x)[0.85 $Na_{0.5}Bi_{0.5}TiO_3$ – 0.15$Ba_{0.8}Ca_{0.2}TiO_3$] – x$LiNbO_3$ ($0 \leq x \leq 0.15$). All the studied compositions are the derivatives of the base composition 0.85$Na_{0.5}Bi_{0.5}TiO_3$ – 0.15$Ba_{0.8}Ca_{0.2}TiO_3$, which lies in the vicinity of MPB between tetragonal BCT and cubic or pseudocubic NBT end members, (as discussed in chapter 4).

6.3 X-ray diffraction study

X-ray powder diffraction patterns of crushed sintered pellets of ceramics (1–x) [0.85$Na_{0.5}Bi_{0.5}TiO_3$ – 0.15$Ba_{0.8}Ca_{0.2}TiO_3$] – x$LiNbO_3$ ($0 \leq x \leq 0.15$) are shown in Figure 6.2. The samples $x \leq 0.08$ displayed a single-phase perovskite structure.

Secondary peaks of similar d-spacing to $NaBaCaNb_5O_{15}$ (ICDD: 04-008-7209) began to appear at $x > 0.08$.

From the observed 200/002 peak splitting (at ~ 45º), a mixed tetragonal phase and cubic/pseudocubic phase was observed for ceramics $x \leq 0.02$, Figure 6.2 (b). The intensity of the middle peak in the triplet at ~ 46 - 47 º2θ, which is attributed to the cubic/pseudocubic phase, increased between $x = 0$ and $x = 0.01$ consistent with an increasing proportion of this phase as the boundary with the single phase cubic/pseudocubic phase field was approached; Figure 6.2 (b)

The variation in *a* and c lattice parameters with x for $x \leq 0.02$ is shown in Figure 6.3, along with values of cubic *a* lattice parameter for $x \geq 0.02$. The geometrical densities were in the range of of ~ 5.7 – 5.3 g/cm^3 (relative density ~ 93 - 96 %).

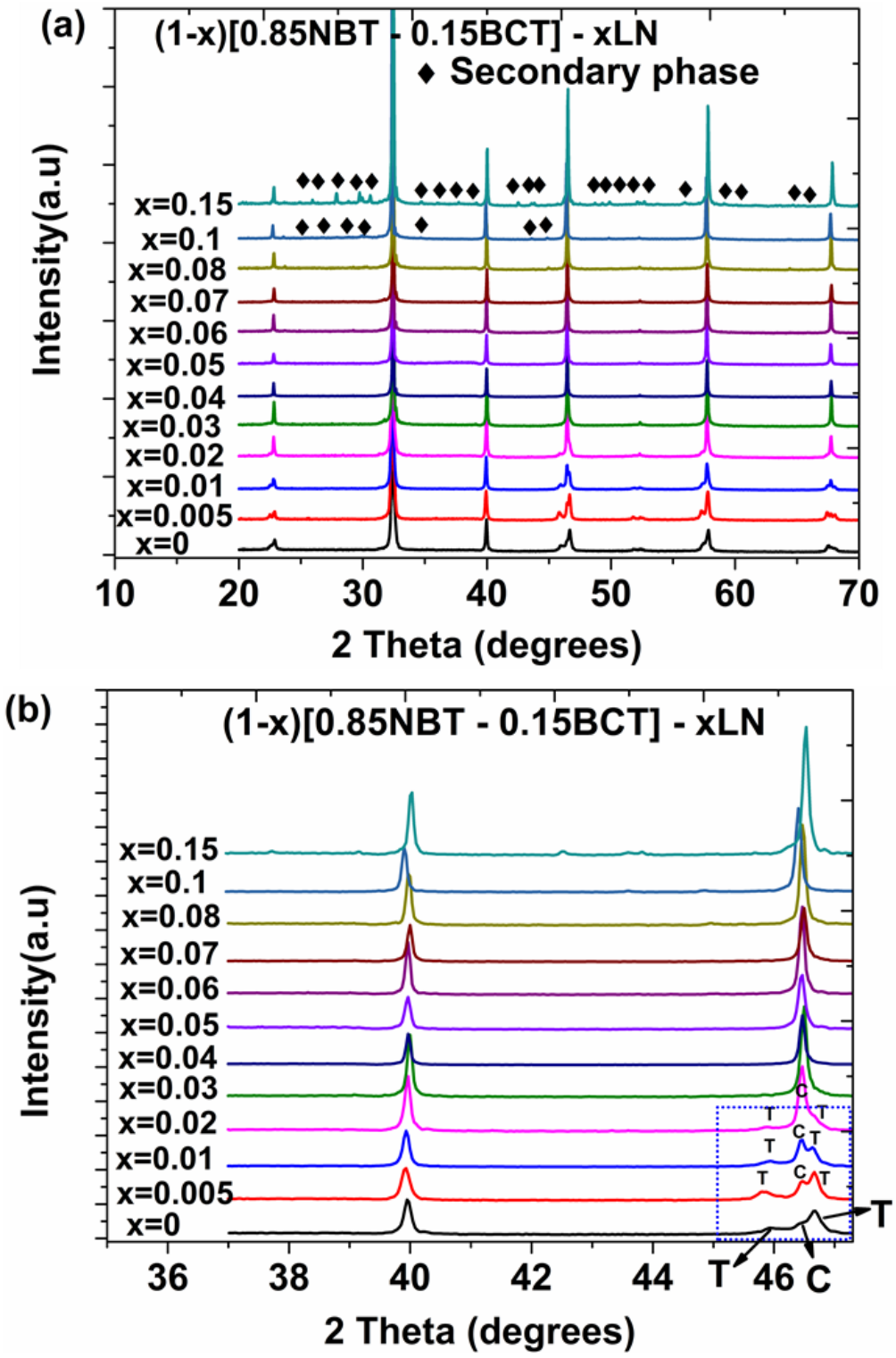

Figure 6.2 (a) X-ray powder diffraction patterns of ceramic system (1–x)[0.85 $Na_{0.5}Bi_{0.5}TiO_3$ – 0.15$Ba_{0.8}Ca_{0.2}TiO_3$] – x$LiNbO_3$, x = 0 – 0.15 and (b) A broad view of 111, 002/200 peaks, (T = Tetragonal, C = Cubic).

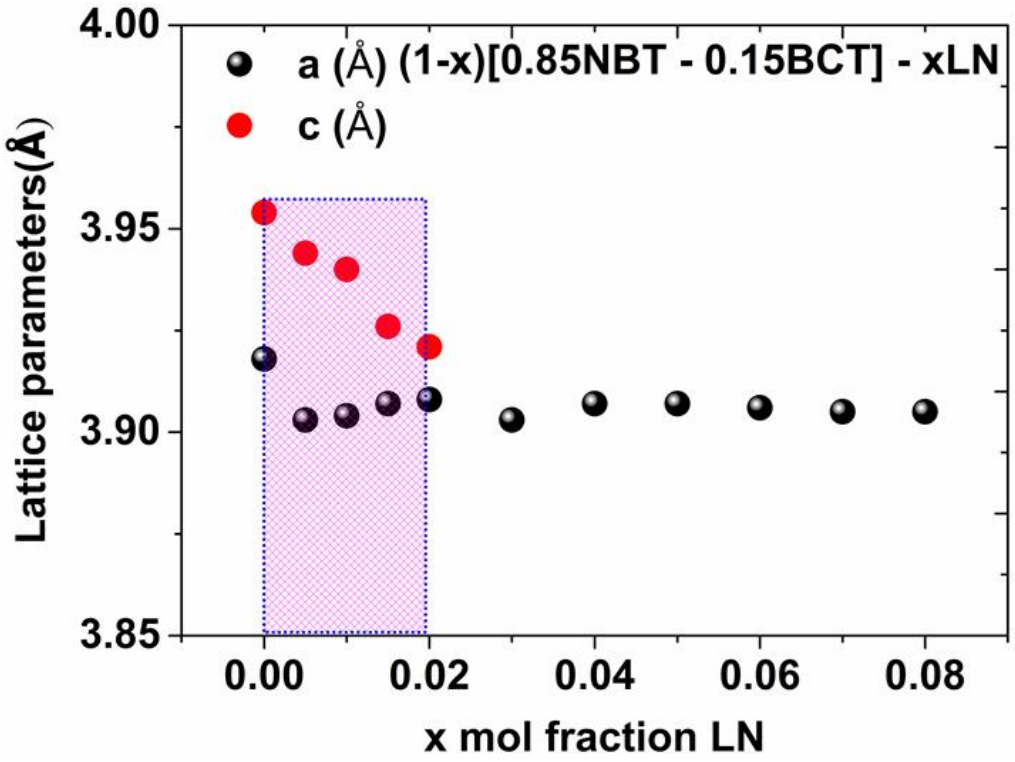

Figure 6.3 Lattice parameters as a function of x mol % $LiNbO_3$ (LN) of, (1–x)[0.85 $Na_{0.5}Bi_{0.5}TiO_3$ – 0.15$Ba_{0.8}Ca_{0.2}TiO_3$] – x$LiNbO_3$ (x = 0 – 0.08).

6.4 Dielectric analysis

Plots of relative permittivity (ε_r) and tanδ versus temperature (T) at 1 kHz – 1 MHz, from ambient temperature to 450 ºC are shown in Figure 6.4 - 6.5. As for a number of compositions described in previous chapters, the x = 0 sample (see Chapters 4,5) displayed a broad dielectric peak at temperature T_2 ~ 250 °C, with a relaxor-type inflection at lower temperature (T_1 ~ 130 ºC) and frequency dispersion in tanδ at T ~ T_1. The x = 0.005 sample displayed a single broad relaxor peak and associated tanδ peak with no clear evidence of any ε_r inflection below T_m (relaxor peak temperature). The x = 0.01 sample was similar to x = 0.05 but at x = 0.15 the ε_r peak become much broader/flatter. However there was a suggestion of a hump toward the lower temperature of the plateau which may be a relic of the inflection observed in x = 0 (T_1). A trend of increasing temperature width of the plateau was

observed as x increased beyond 0.015. The dotted boxes in Figures 6.4 - 6.5 shows the temperature range of stable $\varepsilon_{r,}$ defined as $\varepsilon_r \pm 15\%$. These temperatures, and ranges of low tanδ are summarised in Table 6.2.

A high temperature stable-relative permittivity, $\varepsilon_r \pm 15$ % was also detected for sample, x = 0.1 but permittivity was lower at ~ $\varepsilon_r = 890 \pm 15$ % from 25 ºC to 450 ºC, but losses were low (tan $\delta \leq 0.02$) only from 140 - 290 °C (the presence of secondary phases may have contributed to the lower permittivity and fluctuating values of tanδ). The effects of secondary phases were more pronounced for x = 0.15.

Trends in relative permittivity at 1 kHz for different compositions (selected as the most promising temperature stable materials) are compared in Figure 6.6. A summary of overall dielectric properties for all compositions is presented in Table 6.2.

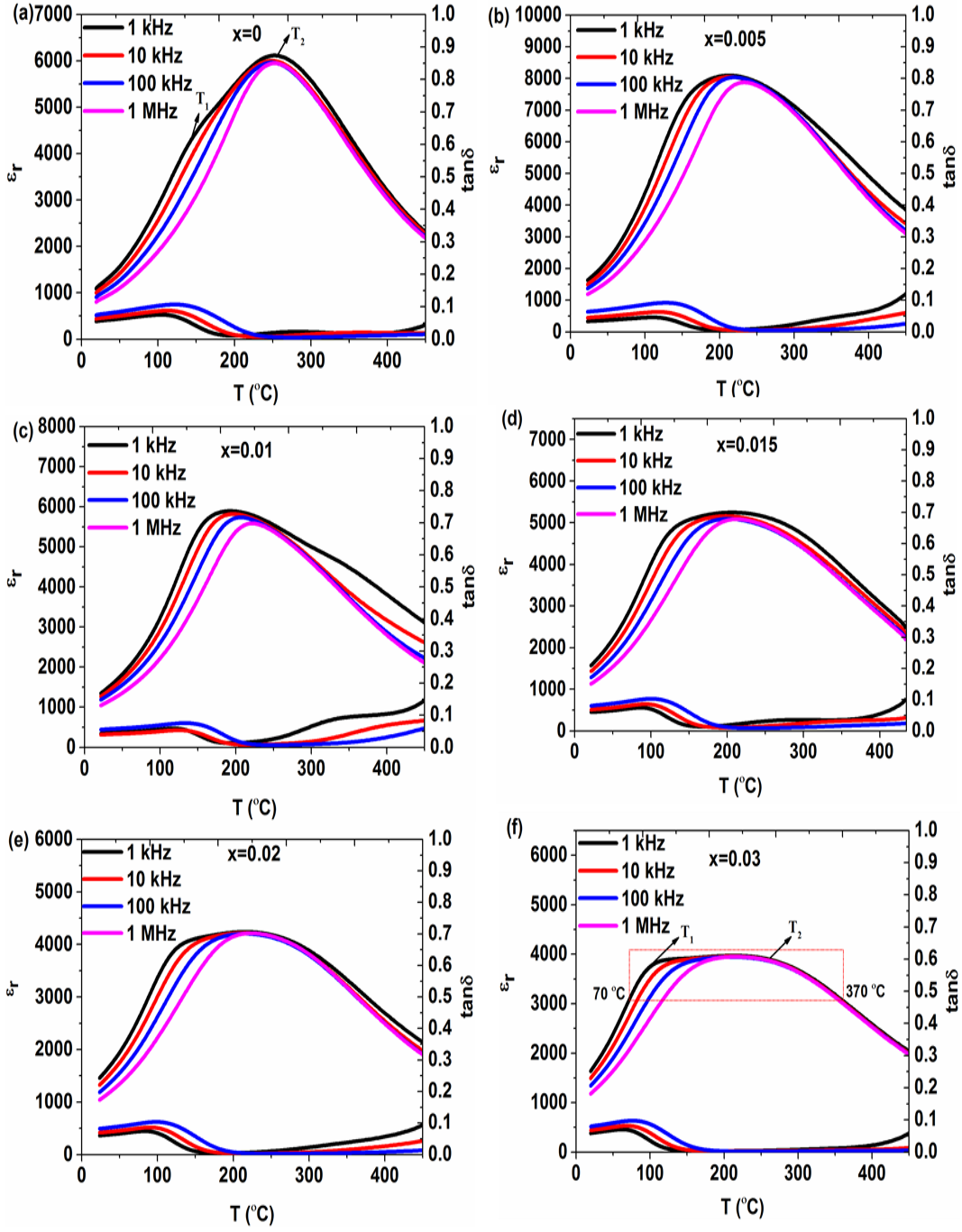

Figure 6.4 Temperature-dependent relative permittivity (ε_r) and tanδ of (1–x)[$0.85Na_{0.5}Bi_{0.5}TiO_3 – 0.15Ba_{0.8}Ca_{0.2}TiO_3$] – $xLiNbO_3$ (a) x = 0, (b) x = 0.005 (c) x = 0.01 (d) x = 0.015 (e) x = 0.02 (f) x = 0.03.(data set continued in Figure 6.5)

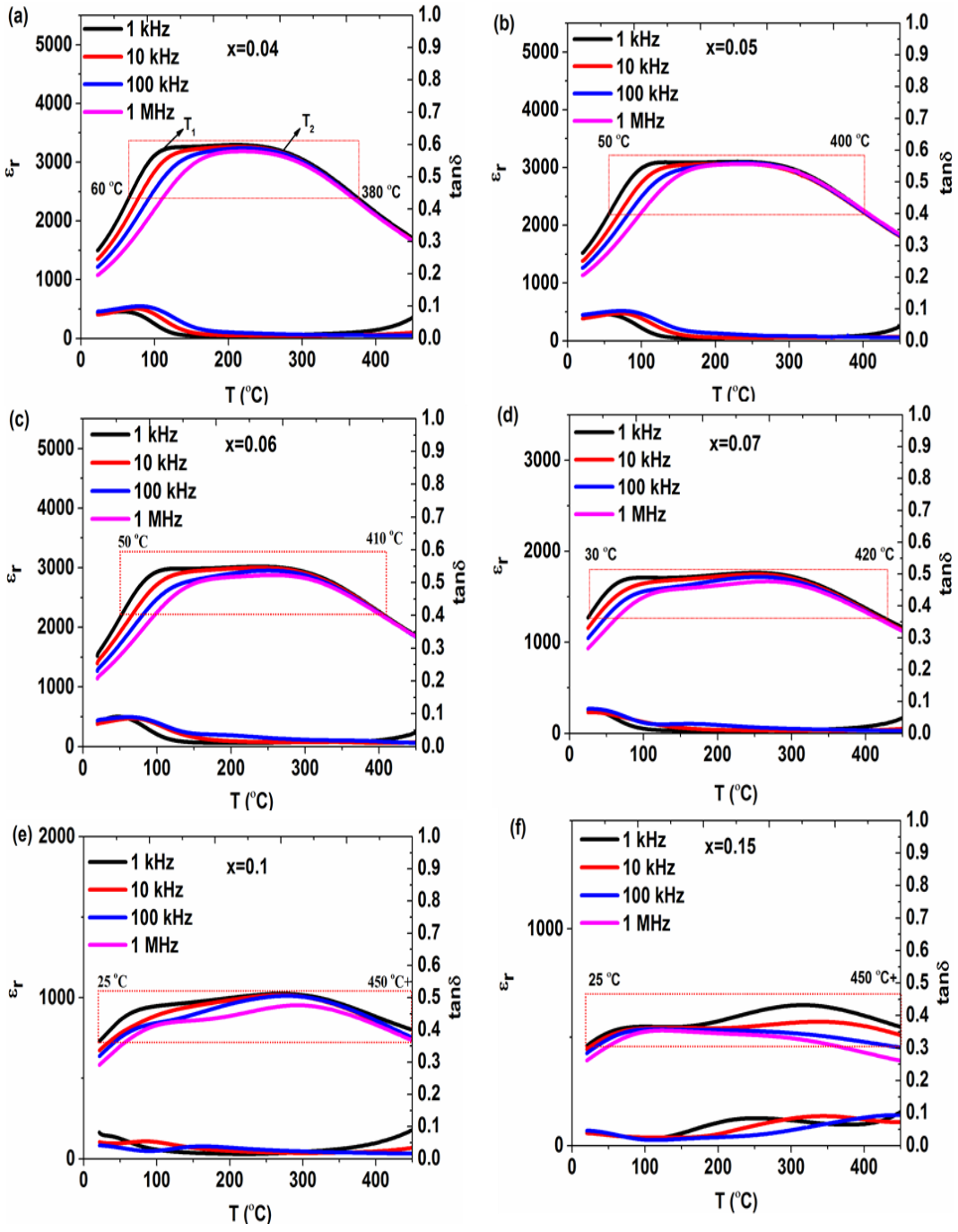

Figure 6.5 Temperature-dependent relative permittivity (ε_r) and tanδ of (1–x)[0.85$Na_{0.5}Bi_{0.5}TiO_3$ – 0.15$Ba_{0.8}Ca_{0.2}TiO_3$] – x$LiNbO_3$, (a) x = 0.04, (b) x = 0. 05, (c) x = 0.06 (d) x = 0.07, (e) x = 0.1, (f) x = 0.15.

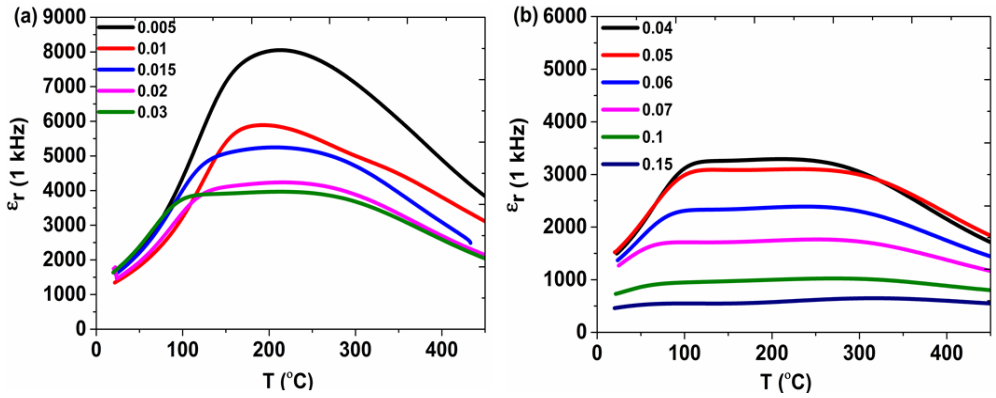

Figure 6.6 Temperature-dependent relative permittivity (ε_r) of (1–x)[0.85 $Na_{0.5}Bi_{0.5}TiO_3$ – 0.15$Ba_{0.8}Ca_{0.2}TiO_3$] – x$LiNbO_3$, (a) x = 0.005 – 0.03 and (b) x = 0.04 – 0.15) (at 1kHz), Note dielectric losses were high in x = 0.15.

Table 6.2 Summary of dielectric properties of ceramics series (1–x)[0.85 $Na_{0.5}Bi_{0.5}TiO_3$ – 0.15$Ba_{0.8}Ca_{0.2}TiO_3$] – x$LiNbO_3$, (0 ≤ x ≤ 0.15) at 1 kHz.

x	$\varepsilon_{25°C}$	T_1 (°C)	ε_1	T_2 (°C)	ε_2	ε_{mid} (1 kHz)	ε_{mid} ± 15 % (1 kHz) (T-range)	T-range tanδ ≤ 0.02
0	1190	130	4420	250	6120	-----	----------	170–410 °C
0.005	1670	-----	-----	210	8090	-----	----------	160–290 °C
0.01	1400	-----	-----	200	5890	-----	----------	170–230 °C
0.015	1640	-----	-----	150	4900	4580	100–350	140–240 °C
0.02	1480	-----	-----	220	4240	3690	100–320	140–300 °C
0.03	1760	110	3840	230	3950	3470	70–370	120–390 °C
0.04	1540	110	3220	260	3250	2870	60–380	120–380 °C
0.05	1590	100	3040	300	3050	2700	50–400	120–410 °C
0.06	1660	100	3020	310	2930	2630	50–410	120–400 °C
0.07	1270	70	1670	320	1710	1530	30–420	90 –400 °C
0.1	750	60	920	340	1020	890	25–450+	140–290 °C
0.15	480	60	650	360	640	570	25–450+	----------

6.4.1 Modified Curie Weiss law

The dielectric data were analysed by again considering the modified Curie Weiss expression, $(1/\varepsilon - 1/\varepsilon_m) = (T - T_m)^{\gamma}/C$, $(1 \leq \gamma \leq 2)$, where C and γ are material constants (Ullah Jan et al., 2014, Park et al., 2007). By fitting experimental data, for the 0.85NBT – 0.15BCT – xLN ceramics, the value of γ lies between 1.37 and 2.37, indicating relaxor character, Figure 6.7.

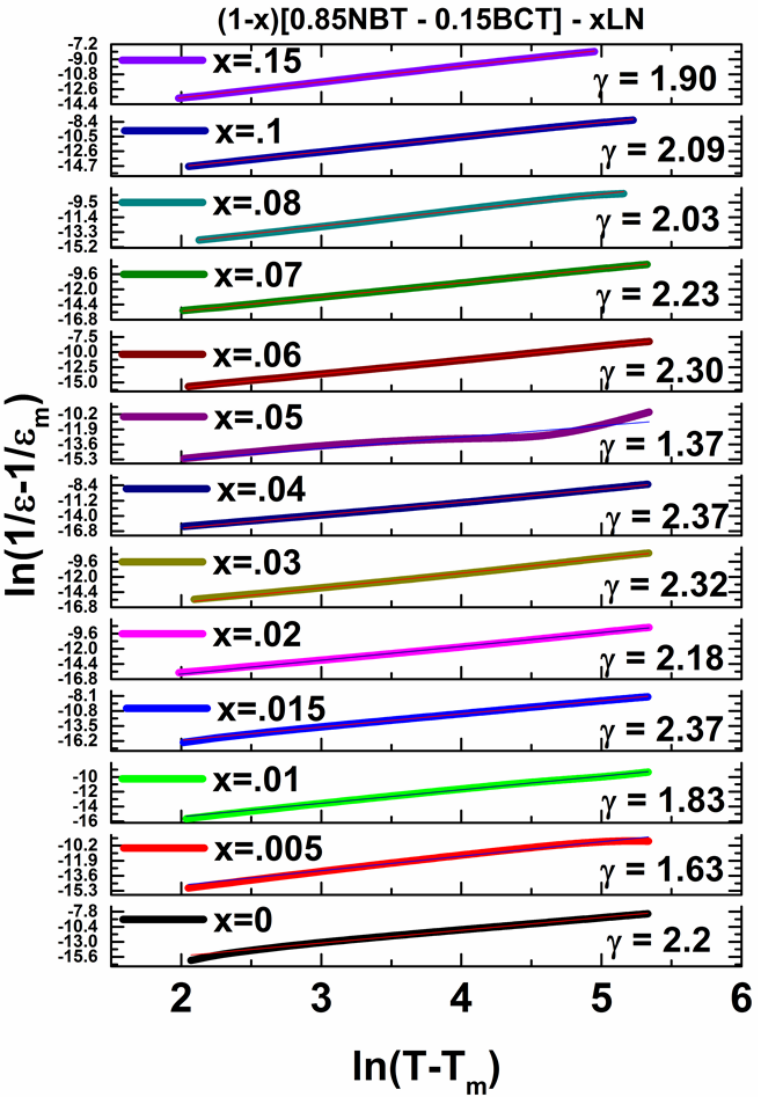

Figure 6.7 plots of $\ln(1/\varepsilon - 1/\varepsilon_m)$ versus $\ln(T - T_m)$ for ceramic system, $(1-x)[0.85Na_{0.5}Bi_{0.5}TiO_3 - 0.15Ba_{0.8}Ca_{0.2}TiO_3] - xLiNbO_3$, $(0 \leq x \leq 0.15)$.

6.5 Microstructural analysis

To examine microstructures of 0.85NBT – 0.15BCT – xLN, x = 0.01, 0.02 ceramics, sintered at 1070 ºC for 10 h, scanning electron microscopy SEM was used to image the cross sectional surfaces of the fractured sintered pellets, Figure 6.8. Inter-granular fracture was observed (fracture along grain boundaries).

The particle size was < 4 μm, for x = 0.01 and < 6 μm for x = 0.02. The geometrical densities were ranged between 5.7 – 5.3 g/cm^3 (Relative density ~93 - 96%)

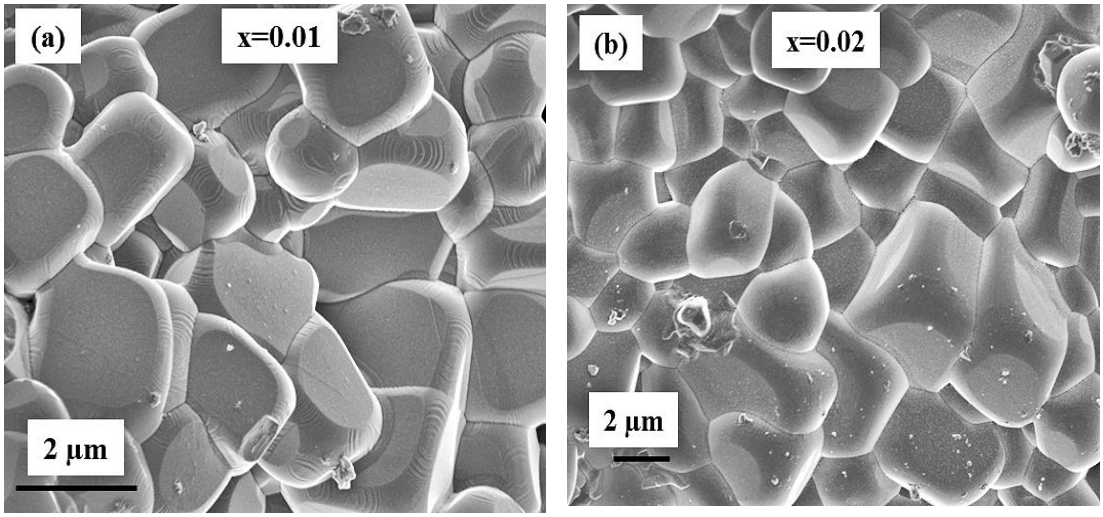

Figure 6.8 SEM micrographs of (1–x)[0.85$Na_{0.5}Bi_{0.5}TiO_3$ – 0.15$Ba_{0.8}Ca_{0.2}TiO_3$] – x$LiNbO_3$ (a) x = 0.01 and (b) x = 0.02, ceramics.

6.6 Piezoelectric measurements

Figure 6.9, shows the piezoelectric constant (d_{33}) as a function of x mol % LN. The d_{33} value decreased from ~ 148 pC/N, x = 0 to ~ 138 pC/N, at x = 0.005 and then increased to 155 pC/N, for x = 0.02), which is competitive with other lead free ceramics, for example KBT – NBT– BT and NBT – BT (Zhang et al., 2007, Qing Xu, 2004). The d_{33} measurements were performed by Aurang Zeb from the

same research group (in future it would be interesting to measure d_{33} for, x = 0.03 as it lies on the cubic side of the mixed phase boundary region).

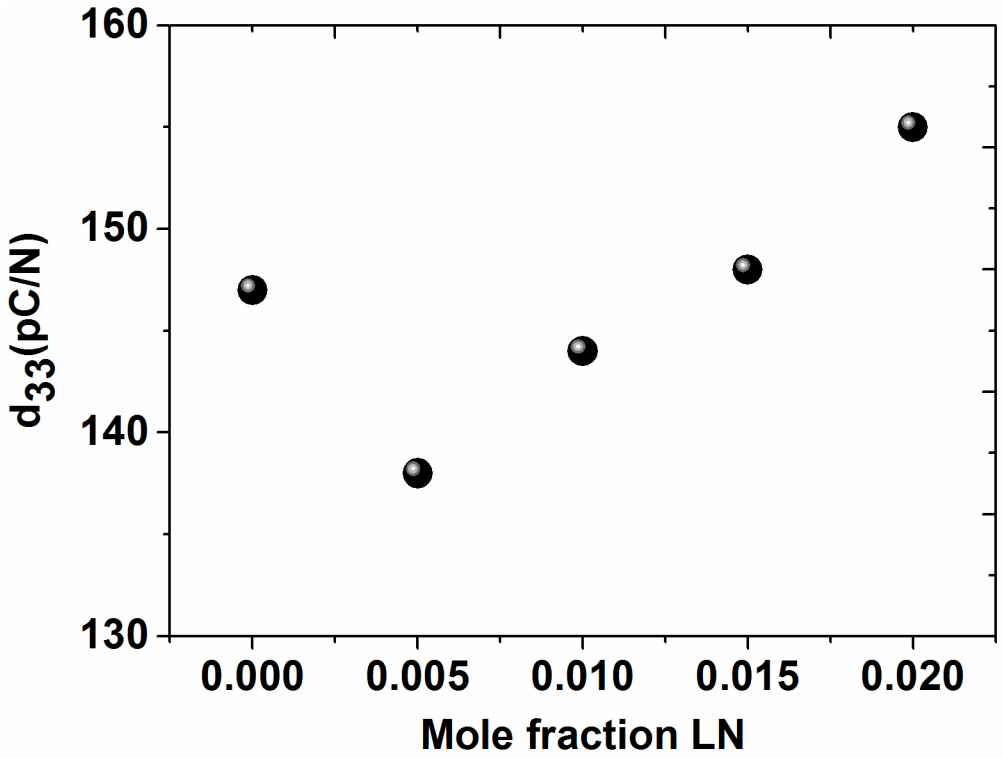

Figure 6.9 Variation of piezoelectric constant (d_{33}) with x mol fraction of LN for $(1–x)[0.85Na_{0.5}Bi_{0.5}TiO_3 – 0.15Ba_{0.8}Ca_{0.2}TiO_3] – xLiNbO_3$, x = 0 – 0.02.

6.7 dc resistivity measurements

High relative permittivity, temperature-stability, low loss tangent are not the only key factors for materials to be of interest for high temperature dielectric capacitor applications. An ideal capacitor would have infinite resistivity, but there is no such capacitor without any leakage current/discharge through its own resistance (real capacitor). Capacitors with high resistivity will give high performance at elevated temperature with minimum leakage current (Dittmer, 2011).

The dc resistivity values as a function of temperature from 250 ºC to 550 ºC are shown in Figure 6.10. The resistivity increased with incorporation of LN (x). A high dc resistivity ~ 10^9 Ω m at 250 ºC was observed for x = 0.04.

The activation energies found from conduction data were 0.58 eV, 0.61 eV and 0.63 eV for x = 0, 0.02 and 0.04 respectively. These values of activation energies are consistent with an oxygen vacancy migration mechanism The activation energy for A-site ions is ~4 eV, B-site ions is ~15eV and for oxygen vacancies is ~ 0.7 eV (Selvamani, 2012).

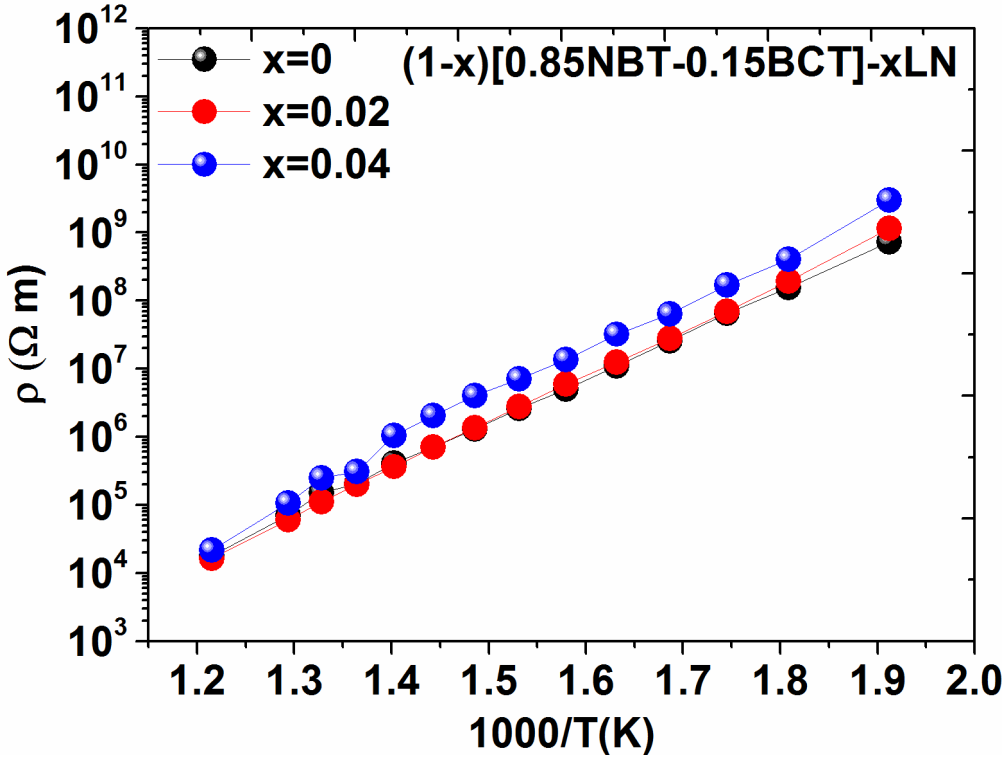

Figure 6.10 Logarithm of dc resistivity as a function of 1/T of (1–x)[0.85 $Na_{0.5}Bi_{0.5}TiO_3$ – 0.15$Ba_{0.8}Ca_{0.2}TiO_3$] – x$LiNbO_3$, x = 0 – 0.04.

6.8 Conclusions

Ceramics, $(1–x)[0.85Na_{0.5}Bi_{0.5}TiO_3 – 0.15Ba_{0.8}Ca_{0.2}TiO_3] – xLiNbO_3$ [85NBT – 15BCT – xLN] ($0 \leq x \leq 0.15$), were synthesised by a mixed oxide route. X-ray powder diffraction patterns were consistent with mixed phases of cubic + tetragonal phases for, $x \leq 0.02$ and cubic for $x \geq 0.03$. Secondary phases were detected for $x > 0.08$.

Relative permittivity-temperature plots revealed a relaxor dielectric character. Maximum relative permittivity ε_{max} increased from ~ 6120 ($x = 0$) to ~ 8090 ($x = 0.005$) and then started to decrease, reaching a minimum of ~ 650 for $x = 0.15$. Values of tanδ at high temperatures were higher for $x = 0.005 – 0.01$ and $x = 0.1 – 0.15$, in contrast to $x = 0$ and $x = 0.015 – 0.07$. Broad diffuse dielectric peaks were observed for, $0 < x \leq 0.02$. Wide plateau developed for $x \geq 0.03$ giving favourable temperature stability in relative permittivity over wide temperature ranges. There was a hint of the T_1 dielectric anomaly continuing to be detected in ε_r–T plots for, $x \geq 0.03$. The temperature ranges of low dielectric loss were more extensive that a number of other systems reported in Chapters 4 – 6. This is also a favourable factor with a view to capacitor applications.

A piezoelectric coefficient d_{33} ~ 155 pC/N was recorded for $x = 0.02$, similar in value to widely studied NBT – BT lead-free piezoelectrics. A high dc resistivity ~ 10^9 Ω m was observed for $x = 0.04$ at 250 ºC. The values of activation energies were consistent with oxygen ion vacancy migration.

Chapter 7

Dielectric properties of ternary system, $(1–x)[0.85Na_{0.5}Bi_{0.5}TiO_3 – 0.15Ba_{0.8}Ca_{0.2}TiO_3] – xNaNbO_3$

7.1 Introduction

The materials examined in this chapter, $(1–x)[0.85Na_{0.5}Bi_{0.5}TiO_3 – 0.15Ba_{0.8}Ca_{0.2}TiO_3] – xNaNbO_3$ ($0 \leq x \leq 0.8$), are similar in formulation to those in Chapter 6, but with the $LiNbO_3$ component being replaced with $NaNbO_3$.

X-ray powder diffraction patterns showed single-phase perovskite for sample compositions $x \leq 0.6$. Secondary phases were detected for $x > 0.6$.

The ε_r-T plots were generally comparable to the $LiNbO_3$ analogue, in that a shoulder and main peak were evident, but for the $NaNbO_3$–modified materials the ε_r(T) plateau extended to much lower temperatures, -70 °C in some cases. The x = 0.3 to 0.6 samples displayed the most promising dielectric properties: for example at x = 0.4, $\varepsilon_r = 1300 \pm 15$ % from -70 to 210 °C.

Table 7.1, presents the wt.% contribution of each precursor in preparation of different batches for samples, x = 0.02 – 0.5.

Table 7.1 The weight percent contribution of each precursor in ceramics series $(1–x)[0.85Na_{0.5}Bi_{0.5}TiO_3 – 0.15Ba_{0.8}Ca_{0.2}TiO_3] – xNaNbO_3$, $(0 \leq x \leq 0.5)$.

x	wt.% $BaCO_3$	wt.% $CaCO_3$	wt.% Bi_2O_3	wt.% Na_2CO_3	wt.% TiO_2	wt.% Nb_2O_5
0.02	10.21	1.30	42.69	10.18	34.40	1.21
0.05	9.98	1.31	41.60	10.61	33.59	2.91
0. 1	9.52	1.18	39.80	11.43	32.07	5.88
0. 2	8.60	1.11	36.09	13.01	29.11	12.10
0. 3	7.71	0.96	32.11	14.69	26.01	18.50
0. 4	6.67	0.90	28.11	16.38	22.71	25.11
0.45	6.30	0.81	25.98	17.31	21.01	28.62
0.5	5.71	0.70	23.87	18.21	19.30	32.12

7.2 Results and discussion

7.2.1 X- ray analysis

The room temperature phase content of $(1–x)[0.85Na_{0.5}Bi_{0.5}TiO_3 – 0.15Ba_{0.8}Ca_{0.2}TiO_3] – xNaNbO_3$ $(0 \leq x \leq 0.8)$ was investigated using X-ray powder diffraction, Figure 7.1.

The base composition, x = 0 was described in Chapter 4, 5 and 6, being mixed cubic and tetragonal. The $x \geq 0.02$ samples were consistent with a single-phase cubic perovskite structure, Figure 7.1b. Secondary phases of $NaNbO_3$ (ICDD: 04–017–2917) appeared for samples $x > 0.6$, indicating the solid solution limit to lie at $x \sim 0.6$. There was little variation in cubic lattic parameter with x for compositions

up to x = 0.3; higher x values showed a slight decrease in lattice parameter, Figure 7.2.

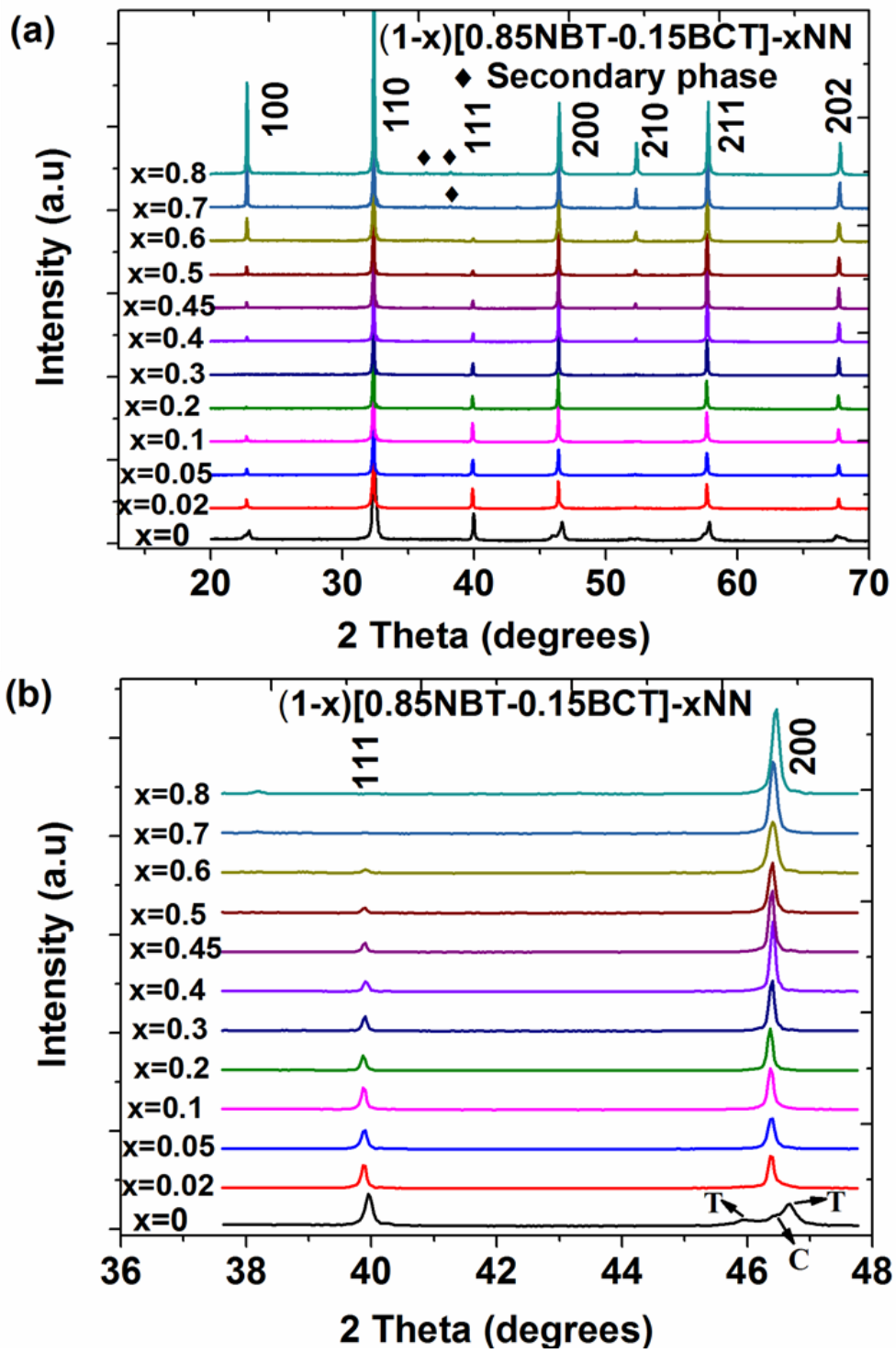

Figure 7.1 (a) X-ray diffraction patterns of ceramic series (1–x)[0.85$Na_{0.5}Bi_{0.5}TiO_3$ – 0.15$Ba_{0.8}Ca_{0.2}TiO_3$] – x$NaNbO_3$, (0 ≤ x ≤ 0.8).and (b) a broad view of 111 and 002/200 peak.

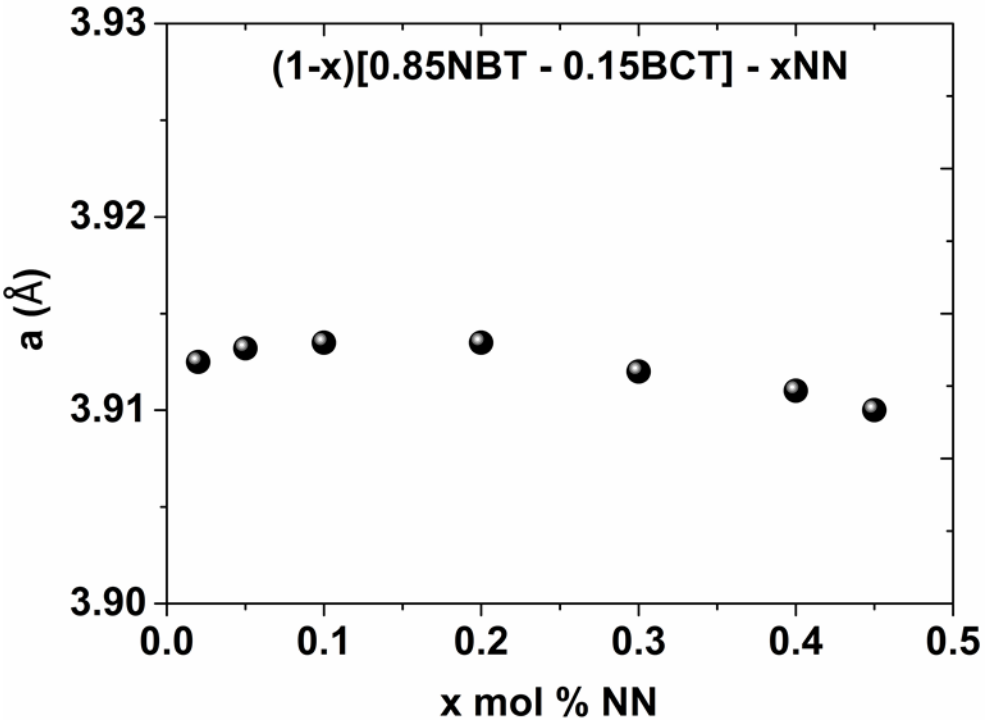

Figure 7.2 The value of *a* lattice parameter of the ceramic system (1–x)[0.85$Na_{0.5}Bi_{0.5}TiO_3$ – 0.15$Ba_{0.8}Ca_{0.2}TiO_3$] – x$NaNbO_3$, (0 ≤ x ≤ 0.45) as function of x mol % NN.

7.3 Dielectric properties

The dielectric constant (ε_r) and loss tangent (tanδ) at 1 kHz – 1 MHz from -70 ºC to 450 ºC of (1–x)[0.85$Na_{0.5}Bi_{0.5}TiO_3$ – 0.15$Ba_{0.8}Ca_{0.2}TiO_3$] – x$NaNbO_3$ (0 ≤ x ≤ 0.8) as a function of temperature are shown in Figure 7.3-7.4. The x = 0 sample is as described in Chapter 4, 5 and 6, showing a broad maximim in relative permittivity with a peak temperature T_2 ~ 250 ºC; a lower temperature shoulder or inflection was present (T_1 ~ 130 °C), most clearly visible at 'low' frequencies 1kHz – 10 kHz.

The x = 0.05 sample showed a more pronounced shouler, and it occured at a temperature lower, T_1 ~ 100 °C (1 kHz) than for x = 0. The form of the x = 0 and x = 0.05 permittivity plots is comparable to $Na_{0.5}Bi_{0.5}TiO_3$, $Na_{0.5}Bi_{0.5}TiO_3$ – $BaTiO_3$

and $Na_{0.5}Bi_{0.5}TiO_3 – K_{0.5}Bi_{0.5}TiO_3$ (Anthoniappen et al., 2015, Zhou et al., 2009, Jo et al., 2011).

In the x = 0.1 sample, the shoulder was the dominant feature, being the maximum in permittivity, ~ 3630 (at similar temperature to x = 0.05); a very minor hump occurred at ~ 200 – 250 °C (T_2). The x = 0.2 sample was generally similar to x = 0.1, but $\varepsilon_{r\,max}$ had decreaed to ~ 1720 . For x = 0.3 there was only one peak with T_m ~ 50 °C and $\varepsilon_{r\,max}$ ~ 1580 (there was no second shoulder). The breadth of the x ≥ 0.3 plots gave rise to temperature stable permittivity, although none displayed the near-flat the plateau seen in Chaper 6, or for $B_{0.8}Ca_{0.2}TiO_3 – BiMg_{0.5}Ti_{0.5}O_3$ (Zeb, 2013) for example. Nevertheless a wide temperture range of ± 15 % stability in ε_r was observed. The temperature range of ε_r ± 15 % extended from -50 to 240 °C for x = 0.3. For sample x = 0.4, ε_r = 1300 ± 15 % from -70 to 210 °C. Temperature ranges of low tanδ were more restricted, Table 7.2.

Dielectric properties are summarised in Table 7.2 highlighting relative permittivities varying by no more than ± 15 % (ε_{mid} ± 15 %) over a wide operational ranges for x = 0 – 0.5, Table 7.2 The dotted box represents a ± 15 % deviation of relative permittivity from the mean value permittivity Figure 7.3 – 7.4. The most promising compositions are x = 0.3 and x = 0.4 (based on temperature ranges).

These long range temperature-stable compositions, might be of great interst for high temperature capacitor applications, with refrence to EIA, X7R – X9R dielectric capacitors.

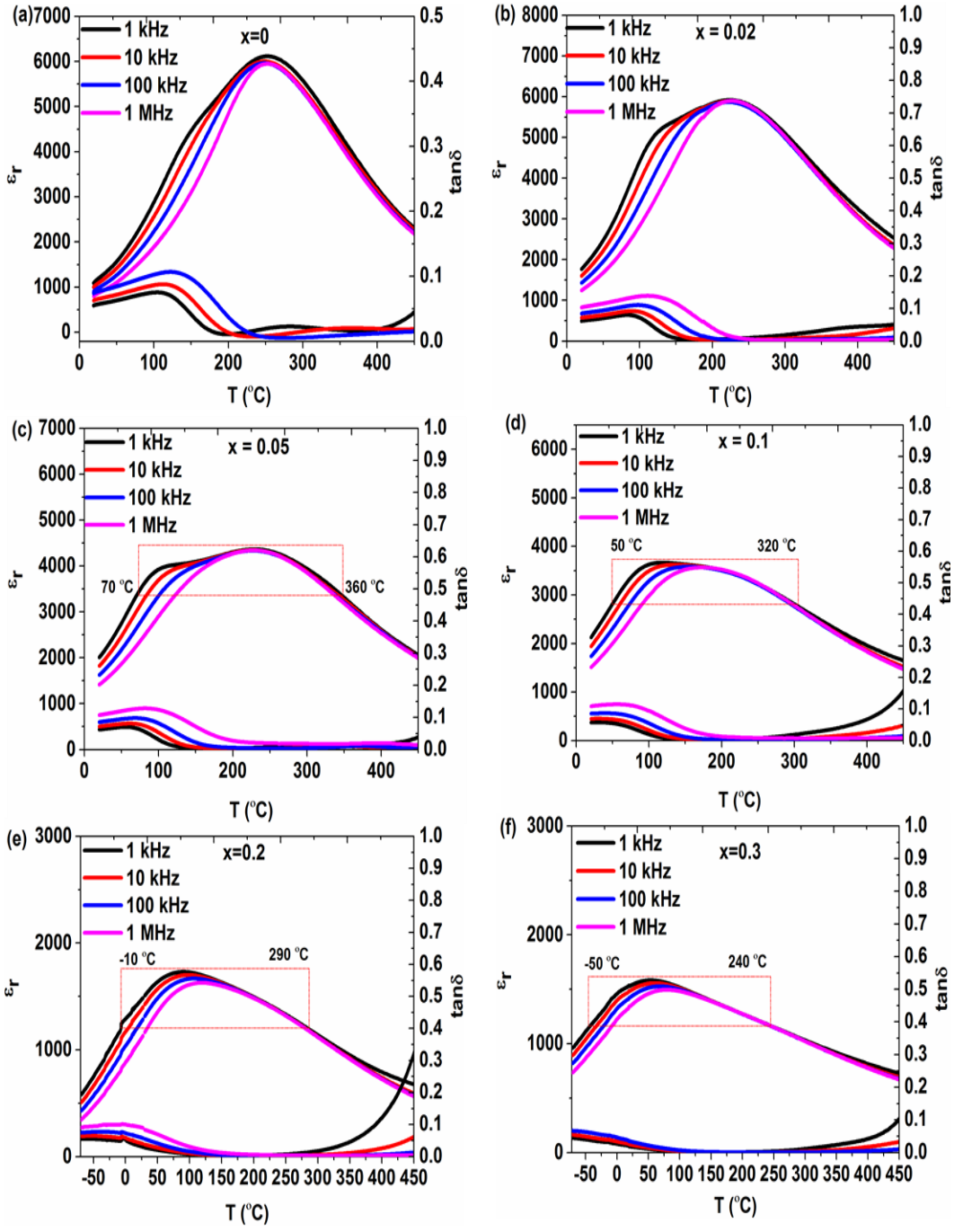

Figure 7.3 a) Temperature-dependent relative permittivity (ε_r) and tanδ of (1–x)[0.85$Na_{0.5}Bi_{0.5}TiO_3$ – 0.15$Ba_{0.8}Ca_{0.2}TiO_3$] – x$NaNbO_3$, (a) x = 0, (b) x = 0.02, (c) x = 0.05, (d) x = 0.1, (e) x = 0.2 and (f) x = 0.3. (data set continued in Figure 7.4)

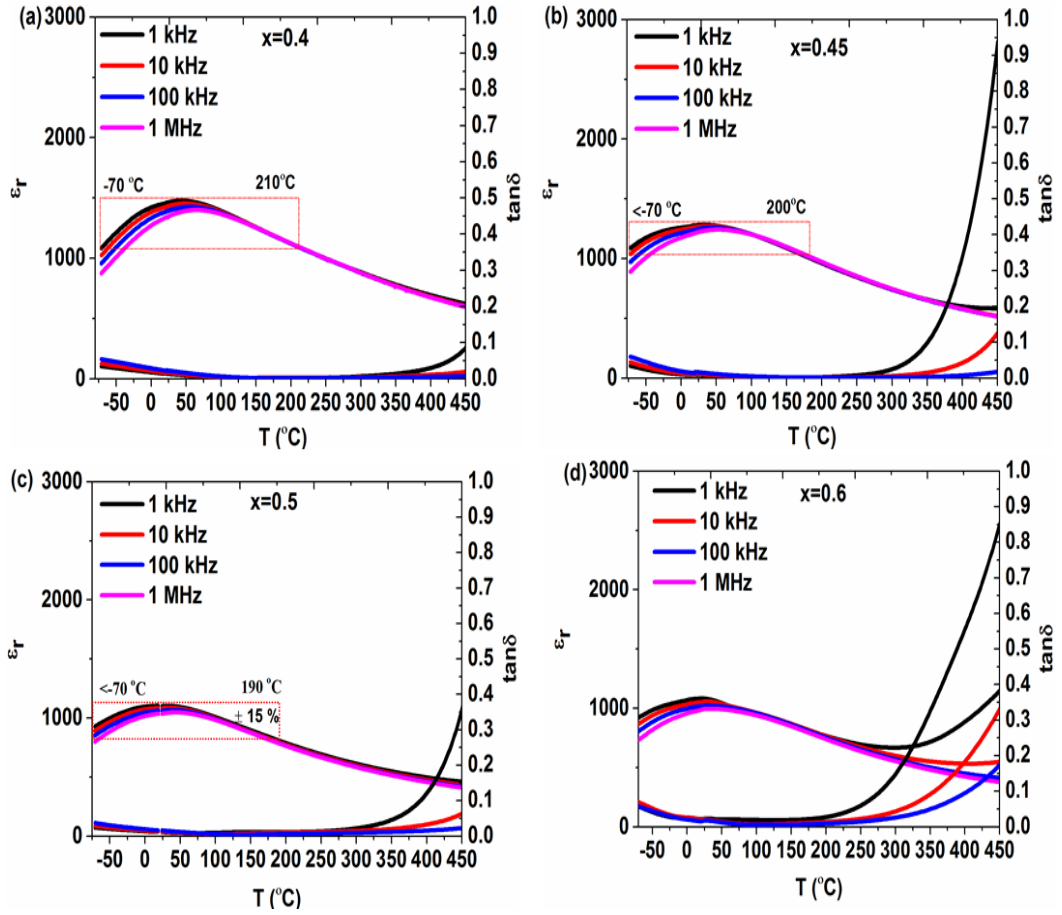

Figure 7.4 Temperature-dependent relative permittivity (ε_r) and tanδ of (1–x)[$0.85Na_{0.5}Bi_{0.5}TiO_3 – 0.15Ba_{0.8}Ca_{0.2}TiO_3$] – $xNaNbO_3$, (a) x = 0.4, (b) x = 0.45, (c) x = 0.5 and (d) x = 0.6.

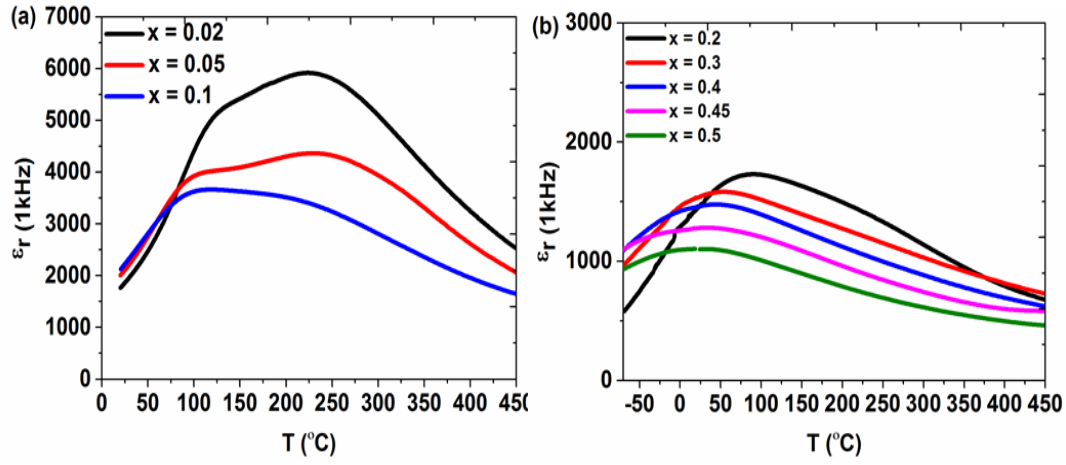

Figure 7.5 Temperature-dependent relative permittivity (ε_r) of (1–x)[$0.85Na_{0.5}Bi_{0.5}TiO_3 – 0.15Ba_{0.8}Ca_{0.2}TiO_3$] – $xNaNbO_3$, (a), x = 0.02 – 0.1 and (b) x = 0.2 – 0.5 (at 1 kHz).

Table 7.2 Summary of the dielectric properties of ceramics system (1–x) [0.85$Na_{0.5}Bi_{0.5}TiO_3$ – 0.15$Ba_{0.8}Ca_{0.2}TiO_3$] – x$NaNbO_3$, ($0 \leq x \leq 0.5$).

x mol%	ε_{25^oC}	T_m (°C)	ε_{max}	ε_{mid}	ε_{mid} ± 15 % T-range (°C)	T-range (°C) (tanδ ≤ 0.02)
0	1190	250	6120	----	----	170 – 410
0.02	1870	220	5690	4950	90 – 350	140 – 310
0.05	2110	230	4360	3800	70 – 360	110 – 420
0.1	2230	100	3630	3190	50 – 320	100 – 310
0.2	1530	90	1720	1500	-10 – 290	50 – 310
0.3	1550	50	1580	1400	-50 – 240	20 – 340
0.4	1460	40	1480	1300	-70 – 210	-10 – 380
0.45	1280	30	1280	1100	-70 – 200	-40 –300
0.5	1100	20	1100	950	<-70 – 190	-50 – 290
0.6	1080	20	1080	940	<-70 – 180	80 – 160

7.3.1 Modified Curie Weiss law

The diffuseness of phase transition of the ceramics system (1–x)[0.85$Na_{0.5}Bi_{0.5}TiO_3$ – 0.15$Ba_{0.8}Ca_{0.2}TiO_3$] – x$NaNbO_3$ ($0 \leq x \leq 0.5$) were determined using modified Curie Weiss law (Du et al., 2008). Figure 7.6, shows plots of $\ln(1/\varepsilon - 1/\varepsilon_m)$ as a function of $\ln(T - T_m)$ for ($0 \leq x \leq 0.5$). A linear relationship was observed for all ceramics. The values of γ were ranged between 1.53 – 2.01, indicating a typical relaxor behaviour for $x \geq 0$ (as explained in previous chapters). A maximum value, $\gamma \sim 2.0$ was observed $x \leq 0.1$.

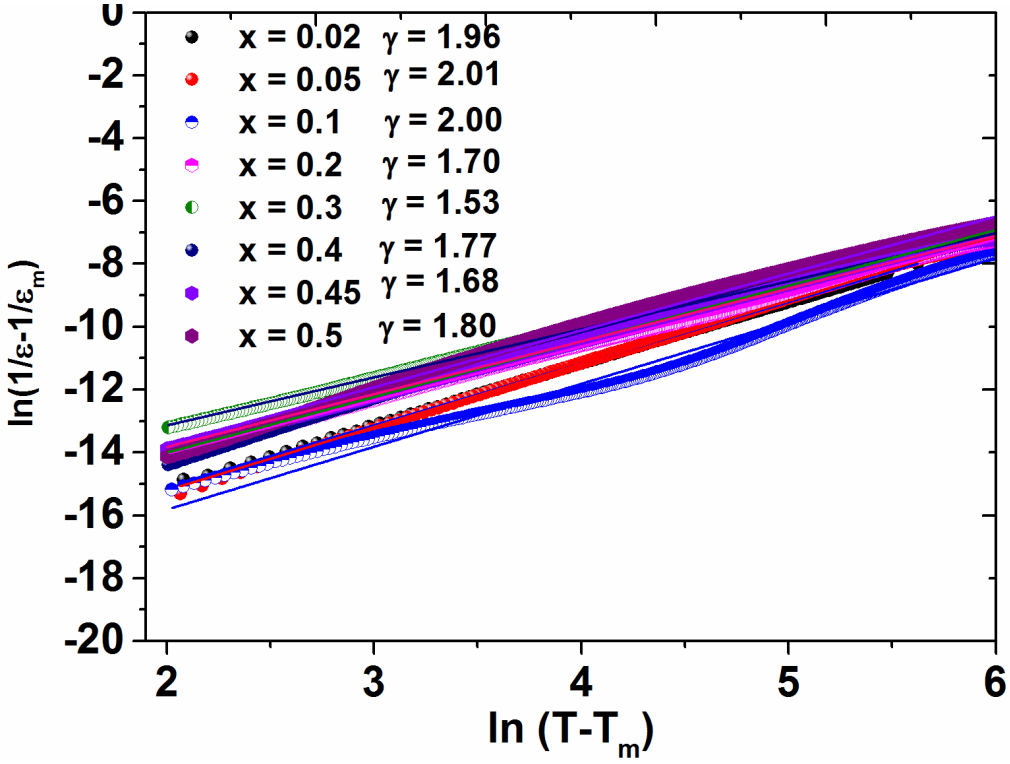

Figure 7.6 Plots of $\ln(1/\varepsilon - 1/\varepsilon_m)$ versus $\ln(T - T_m)$ for, x = 0.02 – 0.5.

7.4 Density and microstructural analysis

The theoratical densities of the ceramics system $(1–x)[0.85Na_{0.5}Bi_{0.5}TiO_3 – 0.15Ba_{0.8}Ca_{0.2}TiO_3] – xNaNbO_3$ were calculated using formula $\rho = (1.66 \sum A)/V$, where A is mass number and V is the volume of the unit cell. The lattice cell parameters and unit cell volume was calculated from XRD peak fitting using software FP suit.

The geomteric and relative densities as a function of x mol % NN are shown in Figure 7.7. SEM micrographs of ceramics $x \leq 0.4$ are shown in Figure 7.8. Scanning electron microscopy showed the maximum grain size was the range of 3 – 6 μm.

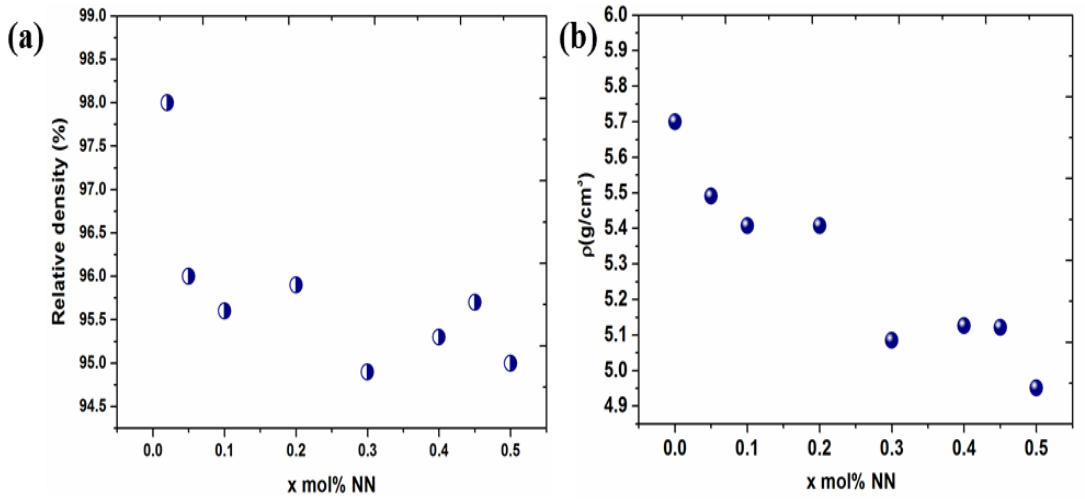

Figure 7.7 Plots of (a) Relative density and (b) Geometric density as a function of x mol% $NaNbO_3$.

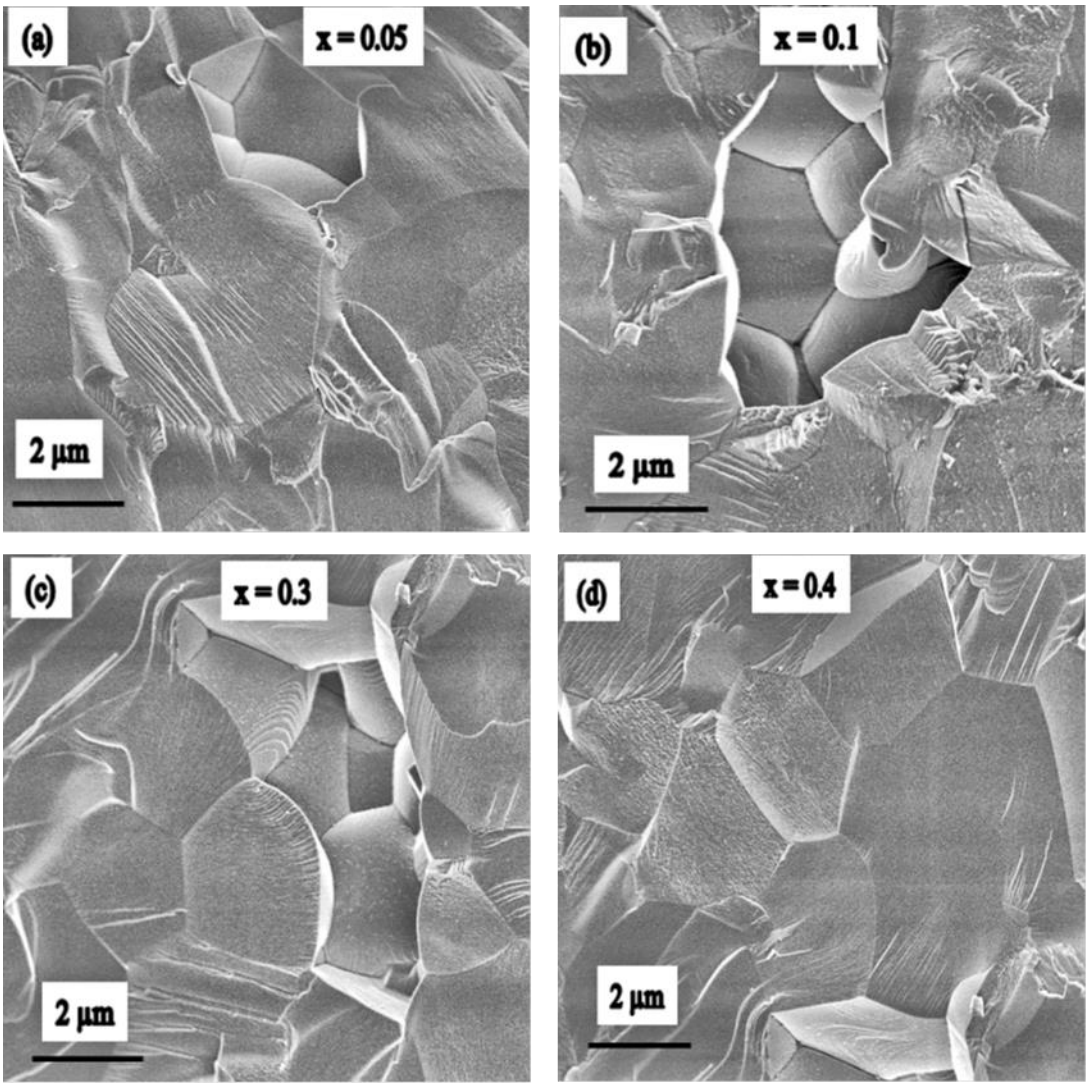

Figure 7.8 SEM micrographs of a) x = 0.05, b) x = 0.1, c) x = 0.3, and d) x = 0.4.

7.5 Resistivity analysis

The dc resistance for x = 0.1 and 0.3 were recorded as a function of temperature in the range 250 ºC – 550 ºC at a fixed voltage of 80 V, is shown in Figure 7.9. All the resistances were taken after a 30 minute stay at each temperature. The resistivity dropped from $\times 10^9$ – $\times 10^8$ Ω m at 250 ºC down to $\times 10^4$ Ω m at 550 ºC, which is comparable to the resistivity observed by Dittmer et al. and Zeb et al., for $Bi_{0.5}Na_{0.5}TiO_3$ – $BaTiO_3$ – $K_{0.5}Na_{0.5}NbO_3$ (x = 0.9 – 0.18) and $Ba_{0.8}Ca_{0.2}TiO_3$–$BiMg_{0.5}Ti_{0.5}O_3$ – $NaNbO_3$ (x =0.2 – 0.3) respectively (Dittmer et al., 2012, Zeb and Milne, 2014a).

The values of activation energy E_a for the electrical conductivity in the temperature rang 250 – 550 ºC, obtained from linear fit of experimental data, were 0.25 eV (x = 0.1), 0.20 eV (x = 0.3) in the studied temperature range. These values of activation energy might be attributed to the oxygen ion migration in perovskites (Zeb and Milne, 2014a, Selvamani et al., 2012, Islam, 2000, Raengthon and Cann, 2012)

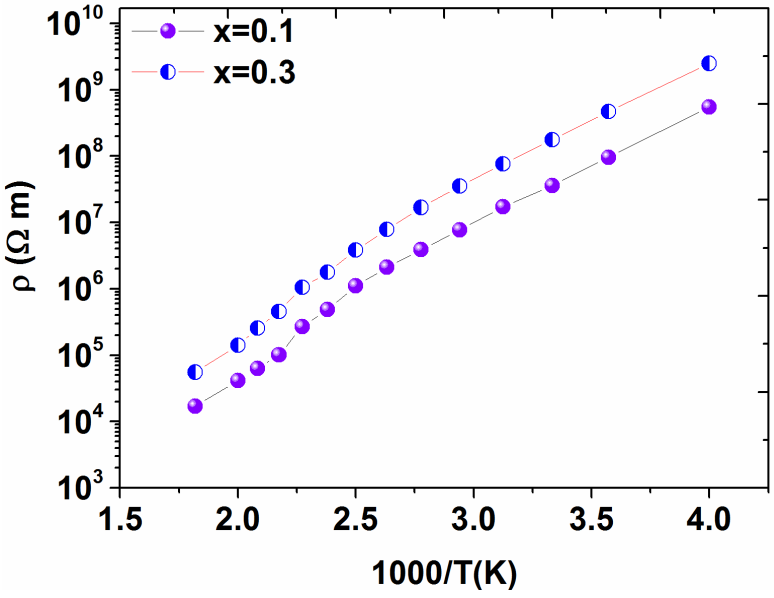

Figure 7.9 Resistivity of ceramics, x = 0.1 and 0.3 as a function of inverse absolute temperature.

7.6 Conclusions

Ceramics in the system $(1–x)[0.85Na_{0.5}Bi_{0.5}TiO_3 – 0.15Ba_{0.8}Ca_{0.2}TiO_3] – xNaNbO_3$ ($0 \leq x \leq 0.8$) were prepared by conventional solid state route. The XRD of ceramic samples, $x > 0$ were consistent with cubic/pseudocubic symmetry.The relative permittivity and the corresponding peak temperature decreased with increasing x. Temperature-stable relative permittivities changing by no more than ± 15 % were ranged between -70 – 200/210 ºC for $x = 0.4$ and 0.5. This ability to maintain consistent permittivity down to to the military standard (EIA) lower limit of -55°C and extend the upper limit from 125 - 175°C for X7R - X9R to ≥ 200 °C is promising in a single material. The $x = 0.3$ sample is also atrractive, with a stability from -50 °C and up to 240 °C. From a charge storage point of view, the relative permittivities of 1100-1400 are also favourable. However in terms of high and stable permittivity allied to low losses, the $x = 0.5$ sample stands out, with $\varepsilon_r \sim 950 \pm 15$ % allied to $\tan \delta \leq 0.02$ from -50 to 290 °C.

Chapter 8

Dielectric properties of (1–x)$Ba_{0.6}Sr_{0.4}Zr_{0.2}Ti_{0.8}O_3$ – x$BiMg_{0.5}Ti_{0.5}O_3$ solid solutions

8.1 Introduction

A series of solid solutions, (1–x)$Ba_{0.6}Sr_{0.4}Zr_{0.2}Ti_{0.8}O_3$ – x$BiMg_{0.5}Ti_{0.5}O_3$ ($0 \leq x \leq 0.8$), abbreviated as BSZT – BMT, were prepared by a mixed oxide route. XRD patterns have shown cubic symmetry but secondary phases were detected for $x > 0.5$. The a-lattice parameters and volume of unit cell decreased with increasing x.

Temperature-stable relative permittivity was revealed for samples, $x = 0.2$ with $\varepsilon_r \sim 500 \pm 15\%$, in the temperature range < -70 – 300 ºC and $\tan\delta \leq 0.02$ in the temperature range -60 – 300 ºC. For $x = 0.3$, $\varepsilon_r \sim 590 \pm 15\%$, in the temperature range -60 – 340 ºC and $\tan\delta \leq 0.02$ in the temperature range -10 – 280 ºC. The compositions $x = 0.2$ and 0.3 are of great interest because they combine a high upper limit of stable permittivity with a lower limit meeting EIA standard military specifications. P-E hysteresis loops for $x = 0.2$ and $x = 0.4$ measured up to 50 kV/cm have shown a linear capacitor response with very low leakage current. A high dc resistivity ~ 10^{10} Ω m was observed for $x = 0$ and 0.2 at 300 ºC.

8.2 Results

8.2.1 X-ray diffraction analysis of $(1–x)Ba_{0.6}Sr_{0.4}Zr_{0.2}Ti_{0.8}O_3 – xBiMg_{0.5}Ti_{0.5}O_3$

Single-phase cubic perovskite XRD patterns were observed for $x \leq 0.5$. The $x > 0.5$ sample showed secondary phase peaks that are in similar positions to strongest reflections from of Bi_2O_3 (ICDD 04-015-0028) Figure 8.1. A linear decrease in lattice parameters and volume of unit cell was observed with increasing x, Figure 8.2. This effect can be seen from a slight shift of XRD peaks towards higher diffraction angles/lower d-spacing. The decrease in lattice parameters might be attributed to the incorporation of smaller size cations Bi^{3+} on A-site (see Appendix 1), leading to the shrinkage of oxygen octahedra.

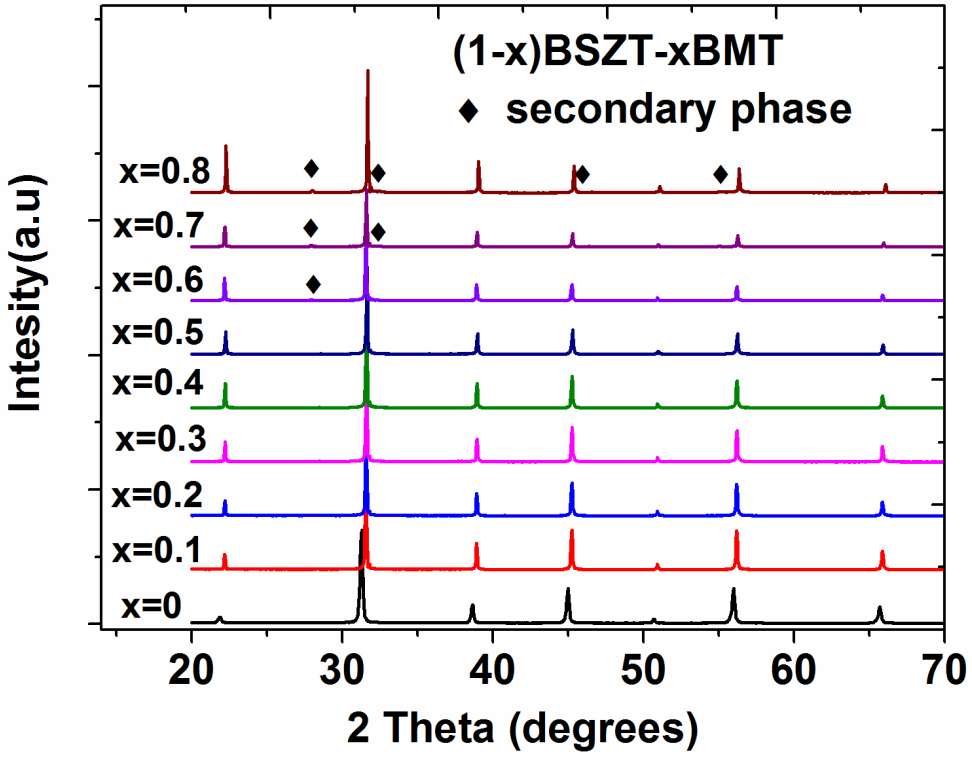

Figure 8.1 XRD patterns of $(1–x)Ba_{0.6}Sr_{0.4}Zr_{0.2}Ti_{0.8}O_3 – xBiMg_{0.5}Ti_{0.5}O_3$ ($0 \leq x \leq 0.8$) at ambient temperature.

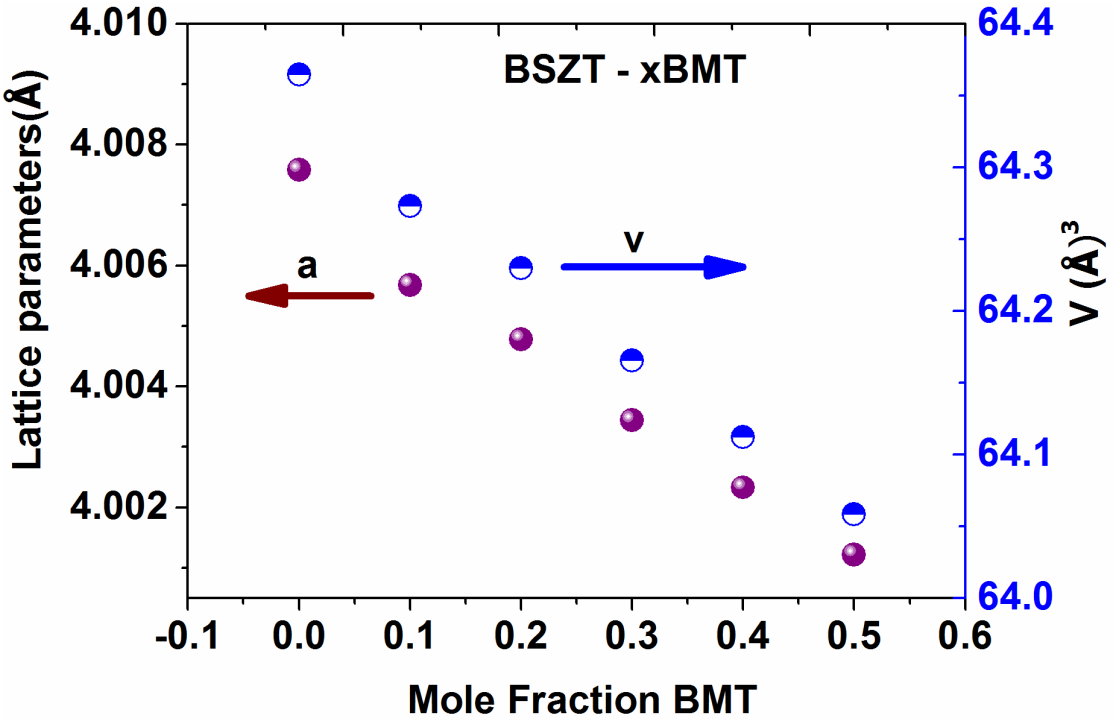

Figure 8.2 Lattice parameters and volume of unit cell versus mol fraction $BiMg_{0.5}Ti_{0.5}O_3$ (BMT).

8.2.2 Relative permittivity of solid solutions (1-x)$Ba_{0.6}Sr_{0.4}Zr_{0.2}Ti_{0.8}O_3$ – x$BiMg_{0.5}Ti_{0.5}O_3$ ($0 \leq x \leq 0.8$).

The evolution of relative permittivity (ε_r) and loss tangent (tanδ) versus temperature (T) for ceramics (1–x)$Ba_{0.6}Sr_{0.4}Zr_{0.2}Ti_{0.8}O_3$ – x$BiMg_{0.5}Ti_{0.5}O_3$ ($0 \leq x \leq 0.8$) over the temperature range -70 – 400 ºC is shown in Figure. 8.3-8.4. The $x > 0$ samples displayed temperature-stable relaxor character, with plateau-like ε_r –T plots . However for $x = 0$, the ε_r-T peak lay below the minimum measurement temperature of the equipment (-70 ºC). For $x > 0$, the incorporation of BMT, raised the temperature of the maximum dielectric constant (T_m), Figure 8.5, reaching ~ 130 ºC for $x = 0.5$, Table 8.1. For $x > 0.1$, maximum ε_r values increased from ≤ 500 at $x = 0.1$ to 1230 at $x = 0.5$, Figure 8.3-8.4. Temperature-stable relative permittivity (Table 8.1) was revealed for samples, $x = 0.1$, ε_r ~ 400 ± 15 %, in the temperature

range < -70 – 125 ºC and tanδ ≤ 0.02, across the temperature range -70 – 125 ºC. For x = 0.2, ε_r ~ 500 ± 15%, in the temperature range < -70 – 300 ºC and tanδ ≤ 0.02, temperature-range -60 – 300 ºC. For x = 0.3, ε_r ~ 590 ± 15%, in the temperature range -60 – 340 ºC and tanδ ≤ 0.02 in the temperature range -10 – 280 ºC. For x = 0.4, ε_r ~ 710 ± 15%, in the temperature range 0 – 400 ºC+ and tanδ ≤ 0.02, temperature range 50 – 270 ºC. For x = 0.5. ~ 1110 ± 15%, in the temperature range 45 – 400 ºC+ and tanδ ≤ 0.02, temperature range 80 – 390 ºC.

With reference to the search for new Class II temperature-stable capacitor materials with 'R' type stability (according to EIA classifications) but with higher operating temperature >> 200 ºC than existing X7R – X9R dielectrics (-55 – 125 ºC for X7R, -55 to 175 ºC for X9R) (Zhang, 2015), composition x = 0.2 and x = 0.3 are of greatest interest. As mentioned earlier in the thesis, the broad temperature-stable permittivity range is thought to relate to distributions of ions with different ionic radii and electronic charges, both on A-site (Ba^{2+}, r =1.61 Å, CN = 12), (Sr^{2+}, r =1.44 Å, CN = 12) (Shannon, 1976) , (Bi^{3+}, estimated, r =1.3-1.39 Å, CN = 12) (Suarez et al., 2001, Sivakumar and Itoh, 2011) and B-site (Zr^{4+}, r = 0.72 Å, CN =6), (Mg^{2+}, r = 0.72 Å, CN =6) , (Ti^{4+}, r = 0.61 Å, CN =6) (Shannon, 1976).

The temperatures of consistent relative permittivity shifted towards higher temperatures with increasing x, from < -70 – 125 ºC, for x = 0.1 to 45 – 400 ºC+ for x = 0.5. The frequency dispersion increased with increasing x. The sample x = 0.7, presented higher losses, which might be attributed to the presence of secondary phases.

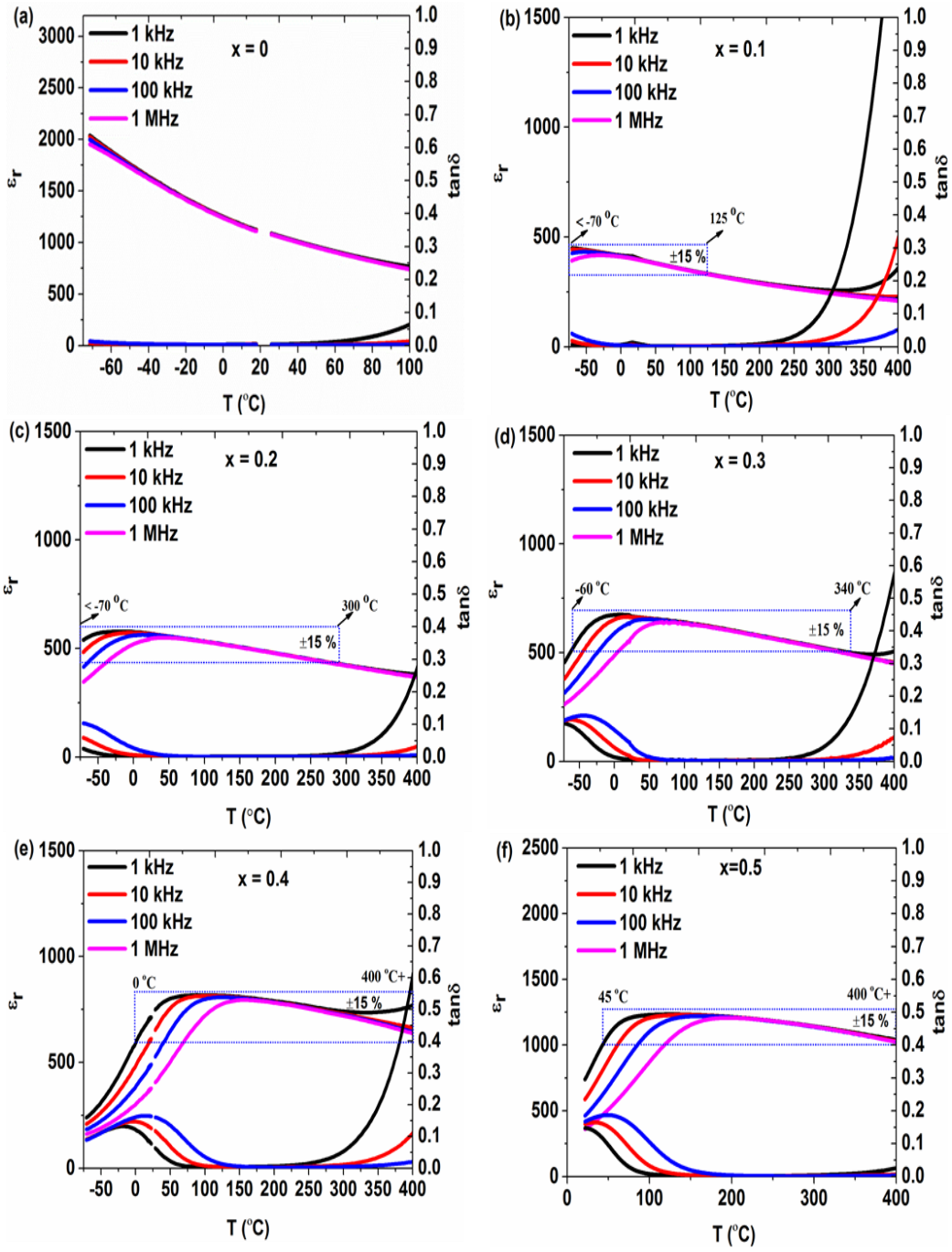

Figure 8.3 Temperature-dependent relative permittivity and tanδ of (1-x)$Ba_{0.6}Sr_{0.4}Zr_{0.2}Ti_{0.8}O_3$ – x$BiMg_{0.5}Ti_{0.5}O_3$, (a) x = 0, (b) x = 0.1, (c) x = 0.2 (d) x = 0.3, (e) x = 0.4 and (f) x = 0.5. (data set continued in Figure 8.4)

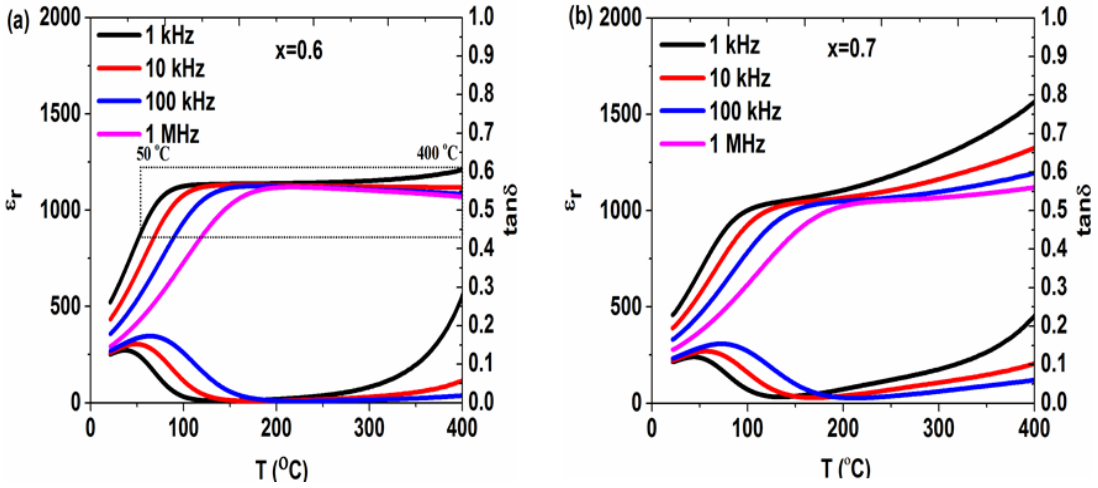

Figure 8.4 Temperature-dependent relative permittivity and tanδ of (1-x)$Ba_{0.6}Sr_{0.4}Zr_{0.2}Ti_{0.8}O_3$ – x$BiMg_{0.5}Ti_{0.5}O_3$, (a) x = 0.6 and (b) x = 0.7.

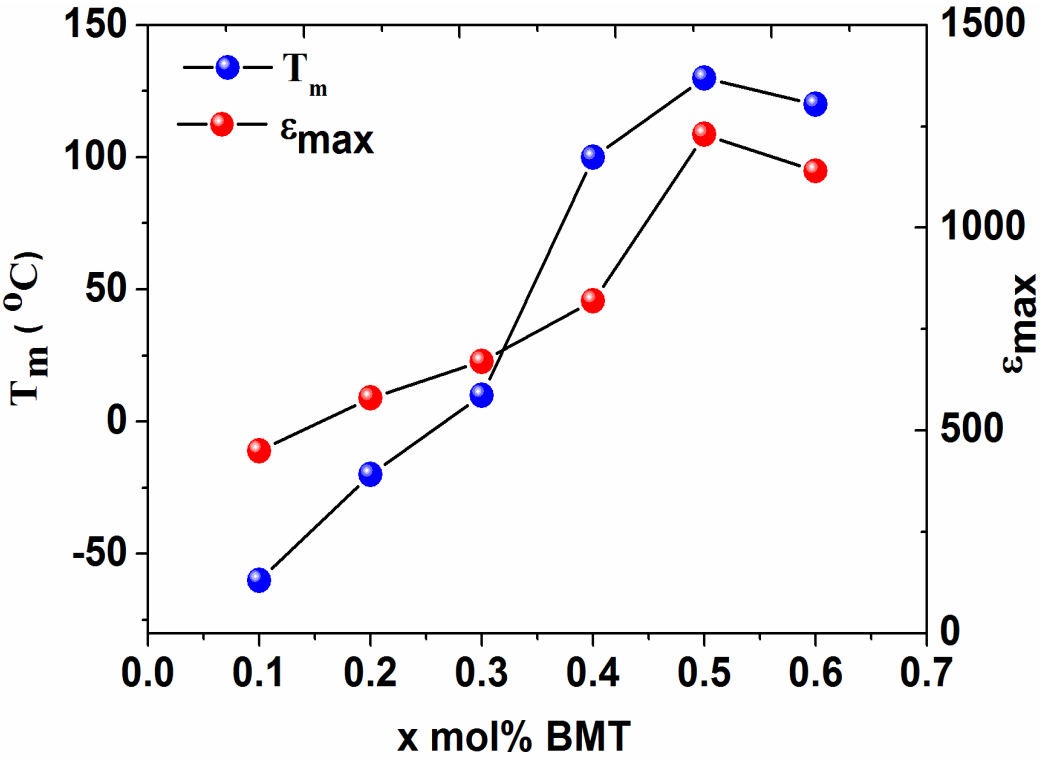

Figure 8.5. Maximum relative permittivity and its corresponding temperature versus mole fraction BMT of (1–x)$Ba_{0.6}Sr_{0.4}Zr_{0.2}Ti_{0.8}O_3$ – x$BiMg_{0.5}Ti_{0.5}O_3$, x = 0.1 – 0.6.

Table 8.1 Summary of dielectric properties of (1–x)$Ba_{0.6}Sr_{0.4}Zr_{0.2}Ti_{0.8}O_3$ – x$BiMg_{0.5}Ti_{0.5}O_3$ ceramics

Sample	**$\varepsilon_{25\,°C}$**	**T_m/°C**	**ε_{max}**	**ε_{mid} ± 15 % and T-range (1 kHz)**	**tanδ ≤ 0.02) 1 kHz (T-range)**
x=0	1090	------	2020	------	-70 °C – 70 °C
x=0.1	400	-60	450	<-70 °C – 125 °C (400 ± 15%)	-70 °C – 230 °C
x=0.2	560	-15	580	<-70 °C – 300 °C (500 ± 15%)	-60 °C – 310 °C
x=0.3	670	10	670	-60 °C –340 °C (590 ± 15%)	-10 °C – 280 °C
x=0.4	750	100	820	0 °C – 400 °C + (710 ± 15%)	50 °C – 270 °C
x=0.5	700	130	1230	45 °C – 400 °C + (1110 ± 15%)	80 °C – 390 °C
x =0.6	560	120	1140	50 – 400 °C+ (990 ± 15%)	100 – 250 °C

8.2.2.1 Modified Curie Weiss law

Using the modified Curie Weiss law, (Uchino, 1994), the value constant (γ), calculated from linear fit plot of ln $(1/\varepsilon - 1/\varepsilon_m)$ vs ln $(T - T_m)$, increased with increasing x, Figure 8.6. This increase in diffuseness constant might be the result of chemical heterogeneity of both A-site and B-site cations.

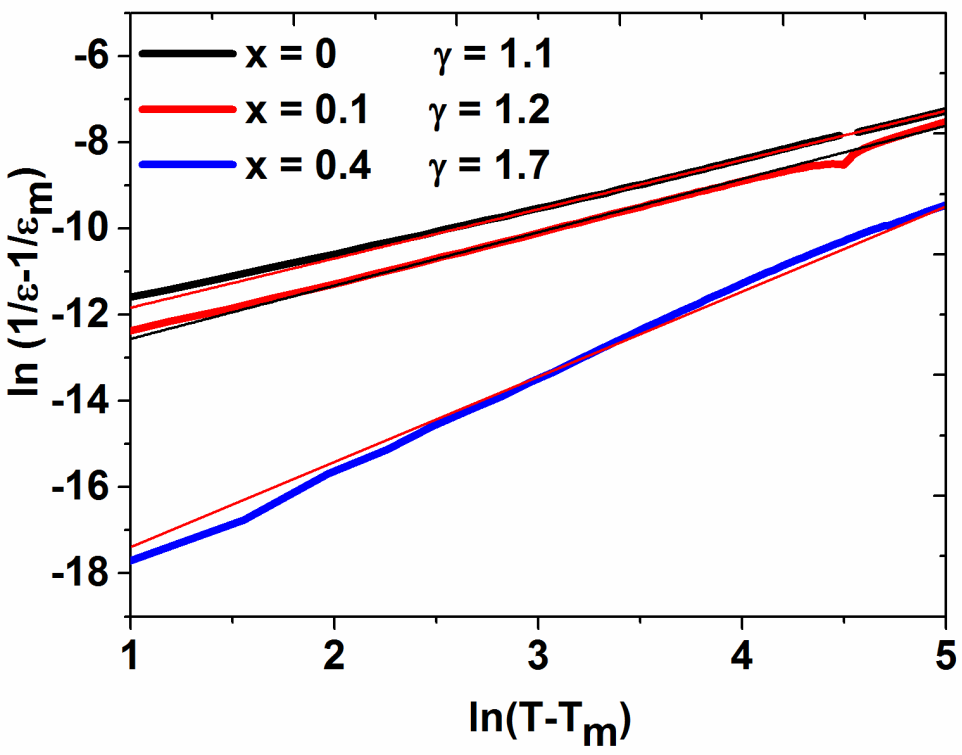

Figure 8.6 plots of linear fit of experimental data, ln ($1/\varepsilon - 1/\varepsilon_m$) V.s ln ($T - T_m$) of $(1–x)Ba_{0.6}Sr_{0.4}Zr_{0.2}Ti_{0.8}O_3 – xBiMg_{0.5}Ti_{0.5}O_3$, x = 0, 0.1 and 0.4 (1 kHz).

8.2.3 Resistivity analysis

The dc resistivity of the ceramics was measured in the temperature range 300 – 550 ºC. The resistivity showed Arrhenius behaviour with predominantly linear curves in the logarithmic plot against inverse absolute temperature Figure 8.7. The maximum resistivity values observed at 300 ºC for x = 0, 0.2 and 0.4 were ~10^{10} Ω m. Such high values of resistivity are comparable to those reported for a number of high-temperature, high permittivity dielectrics (Dittmer, 2011, Acosta, 2012). The activation energy E_a observed for electrical conductivity were 0.81 eV (x = 0), 0.78 eV (x = 0.2) and 0.64 eV (x = 0.4), which might be attributed to the oxygen ion vacancy migration (Zeb, 2014).

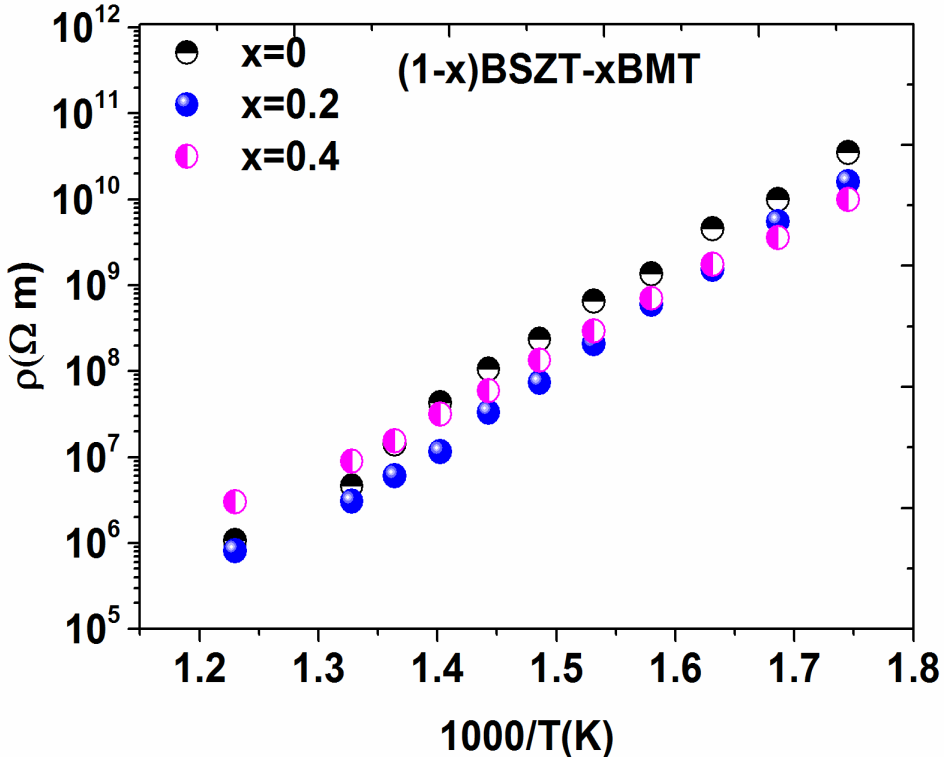

Figure 8.7 plots of log resistivity versus 1/T(K) of (1–x)$Ba_{0.6}Sr_{0.4}Zr_{0.2}Ti_{0.8}O_3$ – x$BiMg_{0.5}Ti_{0.5}O_3$, x = 0 – 0.4.

8.2.4 Polarization-electric field hysteresis loop

Room temperature polarization-electric field hysteresis loops measured for E ≤ 50 kV/cm are shown in Figure 8.8. No ferroelectric behaviour was detected in any sample. Slim P-E loops with no evidence of ferroelectric switching were observed for x = 0 and 0.5. For x = 0.2 and 0.4 a linear P-E response indicates a capacitor with negligible leakage current.

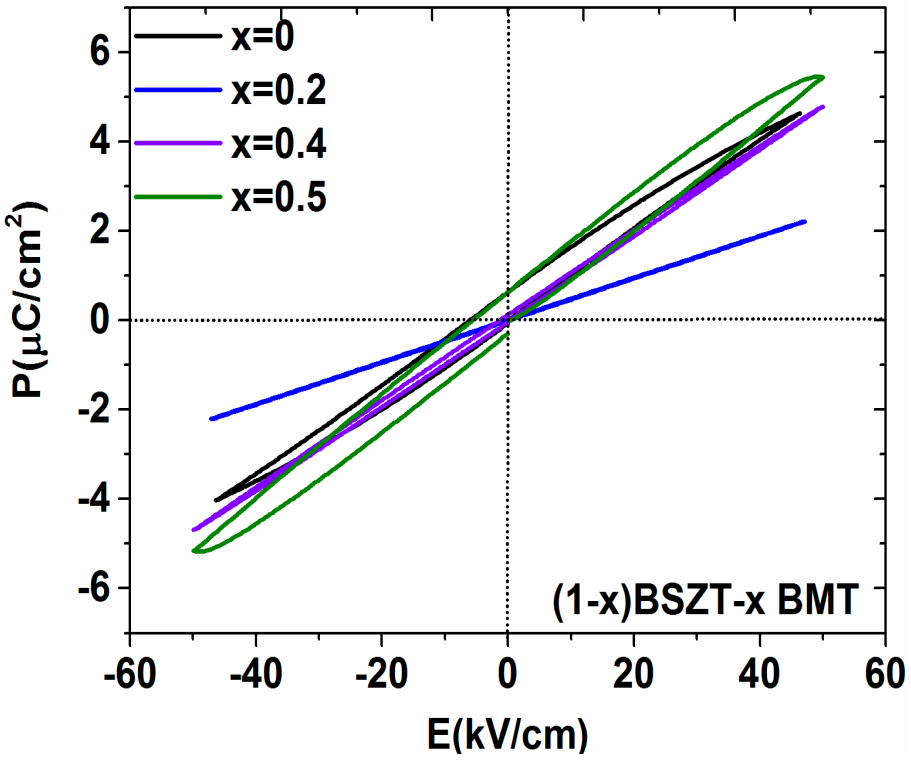

Figure 8.8 P-E response for ceramics compositions, (1–x)$Ba_{0.6}Sr_{0.4}Zr_{0.2}Ti_{0.8}O_3$ – x$BiMg_{0.5}Ti_{0.5}O_3$, x = 0 – 0.5.

8.2.5 Microstructural examination

SEM examination of ceramics BSZT – BMT showed particle size ≤ 4 μm. The particle size decreased from ~ 4 μm (x = 0) to ~ 2 μm (x = 0.3) Figure 8.9. Relative densities of the ceramics were in the range ~90 –93 %

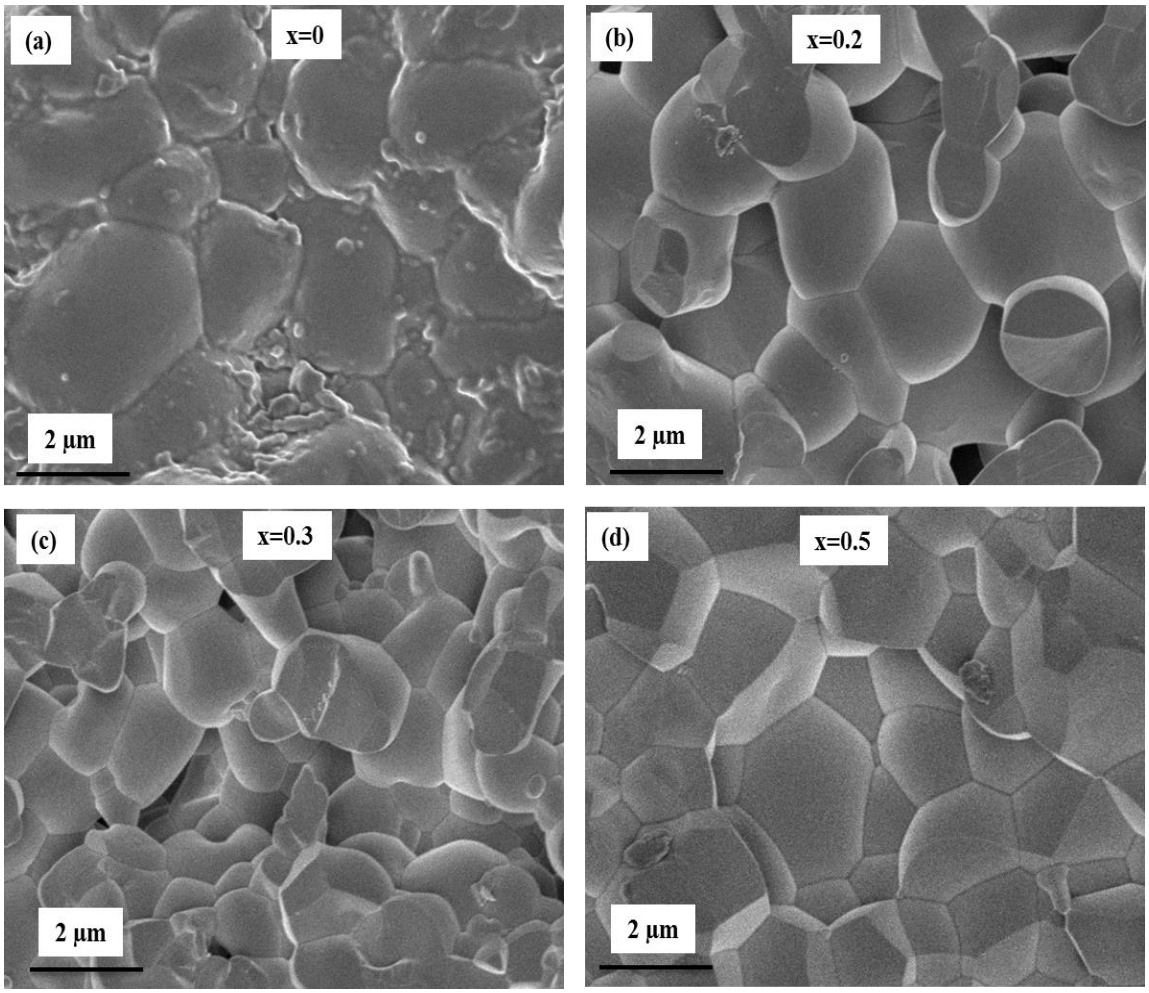

Figure 8.9 SEM micrographs of (1–x)$Ba_{0.6}Sr_{0.4}Zr_{0.2}Ti_{0.8}O_3$ –x$BiMg_{0.5}Ti_{0.5}O_3$, (a) x = 0, (b) x = 0.2, (a) x = 0.3 and (d) x = 0.5.

8.3 Conclusions

X-ray powder diffraction patterns revealed a cubic or pseudocubic structure for ceramics, $x \geq 0$. Secondary phases were detected for samples, $x \geq 0.6$. The a-lattice parameters has shown a linear decrease with increasing x. The temperature corresponding to maximum relative permittivity (T_m) increased with increasing x, reaching a maximum of ~130 ºC for x = 0.5. Temperature-stable relative permittivity was most promising for samples, x = 0.2, ~ 500 ± 15%, in the temperature range < -70 – 300 ºC and $\tan\delta \leq 0.02$, T-range -60 – 300 ºC and for x = 0.3 ~ 590 ± 15%, in the temperature range -60 – 340 ºC and $\tan\delta \leq 0.02$, T-range -10 – 280 ºC. Ceramics, x = 0.2 and 0.3 are of great interest due to high temperature stability ~ 300 ºC, with reference to the present X7R – X9R capacitors. Samples, x = 0.2 – 0.4 gave P-E responses of a dielectric capacitor behaviour with very low leakage current. High resistivity ~ 10^{10} Ω m (at 300 ºC) was observed for samples, x = 0 – 0.2.

Chapter 9

Overall discussions and conclusions

A number of novel perovskite solid solutions explored in this thesis have demonstrated extended temperature-stable permittivity.

Lead-free relaxors were the starting point for compositional modification to supress the peak in relative permittivity-temperature plots and hence reduce the temperature-variation in relative permittivity above the peak temperature T_m. The normal relaxor characteristic (in for example lead magnesium niobate) is generally attributed to the existence of polar nano regions (PNRs) which start to form at the Burns temperature T_B ($T_B >> T_m$) (Kleeman 2012, Shvartsman, 2012). At temperatures just below T_B, the PNRs are weakly correlated and are highly dynamic. The interfacial regions between PNRs are considered to be non-polar.

Upon further cooling below T_B, the size and total volume of PNRs increases, as demonstrated in the literature, and hence relative permittivity increases until a temperature T_m is reached. As T_m is approached, the coupling and re-orientation of PNRs under an electric field becomes energetically more difficult until at $T < T_m$ the energy term dominates over the effects of increased PNR size, and measured permittivity declines. The combined effect is to create a peak in relative permittivity plots. The peak is broad (diffuse) due to the distribution of relaxation times of PNRs present in the sample. The frequency dependence of T_m reflects the kinetics of coupling between PNRs, i.e. re-orientation (relaxation) timescales. Eventually, as temperature falls well below T_m, PNR re-orientation is no longer possible under

low-signal conditions and a 'freezing' temperature T_f is reached: PNRs are no longer dynamic (Shvartsman, 2012).

The above describes normal relaxor behaviour such as in lead magnesium niobate. The reason why PNRs form in relaxor dielectrics perovskites are generally accepted to be due to distributions of mixed valence and different sized cations sizes on either or both the A and B lattice sites. If B-site ions such as Zr or Mg, are present which do not take up off–centre positions in the unit cell, they also disrupt the dipole length scales and contribute to lattice disorder in a relaxor (Shvartsman, 2012). Some literature refers to these effects as chemically ordered regions (CORs). The consequence of a heterogeneous lattice is the formation of random electric fields (RFs) due to cation valence disorder; stress fields arise due to size mismatches. Both effects contribute to the prevention of long range ferroelectric and instead create PNRs.

Appendix 1 lists ionic radii and valence of cations relevant to this thesis. The most likely explanation for the change from normal relaxor to temperature-stable relaxor behaviour, typified by flattened ε_r-T plots in this thesis is that the level of cation disorder is such that the normal thermally induced increases in size of PNRs between T_B and T_m are supressed, and so a sharp rise in permittivity do not occur. In some cases the flattened response is due to the overlap in temperatures of two dielectric anomalies-the main broad peak and the lower temperature inflection; in others a normal relaxor ε_r-T plate evolves into a plateau-like plot.

Another student in my research group has investigated micro and nanostructure using SEM and TEM but found no evidence of core-shell chemical segregation (in lower temperature X7R dielectrics, core-shell microstructures give smearing of a ferroelectric Curie peak and create temperature stable properties). The

absence of obvious core-shell structures suggest the mechanisms behind a temperature-stable relaxor involve heterogeneities on the scale of a few nm or 10s of nm (i.e smaller than the effective electron beam area and volume).

In this study plateau-like permittivity plots with very favourable, temperature ranges of stable permittivity were obtained through compositional engineering of a relaxor base material using high levels of substitution of cations of different charge and size to the host lattice. Such substitutions lead to defects and random electric fields in dielectrics which give rise to PNRs as discussed above.

The solid solution series $(1–x)Na_{0.5}Bi_{0.5}TiO_3 – xBa_{0.8}Ca_{0.2}TiO_3$ [(1–x)NBT – xBCT] was studied initially in this project but showed little evidence of temperature-stable relative permittivity. However, 0.85NBT – 0.15BCT ceramics modified with $BiMg_{0.5}Ti_{0.5}O_3$, [BMT] were more promising. For the series, $(1–x)[0.85Na_{0.5}Bi_{0.5}TiO_3–0.15Ba_{0.8}Ca_{0.2}TiO_3] – xBiMg_{0.5}Ti_{0.5}O_3$ sample x = 0.3, gave ε_r ~ 1720 ± 15 %, in the temperature range 120 to 450 ºC, and low dielectric loss tangent, $\tan\delta \leq 0.02$, over the slightly narrower temperature range, 150 to 360 ºC. Thus an upper operating temperature > 300°C was demonstrated but without achieving sub-zero lower temperature capability. The temperature-stable relaxor character for samples $x \geq 0.3$ might be correlated to high levels of substitution of cations of different charge and size on A- and B- perovskite sites, namely A = Na^+, Ca^{2+} , Ba^{2+}, Bi^{3+} ; B = Ti^{4+}, Mg^{2+} (Appendix 1 gives ionic radii)

Similarly, the system $(1–x)[0.85Na_{0.5}Bi_{0.5}TiO_3 – 0.15Ba_{0.8}Ca_{0.2}TiO_3] – xLiNbO_3$ abbreviated [(1–x)[NBT – BCT] – xLN] gave ε_r ~ 2630 ± 15 % from 50 ºC to 410 ºC, and $\tan\delta \leq 0.02$ from 120 ºC to 400 ºC, at composition x = 0.06. The flattened response in this case appears to involve overlap in the temperature of the main dielectric peak and an inflection at slightly lower temperatures for composition

x = 0.06. It has been speculated that a similar response in a KBT – NBT – KNN temperature stable relaxor may be due to two different types of PNRs ‘high’ and ‘low’ temperature (Dittmer, 2011, 2012). However the true structural reasons have yet to be resolved.

The incorporation of $NaNbO_3$ [NN] in place of $LiNbO_3$ achieved the desired sub-zero temperature capability in relative permittivity, with an upper temperature limit slightly above 200 ºC. Examples include (1–x)[NBT – BCT] – xNN composition x = 0.3 with ε_r = 1400 ±15 % from -50 to 240 °C and tanδ ≤ 0.02 from 20 ºC to 240 ºC; for x = 0.4, ε_r = 1300 ±15 % from -70 to 210 °C and tanδ ≤ 0.02 from -10 ºC to 210 ºC.

In terms of the project goal of achieving a temperature range of stable permittivity combined with a low loss extending from temperatures of -55 °C (to meet the Electronic Industry Alliance military specification) up to 300 °C, the binary solid solution system (1–x)$Ba_{0.6}Sr_{0.4}Zr_{0.2}Ti_{0.8}O_3$ – x$BiMg_{0.5}Ti_{0.5}O_3$ [(1–x)BSZT – xBMT] was most promising. However there was a trade-off in that permittivity values were lower than the foregoing systems. The (1–x)BSZT – xBMT sample composition x = 0.2 gave ε_r ~ 500 ± 15%, in the temperature range -70 to 300 ºC and tanδ ≤ 0.02, in the range -60 to 300 ºC.

Hence the dielectric properties of (1–x)BSZT – xBMT closely matches the target temperature-range of the project, but the volumetric efficiency of a capacitor made from this dielectric would be compromised due its moderate relative permittivity values. Slightly higher values of relative permittivity were obtained for x = 0.3 in the (1–x)BSZT – xBMT, with ε_r ~ 590 ± 15%, across the temperature range -60 to 340 ºC, but in this case the temperature range of low dielectric losses tanδ ≤ 0.02 was restricted to -10 to 280 ºC.

In order to reduce high temperature losses, experiments using excess bismuth oxide to compensate for volatilisation loss, and experiments incorporating manganese cations to alter defect chemistry were conducted. Results were variable, but this aspect is worth pursuing in future work.

A comparison of the temperature-stable relative permittivity of selected compositions from this study and comparison with the best materials reported in the literature are presented in the bar chart, Figure 9.

Majority of the lead-free temperature-stable dielectrics reported in the early literature have shown temperature stability well above 200 ºC, but without achieving the sub-zero level temperature (-55 ºC) in accordance with Electronic Industries Alliance (EIA) specifications for R-type dielectric capacitors, for example, 0.6NBT – 0.4KBT – 0.15KNN, 0.94NBT – 0.06BT – 0.18KNN, 0.45BCT – 0.55BMT and many more, Figure 9 (b).

In this study some of the newly explored ceramic compositions, 0.7[0.85NBT – 0.15BCT] – 0.3BMT, 0.93[0.85NBT – 0.15BCT] – 0.07LN and many more discussed in Chapters, 5, 6, 7 and 8, have shown a wide range of dielectric temperature-stability ($\varepsilon_r \pm 15$ %) extending from temperature ranges, 30 - 120 ºC, to well above 200 ºC, but without achieving the low temperature target, -55 ºC, Figure 9 (a).These novel lead-free compositions have shown comparable relative permittivity values to some of the previously reported compositions, for example, 0.6NBT – 0.4KBT – 0.15KNN, 0.94NBT – 0.06BT – 0.18KNN, but superior properties in terms of low dielectric loss ($\tan\delta \leq 0.02$) over a wide range of temperature.

However, the ceramic compositions 0.7[0.85NBT – 0.15BCT] – 0.3NN, 0.6[0.85NBT – 0.15BCT] – 0.4NN and 0.7BSZT – 0.3BMT, 0.8BSZT – 0.2BMT

have shown temperature-stable dielectric properties extending from ≤ -55 ºC to ~ 210 ºC - > 300 ºC, which make them attractive for high as well as low temperature capacitors applications compared to the most of the previously reported temperature stable dielectrics.

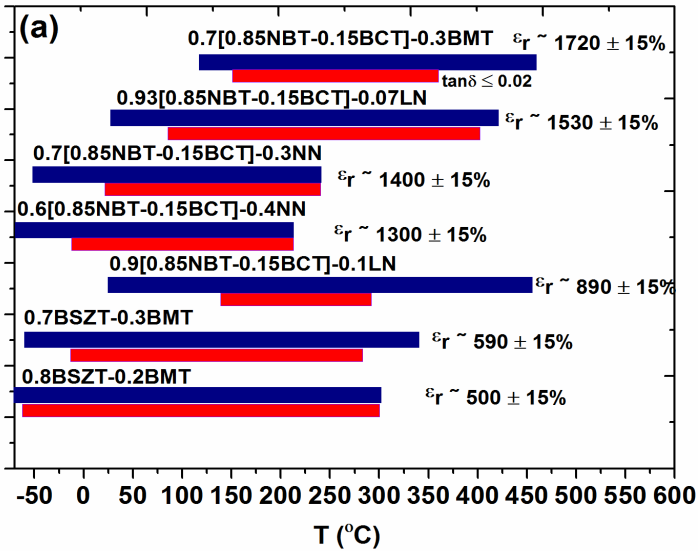

Figure 9 (a) Bar plots representing temperature-stable relative permittivity of selected studied compositions (Navy blue bar) and tanδ ≤ 0.02 (red bar) of $0.7[0.85Na_{0.5}Bi_{0.5}TiO_3 – 0.15Ba_{0.8}Ca_{0.2}TiO_3] – 0.3BiMg_{0.5}Ti_{0.5}O_3$, $0.93[0.85Na_{0.5}Bi_{0.5}TiO_3 – 0.15Ba_{0.8}Ca_{0.2}TiO_3] – 0.07LiNbO_3$, $0.7[0.85Na_{0.5}Bi_{0.5}TiO_3 – 0.15Ba_{0.8}Ca_{0.2}TiO_3] – 0.3NaNbO_3$, $0.6[0.85Na_{0.5}Bi_{0.5}TiO_3 – 0.15Ba_{0.8}Ca_{0.2}TiO_3] – 0.4NaNbO_3$, $0.9[0.85Na_{0.5}Bi_{0.5}TiO_3 – 0.15Ba_{0.8}Ca_{0.2}TiO_3] – 0.1LiNbO_3$, $0.7Ba_{0.6}Sr_{0.4}Zr_{0.2}Ti_{0.8}O_3 – 0.3BiMg_{0.5}Ti_{0.5}O_3$ and $0.8Ba_{0.6}Sr_{0.4}Zr_{0.2}Ti_{0.8}O_3 – 0.2BiMg_{0.5}Ti_{0.5}O_3$(top to bottom) and

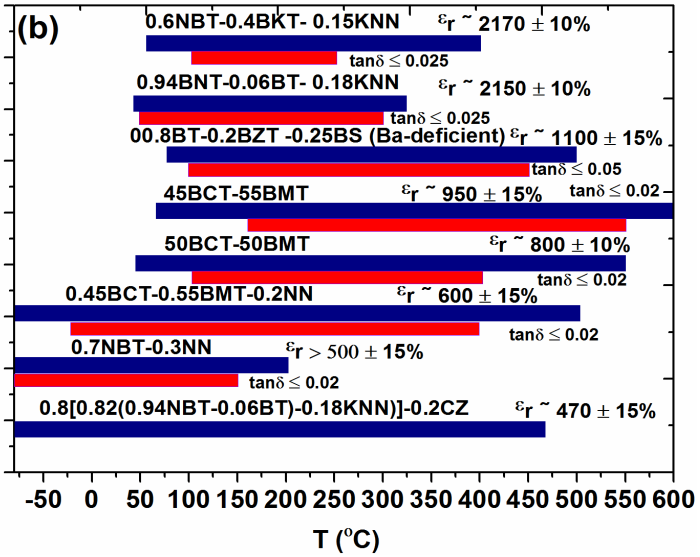

Figure 9 (b) Temperature-stable dielectrics from early literature $0.85[0.685Na_{0.5}Bi_{0.5}TiO_3 – 0.4K_{0.5}Bi_{0.5}TiO_3] – 0.15K_{0.5}Na_{0.5}NbO_3$, (Dittmer, 2012), $0.82[0.0.94Na_{0.5}Bi_{0.5}TiO_3 – 0.06BaTiO_3] – 0.18K_{0.5}Na_{0.5}NbO_3$ (Dittmer, 2011), $0.5BaTiO_3 – 0.25BaZn_{0.5}Ti_{0.5}O_3 – 0.25BiScO_3$ (Ba-deficient) (Raengthon, 2012), $0.45Ba_{0.8}Ca_{0.2}TiO_3 – 0.55BiMg_{0.5}Ti_{0.5}O_3$ (Zeb, 2014), $0.5\ Ba_{0.8}Ca_{0.2}TiO_3 – 0.5\ BiMg_{0.5}Ti_{0.5}$ (Zeb, 2013), $0.45Ba_{0.8}Ca_{0.2}TiO_3 – 0.35BiMg_{0.5}Ti_{0.5}O_3 – 0.2NaNbO_3$ (Zeb, 2014), $0.7Na_{0.5}Bi_{0.5}TiO_3 – 0.3NaNbO_3$ (Bridger, 2010) and $0.8[0.82(0.94Na_{0.5}Bi_{0.5}TiO_3 – 0.06BaTiO_3) – 0.18K_{0.5}Na_{0.5}NbO_3] – 0.2CaZrO_3$ (Acosta, 2012) top to bottom).

Future work

- Further compositional engineering to extend temperature range and attempt to increase values of relative permittivity of for example BSZT-BMT system is recommended.

- P-E loops at higher fields and charge storage measurement will be important to understand the energy storage capabilities for capacitor applications.
- Impedance spectroscopy for dielectrics will help to understand the contributions to dielectric loss mechanisms.
- SEM/TEM-EDX would be valuable technique to identify the elemental composition of materials, and also examine the presence of any chemical segregation.
- High resolution TEM study involving EDX and SAED analysis would be useful in future to examine nanoscale structure of the temperature-stable compositions. A detailed examination of microstructure and compositional segregation of the ceramics would be very useful. Atomic resolution scanning TEM at Super STEM, Daresbury is recommended
- Local structure analysis by EXAFS and XANES (using synchrotron x-ray sources) would complement TEM structural analysis

- For capacitors applications, charge storage density, voltage stability, frequency stability, and dielectric break down strength measurements would be essential in order to fully evaluate the best temperature-stable permittivity materials.

Appendix 1

Table A1.1 List of ionic radii of selected elements discussed in the solid solutions in this study.

Elements	**Ionic radii (Å)**	**Co-ordination number**	**Refrences**
Ba^{2+}	~1.61	12-fold	(Du et al., 2008)
Ca^{2+}	~1.34	12-fold	(Du et al., 2008)
Bi^{3+}	~1.3-1.38 estimated	12-fold	(Suarez et al., 2001, Sivakumar and Itoh, 2011)
Na^{1+}	~1.39	12-fold	(Du et al., 2008)
Sr^{2+}	~1.44	12-fold	(Shannon, 1976)
Mg^{2+}	~ 0.72	6-fold	(Du et al., 2008)
Zr^{4+}	~ 0.72	6-fold	(Shannon, 1976)
Ti^{4+}	~ 0.61	6-fold	(Du et al., 2008)
Nb^{5+}	~ 0.64	6-fold	(Shannon, 1976)

References

Aksel, E., Forrester, J. S., Kowalski, B., Jones, J. L. & Thomas, P. A. 2011. Phase transition sequence in sodium bismuth titanate observed using high-resolution x-ray diffraction. *Applied Physics Letters,* 99**,** 222901.

Aksel, E. & Jones, J. L. 2010. Advances in lead-free piezoelectric materials for sensors and actuators. *Sensors,* 10**,** 1935-1954.

Ang, C. & Yu, Z. 2006. High, Purely Electrostrictive Strain in Lead-Free Dielectrics. *Advanced Materials,* 18**,** 103-106.

Anthoniappen, J., Tu, C. S., Chen, P. Y., Chen, C. S., Chiu, S. J., Lee, H. Y., Ting, Y., Wang, S. F. & Chai, C. K. 2015. Structural phase stability and electric field induced relaxor–ferroelectric phase transition in $(1-x)(Bi_{0.5}Na_{0.5})TiO_3–xBaTiO_3$ ceramics. *Journal of Alloys and Compounds,* 618**,** 120-126.

Bai, W., Li, L., Wang, W., Shen, B. & Zhai, J. 2015. Phase diagram and electrostrictive effect in BNT-based ceramics. *Solid State Communications,* 206**,** 22-25.

Bokov, A. & Ye, Z.-G. 2007. Recent progress in relaxor ferroelectrics with perovskite structure. *Frontiers of Ferroelectricity.* Springer.

Buttay, C., Planson, D., Allard, B., Bergogne, D., Bevilacqua, P., Joubert, C., Lazar, M., Martin, C., Morel, H. & Tournier, D. 2011. State of the art of high temperature power electronics. *Materials Science and Engineering: B,* 176**,** 283-288.

Cao, W. & Randall, C. A. 1996. Grain size and domain size relations in bulk ceramic ferroelectric materials. *Journal of Physics and Chemistry of Solids,* 57**,** 1499-1505.

Chattopadhyay, S., Ayyub, P., Palkar, V. R. & Multani, M. 1995. Size-induced diffuse phase transition in the nanocrystalline ferroelectric $PbTiO_3$. *Physical Review B,* 52**,** 13177-13183.

Chen, Z., Li, G., Sun, X., Liu, L. & Fang, L. 2015. La_2O_3 modified $0.4(Ba_{0.8}Ca_{0.2})TiO_3–0.6Bi(Mg_{0.5}Ti_{0.5})O_3$ Ceramics for High-temperature capacitor applications. *Ceramics International*.

Cheng, S.-Y., Shieh, J., Lu, H.-Y., Shen, C.-Y., Tang, Y.-C. & Ho, N.-J. 2013. Structure analysis of bismuth sodium titanate-based A-site relaxor ferroelectrics by electron diffraction. *Journal of the European Ceramic Society,* 33**,** 2141-2153.

Chung, H.-H., Yang, C.-F., Chen, K.-H. & Diao, C.-C. 2009. The Influences of Excess Bi_2O_3 Content on the Characteristics of $0.8(Bi_{0.5}K_{0.5})TiO_3$-$0.2BaTiO_3$ Ceramics. *Ferroelectrics,* 385**,** 689-96.

Daniels, J. E., Jo, W., Rödel, J. & Jones, J. L. 2009. Electric-field-induced phase transformation at a lead-free morphotropic phase boundary: Case study in a $93\%(Bi_{0.5}Na_{0.5})TiO_3–7\%BaTiO_3$ piezoelectric ceramic. *Applied Physics Letters,* 95**,** 032904.

Directive, R. 2003. Directive 2002/95/EC of the European Parliament and of the Council of 27 January 2003 on the restriction of the use of certain hazardous substances in electrical and electronic equipment. *Official Journal of the European Union,* 13**,** L37.

Dittmer, R., Anton, E. M., Jo, W., Simons, H., Daniels, J. E., Hoffman, M., Pokorny, J., Reaney, I. M. & Rödel, J. 2012. A High-Temperature-Capacitor Dielectric Based on $K_{0.5}Na_{0.5}NbO_3$-Modified $Bi_{1/2}Na_{1/2}TiO_3–Bi_{1/2}K_{1/2}TiO_3$. *Journal of the American Ceramic Society,* 95**,** 3519-3524.

Dittmer, R., Jo, W., Damjanovic, D. & Rodel, J. 2011a. Lead-free high-temperature dielectrics with wide operational range. *Journal of Applied Physics,* 109**,** 034107-034107-5.

Dittmer, R., Jo, W., Daniels, J., Schaab, S. & Rödel, J. 2011b. Relaxor characteristics of morphotropic phase boundary $(Na_{1/2}Bi_{1/2})TiO_3$–$(Bi_{1/2}K_{1/2})TiO_3$ modified with $Bi(Zn_{1/2}Ti_{1/2})O_3$. *journal of the American Ceramic Society,* 94**,** 4283-4290.

DoITPoMS, Polarization mechanism. http://www.doitpoms.ac.uk/tlplib/dielectrics/polarisation_mechanisms.php. University of Cambridge.

Donnelly, N. J., Shrout, T. R. & Randall, C. A. 2007. Addition of a Sr, K, Nb (SKN) combination to PZT (53/47) for high strain applications. *Journal of the American Ceramic Society,* 90**,** 490-495.

Dorcet, V. & Trolliard, G. 2008. A transmission electron microscopy study of the A-site disordered perovskite $Na_{0.5}Bi_{0.5}TiO_3$. *Acta Materialia,* 56**,** 1753-1761.

Dorcet, V., Trolliard, G. & Boullay, P. 2008. Reinvestigation of phase transitions in $Na_{0.5}Bi_{0.5}TiO_3$ by TEM. Part I: First order rhombohedral to orthorhombic phase transition. *Chemistry of Materials,* 20**,** 5061-5073.

Dorcet, V., Trolliard, G. & Boullay, P. 2009. The structural origin of the antiferroelectric properties and relaxor behavior of $Na_{0.5}Bi_{0.5}TiO_3$. *Journal of Magnetism and Magnetic Materials,* 321**,** 1758-1761.

Du, H., Zhou, W., Luo, F., Zhu, D., Qu, S., Li, Y. & Pei, Z. 2008. High T_m lead-free relaxor ferroelectrics with broad temperature usage range: $0.04BiScO_3$-$0.96(K_{0.5}Na_{0.5})NbO_3$. *Journal of Applied Physics,* 104**,** 044104-044104-5.

Elissalde, b. & Ravez, J. 2001. Ferroelectric ceramics: defects and dielectric relaxations. *Journal of Materials Chemistry,* 11**,** 1957-1967.

Gao, J., Xue, D., Wang, Y., Wang, D., Zhang, L., Wu, H., Guo, S., Bao, H., Zhou, C. & Liu, W. 2011. Microstructure basis for strong piezoelectricity in Pb-free $Ba(Zr_{0.2}Ti_{0.8})O_3$-$(Ba_{0.7}Ca_{0.3})TiO_3$ ceramics. *Applied Physics Letters,* 99**,** 092901.

Guo, Y., Gu, M. & Luo, H. 2011. Antiferroelectric Phase and Pyroelectric Response in $(Na_yBi_z)Ti_{1-x}O_3(1-x)–xBaTiO_3$ Ceramics. *Journal of the American Ceramic Society,* 94**,** 1350-1353.

Guo, Y., Kakimoto, K.-i. & Ohsato, H. 2004. Ferroelectric-relaxor behavior of $(Na_{0.5}K_{0.5})NbO_3$-based ceramics. *Journal of Physics and Chemistry of Solids,* 65**,** 1831-1835.

Haertling, G. H. 1999. Ferroelectric ceramics: history and technology. *Journal of the American Ceramic Society,* 82**,** 797-818.

Hu, Z., Cui, B., Li, M. & Li, L. 2013. Novel X8R-type $BaTiO_3$-based ceramics with a high dielectric constant created by doping nanocomposites with Li–Ti–Si–O. *Journal of Materials Science: Materials in Electronics,* 24**,** 3850-3855.

Huang, C.-C. & Cann, D. P. 2008. Phase transitions and dielectric properties in Bi $(Zn_{1/2}Ti_{1/2})O_3$-$BaTiO_3$ perovskite solid solutions. *journal of Applied Physics,* 104**,** 024117-024117-4.

Huang, C.-C., Cann, D. P., Tan, X. & Vittayakorn, N. 2007. Phase transitions and ferroelectric properties in $BiScO_3$-Bi $(Zn_{1/2}Ti_{1/2})O_3$-$BaTiO_3$ solid solutions. *Journal of Applied Physics,* 102**,** 044103-044103-5.

Islam, M. S. 2000. Ionic transport in ABO_3 perovskite oxides: a computer modelling tour. *Journal of Materials Chemistry,* 10**,** 1027-1038.

Jaffe, W. 1971. Cook, and H. Jaffe. *Piezoelectric Ceramics***,** 271-80.

Jiles, D. C. 2001. *Introduction to the electronic properties of materials,* CRC Press.

Jo, W., Schaab, S., Sapper, E., Schmitt, L. A., Kleebe, H.-J., Bell, A. J. & Rödel, J. 2011. On the phase identity and its thermal evolution of lead free ($Bi_{1/2}Na_{1/2}$) TiO_3-6 mol% $BaTiO_3$. *Journal of Applied Physics,* 110**,** 074106.

Jones, G. & Thomas, P. 2002. Investigation of the structure and phase transitions in the novel A-site substituted distorted perovskite compound $Na_{0.5}Bi_{0.5}TiO_3$. *Acta Crystallographica Section B: Structural Science,* 58**,** 168-178.

Ke, X., Zhang, L., Wang, Y. & Ren, X. Crosssover from normal ferroelectrics to relaxor-spontaneous relaxor to normal ferroelectric transition at the crossover compositions. Applications of Ferroelectrics, 2009. ISAF 2009. 18th IEEE International Symposium on the, 2009. IEEE, 1-5.

Kingery, W. D. U., D. R. (Donald Robert) & Bowen, Harvey Kent 1976. *Introduction to ceramics*, Wiley, New York.

Kittel, C. 1951. Domain boundary motion in ferroelectric crystals and the dielectric constant at high frequency. *Physical Review,* 83**,** 458.

König, J., Spreitzer, M., Jančar, B., Suvorov, D., Samardžija, Z. & Popovič, A. 2009. The thermal decomposition of $K_{0.5}Bi_{0.5}TiO_3$ ceramics. *Journal of the European Ceramic Society*, 29**,** 1695-1701.

Kounga, A. B., Granzow, T., Aulbach, E., Hinterstein, M. & Rödel, J. 2008. High-temperature poling of ferroelectrics. *Journal of Applied Physics,* 104**,** 024116.

Kreisel, J., Dkhil, B., Bouvier, P. & Kiat, J.-M. 2002. Effect of high pressure on relaxor ferroelectrics. *Physical Review B,* 65**,** 172101.

Kruea-In, C., Rujijanagul, G., Zhu, F. Y. & Milne, S. J. 2012. Relaxor behaviour of $K_{0.5}Bi_{0.5}TiO_3$-$BiScO_3$ ceramics. *Applied Physics Letters,* 100**,** 202904.

Lee, J.-K., Yi, J. Y. & Hong, K.-S. 2001. Relationship between Structure and Dielectric Property in (1-x)($Na_{1/2}Bi_{1/2}$)TiO_3–x$PbZrO_3$ Ceramics. *Japanese Journal of Applied Physics,* 40**,** 6003.

Leontsev, S. O. & Eitel, R. E. 2010. Progress in engineering high strain lead-free piezoelectric ceramics. *Science and Technology of Advanced Materials,* 11**,** 044302.

Levi, R. D. 2009. *Solid solution trends that impact electrical design of submicron layers in dielectric capacitors.* The Pennsylvania State University.

Li, F., Jin, L., Xu, Z. & Zhang, S. 2014. Electrostrictive effect in ferroelectrics: An alternative approach to improve piezoelectricity. *Applied Physics Reviews,* 1**,** 011103.

Li, M., Feteira, A. & Sinclair, D. C. 2009. Relaxor ferroelectric-like high effective permittivity in leaky dielectrics/oxide semiconductors induced by electrode effects: A case study of CuO ceramics. *Journal of Applied Physics,* 105**,** 114109.

Lim, J. B., Zhang, S., Kim, N. & Shrout, T. R. 2009. High-Temperature Dielectrics in the $BiScO_3$–$BaTiO_3$–($K_{1/2}Bi_{1/2}$)TiO_3 Ternary System. *Journal of the American Ceramic Society,* 92**,** 679-682.

Lines, M. E. & Glass, A. M. 2001. *Principles and applications of ferroelectrics and related materials*, Clarendon press Oxford.

Lu, Z. & Calvarin, G. 1995. Frequency dependence of the complex dielectric permittivity of ferroelectric relaxors. *Physical Review B,* 51**,** 2694.

Ma, C., Guo, H., Beckman, S. P. & Tan, X. 2012. Creation and destruction of morphotropic phase boundaries through electrical poling: a case study of lead-free ($Bi_{1/2}$ $Na_{1/2}$)TiO_3-$BaTiO_3$ piezoelectrics. *Physical review letters,* 109**,** 107602.

Martirena, H. & Burfoot, J. 1974. Grain-size effects on properties of some ferroelectric ceramics. *Journal of Physics C: Solid State Physics,* 7**,** 3182.

Megaw, H. D. 1952. Origin of ferroelectricity in barium titanate and other perovskite-type crystals. *Acta Crystallographica,* 5**,** 739-749.

Merz, W. J. 1954. Domain Formation and Domain Wall Motions in Ferroelectric BaTi O 3 Single Crystals. *Physical Review,* 95**,** 690.

Moulson, A. J. & Herbert, J. M. 2003. *Electroceramics: materials, properties, applications,* John Wiley & Sons.

Nishino, A. 1996. Capacitors: operating principles, current market and technical trends. *Journal of power sources,* 60**,** 137-147.

Ogihara, H., Randall, C. A. & Trolier-McKinstry, S. 2009. High-Energy Density Capacitors Utilizing $0.7BaTiO_3$–$0.3\ BiScO_3$ Ceramics. *Journal of the American Ceramic Society,* 92**,** 1719-1724.

Panda, P. 2009. Review: environmental friendly lead-free piezoelectric materials. *Journal of materials science,* 44**,** 5049-5062.

Park, H.-Y., Cho, K.-H., Paik, D.-S., Nahm, S., Lee, H.-G. & Kim, D.-H. 2007. Microstructure and piezoelectric properties of lead-free $(1-x)(Na_{0.5}K_{0.5})NbO_{3-x}CaTiO_3$ ceramics. *Journal of Applied Physics,* 102**,** 124101-124101-5.

Pietrovito.A, D. P. 2015. *Describing crystallin solids* [Online]. Available: http://www.seas.upenn.edu/~chem101/sschem/solidstatechem.html [Accessed 26 th March 2015].

Prabu, M., Banu, I. S., Gobalakrishnan, S. & Chavali, M. 2013. Electrical and ferroelectric properties of undoped and La-doped PZT (52/48) electroceramics synthesized by sol–gel method. *Journal of Alloys and Compounds,* 551**,** 200-207.

Prakash, S. 2008-09. *VK Physics class XII,* India, V.K Interprises India.

Qiao, S., Wu, J., Wu, B., Zhang, B., Xiao, D. & Zhu, J. 2012. Effect of $Ba_{0.85}Ca_{0.15}Ti_{0.90}Zr_{0.10}O_3$ content on the microstructure and electrical properties of $Bi_{0.51}(Na_{0.82}K_{0.18})_{0.50}TiO_3$ ceramics. *Ceramics International,* 38**,** 4845-4851.

Qing Xu, S. C., Wen Chen, Sujuan Wu, Joonghee Lee, Jing Zhou, Huajun Sun, Yueming Li 2004. Structure, piezoelectric properties and ferroelectric properties of $(Na_{0.5}Bi_{0.5})_{1-x}BaxTiO_3$ system. *Journal of Alloys and Compounds,* 381**,** 221-225.

Qiu, W. & Hng, H. H. 2002. Effects of dopants on the microstructure and properties of PZT ceramics. *Materials chemistry and physics,* 75**,** 151-156.

Raengthon, N., Brown-Shaklee, H. J., Brennecka, G. L. & Cann, D. P. 2013a. Dielectric properties of $BaTiO_3$–Bi $(Zn_{1/2}Ti_{1/2})$ O_3–$NaNbO_3$ solid solutions. *Journal of Materials Science,* 48**,** 2245-2250.

Raengthon, N., Brown-Shaklee, H. J., Brennecka, G. L. & Cann, D. P. 2013b. Dielectric properties of $BaTiO_3$–Bi$(Zn_{1/2}Ti_{1/2})O_3$–$NaNbO_3$ solid solutions. *Journal of Materials Science,* 48**,** 2245-2250.

Raengthon, N. & Cann, D. P. 2012. Dielectric relaxation in $BaTiO_3$–Bi $(Zn_{1/2}Ti1_{/2})$ O_3 ceramics. *journal of the American Ceramic Society,* 95**,** 1604-1612.

Raengthon, N., Sebastian, T., Cumming, D., Reaney, I. M. & Cann, D. P. 2012. $BaTiO_3$–Bi $(Zn_{1/2}Ti_{1/2})$ O_3–$BiScO_3$ Ceramics for High-Temperature Capacitor Applications. *Journal of the American Ceramic Society,* 95**,** 3554-3561.

Rödel, J., Jo, W., Seifert, K. T., Anton, E. M., Granzow, T. & Damjanovic, D. 2009. Perspective on the Development of Lead-free Piezoceramics. *Journal of the American Ceramic Society,* 92**,** 1153-1177.

Royles, A., Bell, A., Daniels, J., Milne, S. & Comyn, T. 2011. Observation of a time-dependent structural phase transition in potassium sodium bismuth titanate. *Applied Physics Letters,* 98**,** 182904-182904-3.

Royles, A., Bell, A., Jephcoat, A., Kleppe, A., Milne, S. & Comyn, T. 2010. Electric-field-induced phase switching in the lead free piezoelectric potassium sodium bismuth titanate. *Applied Physics Letters,* 97**,** 132909-132909-3.

Sehirlioglu, A., Sayir, A. & Dynys, F. 2009. High temperature properties of $BiScO_3$–$PbTiO_3$ piezoelectric ceramics. *Journal of Applied Physics,* 106**,** 014102-014102-7.

Selvamani, R., Singh, G., Tiwari, V. & Gupta, P. 2012. Oxygen vacancy related relaxation and conduction behavior in $(1-x)$NBT-$xBiCrO_3$ solid solution. *physica status solidi (a),* 209**,** 118-125.

Shannon, R. 1976. Revised effective ionic radii and systematic studies of interatomic distances in halides and chalcogenides. *Acta Crystallographica Section A: Crystal Physics, Diffraction, Theoretical and General Crystallography,* 32**,** 751-767.

Shi, J., Fan, H., Liu, X. & Bell, A. J. 2014. Large electrostrictive strain in $(Bi_{0.5}Na_{0.5})TiO_3$–$BaTiO_3$–$(Sr_{0.7}Bi_{0.2})TiO_3$ solid solutions. *Journal of the American Ceramic Society,* 97**,** 848-853.

Shrout, T. R. & Zhang, S. J. 2007. Lead-free piezoelectric ceramics: Alternatives for PZT? *Journal of Electroceramics,* 19**,** 113-126.

Simões, A., da Costa, G., Ramirez, M., Varela, J. A. & Longo, E. 2005. Effect of the excess of bismuth on the morphology and properties of the $BaBi_2Ta_2O_9$ ceramics. *Materials Letters,* 59**,** 656-661.

Sivakumar, T. & Itoh, M. 2011. Ferroelectric phase transitions in new Aurivillius oxides: $Bi_{2+2x}Sr_{1-2x}Nb_{2-x}Sc_xO_9$. *Journal of Materials Chemistry,* 21**,** 10865-10870.

Smolensky, G. 1984. Ferroelectrics with diffuse phase transition. *Ferroelectrics,* 53**,** 129-135.

Streiffer, S., Parker, C., Romanov, A., Lefevre, M., Zhao, L., Speck, J., Pompe, W., Foster, C. & Bai, G. 1998. Domain patterns in epitaxial rhombohedral ferroelectric films. I. Geometry and experiments. *Journal of applied physics,* 83**,** 2742-2753.

Stringer, C., Shrout, T. & Randall, C. 2007. High-temperature perovskite relaxor ferroelectrics: A comparative study. *Journal of Applied Physics,* 101**,** 054107-054107-6.

Suarez, D. Y., Reaney, I. M. & Lee, W. E. 2001. Relation between tolerance factor and Tc in Aurivillius compounds. *Journal of Materials Research,* 16**,** 3139-3149.

Tadashi Takenaka, K.-i. M. a. K. S. 1991. $(Bi_{1/2}Na_{1/2})TiO_3$-$BaTiO_3$ System for Lead-Free Piezoelectric Ceramics. *Japanese Journal of Applied Physics,* 30**,** 2236-2239.

Tang, X., Chew, K.-H. & Chan, H. 2004. Diffuse phase transition and dielectric tunability of $Ba(Zr_yTi_{1-y})O_3$ relaxor ferroelectric ceramics. *Acta Materialia,* 52**,** 5177-5183.

Trolliard, G. & Dorcet, V. 2008. Reinvestigation of phase transitions in $Na_{0.5}Bi_{0.5}TiO_3$ by TEM. Part II: Second order orthorhombic to tetragonal phase transition. *Chemistry of Materials,* 20**,** 5074-5082.

Uchino, K. 1994. Relaxor ferroelectric devices. *Ferroelectrics,* 151**,** 321-330.

Ullah Jan, S., Zeb, A. & Milne, S. J. 2014. Electrical Properties of Ca-modified $Na_{0.5}Bi_{0.5}TiO_3$–$BaTiO_3$ ceramics. *Ceramics International,* 40**,** 15439-15445.

Wada, S., Yamato, K., Pulpan, P., Kumada, N., Lee, B.-Y., Iijima, T., Moriyoshi, C. & Kuroiwa, Y. 2010. Piezoelectric properties of high Curie temperature barium titanate–bismuth perovskite-type oxide system ceramics. *Journal of Applied Physics,* 108**,** 094114.

Wang, S.-F., Li, J.-H., Hsu, Y.-F., Wu, Y.-C., Lai, Y.-C. & Chen, M.-H. 2013. Dielectric properties and microstructures of non-reducible high-temperature stable X9R ceramics. *Journal of the European Ceramic Society,* 33**,** 1793-1799.

Wang, X., Choy, S., Tang, X. & Chan, H. 2005a. Dielectric behavior and microstructure of $(Bi_{1/2}Na_{1/2})TiO_3$–$(Bi_{1/2}K_{1/2})TiO_3$–$BaTiO_3$ lead-free piezoelectric ceramics. *Journal of applied physics,* 97**,** 104101-104101-4.

Wang, X., Tang, X., Kwok, K., Chan, H. & Choy, C. 2005b. Effect of excess Bi_2O_3 on the electrical properties and microstructure of $(Bi_{1/2}Na_{1/2})TiO_3$ ceramics. *Applied Physics A,* 80**,** 1071-1075.

Wolfe, J. 2015. *AC circuits: alternating current electricity* [Online]. Available: http://www.animations.physics.unsw.edu.au//jw/AC.html#capacitors [Accessed 27th March 2015].

Xiong, B., Hao, H., Zhang, S., Liu, H. & Cao, M. 2011. Structure, dielectric properties and temperature stability of $BaTiO_3$–Bi $(Mg_{1/2}Ti_{1/2})O_3$ perovskite solid solutions. *Journal of the American Ceramic Society,* 94**,** 3412-3417.

Xu, Q., Huang, Y.-H., Chen, M., Chen, W., Kim, B.-H. & Ahn, B.-K. 2008. Effect of bismuth deficiency on structure and electrical properties of $(Na_{0.5}Bi_{0.5})$-$0.93Ba_{0.07}TiO_3$ ceramics. *Journal of Physics and Chemistry of Solids,* 69**,** 1996-2003.

Xu, Q., Li, T., Hao, H., Zhang, S., Wang, Z., Cao, M., Yao, Z. & Liu, H. 2015. Enhanced energy storage properties of $NaNbO_3$ modified $Bi_{0.5}Na_{0.5}TiO_3$ based ceramics. *Journal of the European Ceramic Society,* 35**,** 545-553.

Yang, J., Liu, P., Bian, X., Jing, H., Wang, Y., Zhang, Y., Wu, Y. & Song, W. 2011. Dielectric, ferroelectric and piezoelectric properties of $Bi_{0.5}Na_{0.5}TiO_3$–$(Ba_{0.7}Ca_{0.3})TiO_3$ ceramics at morphotropic phase boundary composition. *Materials Science & Engineering B,* 176**,** 260-265.

Yu, H. & Ye, Z.-G. 2008. Dielectric properties and relaxor behavior of a new (1-x)$BaTiO_3$–x$BiAlO_3$ solid solution. *Journal of Applied Physics,* 103**,** 034114-034114-5.

Yun, S., Wang, X., Shi, J. & Xu, D. 2009a. Effects of chemical modification on the structural and electrical properties of $(Ba_{0.90}Ca_{0.10})_{0.90}$ $(Na_{0.5}Bi_{0.5})_{0.10}TiO_3$ ceramics. *Journal of alloys and compounds,* 485**,** 610-615.

Yun, S., Wang, X., Shi, J., Zhu, J. & Xu, D. 2009b. Ferroelectric properties of barium calcium titanate ceramics doped with bismuth oxide. *Materials Letters,* 63**,** 1883-1885.

Zeb, A., Bai, Y., Button, T. & Milne, S. J. 2014. Temperature-Stable Relative Permittivity from− 70 °C to 500 °C in $(Ba_{0.8}Ca_{0.2})TiO_3$–$Bi(Mg_{0.5}Ti_{0.5})O_3$–$NaNbO_3$ Ceramics. *Journal of the American Ceramic Society,* 97**,** 2479-2483.

Zeb, A. & Milne, S. J. 2013a. Dielectric and Piezoelectric Properties of $(1-x)K_{0.5}Bi_{0.5}TiO_3$–x$Ba(Ti_{0.8}Zr_{0.2})O_3$ Ceramics. *Journal of the American Ceramic Society,* 96**,** 3089-3093.

Zeb, A. & Milne, S. J. 2013b. Dielectric Properties of $Ba_{0.8}Ca_{0.2}TiO_3$–$Bi(Mg_{0.5}Ti_{0.5})O_3$–$NaNbO_3$ Ceramics. *Journal of the American Ceramic Society,* 96**,** 3701-3703.

Zeb, A. & Milne, S. J. 2013c. Stability of High-Temperature Dielectric Properties for (1−x) $Ba_{0.8}Ca_{0.2}TiO_3$–xBi $(Mg_{0.5}Ti_{0.5})O_3$ Ceramics. *Journal of the American Ceramic Society,* 96**,** 2887-2892.

Zeb, A. & Milne, S. J. 2013d. Stability of High-Temperature Dielectric Properties for (1−x) $Ba_{0.8}Ca_{0.2}TiO_3$–xBi$(Mg_{0.5}Ti_{0.5})O_3$ Ceramics. *Journal of the American Ceramic Society,* 96**,** 2887-2892.

Zeb, A. & Milne, S. J. 2014a. Low variation in relative permittivity over the temperature range 25–450 °C for ceramics in the system (1−x)[$Ba_{0.8}Ca_{0.2}TiO_3$]–x[$Bi(Zn_{0.5}Ti_{0.5})O_3$]. *Journal of the European Ceramic Society,* 34**,** 1727-1732.

Zeb, A. & Milne, S. J. 2014b. Temperature-stable dielectric properties from−20 °C to 430 °C in the system $BaTiO_3$–Bi $(Mg_{0.5}Z_{0.5})O_3$. *Journal of the European Ceramic Society,* 34**,** 3159-3166.

Zhang, Q., Li, Z., Li, F. & Xu, Z. 2011. Structural and Dielectric Properties of $Bi(Mg_{1/2}Ti_{1/2})O_3$–$BaTiO_3$ Lead-Free Ceramics. *Journal of the American Ceramic Society,* 94**,** 4335-4339.

Zhang, S., Shrout, T. R., Nagata, H., Hiruma, Y. & Takenaka, T. 2007. Piezoelectric properties in $(K_{0.5}Bi_{0.5})TiO_3$-$(Na_{0.5}Bi_{0.5})TiO_3$-$BaTiO_3$ lead-free ceramics. *Ultrasonics, Ferroelectrics, and Frequency Control, IEEE Transactions on,* 54**,** 910-917.

Zhang, X., Chen, Z., Cross, L. E. & Schulze, W. 1983. Dielectric and piezoelectric properties of modified lead titanate zirconate ceramics from 4.2 to 300 K. *Journal of Materials Science,* 18**,** 968-972.

Zhang, Y.-R., Li, J.-F., Zhang, B.-P. & Peng, C.-E. 2008a. Piezoelectric and ferroelectric properties of Bi-compensated $(Bi_{1/2}Na_{1/2})TiO_3$–$(Bi_{1/2}K_{1/2})TiO_3$ lead-free piezoelectric ceramics. *Journal of Applied Physics,* 103**,** 074109.

Zhang, Y. R., Li, J. F. & Zhang, B. P. 2008b. Enhancing Electrical Properties in NBT–KBT Lead-Free Piezoelectric Ceramics by Optimizing Sintering Temperature. *Journal of the American Ceramic Society,* 91**,** 2716-2719.

Zhou, C., Liu, X., Li, W. & Yuan, C. 2009. Microstructure and electrical properties of $Na_{0.5}Bi_{0.5}TiO_3$–$Bi_{0.5}K_{0.5}TiO_3$–$LiNbO_3$ lead-free piezoelectric ceramics. *Journal of Physics and Chemistry of Solids,* 70**,** 541-545.

Zhou, C., Yang, H., Zhou, Q., Chen, G., Li, W. & Wang, H. 2013. Effects of Bi excess on the structure and electrical properties of high-temperature $BiFeO_3$–$BaTiO_3$ piezoelectric ceramics. *Journal of Materials Science: Materials in Electronics,* 24**,** 1685-1689.

Zhu, F., Skidmore, T., Bell, A., Comyn, T., James, C., Ward, M. & Milne, S. 2011. Diffuse dielectric behaviour in $Na_{0.5}K_{0.5}NbO_3$–$LiTaO_3$–$BiScO_3$ lead-free ceramics. *Materials Chemistry and Physics,* 129**,** 411-417.